Technische Universität München
TUM School of Natural Sciences

# The emergence of a new sky: First associations of IceCube high-energy neutrinos with Active Galactic Nuclei

Chiara Bellenghi

Vollständiger Abdruck der von der TUM School of Natural Sciences der Technischen Universität München zur Erlangung einer

Doktorin der Naturwissenschaften (Dr. rer. nat.)

genehmigten Dissertation.

| | |
|---|---|
| Vorsitz: | Prof. Dr. Alejandro Ibarra |
| Prüfende der Dissertation: | 1. Prof. Dr. Elisa Resconi |
| | 2. Prof. Dr. Laura Fabbietti |

Die Dissertation wurde am 30.07.2024 bei der Technischen Universität München eingereicht und durch die TUM School of Natural Sciences am 12.09.2024 angenommen.

# *Abstract*

In 2022, working with the IceCube collaboration, we reported $4.2\,\sigma$ evidence for neutrino emission from NGC 1068, a non-jetted, Seyfert 2 active galactic nucleus (AGN) and the most significant extragalactic neutrino source to date. The detection of high-energy non-thermal emission from a non-jetted AGN invites us to re-evaluate the role of AGN jets in neutrino emission.

This thesis contributes to advancing our understanding of AGN as neutrino emitters. In collaboration with experts, we conduct a comprehensive multi-messenger study of NGC 1068, constraining the neutrino-emitting region to the vicinity of its central core, specifically its X-ray bright corona. Additionally, assuming a correlation between X-ray and neutrino emissions, we provide a model-independent estimate of the total neutrino flux produced by all non-jetted AGN.

To test this correlation, we extend the analysis of IceCube with 50% more data. First, we reassess the neutrino emission from NGC 1068, confirming the previously measured flux. Then, we develop a novel selection of 47 X-ray bright Seyfert galaxies and test them as candidate neutrino sources. The Seyfert 1 galaxy NGC 7469 emerges as the most prominent, with a significance of $2.4\,\sigma$. Furthermore, a population test shows that 11 of our selected sources contribute to a binomial excess at $3.3\,\sigma$ significance, supporting the emergence of X-ray bright AGN as the first population of neutrino sources. The measured neutrino emissions from these AGN exhibit different energies and spectral shapes, suggesting diverse neutrino production mechanisms among bright X-ray sources and paving the way for future studies.

While investigating non-jetted AGN as neutrino emitters, we also validate external claims of a $\sim 5\,\sigma$ correlation between jetted AGN of the blazar type in the 5BZCAT catalog and neutrino hotspots based on 7 years of public IceCube data. Within this work, we develop a novel open-source software tool to search for neutrino point sources in 10 years of IceCube public data. With the new tool, we reassess the claimed correlation on the larger, more sensitive neutrino sample and find it disappears completely. Our results suggest that the claimed discovery was likely due to statistical fluctuations.

Overall, this thesis investigates the emergent class of AGN as prominent neutrino emitters, unexpectedly identifying non-jetted AGN as the primary sources.

# *Zusammenfassung*

Im Jahr 2022 haben wir in Zusammenarbeit mit der IceCube-Kollaboration $4.2\,\sigma$ Hinweise auf Neutrinoemissionen von NGC 1068, einem nicht-gejetten Seyfert-2-Aktivgalaxienkern (AGN) und der bislang bedeutendsten extragalaktischen Neutrinoquelle, berichtet. Der Nachweis hochenergetischer nicht-thermischer Emissionen von einem nicht-gejetten AGN veranlasst uns, die Rolle von AGN-Jets bei der Neutrinoemission neu zu bewerten.

Diese Dissertation trägt dazu bei, unser Verständnis von AGN als Neutrinoemittenten zu erweitern. In Zusammenarbeit mit Experten führen wir eine umfassende Multi-Messenger-Studie von NGC 1068 durch und begrenzen die neutrinoemittierende Region auf die Nähe seines zentralen Kerns, insbesondere seiner röntgenhellen Korona. Zusätzlich liefern wir unter der Annahme einer Korrelation zwischen Röntgen- und Neutrinoemissionen eine modellunabhängige Schätzung des gesamten Neutrinoflusses, der von allen nicht-gejetten AGN erzeugt wird.

Um diese Korrelation zu testen, erweitern wir die Analyse der IceCube-Daten um 50% mehr Daten. Zunächst bewerten wir die Neutrinoemission von NGC 1068 neu und bestätigen den zuvor gemessenen Fluss. Dann entwickeln wir eine neuartige Auswahl von 47 röntgenhellen Seyfert-Galaxien und testen sie als Kandidaten für Neutrinoquellen. Die Seyfert-1-Galaxie NGC 7469 erweist sich als die prominenteste mit einer Signifikanz von $2.4\,\sigma$. Darüber hinaus zeigt ein Populationstest, dass 11 unserer ausgewählten Quellen zu einem binomialen Überschuss mit einer Signifikanz von $3.3\,\sigma$ beitragen, was die Entstehung von röntgenhellen AGN als erste Population von Neutrinoquellen unterstützt. Die gemessenen Neutrinoemissionen dieser AGN weisen unterschiedliche Energien und Spektralformen auf, was auf verschiedene Neutrinoproduktionsmechanismen unter den hellen Röntgenquellen hinweist und den Weg für zukünftige Studien ebnet.

Während der Untersuchung nicht-gejetteter AGN als Neutrinoemittenten validieren wir auch externe Behauptungen einer $\sim 5\,\sigma$-Korrelation zwischen gejetteten AGN vom Blazar-Typ im 5BZCAT-Katalog und Neutrino-Hotspots basierend auf 7 Jahren öffentlicher IceCube-Daten. In dieser Arbeit entwickeln wir ein neuartiges Open-Source-Software-Tool, um Neutrinopunktquellen in 10 Jahren öffentlich zugänglichen IceCube-Daten zu suchen. Mit dem neuen Tool bewerten wir die behauptete Korrelation in der größeren, empfindlicheren Neutrino-Stichprobe neu und stellen fest, dass sie vollständig verschwindet. Unsere Ergebnisse deuten darauf hin, dass die behauptete Entdeckung wahrscheinlich auf statistische Schwankungen zurückzuführen ist.

Diese Dissertation untersucht insgesamt die aufkommende Klasse von AGN als bedeutende Neutrinoemittenten und identifiziert dabei unerwartet nicht-gejettete AGN als die primären Quellen.

# *Contents*

**Abstract** **I**

**List of Figures** **V**

**List of Tables** **IX**

**1 Introduction** **1**

**2 The High-Energy Cosmos** **5**
2.1 The cosmic-ray spectrum . . . . . 5
2.2 The cosmic connections . . . . . 8
2.3 Astrophysical accelerator candidates . . . . . 16

**3 NGC 1068: A Non-Jetted AGN as a Cosmic Laboratory** **23**
3.1 A multi-messenger picture . . . . . 25
3.2 Hidden sources of astrophysical neutrinos . . . . . 32
3.3 An estimation of the diffuse neutrino background from non-jetted AGN . . . . . 34

**4 The IceCube Neutrino Observatory** **39**
4.1 Neutrino detection principle . . . . . 39
4.2 Atmospheric neutrinos . . . . . 43
4.3 The IceCube detector . . . . . 45
4.4 Data acquisition and up-going muon tracks selection . 47
4.5 Directional reconstruction . . . . . 49
4.6 Energy reconstruction . . . . . 52
4.7 Final sample of up-going muon tracks . . . . . 55
4.8 Realtime issue of neutrino alerts . . . . . 60

**5 Methods to Search for Neutrino Point-like Sources** **61**
5.1 Hypothesis test . . . . . 62
5.2 Signal and background PDFs . . . . . 64
5.3 Analysis performance . . . . . 69
5.4 Significance map of the Northern sky . . . . . 75

**6 Point-source Searches with IceCube Public Data** **77**
6.1 The SkyLLH analysis framework . . . . . 77
6.2 The public release of ten years of neutrino data . . . . 78
6.3 A Point-source analysis with public data . . . . . 80
6.4 Recovery of the fit paramenters . . . . . 82
6.5 Sensitivity to an astrophysical signal . . . . . 83

6.6 Time-dependent neutrino emission profiles . . . . . 84
6.7 Applications and outlook . . . . . 86

**7 Methods to Unveil Populations of Weaker Sources 87**
7.1 Neutrino hotspots as a population of sources . . . . . 87
7.2 Neutrino emission from a catalog of subdominant sources: a binomial test . . . . . 98
7.3 Spatial correlation of neutrino hotspots with source catalogs . . . . . 99

**8 Results from Searches for Steady Neutrino Emission 105**
8.1 Search for an emergent population of hotspots . . . . . 105
8.2 Search for neutrino emission in the Northern sky . . . 109
8.3 Are blazars responsible for unassociated hotspots? . . 125

**9 Conclusion 133**

**Acknowledgements 137**

**A Abbreviations and Glossary 139**

**B Supplementary Material for the Hotspot Population Analysis 141**
B.1 Hotspot counts from background simulations . . . . . 141

**C Search for Neutrino Point Sources in the Northern Sky 149**
C.1 Monte Carlo datasets for the up-going muon tracks selection . . . . . 149
C.2 Signal spatial KDE PDF for the IC79 dataset . . . . . 151
C.3 Test-statistic distributions under the null hypothesis . . 152
C.4 Uncertainty on the diffuse astrophysical background . 154
C.5 Neutrino sky maps assuming fixed power-law spectral indices . . . . . 158
C.6 Validation of Wilks' theorem . . . . . 159
C.7 More results on the Seyfert candidate sources . . . . . 161

**D SkyLLH Interface for Point-Source Analyses with 10 Years of IceCube Public Data 165**
D.1 Background test-statistic distributions at various declinations . . . . . 165
D.2 Signal injection from public detector response matrix . 165
D.3 Energy PDF ratio at the location of TXS 0506+056 . . . 167

**Bibliography 169**

# List of Figures

2.1 All Particle spectrum 6
2.2 Contribution from different nuclei to the cosmic-ray spectrum 6
2.3 Attenuation length of protons in the CMB 8
2.4 Attenuation length of photons in the EBL and CMB 11
2.5 Astrophysical diffuse neutrino flux 12
2.6 Comparison of different astrophysical neutrino fluxes 13
2.7 Neutrino flavor flux ratio over astrophysical distances 14
2.8 Multi-messenger diffuse energy densitites 15
2.9 Hillas plot for potential cosmic-ray sources 17
2.10 AGN unification scheme 19
2.11 SED of AGN of different classes 21

3.1 P-value map around NGC 1068 with an impression of the AGN 23
3.2 Example optical spectra of type I and II Seyfert galaxies 25
3.3 Multi-messenger SED of NGC 1068 26
3.4 Radio image of NGC 1068 at 1.7 GHz 29
3.5 Hard X-ray energy flux of NGC 1068 30
3.6 Cross-section of photo-hadronic interactions 33
3.7 Gamma-rays optical depth to pair production near the SMBH 33
3.8 X-ray and gamma-ray sensitivity to point sources 34
3.9 Intrinsic cosmic X-ray background flux 35
3.10 Spectrum fitted to the measured neutrino flux of NGC 1068 36
3.11 Diffuse neutrino background from X-ray AGN 37

4.1 Deep inelastic $\nu$ – Nucleus cross section 41
4.2 Sketch of the Cherenkov cone 41
4.3 Photon propagation in the ice for a $\nu_e$-induced cascade 42
4.4 Photon propagation in the ice for a muon track 42
4.5 Photon propagation in the ice for a $\nu_\tau$-induced double cascade 43
4.6 Muon and neutrino atmospheric fluxes 44
4.7 IceCube design and instrumentation 46
4.8 Trigger level versus final level trigger rates 49
4.9 Residual arrival time of photons and angular resolution 50
4.10 Muon energy losses 53
4.11 Neutrino energy fraction of the muon track 54
4.12 Truncated energy versus DNN energy reconstruction 54
4.13 Neutrino cross-section for absorption in the Earth 56
4.14 Data-MC agreement for the IC86 season 57
4.15 IC79 and IC86 detector geometries 58

4.16 Data-MC agreement for the IC79 season 58
4.17 Effective area as a function of the neutrino energy 59

5.1 Discovery potential evolution over the years 61
5.2 Angular uncertainty term in the signal PDF 66
5.3 Signal spatial PDF for the IC86 dataset modeled with KDEs 68
5.4 Distribution of reconstructed muon energies 68
5.5 Two-dimensional background PDF 69
5.6 Recovery of the injected parameters for $\gamma = 2.0$ 70
5.7 Recovery of the injected parameters for $\gamma = 3.2$ 71
5.8 Recovery of the injected parameters across the Northern sky 71
5.9 Background *TS* distributions at various declinations 73
5.10 Sensitivity and $5\sigma$ discovery potential across the Northern sky 73
5.11 Differential sensitivity in the Northern Sky 74

6.1 Coverage of the angular uncertainty estimator 79
6.2 Pull correction for the angular uncertainty estimator 79
6.3 Internal versus public signal energy PDF 81
6.4 Biases in the fit parameters of the public data analysis 82
6.5 Biases in the fit parameters of the public data analysis 83
6.6 Reproducibility of published results 84
6.7 Public data profile likelihood for the flux parameters of NGC 1068 84
6.8 Fit of the neutrino flare from TXS 0506+056 86

7.1 Hotspot counts above various significance threhosholds 89
7.2 KS test on the Poisson hotspot counts 89
7.3 Parametrization of background hotspots counts 90
7.4 HPA on a simulated sky map 90
7.5 HPA background test-statistic distribution 91
7.6 Hotspot localization at the horizon 93
7.7 Avergae $-\log_{10} p$ versus signal strength 94
7.8 *TS* distributions for the sensitivity to 64 equal strength sources 94
7.9 HPA sensitivity with new signal injection pool 95
7.10 Controlled hotspot injections 95
7.11 Background hotspot counts for various astrophysical backgrounds 96
7.12 HPA sensitvity 97
7.13 5BZCAT and RFC densities on the sky 100
7.14 Declination distribution of 5BZCAT and RFC sources 100
7.15 5BZCAT – hotspots correlation with the 7-yr neutrino sky map 102
7.16 Pseudo-experiments for the correlation with the 5BZCAT 103
7.17 Pseudo-experiments for the correlation with the RFC 103

8.1 HPA result 106
8.2 Trial correction for the hotspot population analysis 106
8.3 HPA result with no astrophysical background 107
8.4 HPA 90% C.L. UL on a population of standard candles 108
8.5 Neutrino sky map for the free spectral index hypothesis 110
8.6 Zoomed-in sky map around NGC 1068 110
8.7 Background TS distribution at the declination of NGC 1068 112

8.8 Profile likelihood for the flux parameters of NGC 1068. 112
8.9 Angular and energy distribution of events around NGC 1068 113
8.10 Best-fit muon-neutrino flux from NGC 1068 113
8.11 Evolution of the NGC 1068's hotspot localization 114
8.12 Binomial excess from the list of gamma-ray sources 115
8.13 Observed versus intrinsic X-ray fluxes 117
8.14 Correlation between $14-195$ keV and $20-50$ keV X-ray fluxes 117
8.15 Background *TS* distribution at the declination of NGC 7469 118
8.16 Profile likelihood for the flux parameters of NGC 1068, NGC 7469, NGC 4151, and CGCG 420−015. 119
8.17 Zoomed-in sky map around NGC 7469 119
8.18 *TS* dependence on single events 120
8.19 Binomial excess from the list of 47 Seyfert galaxies 120
8.20 Binomial excess from the list of 48 Seyfert galaxies 121
8.21 Multi-messenger SED of NGC 1068 and NGC 7469 122
8.22 Multi-messenger SED of NGC 4151 and CGCG 420−015 123
8.23 Diffuse neutrino background from X-ray AGN with 4 sources 124
8.24 Neutrino sky map from the 10-year public data 127
8.25 Point-source localization performance with public data 128
8.26 Blazar – 7-yr hotspot correlations 130
8.27 Blazar – 10-yr hotspot correlations 131

B.1 Hotspot counts above each $-\log_{10} p_{\text{thr}}$ 142
B.2 Hotspot counts above each $-\log_{10} p_{\text{thr}}$ (continued) 143
B.3 Hotspot counts with double the diffuse astrophysical background 144
B.4 Hotspot counts with double the diffuse astrophysical background (continued) 145
B.5 Hotspot counts with no diffuse astrophysical background 146
B.6 Hotspot counts with no diffuse astrophysical background (continued) 147

C.1 Signal spatial PDF for the IC79 dataset modeled with KDEs 151
C.2 Background *TS* distributions for fixed $\gamma = 2.0$ 152
C.3 Background *TS* distributions for fixed $\gamma = 2.5$ 152
C.4 Background *TS* parametrization for free $\gamma$ 153
C.5 Background *TS* distributions for different astrophysical diffuse spectra 154
C.6 Model template for the galactic neutrino emission 155
C.7 Effect of the unmodeled GP flux on the background *TS* distribution 156
C.8 Effect of the unmodeled GP flux on the discovery potential 156
C.9 Effect of the unmodeled GP flux on the MLEs biases for $\gamma = 2.0$ 157
C.10 Effect of the unmodeled GP flux on the MLEs biases for $\gamma = 3.2$ 157
C.11 Neutrino sky map with spectral index fixed to 2.0 158
C.12 Neutrino sky map with spectral index fixed to 2.5 158
C.13 $\chi^2_2$ approximation of the likelihood profiles 160

C.14 Zoomed-in sky maps around the location of the 12 most significant X-ray bright Seyfert galaxies 162
C.15 Location of the Seyfert galaxies superimposed with the GP template 163

D.1 Background *TS* distributions at various declination for the public data analysis 165
D.2 Multi-dataset signal injections 166
D.3 Signal-over-background energy PDF ratio at the location of TXS 0506+056 167
D.4 Signal-over-background energy PDF ratio at the location of TXS 0506+056 168

# *List of Tables*

3.1 Estimated gamma-ray and neutrino powers. 32

4.1 Overview of the experimental data samples 55

8.1 Summary of the sky scans results 111
8.2 Point-source analysis results at the top 12 Seyfert galaxies 121
8.3 Post-trial p-values for the correlation analyses 130

A.1 Abbreviations 139

C.1 Properties of the Monte Carlo datasets 149
C.2 Results of the point-source analysis at 48 Seyfert galaxies 161

# 1 Introduction

Over a century has passed since Victor Hess flew on a balloon in 1912 and discovered, against his expectations, that the level of ionizing radiation increased with altitude.[1] He had found a natural source of high-energy particles: the cosmic rays. Thanks to enormous technological progress in detection techniques, the flux of these charged particles is extensively measured across a wide energy range that reaches up to $10^{20}$ eV. However, several fundamental questions remain unanswered, with one standing out: What are the sources of high-energy cosmic rays?

Associating cosmic rays with their sources is an extremely challenging task, as charged particles are deflected in magnetic fields and lose their directional information. However, interactions of cosmic rays at their production sites generate neutral radiation in the form of gamma rays and neutrinos, which point directly back to the sources. While photons are created in various electromagnetic processes, neutrinos can only be produced in hadronic interactions, making their detection hard evidence of cosmic-ray acceleration at the source. Moreover, neutrinos interact only rarely and weakly, allowing them to travel astrophysical distances almost unimpeded. Consequently, the quest for the sources of the high-energy cosmic rays is closely connected with the search for astrophysical neutrino emitters.

In 2013, the IceCube Neutrino Observatory discovered a diffuse flux of high-energy astrophysical neutrinos.[2] The first association with a source happened four years later, in 2017, when IceCube detected a neutrino that pointed back to the blazar TXS 0506+056.[3] The coincident detection of enhanced gamma-ray activity made TXS 0506+056 the first $\sim 3\,\sigma$ neutrino source candidate[4] and the first case of a multi-messenger detection involving neutrinos. This detection reinforced two beliefs that were already rooted in the community. First, blazars, active galactic nuclei (AGN) with an ultrarelativistic jet pointing toward the Earth, are excellent candidates as neutrino sources. Second, the expected connection between the three messengers is a powerful experimental tool to identify cosmic-ray acceleration sites.

In 2022, a time-integrated search of 9 years of IceCube data found TeV neutrino emission from the X-ray bright, Seyfert 2 galaxy NGC 1068. The $4.2\,\sigma$ detection made NGC 1068 the most significant extragalactic neutrino source in the sky. Surprisingly, the AGN hosted by

[1] Hess, "Über Beobachtungen der durchdringenden Strahlung bei sieben Freiballonfahrten".

[2] IceCube Collaboration, "Evidence for High-Energy Extraterrestrial Neutrinos at the IceCube Detector".

[3] IceCube Collaboration et al., "Multimessenger observations of a flaring blazar coincident with high-energy neutrino IceCube-170922A".

[4] IceCube Collaboration et al., "Neutrino emission from the direction of the blazar TXS 0506+056 prior to the IceCube-170922A alert".

this galaxy lacks a powerful relativistic jet, and its emission is primarily dominated by thermal radiation. Moreover, no gamma rays were detected at the neutrino energies and flux levels, challenging the expected gamma-ray-neutrino connection. While both are AGN, the two extragalactic sources associated with IceCube's high-energy neutrinos show intriguing differences.

This dissertation presents the case of NGC 1068 as the possible first example of neutrino emission from the vicinity of the supermassive black hole within an AGN, specifically its X-ray bright *corona*. Several searches for neutrino point sources using IceCube internal data are performed, including an updated measurement of the neutrino flux from NGC 1068. In particular, a search for neutrino emission from a newly introduced selection of X-ray bright Seyfert galaxies is motivated by a hypothetical correlation between neutrino and X-ray fluxes in these objects.

Next to the research for neutrino emission from Seyfert galaxies, this work includes tests to probe a recently published claim of a $\sim 5\,\sigma$ correlation between neutrinos and blazars from the 5th edition of the Roma-BZCAT Multifrequency Catalogue of Blazars[5] (5BZCAT).[6,7] As opposed to the search for neutrinos from X-ray bright AGN, these tests use a smaller, publicly available, neutrino data sample consisting of ten years of data.[8] The data are analyzed using a novel open-source software interface developed in this work to perform point source searches with the IceCube data release.

The structure of the thesis is as follows:

Chapter 2 sets the stage for the discussion with an introduction to cosmic rays, their multi-messenger connections with gamma rays and neutrinos, and AGN as cosmic-ray sources.

Chapter 3 illustrates a comprehensive multi-messenger picture of NGC 1068. Through observational and theoretical considerations, the neutrino emitting region within this X-ray bright and gamma-ray obscured source is constrained to its central core. Assuming that X-ray emitting AGN could all emit neutrinos with a production mechanism similar to NGC 1068, the cosmic X-ray background is used to produce a model-independent prediction of the cumulative neutrino background produced by these sources.

Chapter 4 introduces the IceCube neutrino telescope, whose data have been extensively used in this work. First, the neutrino detection principle is introduced. Then, a description of the main properties of the atmospheric muon and neutrino backgrounds produced by cosmic-ray interactions in the atmosphere follows. The neutrino sample of 9 years of events used by the analysis that found NGC 1068 in 2022 is extended to include 50% more data. Besides adding three new years of observations, data acquired in 2010 with an incomplete detector configuration are included in this analysis for the first time. The data selection, reconstruction algorithms, and dataset properties are described.

[5] Massaro et al., "The 5th edition of the Roma-BZCAT. A short presentation".

[6] Buson et al., "Beginning a Journey Across the Universe: The Discovery of Extragalactic Neutrino Factories".

[7] Buson et al., "Erratum: "Beginning a Journey Across the Universe: The Discovery of Extragalactic Neutrino Factories" (2022, ApJL, 933, L43)".

[8] IceCube Collaboration, "IceCube Data for Neutrino Point-Source Searches Years 2008-2018".

Chapter 5 details the statistical method for searching neutrino point-like sources. After an introduction to hypothesis testing based on unbinned likelihood ratios, we discuss the discovery potential of the analysis and explain the sky scan method for searching the most significant cluster of astrophysical neutrinos.

Chapter 6 presents a novel open-source software interface developed in this work for point source searches with ten years of IceCube public data. The public neutrino sample is introduced, followed by a description of the implementation of the likelihood-ratio test adapted to the format of the data release. The performance of the point-source analysis on public data is compared to published IceCube results.

Chapter 7 describes three different statistical methods to search for populations of neutrino sources. The first test searches for excess hotspots in the neutrino sky, with particular focus on an improved simulation strategy developed within this work; the second method probes the binomial excess from a population of preselected candidate sources; the third analysis technique searches for a spatial correlation between neutrino hotspots and blazars.

Chapter 8 finally presents the results from all searches for neutrino sources using methods introduced in the previous chapters. The chapter is divided into three main sections:

- Result from the search for a population of hotspots in the Northern neutrino sky based on 9 years of IceCube internal data.
- Results of a comprehensive search of point-like neutrino sources using the extended dataset of 13 years of IceCube internal data. The search was conducted by a team of analyzers led by the author of this dissertation, who was also one of the analyzers. The results include the updated measurement of the neutrino emission from NGC 1068 with 50% more data and the search for neutrino emission from a novel selection of 47 X-ray bright Seyfert galaxies, developed in this thesis.
- Results from several tests aimed at probing the claimed discovery of a neutrino-blazar correlation. These results use IceCube public data using the tool presented in Chapter 6.

Chapter 9 summarizes the main results of this work.

# 2 The High-Energy Cosmos

When Victor Hess flew in a balloon up to 5200 meters, he aimed to demonstrate that the ionizing radiation detected at the Earth's surface originated from radioactive decay in the Earth's crust. Flying high enough, far from the source, should have resulted in a decrease in radiation levels. What he observed instead marked the beginning of modern astrophysics: "[...] the values at the greatest altitude are about 22 – 24 ions higher than at the ground. [...] The results of the present observations seem to be most readily explained by the assumption that a radiation of very high penetrating power enters our atmosphere from above ... Since I found a reduction ... neither by night nor at a solar eclipse, one can hardly consider the Sun as the origin."[1].

In 1912, Hess discovered what we now call *cosmic rays* (CRs):[2] Highly energetic charged particles that reach the Earth's atmosphere from outer space, continuously interacting with its nuclei. The subsequent discovery of additional forms of neutral radiation, such as gamma rays and high-energy neutrinos, has raised new questions about the interconnections between these three cosmic *messengers*. These discoveries provide compelling reasons for fostering multi-messenger research approaches to identify the most powerful cosmic particle accelerators and understand their acceleration and production mechanisms.

This chapter provides an introduction to the properties of cosmic rays, neutrinos, and gamma rays, with a focus on their connections and candidate sources.

[1] https://cerncourier.com/a/a-discovery-of-cosmic-proportions/ The extracts are from a translation of the original paper by Hess, taken from Cosmic Rays by A. M. Hillas, in the series "Selected readings in physics", Pergamon Press 1972.

[2] Hess, "Über Beobachtungen der durchdringenden Strahlung bei sieben Freiballonfahrten".

## 2.1 The cosmic-ray spectrum

Cosmic rays are primarily composed of protons (90%), with approximately 9% of helium nuclei and a small fraction of heavier nuclei.[3] Astrophysical accelerators produce CRs that we measure at Earth with energies spanning over eleven orders of magnitude, from $\sim 10^9$ eV to over $10^{20}$ eV.[4] The lower energy part of the spectrum is more abundant, with about 1,000 CRs per square meter per second. Their vanishingly small flux eventually reduces to less than one particle per square kilometer per century at the highest energies. This vast range in abundance at different energies requires deploying many instruments, each employing different detection techniques to measure the total CR spectrum. Direct measurements are possible

[3] Gaisser, Engel, and Resconi, *Cosmic Rays and Particle Physics: 2nd Edition*.

[4] Bird et al., "Detection of a Cosmic Ray with Measured Energy Well beyond the Expected Spectral Cutoff due to Cosmic Microwave Radiation".

up to approximately $10^{14}$ eV and can usually determine the particle type and precisely measure the energy. These measurements are conducted at the top of the atmosphere by experiments flown on balloons or satellites, such as AMS-02[5] and CALET[6] among the others. At higher energies, ground-based air-shower detectors instrumenting areas of several square kilometers are necessary to measure the low rate of CR, for example, the Pierre Auger Observatory[7] or the Telescope Array.[8] These detectors identify primary CRs by measuring the shower of particles produced by their interaction with the atmosphere (secondary CRs), which significantly reduces the precision in the measurement of the primaries.

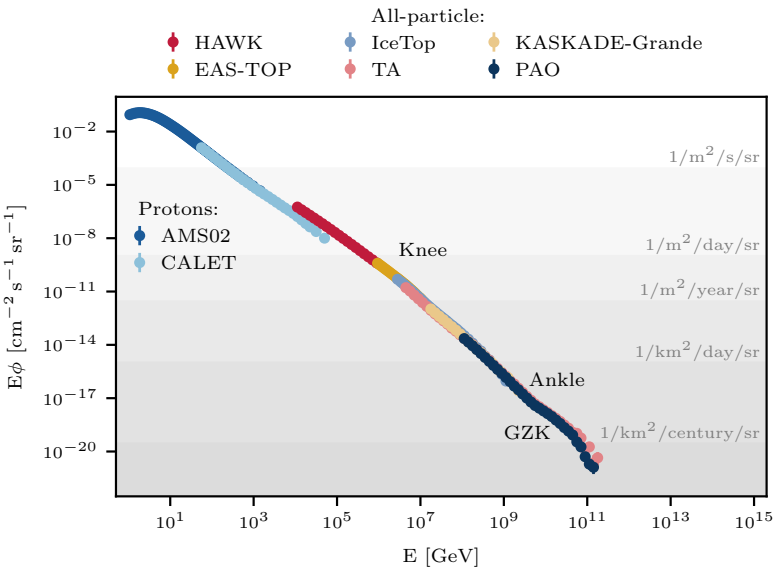


Figure 2.1 shows the overall picture of the CR energy spectrum that emerges when measurements at different energies from various observatories are compiled. Although the sources of CRs have not yet been identified, it is understood that nearly all of them originate from within the galaxy but outside the Solar System. The solar origin of CRs that dominate the spectrum up to $\sim$ 4 GeV has been demonstrated by observing temporal coincidences with violent episodes of solar activity,[9] while at higher energies, this correlation disappears. From 10 GeV up, the spectrum can be approximately described by inverse power-law distributions $\propto E^{-\gamma}$. This spectral shape, very different from the black body thermal emission, indicates that non-thermal processes accelerate CRs to their extreme energies.[10] Some characteristic features appear in the spectrum, which is approximated by a power-law with spectral index $\gamma = 2.7$ up to $\sim$1 PeV but softens to $\gamma = 3.1$ at $\sim$ 3 PeV (the "knee") to then harden again to $\gamma = 2.6$ beyond $\sim$ 4 EeV (the "ankle"). Finally, it seems to cut off at hundreds of EeV.

[5] Aguilar et al., "Precision Measurement of the Proton Flux in Primary Cosmic Rays from Rigidity 1 GV to 1.8 TV with the Alpha Magnetic Spectrometer on the International Space Station".

[6] Adriani et al., "Direct Measurement of the Cosmic-Ray Proton Spectrum from 50 GeV to 10 TeV with the Calorimetric Electron Telescope on the International Space Station".

[7] Abraham et al., "Measurement of the energy spectrum of cosmic rays above $10^{18}$ eV using the Pierre Auger Observatory".

[8] Kawai et al., "Telescope Array Experiment".

Figure 2.1: Cosmic ray energy spectrum between 1 GeV and hundreds of EeV. Various measurements are shown in different colors. The well-known features of the spectrum are highlighted. As a reference, the number of particles per unit of area, time, and solid angle are shown at various energies. Data from 'https://lpsc.in2p3.fr/crdb/'.(Maurin et al., "A cosmic-ray database update: CRDB v4.1")

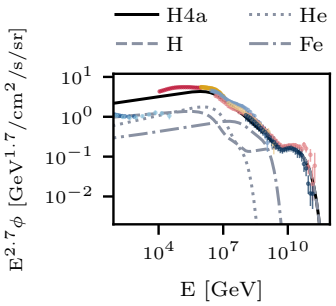


Figure 2.2: The measurements are the same as in Figure 2.1, however the spectrum is multiplied by $E^{2.7}$, highlighting the slope changes. The H4a model with its component is taken from Gaisser, "Spectrum of cosmic-ray nucleons, kaon production, and the atmospheric muon charge ratio".

[9] Adriani et al., "Time Dependence of the Proton Flux Measured by PAMELA during the 2006 July-2009 December Solar Minimum".

[10] Gaisser, Engel, and Resconi, *Cosmic Rays and Particle Physics: 2nd Edition*.

The origin of the knee and the ankle is still debated. Still, these structures are generally believed to be related to changes in the dominant source population accelerating the observed nuclei. CRs with energies below the PeV are believed to be predominantly produced within the Milky Way, possibly by galactic supernova remnants, which reach their maximum acceleration capability around the knee.[11] At this energy, galactic CRs begin their decline in favor of nuclei of extragalactic origin, which finally emerge at the ankle. Simple dimensional considerations further corroborate the extragalactic origin of CR beyond the ankle: At EeV energies, CRs have Larmor radii larger than the size of the Milky Way[12]

[11] Blasi, "Origin of very high- and ultra-high-energy cosmic rays".

[12] Halzen and Hooper, "High-energy neutrino astronomy: the cosmic ray connection".

$$r_L = \frac{pc}{eZB} \overset{E \gg m}{=} \frac{E}{eZB} \tag{2.1}$$

with momentum $p$, charge $Z$, and magnetic field $B$. If we now define the *rigidity* $R$, *i.e.*, the resistance of a relativistic, charged particle against deflection in a magnetic field, via

$$R = \frac{E}{eZ} \tag{2.2}$$

we can rewrite Equation 2.1 as

$$r_L = \frac{R}{B} \tag{2.3}$$

the rigidity is such that a 10 PeV proton is characterized by a rigidity of 10 PV. Consequently, the Larmor radius for a 1 EeV proton in a homogeneous magnetic field with the strength of the Milky Way ($2 - 8\ \mu G$[13]) is several tens of kpc, which is approximately the size of the galactic disc. From this perspective, either no galactic source can accelerate CR beyond the ankle or nuclei accelerated at those energies reach their critical rigidity ($R_c$) and escape the galactic magnetic field.[14]

[13] Han et al., "Pulsar Rotation Measures and the Large-Scale Structure of the Galactic Magnetic Field".

[14] Spurio, *Particles and Astrophysics: A Multi-Messenger Approach*.

A similar argument can be used to study possible nuclear compositions of the spectrum.[15] Several knee-like structures are expected to appear when different nuclei reach $R_c$.[16] From Equation 2.2, we infer that heavier nuclei (with larger $Z$) reach the critical rigidity at higher energies than protons. Following this logic, the H4a model[17] describes the total differential energy spectrum as the sum of all flux contributions

[15] Peters, "Primary cosmic radiation and extensive air showers".

[16] Gaisser, "Spectrum of cosmic-ray nucleons, kaon production, and the atmospheric muon charge ratio".

[17] Ibid.

$$\phi(E) = \sum_i \phi_{0,i} E^{-\gamma_i} e^{-E/(Z_i e R_c)}, \tag{2.4}$$

where the index $i$ runs over all groups of nuclei and $\phi_{0,i}$ is the flux normalizatation of the $i$-th nuclei. Figure 2.2 shows the H4a model approximation of the CR spectrum and the contributions of some groups of nuclei. The observation of a knee-like break of the spectrum of the heavy component of primary CR at about $8 \times 10^7$ GeV seems to support this type of modeling.[18] At the same time, the high-energy tail of the spectrum appears compatible with a single contribution from a population of protons. If verified, this would provide additional confirmation of the sole extragalactic origin of CRs beyond the ankle.

[18] Apel et al., "Kneelike Structure in the Spectrum of the Heavy Component of Cosmic Rays Observed with KASCADE-Grande".

The last feature of the spectrum to note is the so-called GZK cutoff, named after Greisen, and Zatsepin and Kuzmin, who independently proposed an explanation for it.[19,20] They realized that the Universe is opaque to the ultra-high-energy (UHE) protons with energies beyond $\sim 5 \times 10^{19}$ eV. The most important interaction target for protons propagating over extragalactic distances are photons of the *cosmic microwave background* (CMB). The dominant interaction channel is the photoproduction of the $\Delta$ resonance via

$$p + \gamma_{\mathrm{CMB}} \to \Delta^+ \to \pi^0 + p, \quad p + \gamma_{\mathrm{CMB}} \to \Delta^+ \to \pi^+ + n \tag{2.5}$$

above a threshold energy $E_p$ of $2E_p\epsilon_\gamma > (m_\Delta^2 - m_p^2) \approx 50$ EeV.[21] At lower energy, the production of electron-positron pairs plays a role as well

$$p + \gamma_{\mathrm{CMB}} \to p + e^+ + e^-, \tag{2.6}$$

with a lower energy threshold of $\sim 500$ PeV but also a smaller cross-section than photomeson production.[22]

Figure 2.3 shows the attenuation length[23] of photons with energies beyond the ankle. In principle, UHE protons could allow cosmic-ray astronomy up to $\lesssim 10^3$ Mpc. However, magneto-hydrodynamical simulations of cosmic structures have demonstrated that the median deflection of these protons by extragalactic magnetic fields at a distance of $\sim 500$ Mpc is already larger than $1^\circ$.[24] The rigidity decreases for lower energies, and connecting CR to their sources becomes impossible.

However, inelastic interactions of primary protons with radiation fields or matter in the source environment produce mesons that further decay into neutrinos and gamma rays. This neutral flux of high-energy particles travels through astrophysical distances heedless of magnetic fields.

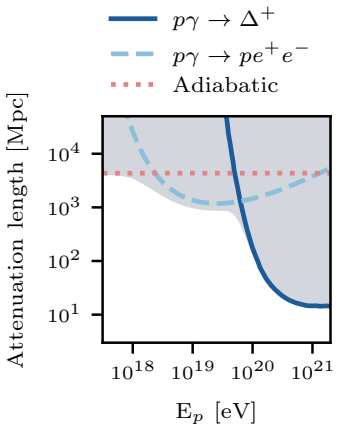


Figure 2.3: Attenuation length for protons in the CMB as a function of the proton energy. The contribution from the $\Delta$ resonance and the pair production are shown as solid and dashed lines, respectively. The dotted line represents the adiabatic losses due to the expansion of the Universe $c/H_0$ inversely proportional to the Hubble constant $H_0$. The shaded area covers distances at which the universe is opaque to protons. Data from Gaisser, Engel, and Resconi, *Cosmic Rays and Particle Physics: 2nd Edition*.

[23] The distance after which the initial flux decreases by $1/e$.

[24] Dolag et al., "Mapping Deflections of Ultrahigh Energy Cosmic Rays in Constrained Simulations of Extragalactic Magnetic Fields".

## 2.2 *The cosmic connections*

Multi-wavelength photon observations enabled astronomers to study the cosmos across the electromagnetic spectrum, from radio waves to gamma rays, and access new astrophysical scales and phenomena. Similarly, multi-messenger astronomy leverages the strengths of different messengers, providing complementary insights that are unattainable through any single observational method alone.

In this section, we start with a brief review of the proton interaction processes that produce astrophysical neutrinos and gamma rays and then continue with an introduction to these two messengers.

Two primary proton interaction processes are believed to be the origin of the observed neutrinos and accompanying gamma rays: photo-meson ($p - \gamma$) and proton-proton ($p - p$) productions. In the former, a primary CR proton interacts with ambient photons and produces pions via

$$p + \gamma \to \Delta^+ \to \pi^0 + p, \quad \text{and} \quad p + \gamma \to \Delta^+ \to \pi^+ + n. \tag{2.7}$$

[19] Greisen, "End to the Cosmic-Ray Spectrum?"

[20] Zatsepin and Kuz'min, "Upper Limit of the Spectrum of Cosmic Rays".

[21] Halzen and Hooper, "High-energy neutrino astronomy: the cosmic ray connection".

[22] Kelner and F. A. Aharonian, "Energy spectra of gamma rays, electrons, and neutrinos produced at interactions of relativistic protons with low energy radiation".

The ratio of charged to neutral pions is $K = 1$. The threshold energy for a proton to produce a pion is[25]

$$E_{p,\mathrm{thr}} \sim \frac{2m_p m_\pi + m_\pi^2}{4\epsilon_\gamma}, \tag{2.8}$$

where $E_p$ and $\epsilon_\gamma$ are the proton and photon energies, and $m_p$ and $m_\pi$ are the proton and pion masses. If we assume an ultraviolet (UV) photon field, as it is typical in astrophysical sources as active galactic nuclei[26], a proton must be accelerated to approximately 100 PeV to produce a pion. However, given the inverse proportionality between the proton and the target photon energies, if the proton acceleration happens in an environment rich in photons with higher energies, *e.g.*, X-rays in the keV band, the required proton energy for pion production decreases to $\sim 100$ TeV.

In $p - p$ interactions, the accelerated proton can interact with ambient gas nuclei in inelastic hadronuclear collisions

$$p + p \to n_\pi \left[\pi^0 + \pi^+ + \pi^-\right] + X, \tag{2.9}$$

where $n_\pi$ is the pion multiplicity, and X is the hadronic cascade produced by the nuclear disintegration. In this case, the charged-to-neutral pions ratio is $K = 2$. The energy threshold for pion production is

$$E_{p,\mathrm{thr}} \sim m_p + \frac{m_\pi(m_\pi + 4m_p)}{2m_p}, \tag{2.10}$$

which is approximately 1.3 GeV, assuming a proton mass of $\sim 1$ GeV. Hence, in the frame where the second proton is at rest, the incident proton needs a kinetic energy of approximately 300 MeV to produce one pion. Consequently, $p - p$ interactions are kinematically favored over $p - \gamma$ when possible. However, the rate of both pion-production mechanisms ultimately depends linearly on the density of target particles. Therefore, depending on the relative density of low-energy photons and protons in the source environment, $p - \gamma$ interactions might be favored.[27]

In both scenarios, approximately $15 - 20\%$ of the incident proton kinetic energy is transferred to the pion, roughly corresponding to the ratio $m_\pi/m_p$.[28] The pion will decay and consequently transfer its energy to the decay products. Neutral pions decay into two gamma rays

$$\pi^0 \to \gamma + \gamma, \tag{2.11}$$

which will share the parent pion energy equally. Charged pions decay into three high-energy neutrinos ($\nu$) and antineutrinos ($\bar{\nu}$) via the decay chain

$$\pi^\pm \to \mu^\pm + \nu_\mu(\bar{\nu}_\mu) \tag{2.12}$$

with subsequent muon decay

$$\mu^\pm \to e^\pm + \nu_e(\bar{\nu}_e) + \bar{\nu}_\mu(\nu_\mu) \tag{2.13}$$

[25] Assuming natural units, $c = 1$.

[26] A description of active galactic nuclei will be given in Subsection 2.3.3. See there Figure 2.11 for the conversion of UV (and other electromagnetic energy bands) energies in eV.

[27] Spurio, *Probes of Multimessenger Astrophysics*.

[28] Kelner and F. A. Aharonian, "Energy spectra of gamma rays, electrons, and neutrinos produced at interactions of relativistic protons with low energy radiation".

Hence, the neutrino flavor ratio at the source is $(\nu_e : \nu_\mu : \nu_\tau) = (1 : 2 : 0)$. On average, the four final state leptons share the energy of the charged pion equally. With these approximations, gamma rays and neutrinos carry respectively $1/2$ and $1/4$ of the energy of the parent pion, *i.e.*, $\langle E_\nu \rangle / \langle E_\gamma \rangle \simeq 1/2$.[29]

[29] Halzen, "High-Energy Neutrinos from the Cosmos".

The dependence on the number density of targets for proton interaction is the origin of different neutrino spectra in the two photoproduction scenarios. Equation 2.10 shows that the interaction probability in $p - p$ collisions does not depend, on first order, on the proton energy provided that it is greater than the threshold. Consequently, the pion and neutrino spectra show the same power-law spectra as the parent CR spectrum. On the contrary, the inverse energy dependence between the proton and target photon energies in $p - \gamma$ interactions (Equation 2.8) implies that for typical photon spectra $\mathrm{d}N_\gamma/\mathrm{d}E \propto E^\alpha$, the number density of target photons with energy above threshold scales as $N_{\gamma,\mathrm{thr}} \propto E$. As a consequence, the resulting neutrino spectrum is flatter than the proton spectrum by a factor of 1: $\mathrm{d}N_\nu/\mathrm{d}E \propto E^{-\gamma_{\mathrm{CR}}+(\alpha-1)}$. For typical observed photon spectra, $\alpha = 2$ and hence $\gamma_\nu = \gamma_{\mathrm{CR}} + 1$.[30]

[30] Gaisser, Engel, and Resconi, *Cosmic Rays and Particle Physics: 2nd Edition*.

It is important to note that in the described framework, hadronic interactions are necessary to produce neutrinos in astrophysical environments. Conversely, gamma rays can be created in purely leptonic processes, as we will see in the next section. Therefore, while the detection of neutrinos indicates hadron acceleration at the source, the detection of gamma rays does not necessarily reveal the nature of the accelerated particles.

### 2.2.1 *The gamma-ray sky*

Gamma-rays constitute the highest-energy electromagnetic radiation, ranging from hundreds of keV to several TeV. They arise directly in nuclear or high-energy processes at (or in the matter surrounding) astrophysical sources and yet, being chargeless, travel in straight lines.[31] This makes them one of the most important messengers of the non-thermal universe, and their study can provide valuable insights into cosmic-ray acceleration. In the previous section, we reviewed the gamma-ray generation in hadronic interactions of CRs through the decay of neutral pions into two photons. However, a purely leptonic origin is also possible via several interaction processes with electrons or ions, abundant in astrophysical source environments.[32] Assuming an electron[33] power-law energy spectrum $\propto E^{-p}$, the following processes can produce a gamma-ray spectrum[34]

[31] Morrison, "On gamma-ray astronomy".

- $\mathrm{e} + \gamma_{\mathrm{low}} \rightarrow \mathrm{e} + \gamma_{\mathrm{high}}$: Inverse Compton (IC) up-scattering of low energy photons with relativistic electrons, which transfer part of their energy to the photons resulting in $\phi_\gamma \propto E_\gamma^{-(p+1)/2}$ or $\phi_\gamma \propto E_\gamma^{-(p+1)}$;[35]
- $\mathrm{e} \rightarrow \mathrm{e} + \gamma$: Synchrotron radiation emitted by electrons in a magnetic field, which results in a photon spectrum $\phi_\gamma \propto E_\gamma^{-(p+1)/2}$;

[32] Völk, F. A. Aharonian, and Breitschwerdt, "The Nonthermal Energy Content and Gamma-Ray Emission of Starburst Galaxies and Clusters of Galaxies".

[33] For simplicity, in this section we refer to both electrons and positrons as electrons.

[34] Bose et al., "Galactic and extragalactic sources of very high energy gamma rays".

[35] Depending on whether the energy $\gamma_{\mathrm{low}}$ is well below the rest mass energy of the electron or not.

- $e + N \rightarrow e + N + \gamma$: Bremsstrahlung radiation produced by the deceleration/bending of electrons when they pass near a nucleus $N$, which results in $\phi_\gamma \propto E_\gamma^{-p}$.

The Fermi Large Area Telescope[36] (*Fermi*-LAT) has successfully detected diffuse gamma-ray emission from the Milky Way in the $0.1 - 100$ GeV energy range. The diffuse gamma-ray emission is produced via high-energy CR interactions with interstellar matter and low-energy radiation fields. The dominant process involves cosmic-ray protons colliding with hydrogen atoms in the interstellar medium, producing neutral pions that subsequently decay into gamma rays. The same interactions inevitably produce also charged pions that decay into neutrinos. Therefore, the Galactic Plane provides a guaranteed source of neutrinos, which have recently been detected by the IceCube Neutrino Observatory,[37] as we will see in the next section.

[36] Atwood et al., "The Large Area Telescope on the Fermi Gamma-Ray Space Telescope Mission".

[37] The IceCube detector is reviewed in detail in Chapter 4.

Complementary to the diffuse galactic emission, the integrated flux from all resolved and unresolved extragalactic gamma-ray sources is known as the *extragalactic gamma-ray background* (EGB). This flux is weaker than the diffuse galactic one. Its spectrum has been measured with good precision from 100 MeV to 820 GeV by *Fermi*-LAT.[38]

[38] Ackermann et al., "The Spectrum of Isotropic Diffuse Gamma-Ray Emission between 100 MeV and 820 GeV".

Although gamma rays play a crucial role in high-energy astronomy, the universe is not transparent to photons of TeV energy and above. Gamma-rays interact with photons from the *extragalactic background light* (EBL) and the CMB, producing electron-positron pairs. The threshold energy for creating a pair is $E\epsilon > (m_e c)^2$, where $E$ and $\epsilon$ are the gamma-ray and background photon energies, respectively. As a result, TeV photons are absorbed by the EBL (ranging from UV to infrared, IR, light), PeV photons by the CMB, and EeV photons by radio waves. Figure 2.4 shows the attenuation length of gamma rays as a function of their energy. For context, it includes the distance to the gamma-ray and neutrino source NGC 1068[39] and that of the Galactic Center. Above energies of $\sim 100$ TeV, the gamma-ray horizon is essentially limited to the Milky Way and nearby sources.

[39] Abbasi et al., "Evidence for neutrino emission from the nearby active galaxy NGC 1068"

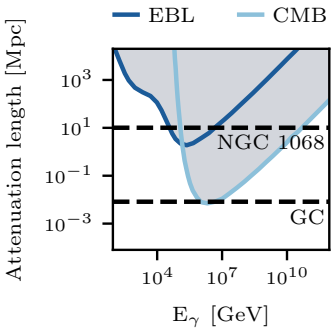


Figure 2.4: Attenuation length for gamma rays in the EBL (blue) CMB (light blue) as a function of the photon energy. For comparison, the distance of the Galactic Center (GC) and of the well-known source NGC 1068 are indicated as a dashed solid line. Above 100 TeV, the observable universe is limited to our galaxy.

### 2.2.2 *The neutrino sky*

Neutrinos are neutral fermions characterized by tiny masses, which have not yet been precisely measured.[40] They are produced through weak interactions and exist in three leptonic flavors, $\nu_e$, $\nu_\mu$, and $\nu_\tau$, interacting solely via the weak force with minimal cross-sections. While this makes their detection rather challenging, it also renders these particles ideal astrophysical messengers. Like gamma rays, they are unaffected by magnetic fields, and their low interaction probability means they are not attenuated en route to Earth.

In 2013, the IceCube collaboration discovered a flux of high-energy astrophysical neutrinos originating beyond our galaxy.[41] The isotropic distribution of the observed events supports their extragalactic origin. From a simplified perspective, sophisticated IceCube analyses aiming at measuring the astrophysical diffuse neutrino background

[40] Most recent results by the KATRIN collaboration place an upper limit on the $\nu_e$ mass at 0.8 eV (Katrin Collaboration, "Direct neutrino-mass measurement with sub-electronvolt sensitivity")

[41] IceCube Collaboration, "Evidence for High-Energy Extraterrestrial Neutrinos at the IceCube Detector".

leverage the difference in the spectral shape between the atmospheric and astrophysical neutrino fluxes. Atmospheric neutrinos originating from the interaction of primary CRs with nuclei of the Earth's atmosphere represent the largest background for neutrino telescopes.[42] They outnumber the astrophysical signal by up to three orders of magnitude at reconstructed energies $\lesssim$ 100 TeV, as seen in the left panel of Figure 2.5. However, the atmospheric flux falls steeply with increasing energy, and eventually, the astrophysical signal emerges. The astrophysical flux is usually modeled as an unbroken power-law

$$\phi(E) = \phi^{100\text{TeV}} \left( \frac{E}{100\text{TeV}} \right)^{-\gamma_{\text{astro}}}, \tag{2.14}$$

with flux normalization at 100 TeV $\phi^{100\text{TeV}}$ and spectral index $\gamma_{\text{astro}}$. The most recent measurement has been provided by an all-flavor combined fit of independent $\nu_\mu$-induced[43] and $\nu_e$-/$\nu_\tau$-induced[44] event samples. It provides the most stringent constraint on the astrophysical flux parameters to date, $\phi^{100\text{TeV}} = 1.80^{+0.13}_{-0.16} \times 10^{-18}$ GeV$^{-1}$ cm$^{-2}$ s$^{-1}$ sr$^{-1}$ and $\gamma_{\text{astro}} = 2.52 \pm 0.04$.[45] A summary of the astrophysical diffuse flux measurements obtained over the years is illustrated in the right panel of Figure 2.5.

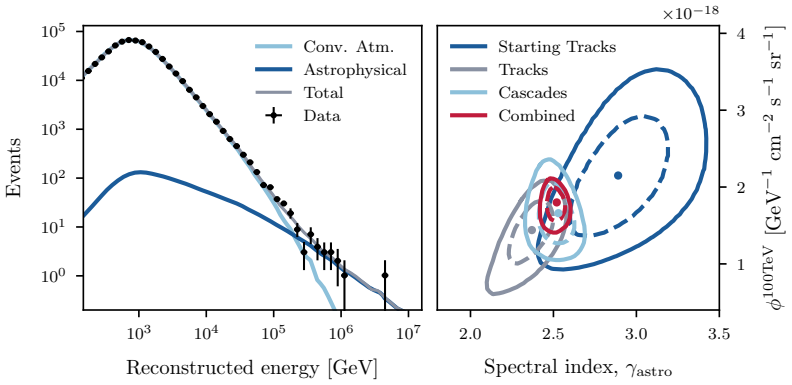


Figure 2.5: **Left:** Number of events per reconstructed energy bin. The events are induced by muon neutrinos and fitted assuming that the sum of an atmospheric and an astrophysical component contributes to the total observation (Abbasi et al., "Improved Characterization of the Astrophysical Muon-neutrino Flux with 9.5 Years of IceCube Data"). **Right:** Best-fit flux normalization at 100 TeV and spectral index with the corresponding 2D uncertainties as different IceCube analyses have measured them. The dashed (solid) lines represent the 68% (95%) confidence contours. The measurement obtained on a sample of high-energy events with vertex contained in the detector (starting tracks, dark blue) is from Schneider, "Characterization of the Astrophysical Diffuse Neutrino Flux with IceCube High-Energy Starting Events". Other references for the data can be found in the text.

A high-energy flux of cosmic neutrinos is now established and well-constrained from a few TeV up to several PeV. We previously mentioned that a neutrino flux of galactic origin, produced in the decay of neutral pions together with gamma rays, is expected.[46,47] In addition to the predicted diffuse emission, the Milky Way is densely populated with numerous high-energy gamma-ray sources, including potential CR accelerators and candidate neutrino sources. Consequently, the Galactic Plane has long been anticipated as a source of neutrinos. The IceCube detection at $4.5\sigma$ level of significance of neutrino emission from the Galactic Plane came a year ago, in 2023.[48] The most significant result is found under the assumption that the $\pi^0$ component of the diffuse gamma-ray emission $\propto E_\gamma^{-2.7}$ can be extrapolated with the same spatial emission profile at TeV

[42] See Section 4.2.

[43] Abbasi et al., "Improved Characterization of the Astrophysical Muon-neutrino Flux with 9.5 Years of IceCube Data"

[44] Aartsen et al., "Characteristics of the Diffuse Astrophysical Electron and Tau Neutrino Flux with Six Years of IceCube High Energy Cascade Data"

[45] Naab et al., "Measurement of the astrophysical diffuse neutrino flux in a combined fit of IceCube's high energy neutrino data".

[46] Stecker, "Diffuse fluxes of cosmic high-energy neutrinos."

[47] Berezinsky et al., "Diffuse radiation from cosmic ray interactions in the galaxy".

[48] Icecube Collaboration, "Observation of high-energy neutrinos from the Galactic plane".

energies, where The IceCube detector is sensitive. The analysis of the data constrains the normalization of the galactic neutrino flux to $\phi_{\text{gal}}^{100\text{TeV}} = 21.8^{+5.3}_{-4.9} \times 10^{-19}$ GeV cm$^{-2}$ s$^{-1}$.

Figure 2.6 compares the flux levels of three different neutrino emission components: the total diffuse emission, the galactic diffuse emission, and an exemplary point-like emission.

The recently measured diffuse galactic emission contributes approximately 17% of the astrophysical flux at 5 TeV. In contrast, the flux from the most luminous point-like source in the extragalactic neutrino sky at $\sim 1 - 10$ TeV[49] accounts for less than 1% of the total unresolved emission.

To date, only two point-like sources have been associated with IceCube neutrinos with significance larger than $3\sigma$, the blazar TXS 0506+056[50,51] and the non-jetted galaxy NGC 1068.[52] They belong to the class of astrophysical objects known as active galactic nuclei (AGN) (see Subsection 2.3.3), which, as we will see in Chapter 3, could potentially explain the vast majority of the total astrophysical neutrino emission.

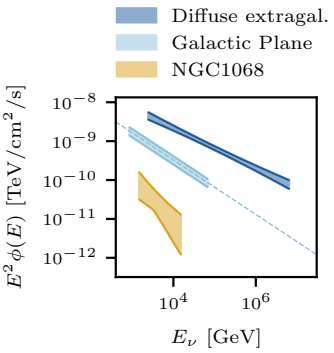


Figure 2.6: Comparison of different, all-flavor, astrophysical neutrino fluxes integrated over the whole sky. The diffuse flux from the Galactic Plane (light blue) is compared to the total neutrino flux (dark blue). The references are in the text. The flux of a point-like neutrino source, NGC 1068 in yellow, is displayed for comparison as well (Abbasi et al., "Evidence for neutrino emission from the nearby active galaxy NGC 1068").

[49] Abbasi et al., "Evidence for neutrino emission from the nearby active galaxy NGC 1068".

[50] IceCube Collaboration et al., "Multimessenger observations of a flaring blazar coincident with high-energy neutrino IceCube-170922A".

[51] IceCube Collaboration et al., "Neutrino emission from the direction of the blazar TXS 0506+056 prior to the IceCube-170922A alert".

[52] Abbasi et al., "Evidence for neutrino emission from the nearby active galaxy NGC 1068".

### *Astrophysical neutrino flavor ratio at Earth*

In Equation 2.12 and Equation 2.13, we derived a neutrino flavor ratio $(\nu_e : \nu_\mu : \nu_\tau) = (1 : 2 : 0)$ expected at the astrophysical source. However, in the previous section, we discussed measurements of all-flavor neutrino fluxes, which suggest a change in the flavor composition by the time these neutrinos reach Earth. Flavor changes are possible because neutrinos have tiny and yet non-zero masses, enabling them to oscillate among different flavor states.[53] The flavor states can be expressed as a superposition of the neutrino mass states through the mixing, unitary matrix $U$[54]

$$\begin{pmatrix} \nu_1 \\ \nu_2 \\ \nu_3 \end{pmatrix} = U \begin{pmatrix} \nu_e \\ \nu_\mu \\ \nu_\tau \end{pmatrix}, \tag{2.15}$$

which is parametrized by three mass mixing angles and a CP-violating phase.[55] A time-dependent Schrödinger equation describes the propagation of the neutrino mass eigenstate in the vacuum. The transition probability for a neutrino of energy $E$ and flavor $\alpha$ to be detected with flavor $\beta$ after it travelled a distance $L$ can be expressed as function of $L/E$ as[56]

$$P_{\alpha\to\beta} = \delta_{\alpha\beta} - 4\sum_{i>j} \text{Re}\left(U^*_{\alpha i} U_{\beta i} U_{\alpha j} U^*_{\beta j}\right) \sin^2\left(\frac{\Delta m^2_{ij} L}{4E}\right) \tag{2.16}$$

$$+ 2\sum_{i>j} \text{Im}\left(U^*_{\alpha i} U_{\beta i} U_{\alpha j} U^*_{\beta j}\right) \sin\left(\frac{\Delta m^2_{ij} L}{2E}\right), \tag{2.17}$$

where $\Delta m^2_{ij} = m^2_j - m^2_i$ and $i, j$ run over the mass eigenstates. The $L/E$ ratio determines the frequency of the oscillation. For high-energy neutrinos traveling over astrophysical distances, it is useful

[53] Pontecorvo, "Inverse beta processes and nonconservation of lepton charge".

[54] Maki, Nakagawa, and Sakata, "Remarks on the Unified Model of Elementary Particles".

[55] Gaisser, Engel, and Resconi, *Cosmic Rays and Particle Physics: 2nd Edition*, p. 153.

[56] Ibid., p. 154.

to convert it to more convenient units:

$$\frac{L}{E} \rightarrow 3.09 \times 10^7 \frac{L}{pc} \frac{PeV}{E}. \tag{2.18}$$

Figure 2.7 illustrates the evolution of the $\nu_\mu/\nu_e$ and $\nu_\tau/\nu_e$ flavor ratios starting from $(\nu_e : \nu_\mu : \nu_\tau) = (1 : 2 : 0)$. After $\sim 10^{-2}$ pc, the flavor ratio of 1 PeV neutrinos converges to $(\nu_e : \nu_\mu : \nu_\tau) = (1 : 1 : 1)$. Therefore, the approximation that we observe an astrophysical neutrino flux with equal contribution from each flavor holds for any source farther than $10^{-2}$ pc. Exemplarily, the Earth is approximately 8 kpc away from the galactic center and $\sim$ 20 pc above the Galactic Plane[57].

[57] Karim and Mamajek, "Revised geometric estimates of the North Galactic Pole and the Sun's height above the Galactic mid-plane"

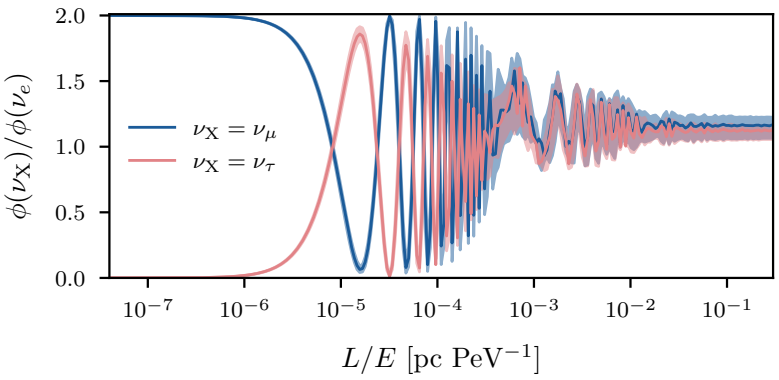


Figure 2.7: Neutrino flavor oscillations as a function of the distance over energy in astrophysical units. The initial flavor ratio $(\nu_e : \nu_\mu : \nu_\tau) = (1 : 2 : 0)$ converges to $(\nu_e : \nu_\mu : \nu_\tau) = (1 : 1 : 1)$ after $\sim 10^{-2}$ pc. The shaded bands represent the propagation of the 1 $\sigma$ uncertainties on the current best-fit oscillation parameters (Esteban et al., "Global analysis of three-flavour neutrino oscillations: synergies and tensions in the determination of $\theta_{23}$, $\delta_{CP}$, and the mass ordering").

### 2.2.3 *Multi-messenger astronomy*

The measurements of the diffuse UHECR energy spectrum by the Pierre Auger Observatory established a spectral cut-off above $10^{19.5}$ eV, compatible with what is expected from the GZK energy losses due to interactions with CMB photons.[58] Since 2008, the Fermi satellite has been tracking a diffuse gamma-ray background extending into the sub-TeV range. Finally, since 2012-2013, IceCube has been detecting a diffuse high-energy neutrino background of astrophysical origin from multi-TeV to PeV energies. When looking at these measurements collectively in Figure 2.8, the energy densities of the three messengers reach comparable levels. This tantalizing connection provides ideal conditions for multi-messenger studies.

Based on the observed energy densities of UHE cosmic rays, Waxmann and Bahcall could derive an upper bound to the higher energy neutrino. This limit is entirely independent of the specific source environment and conditions.[59] The idea is that the production rate of UHE CR can be estimated from the measured energy density under the assumption that the CR sources follow a homogeneous cosmological distribution[60] and that extragalactic protons dominate UHE CRs. These protons could be embedded in environments that act as "traps" for lower energy protons ($\ll$ 1 EeV) due, for example, to

[58] Abraham et al., "Measurement of the energy spectrum of cosmic rays above $10^{18}$ eV using the Pierre Auger Observatory".

[59] Waxman and Bahcall, "High energy neutrinos from astrophysical sources: An upper bound".

[60] Waxman, "Cosmological Origin for Cosmic Rays above $10^{19}$ eV".

magnetic fields. While confined within their trap, protons can produce pions and, therefore, gamma rays and neutrinos via collisions with gas. If the pion production efficiency is maximal (100%), the entire energy carried by trapped CRs could be converted into that of gamma rays and neutrinos in a calorimetric limit. This calorimetric limit, known as the *Waxman-Bahcall limit*, corresponds to a an all-flavor neutrino energy density[61]

$$E_\nu^2 \phi_\nu(E_\nu) \sim 2 \times 10^{-8}\ \mathrm{GeV\,cm^{-2}s^{-1}sr^{-1}}, \tag{2.19}$$

illustrated in Figure 2.8 as a dotted-dashed green line, which is well consistent with the latest measurement of a diffuse flux of muon neutrinos only[62] (orange shaded area).

On the other end of the spectrum, the large neutrino flux in the range of $10 - 100$ TeV challenges a possible trivial connection to the isotropic gamma-ray background (IGRB). Such excess is visible in the latest best-fit neutrino flux resulting from a combined fit of a multi-flavor neutrino sample,[63] shown as a red-shaded area.

The total neutrino and gamma-ray fluxes from pion decays are related by[64]

$$\left.\frac{\mathrm{d}\phi_\nu}{\mathrm{d}E_\nu}\right|_{E_\nu = E_\gamma/2} \approx \frac{1}{2}\left.\frac{\mathrm{d}\phi_\gamma}{\mathrm{d}E_\gamma}\right|_{E_\gamma}. \tag{2.20}$$

Assuming that the total IGRB is induced by photons from the decay of neutral mesons within optically transparent sources, a maximally possible neutrino flux from the same population can be estimated according to Equation 2.20. This limit is illustrated as a dashed blue line in Figure 2.8.

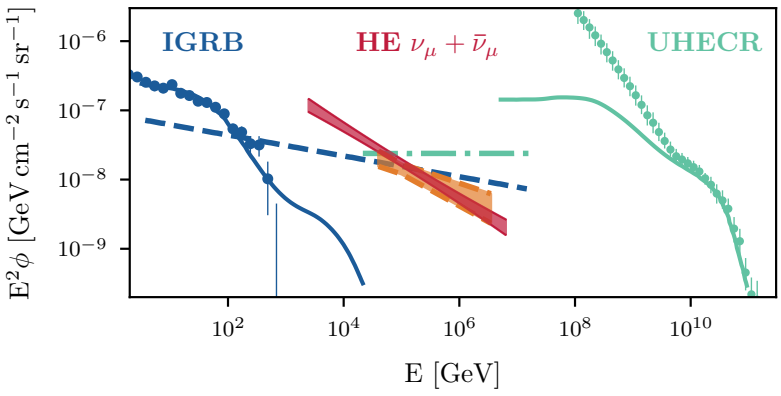


Figure 2.8: Observed spectral energy distribution of diffuse gamma rays, high-energy neutrinos, and UHECRs. The IGRB, neutrino, and UHE CR data are from Ackermann et al., "The Spectrum of Isotropic Diffuse Gamma-Ray Emission between 100 MeV and 820 GeV", Maurin et al., "A cosmic-ray database update: CRDB v4.1", Abbasi et al., "Improved Characterization of the Astrophysical Muon-neutrino Flux with 9.5 Years of IceCube Data". The description of the different lines can be found in the text. The figure is adapted from Ahlers and Halzen, "Opening a new window onto the universe with IceCube", where more details can be found.

Despite suggesting a powerful connection between the gamma-ray and neutrino backgrounds, the relation in Equation 2.20 can have only minimal practical application, primarily for three reasons. First, the assumption that all IGRB photons come from pion decays does not hold, as significant contributions to the EBL are attributed to purely leptonic gamma rays. Second, as discussed in Subsection 2.2.1, TeV gamma-ray emission is attenuated to sub-TeV

[61] Waxman and Bahcall, "High energy neutrinos from astrophysical sources: An upper bound".

[62] Abbasi et al., "Improved Characterization of the Astrophysical Muon-neutrino Flux with 9.5 Years of IceCube Data".

[63] Naab et al., "Measurement of the astrophysical diffuse neutrino flux in a combined fit of IceCube's high energy neutrino data".

[64] Ahlers and Halzen, "Opening a new window onto the universe with IceCube".

energies in pair-production processes with the EBL and CMB,[65] thus making the connection between the intensities from the two messengers non-trivial. Finally and most importantly, the approximation of completely transparent sources is immediately challenged by the fact that fields of optical/UV photons are expected in many astrophysical source environments, as we will see in Section 2.3. Similarly to the case of attenuation with the EBL, TeV gamma rays become prone to absorption already within the source due to pair-production processes, whose cross-section is $\sim 10^4$ times larger than the cross-section for photo-meson production. At the same time, neutrinos associated with the absorbed gamma rays can escape unbothered.

The idea that neutrinos may be produced in the cores of AGNs by photo-meson interaction of protons accelerated to high energy has been revived to explain the diffuse neutrino excess at tens of TeV.[66] In this scenario, neutrinos are produced close to the central black hole where the proton photo-meson optical depth is very high, $\tau_{p\gamma} \sim 100$. In such conditions, the observation of high-energy neutrinos in combination with the non-detection of an accompanying flux of gamma rays as expected from Equation 2.20 is an example of a powerful application of multi-messenger constraints to shed light on the production mechanisms of astrophysical source populations. Further confirmation of the theory would come from the detection of the original gamma-ray flux at lower energies, possibly hard X-rays of MeV photons.[67] The case of NGC 1068, the first ever detected "hidden" neutrino source, is discussed in detail in Chapter 3.

## 2.3 *Astrophysical accelerator candidates*

The mechanism that accelerates CRs has to energize particles from a thermal population so that they occupy a non-thermal high-energy tail that follows the observed spectral shape of a power-law. Acceleration by electric fields is not possible in astrophysical environments, where the matter is in the state of a completely ionized medium with high electrical conductivity where free charges rapidly re-arrange to reach overall neutrality.[68]

It was Enrico Fermi who proposed that charged particles undergoing a series of scattering events with moving clouds of gas or crossing a shock front separating stellar material could be accelerated to relativistic energies.[69,70] As magnetic fields are almost omnipresent in astrophysical objects, they can provide magnetic irregularities for the particles to scatter back and forth across the shock front. The space/-time variations of the magnetic field imply the existence of transient electric fields ($\nabla \times E = -\partial B/\partial t$), which can accelerate charged particles.[71] This type of *diffusive shock acceleration* (DSA) can be applied to the shock waves produced, for example, in supernova explosions or gamma-ray bursts.

Although several other mechanisms have been proposed, diffuse acceleration mechanisms are convincing as they naturally lead to a universal $E^{-2}$ spectrum. Once convolved with the effects of the

[65] Berezinskii and Smirnov, "Cosmic Neutrinos of Ultra High Energies and Detection Possibility".

[66] Murase, Guetta, and Ahlers, "Hidden Cosmic-Ray Accelerators as an Origin of TeV-PeV Cosmic Neutrinos".

[67] Berezinsky, *Proceedings of the International Conference Neutrino '77*.

[68] Spurio, *Probes of Multimessenger Astrophysics*, p. 184.

[69] Fermi, "On the Origin of the Cosmic Radiation".

[70] Fermi, "Galactic Magnetic Fields and the Origin of Cosmic Radiation."

[71] Spurio, *Probes of Multimessenger Astrophysics*, p. 233.

propagation through the galaxies and after accounting for possible inefficient situations, the predicted spectral index softens to $\sim$ 2.6,[72] consistent with the observations (see Figure 2.1). Most importantly, diffusive acceleration does not require the injection of any pre-accelerated seed particles but increases the energy of particles directly from the thermal population.

[72] Gaisser, Engel, and Resconi, *Cosmic Rays and Particle Physics: 2nd Edition*.

The maximum energy attainable by a particle of charge $Z$ is always a function of its Larmor radius (see Equation 2.1). The particle must be confined within the acceleration site long enough to gain the energy needed to explain the highest energy cosmic rays. When the particle's energy is such that its Larmor radius exceeds the size of the accelerator, the particle escapes the acceleration site. The Hillas criterium[73] formalizes the concept by constraining the maximum acceleration energy of a potential source depending on its magnetic field $B$ and size of the acceleration/confinement region $R$:

[73] Hillas, "The Origin of Ultra-High-Energy Cosmic Rays".

$$E_{\max} = Z\beta B \left(\frac{G}{\mu G}\right) R \left(\frac{L}{kpc}\right) \text{EeV}, \tag{2.21}$$

where $\beta = v/c$ is the velocity of the particle in terms of a fraction of the speed of light. Therefore, the magnetic field should be very strong to reach EeV energies in a small source and vice versa. Practically, this relation translates into the famous Hillas plot, where the maximum attainable energy for a given nuclear charge Z is approximately equal to the product of $B$ and $R$. Figure 2.9 shows the relation between these two quantities needed to accelerate relativistic protons ($Z = 1$ and $\beta = 1$) to the highest energies observed. Potential accelerators are placed on the diagram based on their properties: Sources in the lower left corner, below the line corresponding to a certain maximal energy, cannot provide the corresponding acceleration.

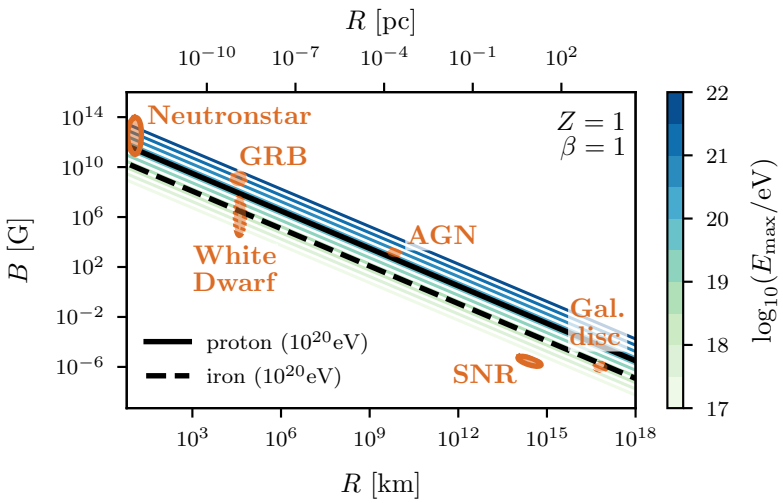


Figure 2.9: Adaptation of the Hillas plot showing classes of astrophysical objects that can provide confinement regions of the right size in appropriate magnetic fields to produce high-energy protons ($Z = 1$ and $\beta = 1$). Lines of different colors indicate $B \cdot R = E_{\max} = const$ for different configurations of the accelerator parameters $R$ and $B$. The maximum observed cosmic-ray energy of $\sim 10^{20}$ eV is highlighted for protons and iron nuclei as solid and dashed black lines, respectively. Figure adapted from Huber, "Multi-Messenger correlation study of Fermi-LAT blazars and high-energy neutrinos observed in IceCube".

At the same time, the diagram identifies a variety of astrophysical objects that are potential source candidates. In the following sections, we introduce a few candidate extragalactic CR and neutrino sources,

namely gamma-ray bursts, starburst galaxies, and AGN. The latter two are of particular interest for this work as both the starburst component and the AGN of the brightest extragalactic neutrino emitter identified to date, NGC 1068,[74] are evaluated as candidate neutrino sources in Section 3.1.

[74] Abbasi et al., "Evidence for neutrino emission from the nearby active galaxy NGC 1068".

### 2.3.1 *Gamma-ray bursts*

Among the extragalactic candidates, it is worth mentioning gamma-ray bursts (GRBs), the most energetic transient eruptions observed in the universe[75]. The mechanism that produces bursts is likely initiated by the collapse of a rapidly rotating massive star or the merging of massive binary systems. The shock dissipates the kinetic energy of the relativistically expanding blast waves generated by the newborn central compact object (*e.g.*, a black hole or a neutron star) and produces non-thermal electrons through DSA. A bright gamma-ray emission is then created through synchrotron emission of the accelerated electrons. In principle, internal shocks can also accelerate non-thermal protons, which are expected to produce high-energy neutrinos via photohadronic collisions.[76] The brightest GRB ever observed happened recently, in October 2022.[77,78,79] On that occasion, the Large High Altitude Air Shower Observatory (LHAASO) observed photons with energies $\gtrsim 10$ TeV from a GRB for the first time.[80] However, not even this extremely powerful event was associated with high-energy neutrinos.[81] This non-observation poses severe constraints on hadronic acceleration in the same source region where gamma rays are produced.[82]

[75] See, *e.g.*, Spurio, *Probes of Multimessenger Astrophysics*.

[76] Kimura, "Neutrinos from Gamma-Ray Bursts".

[77] Dichiara et al., "Swift J1913.1+1946 a new bright hard X-ray and optical transient".

[78] Veres et al., "GRB 221009A: Fermi GBM detection of an extraordinarily bright GRB".

[79] Pillera et al., "GRB 221009A: Fermi-LAT refined analysis".

[80] Huang et al., "LHAASO observed GRB 221009A with more than 5000 VHE photons up to around 18 TeV".

[81] Abbasi et al., "Limits on Neutrino Emission from GRB 221009A from MeV to PeV Using the IceCube Neutrino Observatory".

[82] Murase, Mukhopadhyay, et al., "Neutrinos from the Brightest Gamma-Ray Burst?"

### 2.3.2 *Starburst galaxies*

Global emission of most galaxies across a large part of the electromagnetic spectrum from radio to gamma-ray energies is related to the formation and destruction of massive stars. Starburst galaxies (SBs) are characterized by kpc-scale regions of especially intense star-forming (SF) activity ($100 - 1000\ M_\odot \mathrm{yr}^{-1}$ compared to the average $1 - 5\ M_\odot \mathrm{yr}^{-1}$ of quiescent galaxies like the Milky Way) powered by a high supernova rate.[83] The main tracer of this activity is the far-IR emission,[84] originating from the absorption of UV/optical light from the galaxy by clouds of dust. Far-IR emission dominates the spectral energy distribution of SBs. However, numerous supernovae and supernova remnants provide both the relativistic electrons and the magnetic fields necessary for synchrotron emission, appearing at radio frequencies.[85]

In SBs, CR protons are accelerated in processes creating stellar remnants, like pulsars, pulsar-wind nebulae, and supernova remnants, and can then participate in $p - p$ inelastic collisions with the ambient gas. Therefore, the production of neutrinos and gamma rays from pion decays is expected in SBs. A purely leptonic scenario is also viable, with electrons producing gamma rays via bremsstrahlung or by IC upscattering of low energy photons.[86] Hence, SBs clas-

[83] Tamborra, Ando, and Murase, "Star-forming galaxies as the origin of diffuse high-energy backgrounds: gamma-ray and neutrino connections, and implications for starburst history".

[84] Kennicutt, "Star Formation in Galaxies Along the Hubble Sequence".

[85] Condon, "Radio emission from normal galaxies."

[86] Völk, F. A. Aharonian, and Breitschwerdt, "The Nonthermal Energy Content and Gamma-Ray Emission of Starburst Galaxies and Clusters of Galaxies".

sify as some of the most promising sources of high-energy CRs in the nearby universe, and indeed $0.1 - 100$ GeV gamma-ray emission has been resolved from a few starburst galaxies by *Fermi*-LAT.[87] Neutrinos have been detected from one starburst galaxy, NGC 1068.[88] From the same source, a steady flux of gamma rays has been constantly detected over the years by *Fermi*-LAT.[89] However, as will be discussed in Chapter 3, while the gamma-ray flux convincingly originates from the SB, the observed neutrinos are unlikely to be produced in the same source. Additionally, multi-wavelength studies have shown that the contribution of starburst galaxies to the astrophysical neutrino flux at 100 TeV cannot exceed more than $\sim 30\%$.[90] The constraint is mainly driven by the observation that the vast majority of the extragalactic *Fermi*-LAT detected gamma rays is already associated with blazars,[91] which limits the amount of high-energy gamma rays that should accompany a neutrino flux in starburst galaxies.

[87] Ajello et al., "The $\gamma$-Ray Emission of Star-forming Galaxies".

[88] Abbasi et al., "Evidence for neutrino emission from the nearby active galaxy NGC 1068".

[89] Abdollahi et al., "Fermi Large Area Telescope Fourth Source Catalog".

[90] Bechtol et al., "Evidence against Star-forming Galaxies as the Dominant Source of Icecube Neutrinos".

[91] Abdollahi et al., "Incremental Fermi Large Area Telescope Fourth Source Catalog".

### 2.3.3 *Active Galactic Nuclei*

Active Galactic Nuclei (AGN) are luminous astrophysical sources whose spectral energy distributions span the entire electromagnetic spectrum, from radio waves to TeV gamma rays.[92] They are the most powerful, non-explosive sources in the universe, with bolometric luminosities[93] reaching up to $L_{\rm bol} \approx 10^{48}$ erg/s. Throughout the previous century, multiple different features in the AGN spectra led to their classification into a large variety of sub-classes. Despite their diversity, AGN share some important characteristics: 1. Their luminous energy emission cannot originate from nuclear fusion in stars; 2. They exhibit strong and often Doppler-broadened emission lines in their spectra, indicative of fast-moving, obscuring material; 3. Their highly variable emission suggests small emitting regions with high energy density.

[92] Padovani et al., "Active galactic nuclei: what's in a name?"

[93] The bolometric luminosity is the total amount of energy emitted by the source per unit time, integrated over all wavelengths.

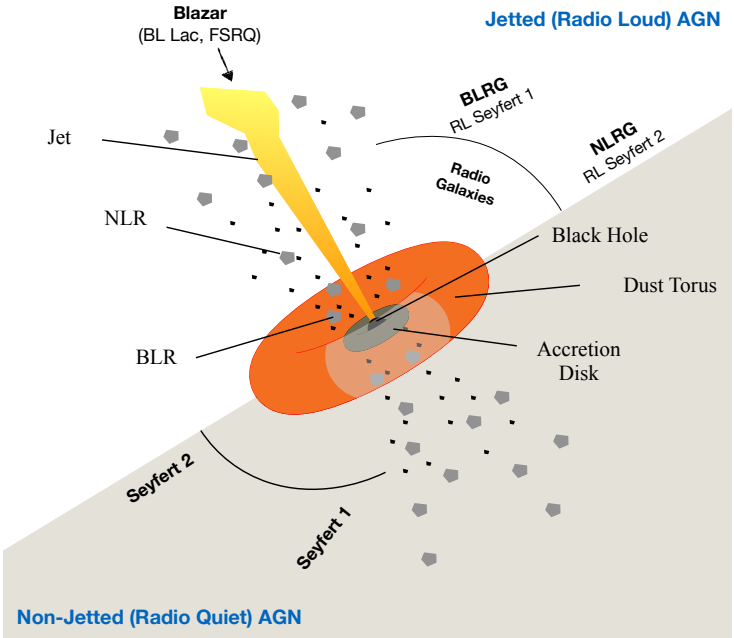


Figure 2.10: A schematic view of the different classes of AGN depending on the viewing angle and the presence or absence of a strong, relativistic jet. The main structures of the AGN, described in the text, are indicated. Abbreviations not explicitly mentioned in the text are BLRG and NLRG, standing for Broad and Narrow Line Radio Galaxy, respectively. Adapted from Urry and Padovani, "Unified Schemes for Radio-Loud Active Galactic Nuclei" and reprinted with permission from Glauch, "The Origin of High-Energy Cosmic Particles: IceCube Neutrinos and the Blazar Case".

Figure 2.10 proposes a schematic view of AGN, which we can generally conceptualize by combining a handful of components that span a wide range of physical scales. Each structure can be probed by studying different components of the broadband spectral emission of AGN, which are illustrated in Figure 2.11 for various classes of sources. In the following, we describe the main physical structures of the AGN and connect them to their respective photon fluxes.

**The spinning supermassive ($M_{\rm BH} > 10^6\ M_\odot$) black hole** (SMBH) at the center of the galaxy powers the AGN by actively accreting hot gas and plasma. The mass of the black hole sets the Eddington limit, that is the maximum luminosity of a source when the outward, accretion-induced radiation pressure is balanced by the inward gravitational force:[94]

$$L_{\rm Edd} = \frac{4\pi G M_{\rm BH} m_{\rm p} c}{\sigma_{\rm T}} \approx 1.26 \times 10^{38} \frac{M_{\rm BH}}{M_\odot}\,{\rm erg/s}, \tag{2.22}$$

where $G$ is the gravitational constant, $m_{\rm p}$ is the proton mass, and $\sigma_{\rm T}$ is the Thomson scattering cross section on electrons. The SMBH extends on $10^{-7} - 10^{-3}$ pc scales.

[94] Gaisser, Engel, and Resconi, *Cosmic Rays and Particle Physics: 2nd Edition*, p. 270.

**The accretion disc** surrounding the SMBH is formed by the accreting material. Highly variable emission ranging from optical to soft X-rays originates from the geometrically thin but optically thick accretion disc. It results in the so-called *blue bump* shown in Figure 2.11 as a dashed-dotted line. The accretion disc extends up to $\sim 1$ pc. Within this same distance, clouds of hot gas of the *broad line region* (BLR) moving at supersonic velocities are ionized by the intense radiation from the accretion disc. The large velocities produce strong, Doppler-broadened emission lines in the optical spectra of AGN. In contrast, the *narrow line region* (NLR) is located further away from the black hole (up to several hundred parsecs), thus having lower densities and moving at lower velocities.[95]

[95] Padovani et al., "Active galactic nuclei: what's in a name?"

**The corona** is a compact region of diffuse, high-energy plasma of hot ($\approx 10^9$ K) electrons situated close to the supermassive black hole, typically above and below the accretion disc. It extends up to $10^{-5}$ pc scales and is responsible for the highly variable emission of non-thermal X-rays through inverse Compton upscattering of UV photons from the disc. The emission extends from soft to hard X-rays, as seen from the dotted line in Figure 2.11, and its intrinsic spectrum is modified by a reflection bump at around 30 keV caused by interaction with matter. As more accretion power is fed into the electrons, their temperature increases and the upscattered photons obtain higher energies. The process continues until the X-ray photons reach the threshold energy for producing electron-positron pairs in a runaway process that converts the additional luminosity into an increased number of pairs instead of increased temperature. Therefore, $\gamma - \gamma$ collisions act as a thermostat that limits the source temperature and thus also the maximum X-ray energy, introducing a spectral cutoff at a few hundred keV.[96]

[96] Fabian, Lohfink, Kara, et al., "Properties of AGN coronae in the NuSTAR era".

**A torus** of gas and dust surrounds the central engine, extending approximately from 1 to 10 pc beyond the BLR. The dust reprocesses the emission from the accretion disc into the IR bump shown as a dashed line in Figure 2.11. It plays a fundamental role in the unified model of AGN,[97] as the orientation of the dusty torus with respect to the line of sight drives the different optical spectral features of type 1 and type 2 AGN. Depending on whether we see the galaxy face-on (directly into the SMBH) or edge-on (through the torus), AGN are classified as type 1 or type 2, respectively. Optical spectra of type 2 AGN exhibit only narrow emission lines because the dusty torus completely obscures the broad line region. Very high gas and dust column densities can obscure even the X-ray emission from the corona, especially the softer one (see Section 3.1 and Subsection 8.2.3). Importantly, host galaxies with high SF activity can rival the luminosity of the AGN in the IR band. However, SF galaxies (*e. g.*, starburst galaxies, Subsection 2.3.2) usually dominate the lower energy IR band (far IR), while the AGN is prominent in the mid-IR.

[97] Urry and Padovani, "Unified Schemes for Radio-Loud Active Galactic Nuclei".

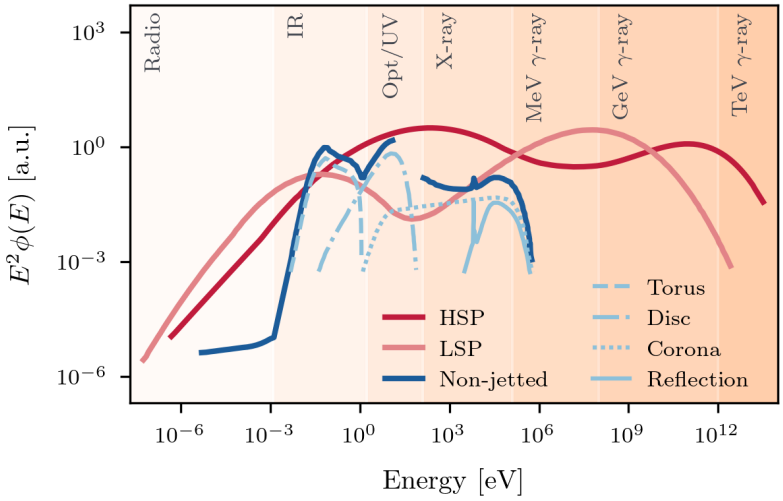


Figure 2.11: Schematic illustration of the typical spectral energy distribution for different classes of AGN: Blazars of the HSP (red) and LSP (rose) type and a non-jetted AGN (blue). Features from the disc-corona accretion and the dusty torus are illustrated as different non-solid lines as described in the legends. Note that their normalization relative to the total emission from a non-jetted AGN is slightly scaled down for better figure readability. The shading in the background represents different energy bands in the electromagnetic spectrum. Figure adapted from Padovani et al., "Active galactic nuclei: what's in a name?"

**Two relativistic jets** of accelerated particles can be emitted from the AGN core perpendicularly to the disc and can extend up to ∼Mpc scales. "Jetted" AGN exhibit enhanced emission in the radio and gamma-ray energy bands. They are rather rare, as less than 10% of all AGN are "jetted".[98] When the jet points at the Earth with an opening angle of $15 - 20°$, we call the AGN a *blazar*. Contrary to non-jetted AGN,[99] the spectral energy distribution of blazars is dominated by the non-thermal emission with a characteristic double-humped shape that hides completely any contributions from the host galaxy or the accretion mechanism. The first peak is associated with synchrotron emission of relativistic electrons, and depending on its position, blazars are further classified as high-/intermediate-/low-synchrotron peak blazars (HSP/ISP/LSP), with the thresholds at $\sim 10^{14}$ Hz and $\sim 10^{15}$ Hz (equivalent to 0.4 eV and 4.1 eV). The

[98] Padovani, "On the two main classes of active galactic nuclei".

[99] AGN that do not exhibit any jet-like feature or have only weak, non-relativistic, sub-kpc jets.

nature of the second hump is more uncertain: In a fully leptonic scenario, it is attributed to IC scattering of the synchrotron photons on the plasma of relativistic electrons (synchrotron self-Compton), while a complementary hadronic scenario could explain the high-energy peak via the production of $\pi^0$.[100] In the latter case, blazars become high-energy neutrino emitters. Exemplary spectral shapes of an LSP and an HSP blazar are illustrated as rose and red lines, respectively, in Figure 2.11. Finally, blazars showing strong optical emission lines are called *flat spectrum radio quasars* (FSRQs), while featureless optical spectra are typical of *BL Lac* type blazars[101].

[100] Padovani et al., "Active galactic nuclei: what's in a name?"

[101] see Padovani, Petropoulou, et al., "A simplified view of blazars: the neutrino background" for a detailed review.

The most abundant class of non-jetted AGN is the one of *Seyfert galaxies*. These AGN have a low luminosity ratio between the central core and the host galaxy. Hence, their spectral emission is usually contaminated by contributions from the galaxy, typically due to star formation.[102] Seyfert galaxies are further classified as type 1 or 2 based on the width of the emission lines in their optical spectra. As mentioned in the description of the dusty torus component of AGN, this distinction is only apparent and not intrinsic, fundamentally due to our viewing angle of the galaxy with respect to the torus.

[102] Padovani et al., "Active galactic nuclei: what's in a name?"

Finally, it is important to mention that many (possibly most) AGN also show large-scale outflows/winds of matter driven by the central BH,[103,104] which are both less collimated and slower than relativistic jets. Outflows play a significant role in galaxy evolution as they may quench the star formation and starve the AGN through the lack of available material for accretion. They come in various "phases" characterized by different temperatures and compositions such as ionized, atomic, and molecular. AGN outflows are accelerated through shock acceleration by the radiation fields surrounding the SMBH and can cover distances that go from $10^{-3}$ to $10^3$ parsec.[105] Outflows velocities have been measured ranging from $\sim 10^2$ km s$^{-1}$ up to semi-relativistic speeds of $\sim 0.3c$ for *ultrafast outflows* (UFOs).[106] If protons are being accelerated in the outflow shells that constitute the shock, they can undergo inelastic collisions and produce pions that will in turn generate neutrinos and gamma rays. Several studies have proposed hadronic acceleration models for outflows.[107,108,109] However, to not violate the measured flux from other cosmic messengers, these studies suggest that the maximum contribution to the EGB and the diffuse neutrino flux are limited to $20 - 30\%$.

[103] Harrison, "Impact of supermassive black hole growth on star formation".

[104] Cicone et al., "The largely unconstrained multiphase nature of outflows in AGN host galaxies".

[105] X. Wang and Loeb, "Probing the gaseous halo of galaxies through non-thermal emission from AGN-driven outflows".

[106] Cicone et al., "The largely unconstrained multiphase nature of outflows in AGN host galaxies".

[107] X. Wang and Loeb, "Cumulative neutrino background from quasar-driven outflows".

[108] Lamastra et al., "Galactic outflow driven by the active nucleus and the origin of the gamma-ray emission in NGC 1068".

[109] Liu et al., "Can Winds Driven by Active Galactic Nuclei Account for the Extragalactic Gamma-Ray and Neutrino Backgrounds?"

# 3 NGC 1068: A Non-Jetted AGN as a Cosmic Laboratory

**Disclaimer:** This part of the thesis is mainly based on discussions that happened during the *Topical Workshop on NGC 1068* held at the Munich Institute for Astro-, Particle and BioPhysics in Garching on March 6 – 10, 2023[1]. Out of that meeting, organized by the author of this thesis, we wrote the review paper Padovani, Resconi, Ajello, Bellenghi, et al. *Supermassive black holes and very high-energy neutrinos: the case of NGC 1068*,[2] which has been accepted for publication in *Nature Astronomy*. Our work inspires the structure of the first half of this chapter, although we refer the reader to the paper and references therein for additional details.

[1] https://indico.ph.tum.de/event/7179/.

[2] Padovani, Resconi, Ajello, et al., "Supermassive black holes and very high-energy neutrinos: the case of NGC 1068".

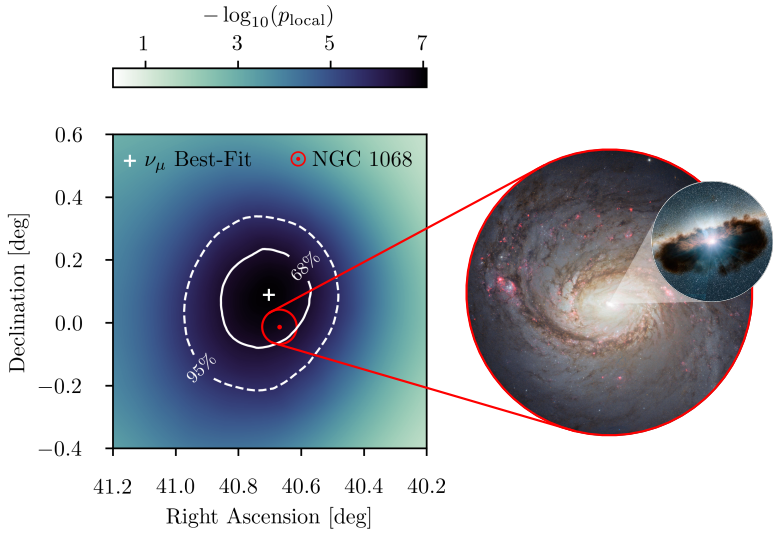


Figure 3.1: Neutrino significance map around the location of NGC 1068. The white cross marks the most significant neutrino emission. The 68% and 95% confidence regions are outlined in white. NGC 1068 is marked by a red dot, with the red circle representing the optical size of the galaxy hosting the AGN. On the right, the two insets show an image of the spiral galaxy and an illustration of its active nucleus surrounded by the dusty torus. Illustration reproduced from NASA/JPL-Caltech.

In 2022, with the IceCube collaboration, we reported evidence for TeV neutrino emission from the nearby prototypical Seyfert 2 galaxy NGC 1068,[3] a non-jetted AGN,[4] showing vigorous starburst (SB) activity.[5] This detection is of special importance to this dissertation, as part of the studies discussed in Chapter 8 are motivated by NGC 1068 currently being the most significant extragalactic source in the neutrino sky. Here, this cosmic accelerator is discussed in more detail.

[3] Abbasi et al., "Evidence for neutrino emission from the nearby active galaxy NGC 1068"

[4] We follow Padovani, "On the two main classes of active galactic nuclei" who pointed out that the distinction between radio-loud and radio-quiet AGN should be replaced by the one between jetted and non-jetted AGN. In fact, the difference in radio power is dominated by the presence or lack of a strong, relativistic jet.

[5] Neff et al., "Ultraviolet Imaging of the AGN + Starburst Galaxy NGC 1068".

We performed an all-sky search for point-like neutrino sources in the Northern sky and found the most significant emission to be located $0.11^\circ$ away from NGC 1068[6] (Figure 3.1). The source was part of a predefined list of gamma-ray emitters searched for point-like emission in the context of that work.[7] The emission from the direction of NGC 1068 showed incompatibility at $4.2\,\sigma$ with the atmospheric and diffuse astrophysical neutrino background assumption. Under the assumption of a single power law, we measured the muon-neutrino energy flux from NGC 1068 at 1 TeV, which has a best-fit normalization $\phi^{1\ \mathrm{TeV}}_{\nu_\mu+\bar{\nu}_\mu} = (5.0 \pm 1.5) \times 10^{-11}\ \mathrm{TeV}^{-1}\,\mathrm{cm}^{-2}\mathrm{s}^{-1}$ and a best-fit spectral index $\gamma = 3.2 \pm 0.2$ in the energy range between 1.5 and 15 TeV.[8] This flux corresponds to an equivalent all-flavor isotropic neutrino luminosity

$$L = 4\pi D_{\mathrm{L}}^2 \int_{E_{\mathrm{min}}}^{E_{\mathrm{max}}} E_\nu \phi^{1\ \mathrm{TeV}}_\nu(E_\nu)\mathrm{d}E_\nu = 10^{42.1\pm0.2}\ \mathrm{erg/s} \tag{3.1}$$

in the same energy range, with $D_{\mathrm{L}} = 10.1$ Mpc and $\phi^{1\ \mathrm{TeV}}_\nu = 3 \times \phi^{1\ \mathrm{TeV}}_{\nu_\mu+\bar{\nu}_\mu}$, assuming an equal contribution from all three neutrino flavors.

Since non-jetted AGN are typically dominated by thermal emission from the accretion disc and the host galaxy, the detection of neutrinos from NGC 1068 surprised many in the field. Jetted AGN, known for their predominantly non-thermal emission, were deemed to be the only class of AGN capable of accelerating protons to the energies necessary for $\sim 0.1 - 1$ PeV neutrino production,[9] which is the energy range where the astrophysical diffuse neutrino flux is constrained.[10] Now, the observation of a neutrino source at TeV energy requires understanding *where* the non-thermal radiation responsible for the generation of ∼TeV neutrinos is produced, and *how* it is created. However, as can be seen from Figure 3.1, the spatial resolution of the IceCube detector allows us to localize the neutrino emission within a $1\,\sigma$ confidence region that encompasses the entire galaxy hosting NGC 1068. Telling where this signal is produced in the galaxy is not possible by only looking at neutrino data. While several studies have tried to model the neutrino emission from NGC 1068 to fit the IceCube data,[11,12,13] here we resort to the study of the multi-messenger features of its spectrum. Using order-of-magnitude estimates, we try to constrain the origin of the astrophysical neutrinos from an observational, phenomenological, and theoretical perspective.

NGC 1068 is among the six spiral galaxies identified by Carl Seyfert in 1943[14] and then named Seyfert galaxies after him. These galaxies show strong emission lines and are classified as Seyfert 1 or Seyfert 2, depending on the inclination at which we observe them. Seyfert 2s, *e. g.*, NGC 1068, are observed edge-on with respect to the dusty torus of molecular gas surrounding the accretion disc, see Figure 2.10. Since the dust extends on scales larger than the region emitting the broad

[6] This is a typical resolution to a strong point-like source emission of dedicated IceCube analyses, see Abbasi et al., "Evidence for neutrino emission from the nearby active galaxy NGC 1068" for more details.

[7] See Subsection 8.2.1 for a description of the selection criteria.

[8] Abbasi et al., "Evidence for neutrino emission from the nearby active galaxy NGC 1068".

[9] See Subsection 2.3.3 for a brief summary of the classification of AGN classes and their properties, and Giommi and Padovani, "Astrophysical Neutrinos and Blazars" for a review on blazars.

[10] Aartsen et al., "Characteristics of the Diffuse Astrophysical Electron and Tau Neutrino Flux with Six Years of IceCube High Energy Cascade Data".

[11] Inoue et al., "On High-energy Particles in Accretion Disk Coronae of Supermassive Black Holes: Implications for MeV Gamma-rays and High-energy Neutrinos from AGN Cores".

[12] Murase, "Hidden Hearts of Neutrino Active Galaxies".

[13] Kheirandish, Murase, and Kimura, "High-energy Neutrinos from Magnetized Coronae of Active Galactic Nuclei and Prospects for Identification of Seyfert Galaxies and Quasars in Neutrino Telescopes".

[14] Seyfert, "Nuclear Emission in Spiral Nebulae."

excitation lines (BRL, see Subsection 2.3.3), only narrow lines, emitted further away and thus less Doppler-broadened, are observed in the optical spectrum. Hence, the optical radiation produced near the central core of Seyfert 2 galaxies is much more absorbed along the line of sight than for Seyfert 1, and the difference in their spectra is indeed not intrinsic but only due to obscuration.[15] Example optical spectra of a Seyfert 1 and a Seyfert 2 galaxies are shown in Figure 3.2.

[15] Antonucci and Miller, "Spectropolarimetry and the nature of NGC 1068."

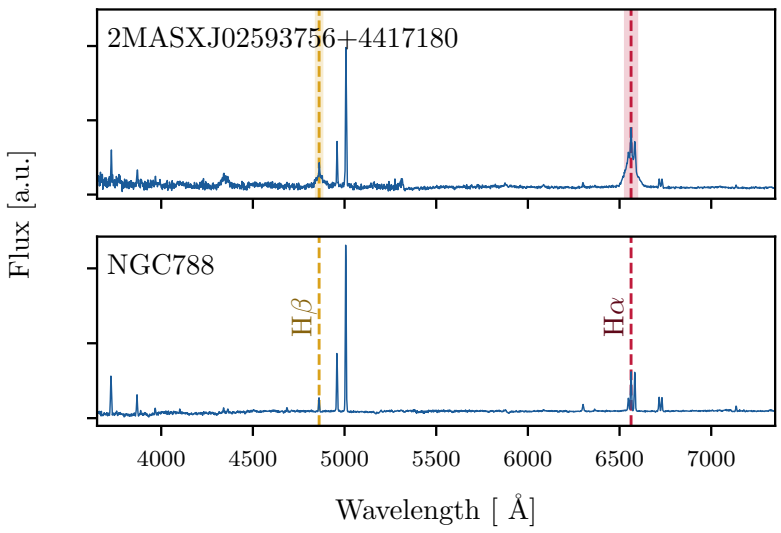


Figure 3.2: Optical spectra of a typical Seyfert 1 (top) and Seyfert 2 (bottom) AGN normalized to arbitrary flux units. The H$\alpha$ and H$\beta$ emission lines are marked on both spectra. While Seyfert 2 galaxies show only narrow emission lines, Seyfert 1s are also characterized by broad lines. Note that both spectra have already been shifted to their nominal wavelength $\lambda_0$ via the redshift correction $\lambda = \lambda_0(z+1)$. Data from https://www.bass-survey.com/dr2.html.

NGC 1068 is located at a luminosity distance $D_{\rm L} = 10.1$ Mpc. Most references in the literature report a luminosity distance of 14.4 Mpc. However, the redshift of this source, $z = 0.0038$, cannot be directly used for the estimation of the luminosity distance by using standard flat $\Lambda$CDM cosmological parameters[16]. In fact, being relatively nearby, the radiation from this source suffers from the anisotropic gravitational pull of local overdensities, which cannot be simply averaged out on such short distances. The BH mass ($M_{\rm BH}$) of NGC 1068 in units of solar masses $M_\odot$ is estimated to be approximately $6.7 \times 10^6\ M_\odot$.[17] Therefore, assuming isotropic accretion-induced emission,[18] we can derive the Eddington luminosity (Equation 2.22) of the source as

$$L_{\rm Edd} \simeq 1.26 \times 10^{38} \frac{M_{\rm BH}}{M_\odot}\,{\rm erg/s} \sim 8.4 \times 10^{44}\,{\rm erg/s}, \tag{3.2}$$

[16] Hubble constant $H_0 = 70\,{\rm km s^{-1} Mpc^{-1}}$, matter density $\Omega_m = 0.3$, and dark energy density $\Omega_\Lambda = 0.7$.

[17] J.-M. Wang et al., "Dynamical evidence from the sub-parsec counter-rotating disc for a close binary of supermassive black holes in NGC 1068".

[18] Rybicki and Lightman, "Radiative Processes in Astrophysics".

## 3.1 *A multi-messenger picture*

The proximity of NGC 1068 makes it possible to spatially resolve its structure into several components. Each can be studied using observations in different electromagnetic bands, offering complementary perspectives on the underlying physics. A multi-messenger spectral energy distribution (SED) of NGC 1068 is displayed in Figure 3.3. Some distinguishable features have been highlighted: 1. The $\nu^{-0.7}$ radio spectrum, typically associated in starburst (SB) galaxies with

synchrotron emission from relativistic plasma accelerated in supernova remnants associated with massive star formation,[19] or with the AGN jet; 2. A template for the spiral SB galaxy emission, the IR bump which extends in the UV as well; 3. A template for emission from the accretion disc, the bump in the UV band here rather overwhelmed by the galactic emission, and the X-ray emission from the corona;[20] 4. The GeV gamma-ray emission most likely associated with SB activity in NGC 1068; 5. The TeV neutrino band, where no gamma-rays have been detected. The best-fit neutrino flux[21] is reported with its 68% uncertainty in the corresponding energy range at 68% confidence level (C.L.) as well.

[19] Condon, "Radio emission from normal galaxies."

[20] Both templates are constructed using the SSDC tool, https://tools.ssdc.asi.it/SED/.

[21] Abbasi et al., "Evidence for neutrino emission from the nearby active galaxy NGC 1068".

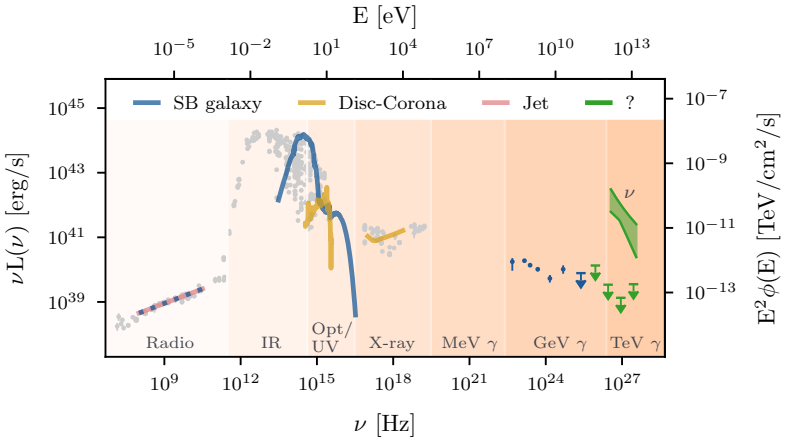


Figure 3.3: The integrated multi-messenger SED of NGC 1068, assembled using the SED builder at the SSDC (https://tools.ssdc.asi.it/SED/). We show the power/energy flux emitted at different frequencies/energies. The color code relates different emissions with the various components of NGC 1068. The radio synchrotron emission could originate both from the SB and the AGN jet. The GeV gamma-ray data points are *Fermi*-LAT measurements. The MAGIC telescope placed the upper limits on TeV gamma-ray emission. More details can be found in the text.

There is one clear, as well as unexpected, feature in the SED: No TeV gamma-rays were observed where the neutrino spectrum was constrained. GeV gamma-rays observed by the *Fermi*-LAT have been associated with NGC 1068 continuously since the first catalog (1FGL[22]) of gamma-ray sources. Since then, NGC 1068 has been included in every *Fermi*-LAT catalog, up to the 4FGL-DR4, at an increasing level of significance.[23] Its average power in the $0.1 - 100$ GeV range over twelve years is $L_\gamma = 10^{40.92 \pm 0.03}$ erg/s,[24] which is $\sim$ 15 times smaller than the all-flavor isotropic neutrino luminosity in $1.5 - 15$ TeV, see Equation 3.1. In the very-high-energy (VHE) band, the source was observed by ground-based Cherenkov telescopes[25,26,27] with no detection. The most stringent constraints on the VHE flux were placed by a 125-hour long observation performed by the MAGIC telescopes, resulting in a 95% C.L. upper limit to the gamma-ray flux above 200 GeV of $E\phi_{\mathrm{VHE}\gamma} = 5.1 \times 10^{-13}$ cm$^{-2}$ s$^{-1}$,[28] which is approximately two orders of magnitude smaller than the observed neutrino flux at $\sim$ TeV energies.

The mechanism accelerating protons and producing the neutrinos observed from the direction of NGC 1068 must also generate a flux of accompanying gamma-rays, see Section 2.2. The non-detection of

[22] Abdo et al., "Fermi Large Area Telescope First Source Catalog".

[23] Abdollahi et al., "Fermi Large Area Telescope Fourth Source Catalog".

[24] Ajello et al., "The $\gamma$-Ray Emission of Star-forming Galaxies".

[25] F. Aharonian et al., "Observations of selected AGN with HESS".

[26] Willox and HAWC Collaboration, "HAWC Follow-up on IceCube evidence from NGC 1068".

[27] Acciari et al., "Constraints on Gamma-Ray and Neutrino Emission from NGC 1068 with the MAGIC Telescopes".

[28] Ibid.

VHE gamma-rays, together with the lower GeV gamma-ray flux compared to the neutrino flux, suggests that this component is entirely absorbed in the source.

The components emerging from the SED of NGC 1068 can be associated with several possible candidates as neutrino sources, namely:

- the SB region in the spiral arms of the host galaxy,
- a $\lesssim$ kpc jet,
- the black hole (BH) vicinity (perhaps the accretion disc-corona system),
- a sub-kpc molecular outflow (perhaps a UFO[29]).

[29] Ultra-fast outflow, see Subsection 2.3.3

The general characteristics of these AGN components have been discussed in Subsection 2.3.3. In the following, we briefly review each of them in the context of NGC 1068 to understand which ones can provide the necessary target for neutrino production in hadronic interactions and, at the same time, entirely absorb the accompanying gamma-ray component. We will try to estimate the maximum gamma-ray power that can be obtained from each source, where possible, and derive the relative neutrino production, assuming all gamma-rays are of hadronic origin.

### *The starburst galaxy*

In star-forming galaxies (SFGs), the creation of stellar remnants leads to the acceleration of CRs. These CRs can collide with the interstellar matter in $p-p$ inelastic scattering, producing gamma-rays and neutrinos from pion decays (see Equation 2.12 and Equation 2.13). As both the gamma-ray and IR emissions are tracers of star-forming activity, SFGs are known to follow a correlation between the luminosities in the two energy bands, empirically parametrized as[30]

$$\log_{10}\left(\frac{L_\gamma}{\mathrm{erg/s}}\right) \simeq 39.3 + 1.2\log_{10}\left(\frac{L_{\mathrm{IR}}}{10^{10}L_\odot}\right), \tag{3.3}$$

[30] Ackermann et al., "GeV Observations of Star-forming Galaxies with the Fermi Large Area Telescope".

where $L_\odot = 10^{33.58}$ erg/s is the total luminosity of the Sun. The observed gamma-ray luminosity of NGC 1068, $L_\gamma = 10^{40.92\pm0.03}$ erg/s, correlates with its IR luminosity $L_{\mathrm{FIR},\,8-1000\,\mu\mathrm{m}} = 10^{44.6\pm0.1}$ erg/s[31] according to Equation 3.3 and has therefore been attributed to star-forming activity.[32] Emissions attributed to the SB galaxy hosting NGC 1068 are shown in blue in Figure 3.3.

[31] Sanders et al., "The IRAS Revised Bright Galaxy Sample".

[32] Ajello et al., "The $\gamma$-Ray Emission of Star-forming Galaxies".

By applying a two-source AGN-starburst model to the observational data of NGC 1068, a recent study has shown that its SB ring cannot be the main source of the IceCube neutrinos.[33] The latter could instead be explained by an optically thick source environment, such as the X-ray bright corona near the AGN core.[34]

[33] Eichmann et al., "Solving the Multimessenger Puzzle of the AGN-starburst Composite Galaxy NGC 1068".

[34] Ibid.

We can nevertheless compute an equivalent neutrino power in $1.5-15$ TeV corresponding to the observed gamma-ray power from the SB. We assume the most optimistic scenario to maximize the neutrino power, namely:

- The observed gamma-rays are of hadronic origin only, which implies $L_\nu \sim L_\gamma/2$, and
- the conversion from $0.1 - 100$ GeV (*Fermi*-LAT sensitive energy range) to $1.5 - 15$ TeV (IceCube sensitive energy range) assumes a spectral index of $\gamma = 2$, which, by using Equation 3.1, implies that $L_\nu[1.5 - 15\ \text{TeV}] \sim L_\gamma[0.1 - 100\ \text{GeV}]/6$. For comparison, using the measured spectral index $\gamma = 3.2$ yields $L_\nu[1.5 - 15\ \text{TeV}] \sim L_\gamma[0.1 - 100\ \text{GeV}]/10^5$.

We obtain a maximal SB-related neutrino power of $L_{\nu,\text{SB}} = 10^{40.1}$ erg/s, corresponding to only 6% of the observed neutrino luminosity.

All these considerations lead us to exclude the SB as the primary source of the IceCube neutrinos from NGC 1068.

### *The sub-kpc jet*

Figure 3.4 shows a radio image of the galaxy and its inner core. In the upper right panel of the figure, a $\sim$ 500 pc jet ending in lobe-like structures is visible, while the lower right panel zooms in even more and resolves a $\sim$ 50 pc jet. A jet of this size is almost two orders of magnitude less extended and much slower ($v < 0.05c$[35]) than the well-studied ultrarelativistic jet of the radio galaxy M87 ($v > 0.99c$[36]). This implies that NGC 1068 is a non-jetted AGN.[37] The total radio power at 1.4 GHz is $L_{1.4\text{GHz}} \simeq 10^{38.9}$ erg/s.[38] However, as both star-forming activities and the jet contribute as the main sources of synchrotron radiation in galaxies, it is not trivial to tell which one is producing the observed radio continuum (pink-blue dashed line in Figure 3.3). To distinguish between the two, we can again use a known correlation between the far IR and radio powers valid for SFGs[39,40]

$$\log_{10}\left(\frac{L_{1.4\text{GHz,SB}}}{\text{erg/s}}\right) \simeq 11.47 + \log_{10}\left(\frac{L_{\text{IR,SB}}}{10^{10}L_\odot}\right), \tag{3.4}$$

and derive $L_{1.4\text{GHz,SB}} \sim 10^{38.6}$, which is approximately half of the total radio power at 1.4 GHz. Hence, the jet can be considered responsible for the other half. Finally, the total jet power can be estimated from $L_{1.4\text{GHz,jet}}$ by studying the X-ray cavities that surround many massive galaxies. X-ray cavities directly measure the mechanical energy generated by AGN through winds or jets.[41] They are often produced by outflows or the radio jet and exhibit a significantly reduced or absent X-ray emission. We use the following relation[42]

$$\log_{10}\left(\frac{L_{\text{jet}}}{10^{42}\text{erg/s}}\right) = \log_{10}\left(\frac{L_{\text{X}_{\text{cav,jet}}}}{10^{42}\text{erg/s}}\right) \simeq 1.91 + 0.75\log_{10}\left(\frac{L_{1.4\text{GHz,jet}}}{10^{40}\text{erg/s}}\right), \tag{3.5}$$

which finally gives us a *total* jet power $L_{\text{jet}} = 10^{42.9}$ erg/s. For comparison, the jet of TXS 0506+056, the only blazar associated with neutrinos by IceCube, produces a 2 – 3 orders of magnitude larger power $L_{\text{jet}} \sim 10^{45} - 4 \times 10^{46}$ erg/s.[43]

[35] Roy et al., "Slow jets in Seyfert Galaxies: NGC 1068".

[36] Park et al., "Kinematics of the M87 Jet in the Collimation Zone: Gradual Acceleration and Velocity Stratification".

[37] Padovani, "On the two main classes of active galactic nuclei".

[38] Condon et al., "The NRAO VLA Sky Survey".

[39] Kennicutt, "Star Formation in Galaxies Along the Hubble Sequence".

[40] Bonzini et al., "Star formation properties of sub-mJy radio sources".

[41] Cavagnolo et al., "A Relationship Between AGN Jet Power and Radio Power".

[42] Ibid.

[43] Ansoldi et al., "The Blazar TXS 0506+056 Associated with a High-energy Neutrino: Insights into Extragalactic Jets and Cosmic-Ray Acceleration".

We now assume conditions beyond optimistic to maximize the gamma-ray power from the jet and assume that it behaves like an absorbed M87-like jet. This assumption is rather unphysical but maximizes the gamma-ray luminosity of the jet beyond any limit. We assume that the ratio between the gamma-ray and 1.4 GHz logarithmic powers of the jet of NGC 1068 is the same as the one between the gamma-ray and core radio powers of M87, *i.e.*, a ratio of approximately 1.08.[44] We obtain a maximal gamma-ray power for the jet $L_{\gamma,\mathrm{jet}} < 10^{41.7}$ erg/s, which translates into a neutrino power of $L_{\nu,\mathrm{jet}} < 10^{40.9}$ erg/s.[45] Once again, the derived neutrino power cannot explain the IceCube observation. Therefore, we can exclude the jet as the neutrino source in NGC 1068.

[44] Padovani, Giommi, et al., "The spectra of IceCube neutrino (SIN) candidate sources - II. Source characterization".

[45] Here, the same optimistic framework used to derive the neutrino power of the SB is used.

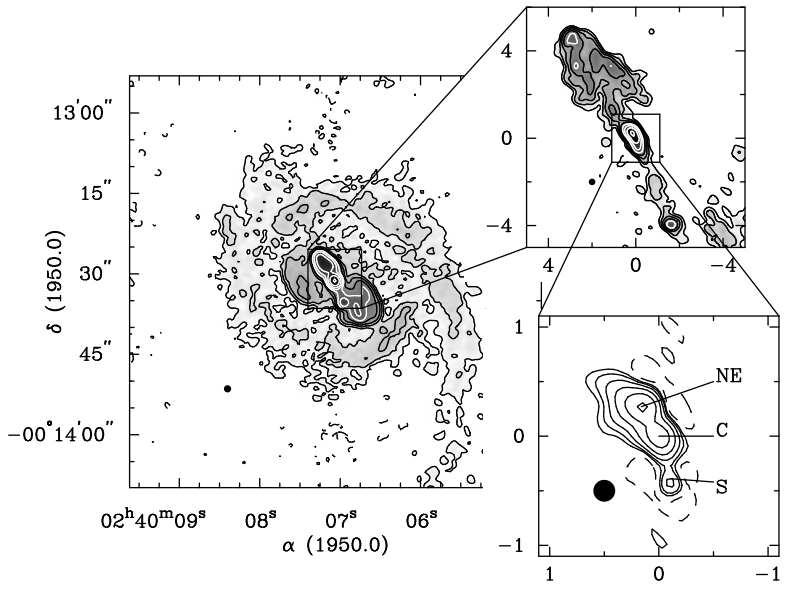


Figure 3.4: Aperture synthesis image of NGC 1068 at 1.7 GHz (18 cm). **Left:** the SB disc; **Top right:** the radio jet; **Bottom right**: the central core. Assuming a distance of 10.1 Mpc, 1″ corresponds to a linear distance of 48.9 pc. Figure reproduced with permission from Gallimore et al., "The Subarcsecond Radio Structure in NGC 1068. I. Observations and Results".

### *The corona*

The AGN corona is responsible for the emission of X-rays through the process of inverse Compton (IC) scattering, where UV photons from the accretion disc are boosted to higher energies by interacting with the hot ($\approx 10^9$ K) electrons in the corona. The study of X-ray emission is of crucial importance to understanding the environment in the immediate proximity of the SMBH, primarily because high energy X-rays ($\gtrsim 10$ keV) can penetrate large column density of gas that might be obscuring the central engine of the AGN. However, AGN classified as Compton-thick (*i.e.*, with neutral hydrogen column density $N_\mathrm{H} \gtrsim 10^{24}\,\mathrm{cm}^{-2}$) are hard to penetrate even for the highest energy X-ray radiation. This is the case of NGC 1068, whose X-ray continuum has been described by a recent study[46] with a highly absorbed ($N_\mathrm{H} \simeq 10^{25}\,\mathrm{cm}^{-2}$) power-law spectrum with a photon index $\approx 2.1$ and an energy cutoff at $E_\mathrm{cut} \simeq 130$ keV. The same study

[46] Zaino et al., "Probing the circumnuclear absorbing medium of the buried AGN in NGC 1068 through NuSTAR observations".

reproduced the complex structure of the circumnuclear matter multicomponent reflector with three distinct column densities, as shown in Figure 3.5.

Despite the difficulty of observing the inner region of NGC 1068, extensive monitoring campaigns with the space-based X-ray observatory *NuSTAR* detected an excess above 20 keV. They discovered a temporary decrease in the column density along the line of sight to $7 \times 10^{24}\,\mathrm{cm}^{-2}$. This "unveiling event" allowed a direct measurement of the intrinsic coronal X-ray luminosity of NGC 1068, namely $L_{2-10\ \mathrm{keV}} = 3^{+3}_{-2} \times 10^{43}$ erg/s.[47]

Plugging this measurement into the so-called X-ray bolometric correction $K_X = L_{\mathrm{bol}}/L_X$, we can estimate the bolometric luminosity of the source. We use $K_X = 11.48 \pm 0.01$ with a spread of the correlation of 0.37 dex[48] and obtain $L_{\mathrm{bol,X}} \approx 10^{44.5}$. Another estimate based on the IR luminosity of emission lines yields $L_{\mathrm{bol,IR}} \approx 10^{44.8}$.[49] We adopt the logarithmic mean of these two values for the bolometric luminosity of NGC 1068, which, therefore, is $L_{\mathrm{bol}} \approx 10^{44.7}$. Using the result of Equation 3.2, we can derive an Eddington ratio $L_{\mathrm{bol}}/L_{\mathrm{Edd}} \sim 0.6$.

No obvious connection to the gamma-ray emission from the innermost region of the AGN can be established, as the optically thick environment prevents the escape of this radiation, see Section 3.2. Hence, an estimation of the neutrino power based on the gamma-ray contribution from the corona is not feasible.

The UV and X-ray spectra produced by the disc-corona system in NGC 1068 are shown in yellow in Figure 3.3.

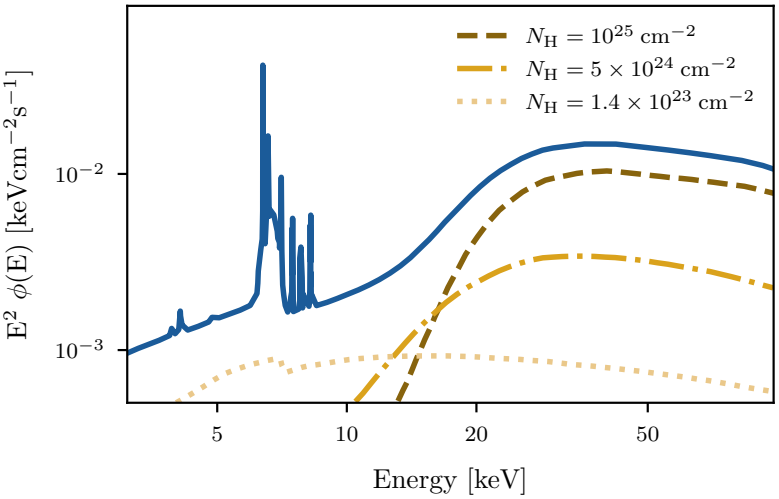


Figure 3.5: The best-fitting model of the X-ray energy flux of NGC 1068 is shown as a solid blue line. The X-ray emission above 2 keV is well described by a 3-component reflection arising from different column densities, each represented by a different line style and shade of yellow. Some emission lines are also visible, including the typical Fe K$\alpha$ iron fluorescence at $\sim$ 6.4 keV. Figure adapted from Zaino et al., "Probing the circumnuclear absorbing medium of the buried AGN in NGC 1068 through NuSTAR observations", where more details can be found.

### *The outflow*

The Atacama Large Millimeter Array (ALMA)[50] observatory detected a massive molecular outflow which has been associated with NGC 1068.[51,52] This outflow, which extends over $\sim$ 100 pc scales,

[47] Marinucci et al., "NuSTAR catches the unveiling nucleus of NGC 1068".

[48] From table 1 of Duras et al., "Universal bolometric corrections for active galactic nuclei over seven luminosity decades".

[49] Spinoglio, Fernández-Ontiveros, and Malkan, "The High-ionization IR Fine Structure Lines as Bolometric Indicators of the AGN Power: Study of the Complete 12 $\mu$m AGN Sample".

[50] https://www.almaobservatory.org/en/about-alma/

[51] García-Burillo et al., "Molecular line emission in NGC 1068 imaged with ALMA. I. An AGN-driven outflow in the dense molecular gas".

[52] Impellizzeri et al., "Counter-rotation and High-velocity Outflow in the Parsec-scale Molecular Torus of NGC 1068".

may be launched from the accretion disc. During their propagation, they are expected to develop the characteristic structure of AGN diverging flows, with an inner wind termination shock and an outer forward shock. The shocks in the circumnuclear disc can accelerate CRs. The accelerated protons participate in $p-p$ inelastic scatterings with protons in the interstellar medium, producing pions that can decay and produce gamma-rays and neutrinos. To derive the non-thermal emissions from shock-accelerated particles in the outflow, we need an estimate of the kinetic energy injected into the interstellar medium during the outflow timescale. The kinetic power of an outflow can be estimated as[53]

$$L_{\rm kin} = \frac{1}{2}\frac{{\rm dM_{out}}}{{\rm dt}} v_{\rm out,p}^2, \tag{3.6}$$

where ${\rm dM_{out}/dt}$ is the mass outflow rate and $v_{\rm out}$ is the outflow velocity. Estimates for the gas mass, average radius, and projected radial velocity are $M_{\rm out} = 1.8^7 M_\odot$, $R_{\rm out} \approx 100$ pc, and $v_{\rm out,p} \simeq 100$ km/s.[54] Assuming a multi-conical outflow geometry,[55] the mass outflow rate is

$$\frac{{\rm dM_{out}}}{{\rm dt}} = 3\, v_{\rm out} \frac{M_{\rm out}}{R_{\rm out}}\, \tan\alpha \simeq 63 M_\odot {\rm yr}^{-1}, \tag{3.7}$$

where $\alpha$ is the angle between the outflow and the line of sight. Assuming that the outflow is co-planar with the galaxy, $\alpha$ is the complementary angle to the disc inclination angle of $35^\circ$,[56] which means that $\alpha = 90^\circ - 35^\circ = 55^\circ$. Finally, with $v_{\rm out} = v_{\rm out,p}/\cos\alpha$, we derive

$$L_{\rm kin} = \frac{3}{2}\frac{M_{\rm out}\, v_{\rm out}^3}{R_{\rm out}}\frac{\tan\alpha}{\cos^2\alpha} = 10^{41.6}\ {\rm erg/s} \tag{3.8}$$

with $\alpha$ being the main source of the uncertainty.

Interestingly, gamma-ray emission has been detected from a sample of nearby SB galaxies/AGN hosting a molecular outflow, including NGC 1068.[57] Unfortunately, no clear correlation between the gamma-ray power and the kinetic power of the outflow has been identified. Therefore, we cannot derive an estimate for the contribution to the gamma-ray power from the molecular outflow.

However, recent studies[58] have reported the detection of gamma-rays also from a sample of nearby AGN featuring winds that are particularly fast and highly ionized. In principle, a UFO of semi-relativistic velocity could be emitted from NGC 1068, as the strong X-ray obscuration makes it impossible to probe its existence. The same study that found a gamma-ray emission from UFOs also identified a linear relation between the kinematic power of the UFO and the gamma-ray power. The kinetic power, in turn, can be estimated using the correlation coefficient between the bolometric and kinetic powers for UFOs.[59] By using the bolometric luminosity we estimated from the X-ray power of NGC 1068 and including the uncertainty in the correlation between the kinetic and gamma-ray powers, we find that the UFO gamma-ray power $L_{\gamma,\rm UFO}$ can vary between $10^{39.6}$ erg/s and $10^{41.2}$ erg/s. Notably, this gamma-ray power could overcome the experimentally observed one.

[53] Lamastra et al., "Galactic outflow driven by the active nucleus and the origin of the gamma-ray emission in NGC 1068".

[54] García-Burillo et al., "Molecular line emission in NGC 1068 imaged with ALMA. I. An AGN-driven outflow in the dense molecular gas".

[55] Ibid.

[56] http://atlas.obs-hp.fr/hyperleda/ledacat.cgi?o=NGC1068

[57] McDaniel, Ajello, and Karwin, "Gamma-Ray Emission from Galaxies Hosting Molecular Outflows".

[58] Ajello et al., "Gamma Rays from Fast Black-hole Winds".

[59] We use the value in Table 1 of Fiore et al., "AGN wind scaling relations and the co-evolution of black holes and galaxies".

As before, to estimate the corresponding neutrino power, we assume the best possible conditions, *i.e.*, $L_{\gamma,\mathrm{UFO}} = 10^{41.2}$ erg/s, alongside the previously used assumptions that the gamma-rays are all hadronic and the spectral index of the neutrino spectrum is harder than the observed one. We obtain a maximal neutrino contribution from the outflow of $L_{\nu,\mathrm{UFO}} = 10^{40.4}$ erg/s. Not even the UFO can provide a sizeable portion of the observed neutrino power.

Table 3.1 summarizes the maximum gamma-ray and neutrino powers we could derive for each candidate source within NGC 1068. Even by summing the maximized neutrino powers for all components, we do not reach the observed neutrino luminosity, which remains larger by an order of magnitude.

| Component | Scale | $L_\gamma$ $(0.1-10$ GeV$)$ | $L_\nu$ $(1.5-15$ TeV$)$ |
|---|---|---|---|
| Star formation | $>$ kpc | $\sim 10^{40.9}$ | $\lesssim 10^{40.1}$ |
| Jet | $\sim$ kpc | $< 10^{41.7}$ (M87-like) | $< 10^{40.9}$ |
| Outflow (UFO) | $\sim$ pc | $< 10^{41.2}$ | $< 10^{40.4}$ |
| BH vicinity | $\sim 0.02$ mpc ($\sim 30\ R_\mathrm{s}$) | ? | ? |
| | Total | $\lesssim 10^{41.9}$ | $\ll 10^{41.1}$ |
| | Observed | $10^{40.92\pm0.03}$ | $10^{42.1\pm0.2}$ |

All powers in erg s$^{-1}$; $R_\mathrm{s} = (2GM_\mathrm{BH})/c^2$ is the Schwarzschild radius.

Table 3.1: Estimated gamma-ray and neutrino powers.

However, we could not derive an equivalent neutrino power for the X-ray corona, which remains our last viable neutrino source candidate. In the next section, we evaluate whether AGN coronae meet the requirements the source environment should satisfy.

## 3.2 *Hidden sources of astrophysical neutrinos*

The first papers suggesting that neutrino sources might lack a photon counterpart appeared in the late seventies and early eighties.[60,61,62] More recently, it has been pointed out that the existence of "hidden sources" of neutrinos would explain the diffuse neutrino flux level at $\sim 10$ TeV without violating the extragalactic gamma-ray background observed by *Fermi*-LAT,[63] see Section 2.2.

The photons produced with the neutrinos from NGC 1068 must have an intrinsic flux $\sim 40$ times higher than the MAGIC upper limits. Therefore, Figure 3.3 implies that the VHE gamma-rays have to be completely absorbed. NGC 1068 is, therefore, the first "hidden source" to be detected. We can evaluate what characteristics its emission region needs to have to provide a suitable target for neutrino production and, at the same time, absorb the accompanying gamma-rays entirely. We assume a $p-\gamma$ scenario, as the presence of a low-energy photon field naturally offers a high chance of gamma-ray absorption.[64]

The $p-\gamma$ cross section is characterized by a pronounced peak just above the threshold for pion production,[65] as seen in Figure 3.6.

[60] Berezinsky, *Proceedings of the International Conference Neutrino '77*.

[61] Eichler, "High-energy neutrino astronomy: a probe of galactic nuclei?"

[62] Silberberg and Shapiro, "Neutrinos as a Probe for the Nature of and Processes in Active Galactic Nuclei".

[63] Murase, Guetta, and Ahlers, "Hidden Cosmic-Ray Accelerators as an Origin of TeV-PeV Cosmic Neutrinos".

[64] However, $p-p$ interactions could also be possible with a high enough gas density.

[65] Mücke et al., "Photohadronic Processes in Astrophysical Environments".

Therefore, most $p-\gamma$ interactions result in the creation of a single pion, either charged or neutral. At the threshold, the final state neutron/proton and pion are produced at rest in the center-of-mass frame (see Equation 2.7). As discussed in Section 2.2, the relativistic kinematics of the process require that, in the lab frame, the proton transfers a fraction $m_\pi/m_p \sim 0.15$ of its energy to the pion, which will then decay into four stable leptons, including three neutrinos.

These leptons will share the pion energy equally so that each neutrino has an energy $E_\nu \sim (m_\pi/4m_p)E_p \sim 0.04 \times E_p$. The neutrinos observed by IceCube in the $1.5-15$ TeV range are therefore generated by CR protons of energy $\sim 40-400$ TeV. Hence, from Equation 2.8, which we report here for clarity,

$$\epsilon_{\gamma,\mathrm{thr}} \sim \frac{2m_p m_\pi + m_\pi^2}{4E_p}, \tag{3.9}$$

we obtain that soft X-ray photons with energy $\gtrsim 0.2-2$ keV interacting with $\sim 40-400$ TeV protons allow photomeson production with consequent creation of neutrinos in the observed energy range. Hence, the X-ray flux from the corona could be directly related to the observed flux of neutrinos.

At the same time, lower energy ambient photons could suppress the accompanying TeV gamma-rays via the production of electron-positron pairs, which is preferred over the pion production because of the lower energy it requires. The threshold condition $E_\gamma \epsilon_\gamma > (m_e c^2)^2 \sim 0.26$ MeV$^2$ for pair production[66] translates into a minimum ambient photon energy

$$\epsilon_\gamma > 0.26\ (E_\gamma/\mathrm{TeV})^{-1}\ \mathrm{eV}, \tag{3.10}$$

*i.e.*, photons in the IR domain and above.

The conditions required by equations (3.9) and (3.10) are easily satisfied very close to the SMBH at the center of the AGN, namely in the disc-corona. This region provides X-ray and optical/IR photons in abundance.

Figure 3.7 shows the optical depth of gamma-rays to pair production obtained from simulations assuming different sizes of the interaction regions.[67] GeV-TeV gamma-rays cannot escape a source with the typical size of the corona ($\sim 30R_\mathrm{s}$), and the source can be transparent to $\lesssim 10$ MeV photons.

Kinematic considerations support, in fact, the escape of gamma-rays degraded to MeV energies through electromagnetic cascades. The generated electron-positron pairs IC-scatter ambient photons up to the gamma-ray domain, thereby initiating an electromagnetic cascade sustained by alternate IC and pair production processes. The cascade reaches its natural end when the gamma-ray photon energy equals the threshold for pair production: $E_\gamma^{th} = (m_e c^2)^2/\epsilon_\gamma$. Since the spectrum of ambient photons in the AGN corona extends well into the keV range, the cascade terminates when $E_\gamma$ reaches $E_\gamma^{th} \sim 130$ MeV and produces the last pair with a 2 keV photon. The last electron/positron has an energy $E_e^{min} \sim E_\gamma^{th}/2$, and can IC

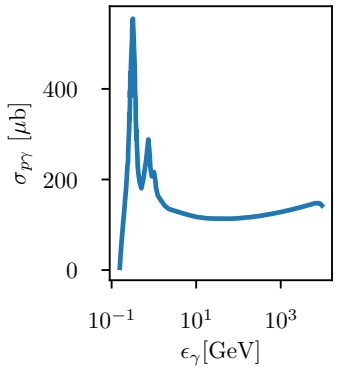


Figure 3.6: Cross-section of photo-hadronic interactions as a function of the required photon energy in the proton's rest frame. The interaction probability peaks sharply around the pion rest mass, $\sim 140$ MeV/c, dominated by the $\Delta^+$-resonance production. Figure adapted from Kelner and F. A. Aharonian, "Energy spectra of gamma rays, electrons, and neutrinos produced at interactions of relativistic protons with low energy radiation" and courtesy of Theo Glauch.

[66] For simplicity we always assume head-on collisions. An angle $\theta$ between the two photons would produce a factor $(1-\cos\theta)$, which multiplies the left side of the inequality.

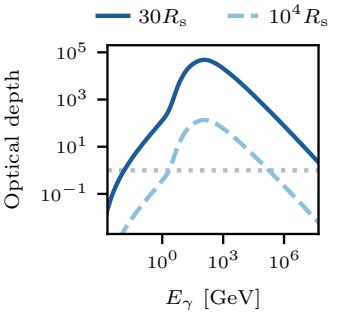


Figure 3.7: Optical depths for two-photon pair annihilation. The solid line represents the optical depth for densities as high as found within $\sim 30R_\mathrm{s}$, corresponding to the typical size of the corona. The dashed line illustrates the optical depth expected in a source of size $\sim 10^4 R_\mathrm{s}$, corresponding to the typical BLR radius. The source is opaque for optical depths much larger than 1 (dotted grey line). Data from Murase, "Hidden Hearts of Neutrino Active Galaxies".

[67] Murase, "Hidden Hearts of Neutrino Active Galaxies".

upscatter ambient photons to an energy[68]

$$E_\gamma^{esc} = (4/3)(E_e^{min}/m_e c^2)^2 \epsilon_\gamma = E_\gamma^{th}/3 \sim 40 \text{ MeV}. \quad (3.11)$$

Photons of such energy cannot produce pairs in the ambient photon gas and will freely escape the region. Figure 3.8 illustrates the experimental sensitivity to point sources in the X-/gamma-ray domain to date. Unfortunately, the MeV region is the most poorly explored. Future missions, for example e-ASTROGAM[69] or AMEGO-X,[70] will be able to provide the indispensable missing piece of information: The detection of a MeV photon flux level comparable with the measured neutrino flux would foster the scenario where the X-ray corona of AGN is a major source of NGC 1068's neutrinos.

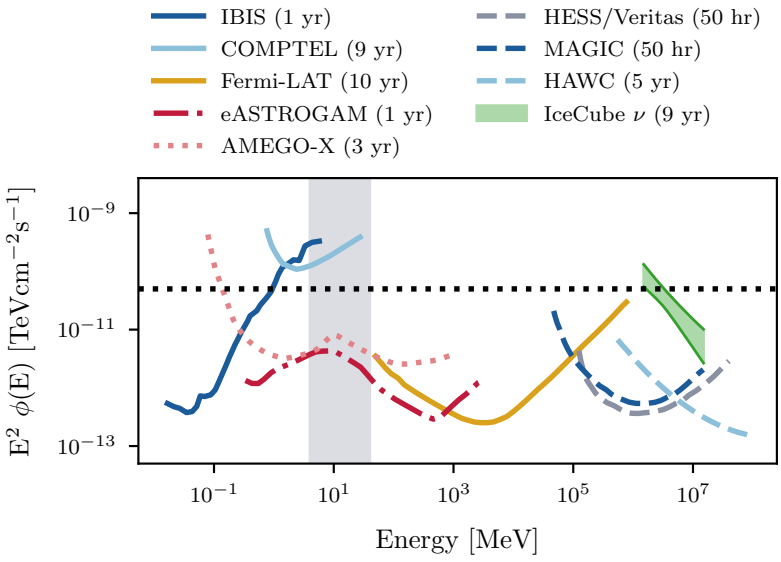


Figure 3.8: Point source continuum differential sensitivity of different X- and gamma-ray instruments alongside the IceCube measurement of the neutrino flux from NGC 1068. The figure illustrates the best sensitivities to date with the corresponding detector exposures in parentheses. The predicted 3$\sigma$ sensitivities of the eASTROGAM and AMEGO-X future missions are highlighted as red dash-dotted and dotted lines, respectively. The black dotted line and the grey shaded area illustrate where the gamma rays produced together with the IceCube neutrinos are approximately expected to cascade. Figure adapted from de Angelis et al., "Science with e-ASTROGAM. A space mission for MeV-GeV gamma-ray astrophysics", where the curves' references can be found. Data for the sensitivity of AMEGO-X from Caputo et al., "All-sky Medium Energy Gamma-ray Observatory eXplorer mission concept".

## 3.3 *An estimation of the diffuse neutrino background from non-jetted AGN*

**Disclaimer:** This section is based on the publication, *Padovani, Gilli, Resconi, Bellenghi, Henningsen, A&A 684, 2024.*[71] The author of this dissertation contributed to the interpretation and discussion of the results and to the writing of the corresponding sections in the manuscript. The discussion closely follows the one in our paper.

In the previous section, we analyzed the multimessenger observations of NGC 1068 using simple order-of-magnitude calculations. These suggest that the only source fulfilling all the requirements to be a neutrino source is the closest region to the SMBH, most likely the X-ray corona. In fact, the X-ray corona could have both the right density of photons needed to produce neutrinos in photomeson production processes and to absorb the expected but unobserved gamma-rays.

[68] Berezinskii, Bulanov, et al., *Astrophysics of cosmic rays*.

[69] de Angelis et al., "Science with e-ASTROGAM. A space mission for MeV-GeV gamma-ray astrophysics".

[70] Caputo et al., "All-sky Medium Energy Gamma-ray Observatory eXplorer mission concept".

[71] Padovani, Gilli, et al., "The neutrino background from non-jetted active galactic nuclei".

Currently, NGC 1068 is the only non-jetted AGN from which we observed high-energy neutrinos at a significance larger than $3\sigma$. Other analyses carried out by the IceCube collaboration searching for neutrino emission from X-ray bright non-jetted (Seyfert) AGN have found indications ($\lesssim 3\sigma$) of possible point-like neutrino emission from NGC 4151[72] and CGCG 420−015,[73] a moderately obscured ($N_{\mathrm{H}} = 10^{22-24}\,\mathrm{cm}^{-2}$) and a Compton-thick Seyfert galaxy, respectively. Additionally, an external work using data released by the IceCube collaboration associated neutrino emission to the Compton-thick Seyfert galaxy, NGC 3079, adding to the growing indications of neutrino emission from non-jetted AGN.[74] Clearly, there is a well-motivated interest in understanding whether NGC 1068 is a unique object or if the large population of AGN shares the same neutrino production mechanism with it.

We tackle the question from an observational, population-wide perspective. In the following, we provide an estimate of the diffuse neutrino background that could be produced by all non-jetted AGN contributing to the cosmic X-ray background (CXB).

[72] Goswami, "Search for high-energy neutrino emission from hard X-ray AGN with IceCube".

[73] Glauch et al., "Searching for High-Energy Neutrino Emission from Seyfert Galaxies in the Northern Sky with IceCube".

[74] Neronov, Savchenko, and Semikoz, "Neutrino Signal from a Population of Seyfert Galaxies".

### 3.3.1 *The X-ray background and prediction of the neutrino background*

The first ingredient of our study is a population synthesis model for the CXB. We use the model of the CXB by Gilli, Comastri, and Hasinger, "The synthesis of the cosmic X-ray background in the Chandra and XMM-Newton era". The model explains some remarkable features of the X-ray source population. Most importantly, it suggests that moderately obscured, Compton-thin AGN need to outnumber unobscured AGN (by a factor decreasing from 4 to 1 with increasing luminosity) to reproduce the measured $2-10$ keV AGN X-ray luminosity.[75] Although the model adopted here dates back to 2007, it agrees remarkably well with the most recent estimates of the X-ray luminosity[76] and flux measurements by CHANDRA.[77] Notably, the X-ray luminosity function used by the model consists of non-jetted AGN for more than 90%, and, hence, all our following considerations solely refer to the population of non-jetted AGN.

The CXB flux, including both obscured and unobscured AGN and integrated up to the luminosity distance of NGC 1068 and to $z = 5$, is shown in Figure 3.9. We show the intrinsic X-ray fluxes, *i.e.*, corrected for absorption along the line of sight. This correction is necessary in a scenario as the one described in Section 3.2, where high-energy neutrinos correlate with the X-ray flux from the corona before it is attenuated by interactions in the dusty torus and interstellar medium.

To translate the X-ray flux in Figure 3.9 to the neutrino domain, we need a neutrino spectral shape, our second ingredient. A putative spectral shape is constrained to be rather hard at low energies so as not to violate the Eddington luminosity of the source. In fact,

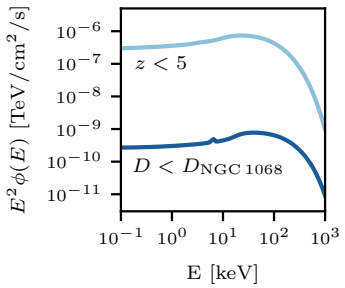


Figure 3.9: Cosmic X-ray background flux modelled by Gilli, Comastri, and Hasinger, "The synthesis of the cosmic X-ray background in the Chandra and XMM-Newton era". The dark blue curve represents the flux integrated up to the luminosity distance of NGC 1068, while the light blue curve goes up to $z = 5$. The fluxes include both obscured and unobscured AGN, and they are intrinsic, meaning that they have been corrected for absorption in the gas surrounding the AGN. Data by courtesy of Roberto Gilli.

[75] Ueda, Akiyama, Ohta, et al., "Cosmological Evolution of the Hard X-Ray Active Galactic Nucleus Luminosity Function and the Origin of the Hard X-Ray Background".

[76] Ueda, Akiyama, Hasinger, et al., "Toward the Standard Population Synthesis Model of the X-Ray Background: Evolution of X-Ray Luminosity and Absorption Functions of Active Galactic Nuclei Including Compton-thick Populations".

[77] Nanni et al., "The deep Chandra survey in the SDSS J1030+0524 field", https://chandra.harvard.edu/.

in $p-p$ or $p-\gamma$ reactions, neutrinos of $E_\nu \sim 1$ TeV require a proton energy $E_p \sim 25$ TeV. Assuming that the protons dump all their energy near the black hole, their power will be approximately equal to the neutrino power, *i.e.*, $L_p \sim 10^{42}$ erg/s at $> 25$ TeV. If we now extrapolate the luminosity at 1 GeV assuming the measured neutrino spectral index of 3.2, we get $L_p[\sim 1\,\mathrm{GeV}] \sim 5 \times 10^{46}$ erg/s. This value is more than one order of magnitude larger than both the bolometric and Eddington luminosities derived in the previous section (see Equation 3.2).[78] Therefore, the most natural explanation for a steep neutrino spectrum is that it reflects a cutoff in the parent proton spectrum at high energies. In contrast, there should be a turnover to a rather hard slope at low energies to avoid overshooting the AGN's energetics.

[78] The real proton power in this scenario will be even higher, as here we are neglecting the energy needed to feed the thermal and magnetic energy of the corona.

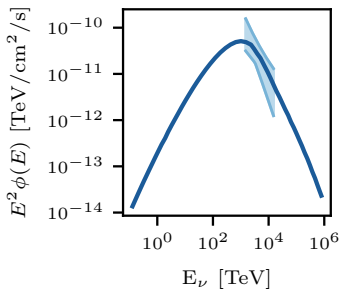


Figure 3.10: Neutrino spectral shape adopted for the model of the neutrino background from non-jetted AGN. The spectrum results from the *minimal* $p-p$ scenario in which the spectrum has a low-energy cutoff at 10 TeV to explain the neutrino spectrum above 1.5 TeV, illustrated by the shaded area. Figure adapted from Murase, "Hidden Hearts of Neutrino Active Galaxies", where more details on the model can be found.

[79] Murase, "Hidden Hearts of Neutrino Active Galaxies".

[80] Where the neutrino spectrum is the most constrained. See, *e.g.*, Figure 3.10.

The third and last ingredient to produce an estimation of the total neutrino flux from the X-ray flux of AGN is the relation linking the two. As NGC 1068 is the only non-jetted AGN detected both in neutrinos and X-rays, we anchor the relative normalization between the two spectra to the ratio of its observed fluxes. The intrinsic X-ray flux density at 1 keV (see previous section) is $f_X^{1\mathrm{keV}} = 1.44 \times 10^{-9}$ erg cm$^{-2}$ s$^{-1}$ keV$^{-1}$. The all-flavour neutrino flux density at $\sim$ 4 TeV[80] can be estimated by multiplying the spectrum measured by IceCube by a factor of 3, $E^2\phi(E) = 5 \times 10^{-11}(E/1\mathrm{TeV})^{3.2-2}$ TeV cm$^{-2}$ s$^{-1}$. We obtain $f_\nu^{4\mathrm{TeV}} = 1.14 \times 10^{-20}$ erg cm$^{-2}$ s$^{-1}$ keV$^{-1}$. Hence, the ratio of the two energy densities is given by

$$\nu f_X^{1\mathrm{keV}} / \nu f_\nu^{4\mathrm{TeV}} \simeq 32, \tag{3.12}$$

where $\nu$ indicates the frequency (and therefore the energy), while the subscript $\nu$ indicates the neutrino flux. The propagation of the uncertainties on both the neutrino and X-ray fluxes results in a $\sim$ 0.5 dex[81] uncertainty on their ratio.

[81] $\mathrm{dex(x)} = \log_{10}(\mathrm{x})$.

Now, we can compute the expected neutrino spectrum as

$$F(E) = \frac{1}{4\pi} \int_0^{z_{max}} \frac{1+z}{4\pi {D_L}^2} \frac{\mathrm{d}V}{\mathrm{d}z} \int_{L_{min}}^{L_{max}} f[E(1+z)]\Phi[L,z]L\,\mathrm{dL}\,\mathrm{dz}\,, \tag{3.13}$$

with $\frac{\mathrm{dV}}{4\pi \mathrm{dz}}$ being the comoving volume element in a flat Universe integrated over the entire solid angle[82]

$$\frac{\mathrm{dV}}{\mathrm{d}\Omega\,\mathrm{dz}} = \frac{c\,D_\mathrm{L}^2(z)}{H(z)\,(1+z)^2} \quad \text{where } \mathrm{H(z)} = \mathrm{H_0}\sqrt{\Omega_\mathrm{m}(1+z)^3 + \Omega_\Lambda}, \tag{3.14}$$

[82] Hogg, "Distance measures in cosmology".

$\Phi[L,z]$ is the total, intrinsic comoving AGN X-ray luminosity function as per the CXB model, and $f[E(1+z)]$ is the neutrino flux density at the energy $E(1+z)$ normalized to the X-ray emission. We integrated the AGN X-ray luminosity function in the range $L_{0.5-2keV} =$

$[10^{42} - 10^{48}]$ erg s$^{-1}$ and in the redshift interval $z = [0 - 5]$. The contribution of AGN at $z > 5$ to the total background flux is negligible, whereas integrating the AGN X-ray luminosity function down to $L_{0.5-2keV} = 10^{41}$ erg s$^{-1}$ to include the contribution of low-luminosity AGN increases the total background flux by ∼16% at most. For comparison, we also computed the neutrino diffuse background expected in the very local Universe, *i.e.*, within the distance of NGC 1068.

### 3.3.2 *Results and discussion*

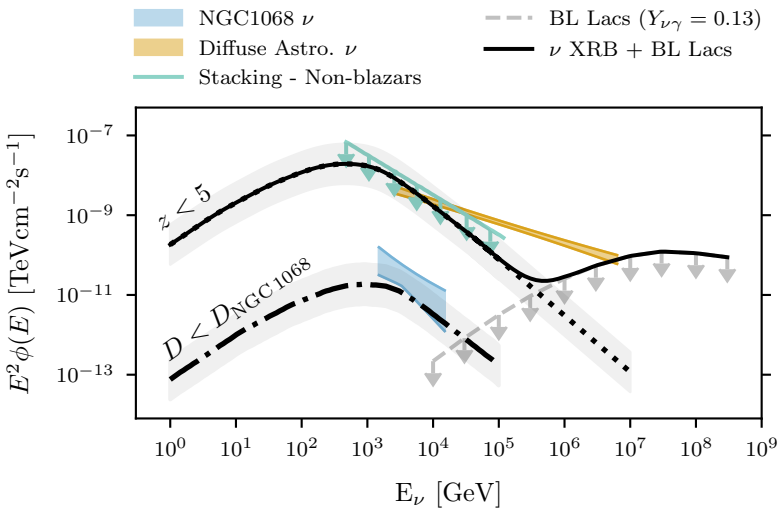


Figure 3.11: All-flavour neutrino background derived from an X-ray AGN population synthesis. Black curves show the computed neutrino backgrounds for source populations integrated up to the distance of NGC1068 and redshift $z = 5$ (dash-dotted and dotted, respectively). A high-energy linear extrapolation is added to the integrated spectrum for $z = 5$ and combined with a blazar neutrino background model (dashed grey curve) to highlight the structure of the combined AGN neutrino background flux ("double-humped" black solid curve). The estimated uncertainty on the neutrino flux from X-ray AGN is 0.5 dex (grey bands). Also shown are the current best-fit astrophysical diffuse neutrino flux (yellow area), IceCube upper limits from stacking analyses of non-blazar AGN (green solid line), and the point-source neutrino flux of NGC 1068 (blue area). See the text for more details and references.

Figure 3.11 shows the resulting all-flavor neutrino background integrated up to redshift $z = 5$ (dotted black line). The comparison with the latest measurement of the astrophysical diffuse neutrino flux[83] (yellow shaded area) shows that the assumption that all non-jetted AGN behave like NGC 1068 in terms of their neutrino properties is consistent with IceCube data above ≈ 10 TeV. It is worth noting that the results presented here are essentially neutrino model-independent, as any model capable of reproducing the IceCube data for NGC 1068 would yield similar curves in the energy range of the diffuse neutrino energy spectrum.

We also compared our prediction to a recent IceCube analysis that probed the neutrino emission from non-blazar (therefore mostly non-jetted) AGN in the BAT Spectroscopic Survey (BASS[84]) catalog.[85] They performed a weighted stacking analysis of the signals from all selected sources under the assumption that the neutrino flux correlates linearly with the intrinsic X-ray flux and that, therefore, brighter X-ray AGN would be brighter in neutrinos[86]. The result of this analysis is compatible with a diffuse astrophysical and atmospheric neutrino background. Hence, they place an upper limit at 90% C.L. on the total neutrino flux that can be produced by non-blazar, hard X-ray AGN[87] (the green line in Figure 3.11). Our prediction is also

[83] Naab et al., "Measurement of the astrophysical diffuse neutrino flux in a combined fit of IceCube's high energy neutrino data".

[84] Ricci et al., "BAT AGN Spectroscopic Survey. V. X-Ray Properties of the Swift/BAT 70-month AGN Catalog"

[85] Goswami, "Search for high-energy neutrino emission from hard X-ray AGN with IceCube"

[86] Their weighting scheme also takes into account the declination dependent detection efficiency of the IceCube detector, see Chapter 4

[87] corrected for the catalog incompleteness, *i.e.*, the missing unresolved sources, by estimating the total expected neutrino flux from the X-ray luminosity function (Ueda, Akiyama, Hasinger, et al., "Toward the Standard Population Synthesis Model of the X-Ray Background: Evolution of X-Ray Luminosity and Absorption Functions of Active Galactic Nuclei Including Compton-thick Populations").

compatible with this recently published upper limit, although at the same flux level.

The neutrino prediction in the very local Universe is also shown up to the luminosity distance of NGC 1068 (dash-dotted black line in Figure 3.11). In this case, the prediction is barely compatible with the IceCube measurement within the uncertainties. However, it is important to note that the CXB model used in this work is severely limited at low redshift. Being based on observational data from X-ray surveys, it suffers from the lack of statistics in the nearby Universe, where only three AGN with intrinsic $L_{0.5-2keV} \geq 10^{42}$ erg/s in the BASS DR2 catalog[88] (including NGC 1068) are closer than 10.1 Mpc. However, the accuracy of the model's predictions improves to the percent level when including all redshifts up to $z = 5$.

[88] Koss et al., "BASS. XXII. The BASS DR2 AGN Catalog and Data".

Finally, to place our result in the larger context of neutrino emission from both jetted and non-jetted AGN, we have superimposed a prediction of the neutrino diffuse flux from blazar jets, shown as a dashed grey curve in the figure. This cumulative neutrino emission is calculated within a photohadronic framework for the gamma-ray emission, assuming a correlation between the neutrino and gamma-ray flux $F_{\nu,\mathrm{tot}} = Y_{\nu\gamma} F_\gamma (E > 10^5 \text{ GeV})$.[89] The $Y_{\nu\gamma}$ parameter encompasses information about the photomeson cross-section and the proton luminosity and has been constrained to 0.13 by IceCube upper limits on the neutrino flux above $10^9$ GeV.[90,91] Summed with the extrapolation to higher energies of the neutrino background from non-jetted AGN, we get an approximate estimate of the total neutrino background from AGN. The shape of such emission would then be characterized by a "double-humped" spectrum, proposing a scenario where non-jetted AGN contribute mainly to the low-energy ($\lesssim 1$ PeV) IceCube diffuse whereas blazars dominate the high-energy part.

[89] Padovani, Petropoulou, et al., "A simplified view of blazars: the neutrino background".

[90] Aartsen et al., "Constraints on Ultrahigh-Energy Cosmic-Ray Sources from a Search for Neutrinos above 10 PeV with IceCube".
[91] Aartsen and Aartsen, "Erratum: Constraints on Ultrahigh-Energy Cosmic-Ray Sources from a Search for Neutrinos Above 10 PeV with IceCube [Phys. Rev. Lett. 117, 241101 (2016)]".

Importantly, it should not be overlooked that extrapolating the neutrino emission from a population of non-jetted AGN based on the observed X-ray and neutrino spectra of a single object poses some non-negligible caveats. The observation of neutrinos from more non-jetted AGN could help determine whether the entire population shares the same neutrino production mechanisms as NGC 1068.

As part of the work presented in this thesis, we searched for neutrino emission from X-ray bright, non-jetted AGN in the Northern sky using 13 years of IceCube data. The selection of the candidate sources and the analysis results are discussed in Subsection 8.2.4. We will see that the very recent observation of PeV neutrino emission from the non-jetted Seyfert 1 galaxy NGC 7469 already challenges the simple scenario where non-jetted AGN accelerate CRs at medium energies, reserving $\gtrsim 1$ PeV proton acceleration for jetted AGN.

# 4 The IceCube Neutrino Observatory

In 1960, Markov and Zheleznykh proposed using large volumes of water to detect neutrinos resulting from pion decays in the atmosphere.[1] Marokov immediately realized that beyond an atmospheric neutrino flux,"[...] maybe there are neutrinos from the galaxy. Maybe the intensity of these neutrinos is different.".[2] The core idea was to use a large volume of a transparent medium, such as water or clear ice, to identify the charged byproducts of neutrino interactions through the detection of Cherenkov radiation. AMANDA was the first neutrino telescope built in the deep, clear ice at the geographic South Pole, and in 2001, it detected the atmospheric neutrino flux.[3] However, it could only set upper limits on the much lower astrophysical flux. This made the case for constructing an approximately 50 times larger detector and currently the largest operating neutrino telescope worldwide, the IceCube Neutrino Observatory. In this chapter, we describe the experimental signatures used by these types of telescopes to identify neutrinos and briefly discuss the IceCube detector. Furthermore, we describe the muon neutrino dataset used for a point-source analysis, whose methods and results are detailed in Chapter 5 and Section 8.2, respectively.

[1] Markov, "On high energy neutrino physics".

[2] Ibid.

[3] Andrés et al., "Observation of high-energy neutrinos using Čerenkov detectors embedded deep in Antarctic ice".

## 4.1 Neutrino detection principle

Neutrinos only weakly interact with matter and can cross cosmic distances unhindered. This low interaction probability renders their detection challenging. Early estimates of the expected flux of high-energy astrophysical neutrinos indicated that neutrino observatories require gigaton masses of detection medium to observe a few neutrino interactions per year.[4] Nature can provide the necessary volumes if the desired medium is water or ice. Such transparent media offer the possibility to detect the Cherenkov light produced by relativistic charged particles created in high-energy neutrino interactions.

[4] Waxman and Bahcall, "High energy neutrinos from astrophysical sources: An upper bound".

For astrophysical studies, we are interested in interactions of neutrinos with energies $\gtrsim$ 1 TeV. At these high energies, the neutrino cross section for interactions with matter is dominated by deep inelastic scatterings of two types, depending on whether the final state includes a neutrino or a charged lepton:

- *Neutral current* (NC) interactions are mediated by the neutral gauge boson $Z^0$. A neutrino with the same flavor as the incident neutrino and with a fraction of its energy is found in the final state

$$\nu_l + X \xrightarrow{Z^0} \nu_l + X. \tag{4.1}$$

- *Charged current* (CC) interactions are mediated by the $W$ boson, resulting in the conversion of the neutrino into the same flavor lepton

$$\nu_l + X \xrightarrow{W^\pm} l^\pm + X. \tag{4.2}$$

Both processes involve a neutrino scattering off an individual quark inside the nucleon $X$, disrupting the target nucleus and creating a hadronic cascade.

Neutrino–electron scattering is generally negligible at these energies due to the small target mass. However, interactions of electron anti-neutrinos with electrons bound to the ice nuclei can result in the resonant production of a $W$ boson, which then decays into hadrons and/or leptons

$$\bar{\nu}_e + e^- \rightarrow W^- \rightarrow X/l. \tag{4.3}$$

The W resonance peaks at $E_{\bar{\nu}_e} \sim \mathrm{m_W^2}/(2\mathrm{m_e}) \sim 6.3$ PeV, and at this energy, the cross-section of this process overcomes the ones of the nuclear interactions described above. Glashow initially predicted the process in 1960,[5] and recently, IceCube discovered an electron neutrino produced in the *Glashow resonance* process.[6] The upper panel of Figure 4.1 shows the three cross-sections as a function of the neutrino energy. The ratio of the CC and NC cross-sections is $\sim 2.4$, independent of energy. While neutrinos and anti-neutrinos can be distinguished due to the valence quark composition of the nucleons at lower energies, scattering at sea quarks becomes dominant above 1 PeV, making the two cross-sections nearly identical.[7]

When willing to measure the incoming neutrino energy, the fraction of energy transferred to the hadronic system in the final state is important. This is quantified by the *inelasticity*[8]

$$y = \frac{E_{\mathrm{had}}}{E_\nu} = \frac{E_\nu - E_l}{E_\nu}. \tag{4.4}$$

By inverting Equation 4.4, we get the distribution of the fraction of energy shared with the final state lepton: $E_l = (1-y)E_\nu$. The average inelasticity for the CC and NC interactions is shown in the lower panel of Figure 4.1 for both neutrinos and anti-neutrinos.

In the case of NC scattering, the outgoing neutrino is not reconstructed. Thus, experimentalists have to infer all event information from the hadronic shower. Conversely, in CC interactions, the outgoing lepton carries a sizeable fraction of the energy that will be lost in the detection medium. If the traversed medium is ice or water, the energy loss is visible as Cherenkov radiation.

[5] Glashow, "Resonant Scattering of Antineutrinos".
[6] IceCube Collaboration, "Detection of a particle shower at the Glashow resonance with IceCube".
[7] Formaggio and Zeller, "From eV to EeV: Neutrino cross sections across energy scales".
[8] Gaisser, Engel, and Resconi, *Cosmic Rays and Particle Physics: 2nd Edition*.

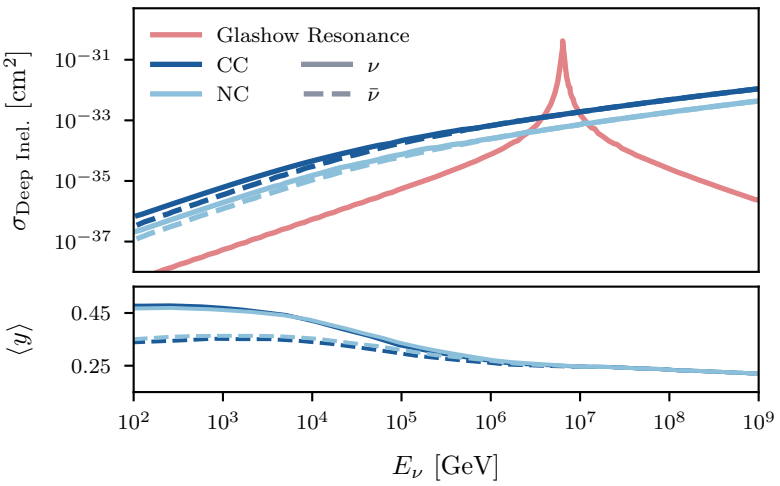


Figure 4.1: **Top:** Deep-inelastic neutrino cross sections for neutrino interactions with matter as a function of the neutrino energy. **Bottom:** Average fraction of the neutrino energy transferred to the nucleon. Different colors represent different processes. Solid and dashed lines indicate neutrinos and antineutrinos, respectively. Data from Gandhi et al., "Ultrahigh-energy neutrino interactions".

Cherenkov radiation is produced when a charged particle travels through a medium at a speed greater than the speed of light in the medium itself. As the particle moves, it polarizes the surrounding molecules, which return to their normal state by emitting a faint, blueish light. The emitted light forms a coherent shockwave, similar to a sonic boom, which propagates as a cone along the particle's path[9]. The opening angle of the cone is

$$\cos\theta_c = \frac{1}{\beta n(\lambda)} \tag{4.5}$$

for a charged particle moving with velocity $v/c = \beta$ in a medium with wavelength-dependent refractive index $n$. In the ice, $n \approx 1.32$[10] and a particle moving at approximately the speed of light produces a light cone with $\theta_c \approx 41°$. A sketch of the propagation of Cherenkov light is illustrated in Figure 4.2.

The number of photons emitted per unit wavelength ($\lambda$) and unit path length ($x$) by a charged particle can be approximately estimated using the Frank-Tamm formula[11]

$$\frac{\mathrm{d}N}{\mathrm{d}x\mathrm{d}\lambda} \approx \frac{2\pi\alpha}{\lambda^2}\left(1 - \frac{1}{\beta^2 n^2(\lambda)}\right), \tag{4.6}$$

where $\alpha = e^2/4\pi$ is the fine-structure constant. If we combine Equation 4.5 and Equation 4.6, we obtain a direct relation between the Cherenkov angle and the number of photons emitted by the charged particle:

$$\frac{\mathrm{d}N}{\mathrm{d}x\mathrm{d}\lambda} \approx \frac{2\pi\alpha}{\lambda^2}\sin^2\theta_c. \tag{4.7}$$

The total light yield of the electromagnetic cascade caused by the energy losses is proportional to the energy of the primary particle.[12] This relation is crucial for neutrino-induced event reconstructions in neutrino telescopes. Equation 4.7 implies that shorter wavelengths

[9] Rädel and Wiebusch, "Calculation of the Cherenkov light yield from electromagnetic cascades in ice with Geant4"

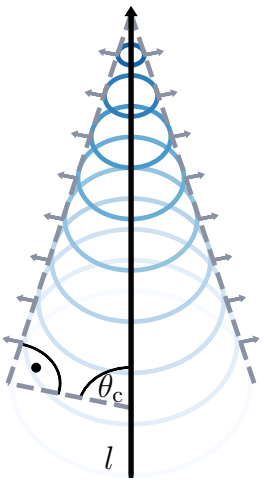


Figure 4.2: Illustration of the Cherenkov cone emitted by a relativistic charged particle $l$. The light propagates as illustrated by the superimposition of the colored circles. The resulting Cherenkov cone opening angle is $\theta_c = 41°$ when a $\beta \sim 1$ particle travels through the ice. Figure adapted from Huber, "Multi-Messenger correlation study of Fermi-LAT blazars and high-energy neutrinos observed in IceCube".

[10] Aartsen et al., "Measurement of South Pole ice transparency with the IceCube LED calibration system"

[11] Frank and Tamm, "Coherent Visible Radiation of Fast Electrons Passing Through Matter".

[12] Rädel and Wiebusch, "Calculation of the Cherenkov light yield from electromagnetic cascades in ice with Geant4".

produce a more abundant light yield. However, the refractive index drops below 1 for $\lambda \lesssim 300$ nm, effectively suppressing the propagation of Cherenkov photons. Hence, the optimal detector of Cherenkov radiation should be sufficiently dense to cause the electromagnetic cascade and, simultaneously, transparent to the optimal photon wavelength, between 300 and 600 nm. Clear water and ice are available in large volumes in nature and satisfy the required conditions. In the following, we will always refer to particle interactions in the ice, as that is the detection medium used by the IceCube neutrino telescope.

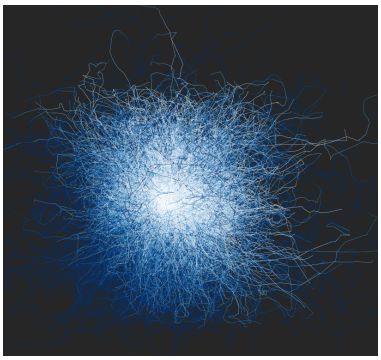

Figure 4.3: Simulations of the propagation of Cherekov photons produced by a 100 TeV $\nu_e$-CC event. The color gradient represents the time from white (early) to blue (late). The optical properties of the medium are characterized by an average scattering length of $\lambda_{\text{scat}} = 2.5$ m and an average absorption length of $\lambda_{\text{abs}} = 100$ m, which is a typical parameterization for the Antarctic ice in IceCube(Aartsen et al., "Measurement of South Pole ice transparency with the IceCube LED calibration system"). Courtesy of T. Glauch.

### 4.1.1 *Event topologies*

Depending on the neutrino flavor participating in the inelastic scattering with the ice nuclei, the resulting Cherenkov light pattern presents different topological features. Leveraging these differences, one can identify various event signatures.

#### *Cascade-like events*

Events produced by $\nu_e$-CC interactions and NC interactions of any neutrino flavor feature a nearly spherical emission profile, resulting from the short propagation lengths of electromagnetic and hadronic components. Figure 4.3 shows the typical diffusion of Cherekov photons for this type of event. Cascade events allow limited angular resolution to the original direction of the incident neutrino, with an average of $10 - 15^\circ$ below 10 TeV, which improves to $5 - 7^\circ$ above 100 TeV.[13] The possibility of calorimetric energy measurements compensates for the poor angular resolution. In $\nu_e$-CC interactions, the neutrino energy is entirely transferred to the hadronic and electromagnetic cascades. Hence, the neutrino energy can be directly measured if the interaction vertex happens within the detection volume. In NC interactions, the neutrino in the final state carries away part of the energy.

[13] Icecube Collaboration, "Observation of high-energy neutrinos from the Galactic plane".

#### *Track-like events*

Unlike electrons, muons produced in $\nu_\mu$-CC interactions or in atmospheric showers (see Section 4.2)[14] can travel several kilometers before decaying. For example, on average, a 2 TeV muon travels slightly less than 5 km in the ice.[15] The signature is a track-like, long, light pattern. Depending on whether the interaction vertex is contained in the detection volume or not, the track is named *starting* or *through-going*.

The elongated shape allows good angular resolution on the muon direction, smaller than $1^\circ$ above TeV energies. For $\gtrsim 1$ TeV muons created in $\nu_\mu$-CC interactions, the kinematic angle between the parent neutrino and the muon is negligible (see Equation 4.13), and the direction of the incident neutrino can be inferred with the same precision as the muon one. Hence, this event morphology is preferred

[14] A much smaller fraction of high-energy muons is produced in $\tau$ decays or from the decay of the $W$ boson created in the Glashow resonance.

[15] Chirkin and Rhode, "Propagating leptons through matter with Muon Monte Carlo (MMC)".

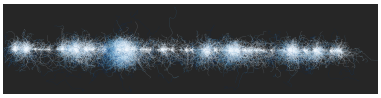

Figure 4.4: Simulation of the Cherenkov photons propagation in a 100 TeV muon track in the ice. Stochastic energy losses along the track create the light pattern. The timing of the photon arrivals (color scale as in Figure 4.3) permits the determination of the direction of the track. Courtesy of T. Glauch.

for searching for point-like sources of astrophysical neutrinos. On the other hand, only the fraction of energy that the muons deposit in the detection volume is visible. The total muon energy can only be determined statistically, adding significant uncertainty. The energy losses of a 100 TeV muon along the track are shown in Figure 4.4.

### *Double bangs*

CC interactions of tau neutrinos produce a hadronic cascade and a $\tau$, which carries most of the initial energy. The $\tau$ is unstable and travels only $\sim$ 50 m per PeV of energy before decaying into pions (hadronic, $\sim$ 65%) or into $\nu_\tau e \nu_e / \nu_\tau \mu \nu_\mu$ (leptonic, $\sim$ 17.5% each).[16]

The hadronic decay and the leptonic decay into an electron cause another cascade. In this case, the signature is a pair of cascades (a *double bang*) connected by a short track of light induced by the moving tau. Double bangs induced by $\nu_\tau$ with energies below the PeV are indistinguishable from single cascades, as the $\tau$ lepton decays too short after its creation. On the other hand, detecting a double bang corresponds most likely to identifying tau neutrinos of astrophysical origin, as $\nu_\tau$ production in atmospheric showers is strongly suppressed (see Figure 4.6). Earlier this year (2024), IceCube reported on the detection of seven $\nu_\tau$-induced events and rejected the hypothesis of the absence of an astrophysical $\nu_\tau$ flux at $5\,\sigma$ significance.[17] A simulation of a double bang is displayed in Figure 4.5.

[16] Particle Data Group, "Review of Particle Physics".

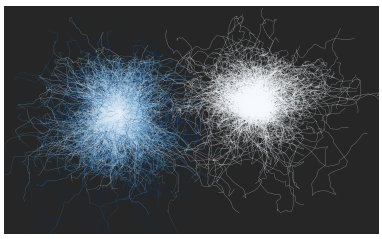

Figure 4.5: Simulation of the Cherenkov photons propagation in a double bang event from the interacton of a $\nu_\tau$. Their different colors show the time difference between the two cascades. Courtesy of T. Glauch.

[17] Abbasi et al., "Observation of Seven Astrophysical Tau Neutrino Candidates with IceCube".

## 4.2 *Atmospheric neutrinos*

All analyses trying to identify an astrophysical signal with a neutrino telescope have to deal with two main background components: atmospheric muons and atmospheric neutrinos, both byproducts of *particle showers* induced by cosmic-ray interactions in the atmosphere. These particles produce signatures identical to their astrophysical counterparts in the detector. Hence, understanding the properties of these background fluxes is of crucial importance for the correct interpretation of experimental results.

The fluxes of atmospheric muons and neutrinos are closely related to the production and decay of mesons. Cosmic ray hadronuclear interactions with air nuclei create mesons at around 15-20 kilometers altitudes. The decay of neutral pions results in two photons, which will produce an electron-positron pair and initiate an *electromagnetic shower*. The decay of charged pions and kaons produces the *conventional* atmospheric neutrino flux. The main decay channels are:[18]

[18] Particle Data Group, "Review of Particle Physics".

$$\pi^\pm \to \mu^\pm + \nu_\mu \, [+\bar{\nu}_\mu] \qquad (\sim 99.99\%), \tag{4.8}$$

$$K^\pm \to \mu^\pm + \nu_\mu \, [+\bar{\nu}_\mu] \qquad (\sim 64\%), \tag{4.9}$$

$$K^0_L \to \pi^\mp + e^\pm + \nu_e \, [+\bar{\nu}_e] \qquad (\sim 41\%), \tag{4.10}$$

$$K^0_L \to \pi^\mp + \mu^\pm + \nu_\mu \, [+\bar{\nu}_\mu] \qquad (\sim 27\%), \tag{4.11}$$

$$K^0_L \to \pi^+ + \pi^- + \pi^0 \qquad (\sim 13\%), \tag{4.12}$$

with the percentages indicating the respective branching ratios. The shower develops further as each new pion decays in muons and neutrinos. An additional contribution to the total neutrino spectrum comes from the decay into electrons and neutrinos of muons, which are not accelerated enough to reach the surface.

Each shower's extension and depth strongly depend on the type and energy of the primary particle. The initial hadronic interaction and the complex dynamics of the shower development as a function of energy and depth are described by a set of differential equations.[19] Due to their complexity and non-linearity, they are typically solved numerically. Figure 4.6 displays the numerical solutions for the atmospheric lepton fluxes resolved in the contributions from the decay of different particles. The dominant fluxes at Earth are the muon and muon neutrino fluxes. As we will see in the following sections, we select a sample of muon neutrinos optimized for searching point-like sources of astrophysical neutrinos. Hence, these backgrounds are the most concerning ones in the context of this work.

[19] Gaisser, Engel, and Resconi, *Cosmic Rays and Particle Physics: 2nd Edition*, pp. 107-122.

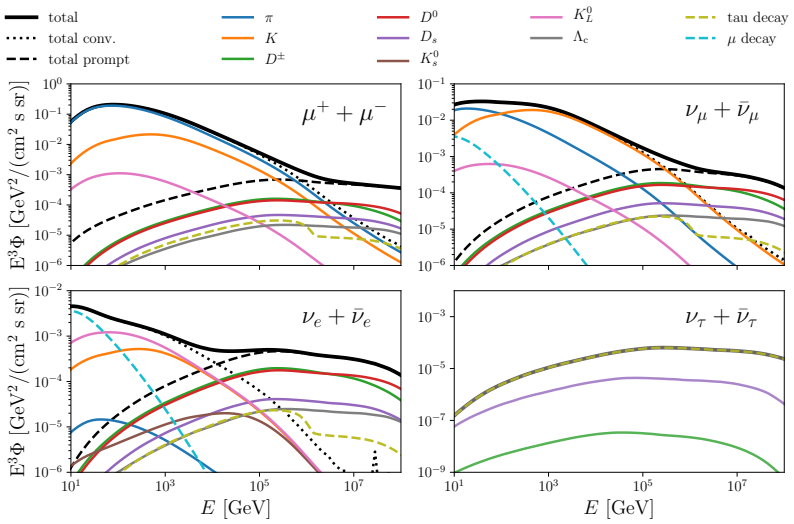


Figure 4.6: Contributions to the overall atmospheric flux of muons (top left), muon neutrinos (top right), electron neutrinos (bottom left), and tau neutrinos (bottom right). The solid black line illustrates the sum of all contributions. The dotted and dashed black lines represent the total conventional and prompt fluxes. The primary cosmic ray spectrum is based on the H3a model (Gaisser, "Spectrum of cosmic-ray nucleons, kaon production, and the atmospheric muon charge ratio"). Figure reprinted with permission from Huber, "Multi-Messenger correlation study of Fermi-LAT blazars and high-energy neutrinos observed in IceCube", adapted from Fedynitch et al., "Calculation of conventional and prompt lepton fluxes at very high energy".

When a meson is created, depending on its energy, one between the two competing processes of decay and interaction is more likely to happen. The muon flux is dominated by pion decays. For the $\nu_\mu + \bar{\nu}_\mu$ and $\nu_e + \bar{\nu}_e$ fluxes, at energies $\lesssim$ 100 GeV, the dominant contributions come from the pion decay and the decay of the pionic muon[20], respectively. At higher energies, the pion loses a more significant fraction of its energy in interactions before decaying. Hence, the byproducts of kaon decay become dominant. From $\sim$ 1 TeV, the interaction becomes more likely than the decay for kaons, too. Hence, above 1 TeV, energy losses through interactions are dominant for both pions and kaons, and the conventional neutrino energy spectrum softens from $\sim E^{-2.7}$ (the primary cosmic ray spectrum, see Section 2.1) to $\sim E^{-3.7}$.

[20] The muon produced in the pion decay.

All lepton fluxes in Figure 4.6 show the emergence of a new component around 100 TeV. This additional flux results from the decay of a subdominant fraction of heavier, charmed mesons, $D$ and $\Lambda$. Due to the higher masses, their lifetimes are shorter, and they decay promptly after production into lighter mesons, muons, and neutrinos[21]. Hence, this flux is known as the *prompt* flux. Not having time to lose their energy in interactions, the charmed mesons transfer all their energy to the decay products. Therefore, the prompt spectrum follows again the primary cosmic ray spectrum. As of today, no detection of a prompt atmospheric neutrino flux has been reported by the IceCube collaboration, and the reason for this non-detection remains an open question.[22,23]

[21] Charmed mesons can also produce electrons via semileptonic decays (Particle Data Group, "Review of Particle Physics"), but here we are interested in the hadronic components of the shower.

[22] Aartsen et al., "Characteristics of the Diffuse Astrophysical Electron and Tau Neutrino Flux with Six Years of IceCube High Energy Cascade Data".

[23] Abbasi et al., "Improved Characterization of the Astrophysical Muon-neutrino Flux with 9.5 Years of IceCube Data".

IceCube detects conventional atmospheric muons and neutrinos at a very high rate of $\sim$ 2.5 kHz. Experimentally, separating them from astrophysical neutrino-induced muons is challenging and requires sophisticated filtering strategies. The basic idea, however, is that conventional atmospheric fluxes show a softer energy spectrum compared to the expected astrophysical neutrino flux. Lower energy muons present different energy loss patterns in the ice compared to muons above TeV energies.[24] These differences can be leveraged to effectively separate signal and background. However, atmospheric showers usually produce muons in bundles, which imitate the signature of a single high-energy muon,[25] thus limiting the background suppression efficiency.[26] Conveniently, astrophysical neutrino detectors can use the Earth as an effective absorber of the atmospheric muon flux. This strategy is adopted for the event selection used in this work, as we will see in Section 4.4.

[24] See Section 4.6 and Figure 4.10 for a review on muon energy losses in the ice.

[25] Aartsen et al., "All-sky Search for Time-integrated Neutrino Emission from Astrophysical Sources with 7 yr of IceCube Data".

[26] See Section 6.1 of Coenders, "High-energy cosmic ray accelerators: searches with IceCube neutrinos. Probing seven years of IceCube muon data for time-integrated emission of point-like neutrino sources" for a review.

## 4.3 *The IceCube detector*

When neutrino telescopes were initially envisioned, it was proposed to use large volumes of water to indirectly detect high-energy neutrinos via the Cherenkov radiation emitted by secondary charged particles produced in their interactions.[27] The necessity of large instrumented volumes can be understood by recalling the Waxman-Bahcall limit (Equation 2.19), which suggests an all-flavor neutrino energy density of $\sim 2 \times 10^{-8}$ GeV cm$^{-2}$s$^{-1}$sr$^{-1}$. This estimate aligns with the most recent measurements[28]. When integrated over the sky, the energy density of Waxman and Bahcall translates into $\sim 20 - 50$ high-energy ($\gtrsim$ 100 TeV) neutrino-induced muons per square kilometer per year,[29] a rate several orders of magnitude smaller than the expected atmospheric muon and muon neutrinos fluxes. Therefore, a kilometer-scale neutrino telescope is required to detect a statistically significant number of astrophysical neutrinos.

[27] Markov, "On high energy neutrino physics".

[28] see (Naab et al., "Measurement of the astrophysical diffuse neutrino flux in a combined fit of IceCube's high energy neutrino data") and Subsection 2.2.3

[29] Gaisser, "Neutrino Astronomy: Physics Goals, Detector Parameters".

The IceCube detector, constructed in the deep Antarctic ice at the South Pole, addresses this need. The ice is transparent enough to allow the propagation of Cherenkov photons while also being naturally abundant. IceCube instruments approximately a cubic kilometer of ice between 1450 m and 2450 m in depth. By positioning the instrumented volume deep underground, the overlying ice acts as a shield, reducing the background flux of atmospheric muons.

Completed in 2011, IceCube comprises 5160 *digital optical modules* (DOMs) deployed on 86 cables (*strings*) arranged in a hexagonal pattern. Of these, 79 strings are spaced about 125 meters apart and make up the *InIce Array*. The geometry of the InIce Array is optimized for detecting astrophysical neutrinos with energies ranging from 100 GeV to PeV.[30] At the center of the detector lies a more densely instrumented region called *DeepCore*, featuring 7 additional strings placed only 72 m apart. This configuration lowers the energy threshold to $\sim$ 10 GeV.[31] The DeepCore detector is primarily used for particle physics studies involving atmospheric neutrinos, such as measuring oscillation parameters in the muon neutrino sector.[32] Finally, the *IceTop* detector is located on the surface and consists of 82 Cherenkov tanks.[33] IceTop measures air showers produced by cosmic rays impinging on the top of the atmosphere and, at the same time, acts as a veto for the InIce Array. An illustration of the IceCube detector, showing all its components, is provided in Figure 4.7.

[30] Aartsen et al., "In-situ calibration of the single-photoelectron charge response of the IceCube photomultiplier tubes".

[31] Ibid.

[32] Abbasi et al., "Measurement of atmospheric neutrino mixing with improved IceCube DeepCore calibration and data processing".

[33] Abbasi et al., "IceTop: The surface component of IceCube. The IceCube Collaboration".

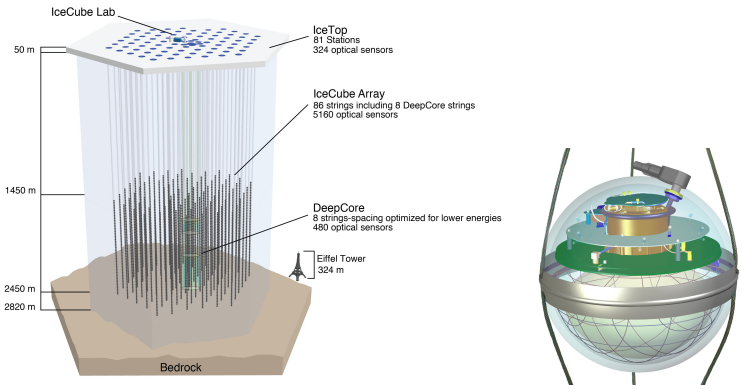


Figure 4.7: Schematic view on the IceCube detector (left) and a single In-Ice DOM (right). The 86 IceCube strings reach from the surface down to a depth of around 2500 m. The surface IceTop array vetoes atmospheric air showers from cosmic ray interactions while measuring the cosmic ray spectrum. A more densely instrumented region at the center, the DeepCore, lowers the detection energy threshold to $\sim$ 10 GeV. IceCube instruments approximately one cubic kilometer of ice with 5160 DOMs, drawn as circles on the strings. Images from Aartsen et al., "The IceCube Neutrino Observatory: instrumentation and online systems" and https://gallery.icecube.wisc.edu/internal/v/GraphicRe/visuals/dom/DOMNoHarnessWhiteback_lg.jpg.html.

### 4.3.1 *Photon attenuation in the Antarctic ice*

The amount of observed Cherenkov light that propagates through the detector depends on the local properties of the ice. Short-term climate variations from volcanoes and longer-term variations from atmospheric dust affect the optical properties of the ice, producing nearly horizontal layers.[34] This layered structure affects how much light the DOMs detect. Hence, the characterization of the ice properties is necessary to calibrate the detector response to photon hits.

The enormous pressure the ice has to sustain at a depth of 1.5 km removes most of the air bubbles created by snowfall accumulations over the centuries. Therefore, the deep Antarctic ice is highly transparent and optimal for measuring optical photons. However, the

[34] Aartsen et al., "Measurement of South Pole ice transparency with the IceCube LED calibration system".

transmission cannot be perfect, and two main processes cause photon attenuation in the ice: absorption, which effectively reduces the number of photons that reach the DOMs, and scattering of photons on dust molecules trapped in the ice. The latter is the most critical in the ice, with an attenuation length[35] which can be as small as $20 - 25$ m. Hence, with an intra-string spacing of 125 m, Cherenkov photons will scatter multiple times before reaching a DOM.[36]

LED flashers mounted in each DOM are used to calibrate the absorption and scattering parameters of the ice in calibration routines run once per year.[37] In addition, in-situ measurements using Cherenkov light from low-energy muons are used to determine the effect on photon propagation of the refrozen ice, which was melted during the IceCube deployment (*hole ice*).[38]

[35] Propagation length after which the photon intensity is reduced by a factor $1/e$.

[36] Aartsen et al., "Measurement of South Pole ice transparency with the IceCube LED calibration system".

[37] Aartsen et al., "The IceCube Neutrino Observatory: instrumentation and online systems".

[38] Ibid.

## 4.4 *Data acquisition and up-going muon tracks selection*

The large background of atmospheric muons (see Section 4.2) can be efficiently reduced by using the Earth as a filter, *i.e.*, by selecting events that originate from the Northern hemisphere. While propagating through the Earth, muons are absorbed, while neutrinos are less affected. Several IceCube works have already limited the searches for neutrino sources to the Northern hemisphere only.[39,40] Accordingly, we also trade the Southern hemisphere for a purer neutrino sample.

This section reviews the data acquisition, triggering, and filtering procedures adopted in this work. The outcome is a highly pure selection of neutrino-induced muon tracks, optimized for searching neutrino point-like sources. The results of point-source analyses (see Chapter 5) using this event selection are presented in Section 8.2.

[39] Aartsen et al., "Search for steady point-like sources in the astrophysical muon neutrino flux with 8 years of IceCube data".

[40] Abbasi et al., "Evidence for neutrino emission from the nearby active galaxy NGC 1068".

**Data Acquisition**

The fundamental detector unit is the DOM, which hosts a 10-inch, downward-looking photomultiplier tube (PMT) alongside on-board read-out electronics (see Figure 4.7). When a photon reaches a PMT and triggers a response exceeding the threshold of $\sim 0.23$ times the single photoelectron[41], the DOM records a hit. This hit contains information about the charge measurement over time, resulting in a waveform. The waveform is digitized using an Analog Transient Waveform Digitizer (ATWD) and a Fast Analog to Digital Converter (FADC), allowing data collection over various time ranges.[42] The waveform is then deconvolved into a pulse series. Therefore, for each DOM, the pulse series corresponds to a list of single photoelectron charges and their time distribution, the two fundamental observables to reconstruct the direction and energy of events.

[41] The charge distribution over time induced by a single electron created, due to the photoelectric effect, when the photon hits the photocathode of the PMT.

[42] Aartsen et al., "The IceCube Neutrino Observatory: instrumentation and online systems".

**Triggering and filtering – Level 2**

When a DOM records a hit, the occurrence of coincident hits in the nearest or next-to-nearest neighboring DOMs within $\pm 1$ µs satisfies the *Hard Local Coincidence* (HLC) criteria. When the HLC condition is met, the entire digitized waveform is stored and sent to the surface.

For example, the selection used in this work requires 8 HLC within 5 μs, a *Simple Multiplicity Trigger* known as SMT-8.[43] When the SMT is satisfied, IceCube records all DOM signals between $-4$ μs and 6 μs as a single event.

[43] Aartsen et al., "The IceCube Neutrino Observatory: instrumentation and online systems".

The SMT-8 trigger rate is approximately 2.5 kHz, dominated by atmospheric muons. A series of software filters are applied to further reduce the data transmitted to the North. Our selection passes through the *Muon Filter*, optimized to select events with a track-like signature. In general, this phase of the selection is based on quality cuts applied to the output of simple and inexpensive directional reconstruction algorithms and to the total charge, used as a proxy for the muon energy to suppress low-energy atmospheric events[44].

[44] See chapter 5 of Reimann, "Search for the sources of the astrophysical high-energy muon-neutrino flux with the IceCube neutrino observatory" and references therein for more details.

Events that pass the Muon Filter are transferred North via satellite to the IceCube computing facilities for further data processing. The data stream at this stage is about 34 Hz.

**Muon Level 3**

More complex track reconstruction algorithms are applied to the events that survive the filtering. These include the splineMPE algorithm used for the NorthernTrack selection, which will be introduced in Subsection 4.5.1. The Muon Level 3 applies a different selection to up-going and down-going events from the Northern and Southern hemispheres, respectively. Stringent cuts on the reconstruction quality reduce the contamination of down-going events misreconstructed as up-going.[45] We select only up-going muon tracks, with reconstructed declination $\delta > -5^\circ$. For these events, it has been estimated from simulations that approximately 89% of a benchmark neutrino flux following an $E^{-2}$ energy spectrum survives the muon Level 3 filter. In contrast, only about 8.7% of atmospheric muons remain in the sample.[46] We are left with a data stream of approximately 3 Hz, still dominated by atmospheric muons.

[45] Rädel, "Measurement of High-Energy Muon Neutrinos withthe IceCube Neutrino Observatory".

[46] Ibid.

**Level 4-5**

In the final selection steps, multi-variate methods are used to further reduce background contaminations. Two boosted decision trees (BDTs) are applied to select only tracks from the Northern Hemisphere and reject mis-reconstructed down-going atmospheric muons. The first BDT separates atmospheric muons from $\nu_\mu$-CC interactions with an angular resolution better than $5^\circ$;[47] the second BDT is meant to remove any remaining $\nu_e$-induced cascades, which have a much worse angular resolution,[48] see Figure 4.3.

[47] Ibid.

[48] Ibid.

Finally, to ensure the stability of all reconstruction algorithms, we require that data-taking runs have no more than 1 non-active string and 100 non-active DOMs.

Figure 4.8 shows a comparison between the event rates at the SMT-8 trigger level and the up-going muon tracks selection used in this work. Based on Monte Carlo (MC) simulations, 99.7% of the selected events are induced by neutrinos, and only $\sim$ 0.3% of the sample consists of atmospheric muons.[49]

[49] Ibid.

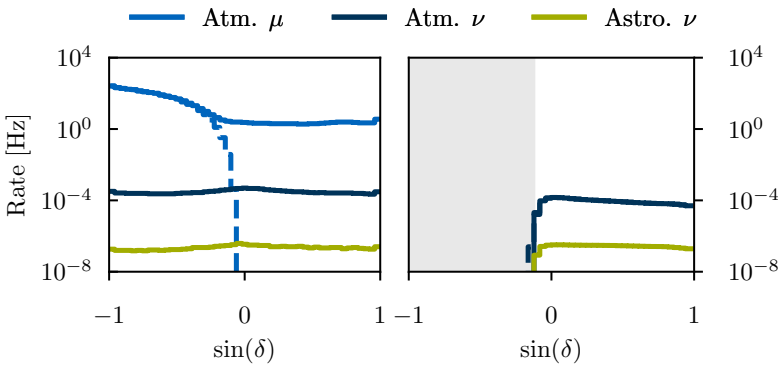


Figure 4.8: **Left:** The event rate at the trigger level is shown as a function of the declination. The background of atmospheric muons originates exclusively from the Southern sky (dashed line), as the Northern sky benefits from the shielding of the Earth. Nevertheless, mis-reconstructed atmospheric muons dominate the data rate in the Northern hemisphere. **Right:** Final level sample of well-reconstructed up-going muon tracks. Figure reprinted with permission from Glauch, "The Origin of High-Energy Cosmic Particles: IceCube Neutrinos and the Blazar Case".

## 4.5 *Directional reconstruction*

The photoelectron charges and time stamps are the fundamental quantities to reconstruct the two most relevant event properties: the energy and the direction of the incoming neutrinos. Inferring the direction of the parent neutrino is crucial for searching for accumulations of astrophysical neutrinos from the direction of astrophysical sources. Muon events induced by $\nu_\mu$-CC interactions result in track-like light patterns. The long pattern of energy losses facilitates an accurate angular reconstruction of the muon direction. Furthermore, as the angular separation between the muon and the parent neutrino decreases with increasing energy[50]

$$\psi_{\nu\mu} = 0.7^\circ \left(\frac{E_\nu}{\text{TeV}}\right)^{-0.7}, \tag{4.13}$$

the direction of the parent neutrino can be inferred with the same precision as the muon one for high-energy events. At TeV energies and below, the kinematic angle $\psi_{\nu\mu}$ poses an unbeatable limit for the angular resolution of any reconstruction.

As previously discussed, simple and fast reconstruction algorithms are applied during the early processing stages. Based on their outputs, quality cuts to suppress the background rates are applied to the data sample. Furthermore, first-guess reconstructions are used as a seed for more complex algorithms. The SplineMPE reconstruction algorithm is applied to the up-going muon sample used in the point-source analysis performed in this work.

[50] Learned and Mannheim, "High-Energy Neutrino Astrophysics".

### 4.5.1 *SplineMPE*

SplineMPE[51] reconstructs track-like events by assuming a straight-line trajectory crossing the detector at the speed of light, with continuous energy losses along the path. The differences between the observed hit times and the expected time distributions from geometrical propagation of unscattered Cherenkov photons can be analytically approximated by a *Pandel* function.[52] The left panel of

[51] Abbasi et al., "A muon-track reconstruction exploiting stochastic losses for large-scale Cherenkov detectors".

[52] van Eijndhoven, Fadiran, and Japaridze, "Implementation of a Gauss convoluted Pandel PDF for track reconstruction in neutrino telescopes".

Figure 4.9 shows the distribution of the residual time modeled by a Pandel function for different distances between the track and the DOM. The photon travels multiple scattering lengths with increasing distance, and the distribution broadens. The Pandel modeling includes parameters that account for the scattering length of photons in the ice and the detection efficiency and dark noise level of the PMTs. However, it does not account for the variations in the optical properties of the ice in different regions of the detector. This limitation can be overcome using MC simulations of photon propagation in the ice from light sources at various locations and with different orientations in the detector. These simulations assume a muon track of infinite length. The resulting time residual PDFs (probability density functions) are stored in numerical tables and then interpolated using penalized B-splines[53].

[53] Whitehorn, van Santen, and Lafebre, "Penalized splines for smooth representation of high-dimensional Monte Carlo datasets"

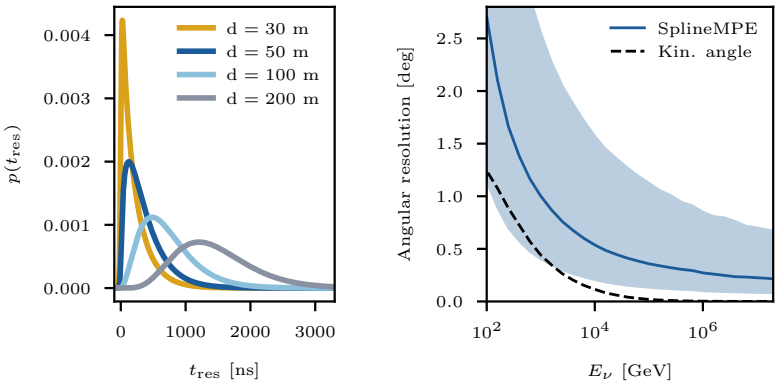


Figure 4.9: **Left:** Pandel function to approximate the probability density function of the residual arrival time of Cherekov photons for different distances from the DOM. Courtesy of M. Huber. **Right:** The median angular resolution of the SplineMPE reconstruction algorithm (blue) is compared to the median kinematic angle between the parent neutrino and the muon. The shaded band represents the 68% central quantile of the reconstructed muon directions.

Intuitively, the track direction could be inferred from the likelihood of the recorded arrival times of *all* photon hits at each DOM. However, this likelihood construction suffers from PMT effects such as afterpulses or late pulses,[54] which are not modeled in the time residual PDFs. To make the approach insensitive to such PMT effects, SplineMPE uses only the combined likelihood of the residual arrival time of the *first* photon hit, $t^1_{res}$, at each DOM:[55]

[54] Haack, "Observation of high-energy neutrinos from the galaxy and beyond".

[55] Abbasi et al., "A muon-track reconstruction exploiting stochastic losses for large-scale Cherenkov detectors".

$$\mathcal{L}_{MPE} = \prod_{i}^{N_{\text{DOMs}}} p(t^1_{res,i} \,|\, \mathbf{x}_i, H) \left( \int_{t^1_{res,i}}^{\infty} p(t \,|\, \mathbf{x}_i, H) \mathrm{d}t \right)^{N_{\text{pulses},i}-1} . \quad (4.14)$$

In Equation 4.14, the likelihood of the observed first hits, $p(t^1_{res,i} \,|\, \mathbf{x}_i, H)$, at DOM position $\mathbf{x}_i$ and under the track hypothesis $H$, is multiplied by the probability of observing $N_{\text{pulses}} - 1$ pulses at a later time.[56] The product is over all DOMs, $N_{\text{DOMs}}$.

[56] Haack, "Observation of high-energy neutrinos from the galaxy and beyond".

The direction of a muon track is obtained by minimizing the negative logarithm of Equation 4.14 over $H$. The right panel of Figure 4.9 displays the angular separation between the median splineMPE reconstruction and the parent neutrino direction as a function of the neutrino energy. In the same figure, the kinematic angle between the

muon and neutrino is shown as well. The median angular resolution drops below 0.5° at TeV energies and further improves to 0.2° above 1 PeV.

### 4.5.2 *Uncertainty on the reconstructed direction*

Estimating the uncertainty of the reconstructed event direction is crucial for evaluating the probability that the event originates from a specific direction in the sky, *e.g.*, from a point-like astrophysical source. An accurate per-event angular uncertainty estimation could be obtained from re-simulations of the detected events with subsequent application of the SplineMPE reconstruction.[57,58] However, high-statistics event samples pose computational constraints that require less expensive solutions.

Here, we report on two angular uncertainty estimation methods: *Paraboloid*, which is used in the public neutrino data sample described in Chapter 6, and a multivariate estimation method based on BDTs,[59] which is applied to the up-going neutrino sample for the point-source analysis described in Chapter 5.

[57] Abbasi et al., "Studies of systematic uncertainty effects on IceCube's real-time angular uncertainty".

[58] Sommani, Lagunas Gualda, Niederhausen, et al., "Towards a more robust reconstruction method for IceCube's real-time program".

[59] Abbasi et al., "Evidence for neutrino emission from the nearby active galaxy NGC 1068".

#### *Paraboloid*

One angular uncertainty estimation is based on the *Paraboloid* algorithm,[60] which approximates the SplineMPE log-likelihood function around the best-fit position using a bi-dimensional parabola. A circular angular uncertainty $\sigma'_p$ can be obtained by taking the mean square of the paraboloid axes along the two spatial dimensions. The underlying assumption is that the angular resolution is normally distributed around the true direction, with standard deviation $\sigma'_p$.[61] Most IceCube analyses use a circle containing 50% of the distribution as the angular uncertainty estimator. Conveniently, this median angular resolution can be obtained as $\sigma_p = 1.177\sigma'_p$.[62]

$\sigma_p$ does not account for the uncertainty due to the kinematic angle between the parent neutrino and the muon (Equation 4.13). Hence, a point spread function based on $\sigma_p$ could underestimate the scattering of the reconstructed tracks around the neutrino source by up to a factor of $\sim 2$.[63] To include this additional uncertainty, the median angular uncertainty is shifted using an energy-dependent correction factor estimated from MC simulations assuming an $E^{-2}$ astrophysical neutrino spectrum. The correction factor rescales $\sigma_p$ to equal the median opening angle between the primary neutrino and the secondary muon track at a given muon track energy. However, the resulting $\sigma_p$ does not fully describe the distribution of kinematic angles for a given reconstructed muon energy, which is non-trivial as it originates from events induced by neutrinos with very different energies.

[60] Neunhöffer, "Estimating the angular resolution of tracks in neutrino telescopes based on a likelihood analysis".

[61] Ibid.

[62] Ibid.

[63] Abbasi et al., "Evidence for neutrino emission from the nearby active galaxy NGC 1068".

*Multi-variate angular uncertainty estimation*

The approximation of a Gaussian spatial distribution of the muon tracks around the source is not always valid, especially for low-energy events, as we will see in Section 5.1. Primarily, the deviation from the normal distribution is caused by the kinematic angle between the neutrino and the secondary muon. Moreover, depending on the muon track energy and underlying neutrino spectrum, $2-10\%$ of the Paraboloid fits fail.[64]

An alternative estimator is based on a BDT, which parametrizes the median angular separation between the reconstructed and the true muon directions as a function of 17 observables, including the paraboloid angular uncertainty, an estimate of the position of the largest energy deposition in the detector, a measure of the stochasticity of the event energy loss pattern, the track declination as estimated by SplineMPE, and angular separations between different track reconstruction methods.[65] Hence, the BDT can account for the large variety of characteristics in different track-like signatures while also producing a reliable angular error estimate when the $\sigma_p$ estimation fails.[66]

The BDT angular uncertainty is applied to the upgoing muon track sample developed for point-source searches. The kinematic angle contribution to the overall uncertainty is modeled in the point spread function (PSF) of the point-source analysis described in Section 5.1. As the PSF is modeled for different power-law spectral indices, the dependence of the kinematic angle on the underlying neutrino energy spectrum can be naturally folded in.

[64] Abbasi et al., "Evidence for neutrino emission from the nearby active galaxy NGC 1068".

[65] Ibid.

[66] In this case, the input variable is ignored by the BDT, which relies on the other observables to produce a stable output.

## 4.6 Energy reconstruction

In any search for astrophysical neutrinos, the muon energy is the primary observable that helps distinguish between atmospheric and astrophysical events. Furthermore, the distribution of the observed energies is crucial to characterize the underlying energy spectrum of neutrino sources. Hence, an accurate energy reconstruction is required. However, the inference of the energy of a high-energy muon crossing the detector is a challenging task. The muon is usually not fully contained. Therefore, only a segment of its track is seen in the detector, and a calorimetric measurement is not possible.

Generally, as a muon travels through matter, it loses energy due to ionization losses, bremsstrahlung, photo-nuclear interaction, and pair production.[67] Losses due to ionization vary slowly with energy, while radiative losses increase with energy. The average energy loss per propagation length $\mathrm{d}x$ can be described as

$$-\frac{\mathrm{dE}}{\mathrm{dx}} = a(E) + b(E)E. \tag{4.15}$$

As seen in Figure 4.10, the two coefficients $a(E)$ and $b(E)$ are approximately constant. Equation 4.15 implies a proportionality between energy losses and muon energy. Above 1 TeV, the energy loss

[67] Chirkin and Rhode, "Propagating leptons through matter with Muon Monte Carlo (MMC)".

increases proportionally to the muon energy and is therefore proportional to the number of photoelectrons detected. The mean energy loss in Equation 4.15 can then be estimated as the ratio of the total number of photoelectrons detected for a given event to the expected number for a minimum ionizing muon losing 1 GeV/m along the same trajectory, multiplied by 1 GeV/m[68].

[68] Abbasi et al., "An improved method for measuring muon energy using the truncated mean of dE/dx"

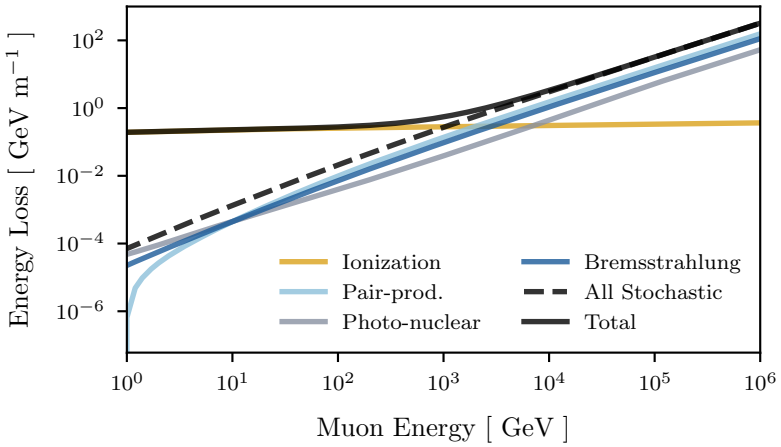


Figure 4.10: Contribution from ionization and stochastic radiative processes to the muon energy loss in ice displayed with different colors as a function of the muon energy. The solid black line shows the total energy loss given by the sum of all contributions. The dashed black line represents the sum of all stochastic processes. Adapted from Huber, "Multi-Messenger correlation study of Fermi-LAT blazars and high-energy neutrinos observed in IceCube".

Above 1 TeV, stochastic radiative processes become dominant over ionization. As a result, variable energy loss patterns can be caused by muons of the same energy (see Figure 4.4). Hence, the spread of dE/dx increases, and the inference of the muon energy becomes more challenging. Additionally, large energy depositions that saturate the PMTs cause an overestimation of the muon energy.[69]

[69] Abbasi et al., "An improved method for measuring muon energy using the truncated mean of dE/dx".

Here we report on two energy reconstruction algorithms tackling the issues related to stochasticity in different ways: *Truncated Energy*, which is used in the public neutrino data sample described in Chapter 6, and an energy reconstruction algorithm based on deep neural networks,[70] which is applied to the up-going neutrino sample for the point-source analysis described in Chapter 5.

[70] Glauch, "The Origin of High-Energy Cosmic Particles: IceCube Neutrinos and the Blazar Case".

### 4.6.1 *Truncated Energy*

The Truncated Energy algorithm calculates the losses for each DOM within 60 m of the track and excluding the half with the highest observed-to-expected photoelectron ratio. The estimated dE/dx is then calculated by averaging the contributions from the remaining 50% DOMs. The left panel of Figure 4.12 shows the performance of this reconstruction. On average, high-energy events are correctly reconstructed, while a degeneracy in the reconstructed energy of sub-TeV tracks is likely caused by the truncation of the already small information content.[71]

[71] Ibid.

### 4.6.2 *Deep neural network for energy reconstruction*

An alternative energy reconstruction method uses a *deep neural network* (DNN) optimized for up-going muon tracks.[72] The DNN energy estimator takes as input the DOMs pulse maps and has 15 input features, including the total charge and several quantiles of the charge distribution, the hit times, and the amount of charge collected as a function of time.[73] It has been trained on approximately 6 million up-going tracks reconstructed assuming different ice models to gain stability against the systematic uncertainty on the ice properties.[74] The network is trained to predict the muon energy when it enters the detector volume.[75]

Compared to the deposited energy in the detector volume, the energy on detector entry has the advantage of being independent of the actual track length in the detector[76]. Hence, it approximates the parent neutrino energy more closely, as seen in Figure 4.11. The muon energy on detector entry is an especially good proxy of the neutrino energy for low-energy events, which are statistically mainly detected when the neutrino interacts near the detector volume: On average, more than 50% of the neutrino energy below 1 TeV is seen as muon energy, with a relatively narrow distribution spread, see Figure 4.11.

Overall, the DNN energy estimator uses more event information compared to Truncated Energy. As a result, it improves the energy resolution by up to 50%[77] and removes the energy degeneracy at muon energies $\lesssim 1$ TeV (see Figure 4.12). As most events in the data sample are induced by low-energy atmospheric neutrinos, the DNN improves the energy estimates for a significant fraction of the sample. Moreover, an unbiased energy estimation allows the correct attribution of a kinematic angle to reconstructed muons, which is especially important at low energies (see the right panel of Figure 4.9).

The DNN energy reconstruction is applied to the upgoing muon track sample developed for point-source searches.

[72] Abbasi et al., "Evidence for neutrino emission from the nearby active galaxy NGC 1068".

[73] Glauch, "The Origin of High-Energy Cosmic Particles: IceCube Neutrinos and the Blazar Case".

[74] Ibid.

[75] For starting events, it is the muon energy at the interaction vertex contained in the detector volume.

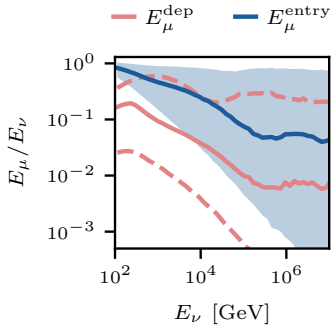


Figure 4.11: Fraction of the parent $\nu_\mu$ visible as muon energy in the detector estimated from MC simulations. The solid blue line indicates the median muon energy at its first intersection with the detector volume, $E_\mu^{\mathrm{entry}}$, while the blue band represents the 90% central quantile of the distribution. The solid pink line shows the median energy deposited in the detector volume by a muon track, $E_\mu^{\mathrm{dep}}$, with the dashed lines representing the 90% central quantile.

[76] Glauch, "The Origin of High-Energy Cosmic Particles: IceCube Neutrinos and the Blazar Case"

[77] Ibid.

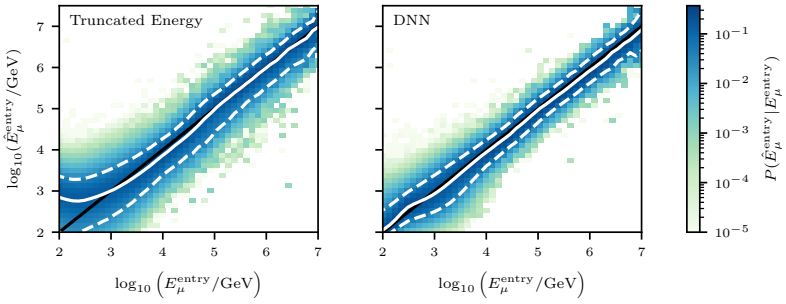


Figure 4.12: Comparison of the DNN-based (left) and Truncated Energy (right) muon energy reconstruction. The color scale maps the column-normalized PDF of the reconstructed muon energy at the point where the track intersects the detector volume ($\hat{E}_\mu^{\mathrm{entry}}$). The black solid line represents the ideal case of unbiased predictions. The Solid white line shows the median reconstructed energy

## 4.7 Final sample of up-going muon tracks

The final sample of up-going muon tracks that will be used to perform several searches for neutrino point-like sources in the Northern sky consists of 13 years of experimental data. Compared to the previous work that used the same event selection and reconstructions,[78] we include three more data-taking seasons for the complete detector configuration, *IC86* (IceCube with 86 strings), and one year of data collected in 2010, when IceCube consisted of 79 strings only. This incomplete detector configuration is known as *IC79*. Overall, the data sample is increased by 50% compared to the previous work.

[78] Abbasi et al., "Evidence for neutrino emission from the nearby active galaxy NGC 1068".

After the Level 4 and Level 5 processing levels described in Section 4.4, the DNN energy and BDT angular uncertainty estimators are applied to the data sample. Events with reconstructed energy below 100 GeV are excluded, and the minimum angular uncertainty of events is 0.1°. Table 4.1 reports the characteristics of each experimental data sample, summarizing the start and end times in Modified Julian Date format (MJD), the total number of selected events, and the corresponding detector uptime (livetime). The livetime is calculated based on events that pass the Level 2 processing. Our selection retains 991499 events for a total livetime of about 4767 days, corresponding to a rate of about 2.41 mHz. The expected atmospheric and astrophysical neutrino rates are 2.39 mHz and 9.8 μHz, respectively, as estimated from simulations.

| Season | MJD Start | MJD Stop | N Events | Livetime [days] |
|---|---|---|---|---|
| IC79 2010 | 55348.8 | 55694.4 | 61263 | 312.12 |
| IC86 2011 | 55694.4 | 56062.4 | 70185 | 338.09 |
| IC86 2012 | 56062.4 | 56414.4 | 68446 | 325.43 |
| IC86 2013 | 56400.5 | 56783.2 | 73513 | 352.28 |
| IC86 2014 | 56757.4 | 57160.0 | 74892 | 360.88 |
| IC86 2015 | 57136.1 | 57528.9 | 76138 | 364.60 |
| IC86 2016 | 57528.9 | 57891.2 | 74332 | 355.78 |
| IC86 2017 | 57891.2 | 58309.1 | 85726 | 409.91 |
| IC86 2018 | 58288.8 | 58682.0 | 76804 | 368.09 |
| IC86 2019 | 58682.0 | 58998.8 | 65257 | 311.04 |
| IC86 2020 | 58977.2 | 59361.8 | 75366 | 361.21 |
| IC86 2021 | 59337.9 | 59794.6 | 89220 | 428.85 |
| IC86 2022 | 59771.6 | 60276.9 | 100357 | 479.01 |
| Total | | | 991499 | 4767.31 |

Table 4.1: Overview of the experimental data samples, including start and end times in MJD format, the number of selected events, and the livetime in days. The newly added seasons are highlighted in blue.

### 4.7.1 Simulations of the IC86 detector

Simulations of the detector response to neutrino-induced muons are crucial for interpreting experimental results of physics analyses. As will be described in detail in Section 5.1, the point-source analysis employed in this work is based on a likelihood-ratio test where

the PDFs of the events are inferred from the distributions of simulated events. The PDFs depend on three reconstructed observables—the muon energy, direction, and uncertainty on the reconstructed direction—and on the parameters describing the tested hypotheses. Hence, event simulations must cover a large, multi-dimensional parameter space. For these reasons, our MC simulations of events need to satisfy two requirements:

- excellent agreements with the distribution of the experimental data to ensure that PDFs modeled on simulations correctly represent the observed neutrino events, and
- high statistics, at least an order of magnitude greater than the number of events in the experimental data sample.

Compared to the previous point-source analysis using 9 years (IC86 2011-2019) of the same data selection, we double the statistics of $\nu_\mu$ simulations and include $\nu_\tau$ simulations.

As discussed in Subsection 4.1.1, $\nu_\tau$-CC interactions can produce a $\nu_\mu$ flux from the decay of $\tau$ leptons. This regenerated flux has a relevant contribution at high declinations. In fact, the Earth is not transparent for high-energy neutrinos because of the increasing cross-section of CC interactions with the incident neutrino energy (see Figure 4.1)[79]. Muons produced in CC interactions of high-energy neutrinos in the Earth quickly lose most of their energy due to the exponential energy loss trend at high energies (see Figure 4.10). Conversely, tau leptons produced in $\nu_\tau$ interactions promptly decay, regenerating a $\nu_\tau$ before losing too much energy. This mechanism extends the range over which the secondary products of a $\nu_\tau$ flux can be detected.[80] Thanks to the regenerated neutrino flux, the detection efficiency of IceCube towards the pole improves (see the central panel of Figure 4.17). The critical absorption cross-section at which the transmission probability of neutrinos of various energies is reduced to $1/e \approx 0.37$ is shown in Figure 4.13 as a function of declination.

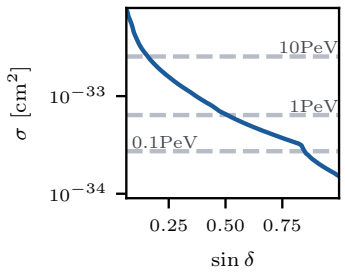


Figure 4.13: Absorption cross-section for neutrino traversing the Earth at which the transmission probability is reduced to $1/e \approx 0.37$ shown as a function of the sine of declination ($\delta$). Horizontal dashed lines indicate the critical cross-section for three exemplary neutrino energies. Figure adapted from Palladino, Spurio, and Vissani, "Neutrino Telescopes and High-Energy Cosmic Neutrinos".

[79] The cross-section for NC interactions increases similarly. However, NC processes produce a neutrino with reduced energy, thus less prone to absorption in the Earth.

[80] Bugaev et al., "Propagation of $\tau$-neutrinos and $\tau$-leptons through the Earth and their detection in underwater/ice neutrino telescopes".

Including $\nu_\mu$ and $\nu_\tau$ simulations, we use approximately 28 million MC events simulated in the IC86 detector. A list of the simulation datasets and their properties can be found in Appendix C.1. The simulated samples are weighted according to the sum of expected atmospheric and astrophysical fluxes. We calculate the atmospheric flux using the Cascade Equation solver MCEq[81] assuming the GST primary cosmic ray model[82] and the SYBILL 2.3c hadronic interaction model.[83] To match the observed rate of atmospheric neutrinos in the experimental data, the predicted flux is scaled up by a constant factor of $\sim 1.2$. The remaining mismatches of a few percent between experimental data and MC are further corrected by applying a bi-dimensional spline, which models the small differences in the declination-energy parameter space. The almost perfect agreement with the IC86 data resulting from this procedure is shown in Figure 4.14 for the three reconstructed muon observables: the DNN

[81] Fedynitch et al., "Calculation of conventional and prompt lepton fluxes at very high energy", available on GitHub at https://github.com/mceq-project/MCEq.

[82] Gaisser, Stanev, and Tilav, "Cosmic ray energy spectrum from measurements of air showers".

[83] Riehn et al., "The hadronic interaction model Sibyll 2.3c and Feynman scaling".

energy, the SplineMPE declination, and the $\sigma_{\mathrm{BDT}}$ angular uncertainty between the true and reconstructed muon. The agreement ensures that PDFs modeled on simulations correctly describe the experimental data.

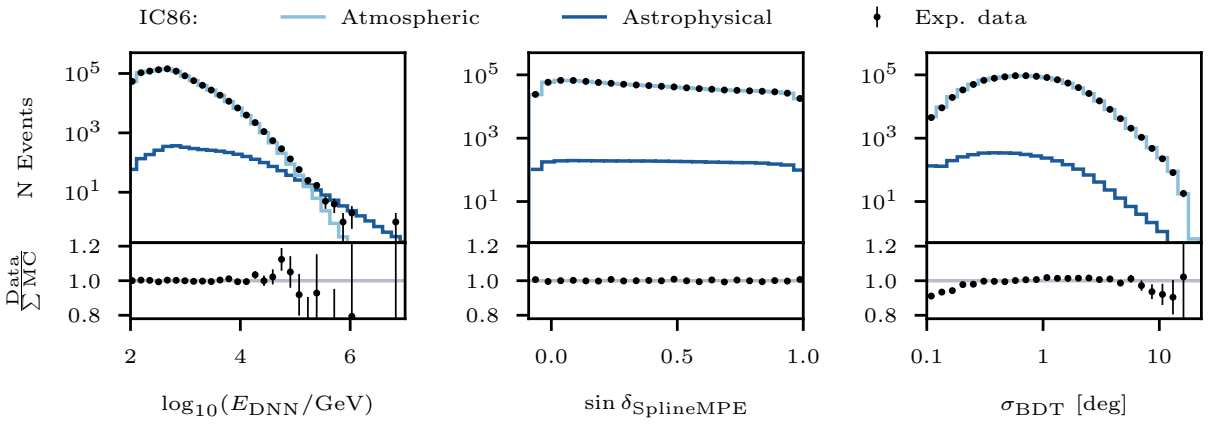


Figure 4.14: Data-MC agreement for the IC86 seasons in the reconstructed muon observables: the DNN energy, the SplineMPE declination, and the $\sigma_{\mathrm{BDT}}$ angular uncertainty. In the upper panel, the black dots and error bars represent the experimental data with statistical uncertainties, while the blue and light blue histograms show the expected atmospheric and astrophysical neutrino fluxes. Simulations assume the baseline ice configuration and DOM efficiency. The lower panel shows the ratio agreement between the experimental data and the sum of the two simulated flux components.

The slight overestimation of events with $\sigma_{\mathrm{BDT}} \lesssim 0.2^\circ$ in simulations compared to data is due to an excess of MC events with energy below 500 GeV which unexpectedly have good angular resolution according to the BDT estimator. However, these low-energy events have a large kinematic angle between the parent neutrino and the secondary muon. Hence, when this additional uncertainty is taken into account, the total angular uncertainty is

$$\sigma_{\mathrm{tot}} = \sqrt{\sigma_{\mathrm{BDT}}^2 + \psi_{\nu\mu}^2} \tag{4.16}$$

and the median value of $\sigma_{\mathrm{tot}}$ increases to $\sim 0.5^\circ$. Hence, the point spread function of these mis-reconstructed events becomes extremely wide and flat,[84] and their contribution to a point-source signal is washed out, together with the overall effect of the slight disagreement between data and MC which becomes negligible.

[84] The point spread function of the point-source analysis is discussed in Section 5.1.

### 4.7.2 *Simulations of the IC79 detector*

The IC79 data sample is added for the first time in this work.[85] A high-statistics sample of MC simulations ($\mathcal{O}(10^7)$) does not exist for this detector configuration. Generating a large amount of new simulations for an old dataset is very resource- and time-consuming. However, the IC79 detector is almost as big as IC86, as their InIce Arrays differ by five strings only, as visible in the left panel of Figure 4.15. Hence, including it in the data sample is almost as convenient as adding one more year of complete detector configuration.

Although the two detector configurations are similar, the distributions of MC events in the IC86 detector do not match the experimental data from the IC79 detector. This is especially true for the reconstructed energy distribution. In fact, events whose light could

[85] Bellenghi, Ha Minh, et al., "Extending the IceCube search for neutrino point sources in the Northern sky with additional years of data".

be detected by the newest five strings might have a different muon energy on detector entry, *i.e.*, the energy proxy predicted by the DNN (see Subsection 4.6.2), depending on whether those strings are there or not. In general, IC79 data are expected to show a distribution of muon energies slightly shifted to lower energies compared to IC86 data. This is visualized in the right panel of Figure 4.15, where the muon energy on detector entry of MC events in the IC79 detector has been calculated by removing the additional strings from the IC86 detector geometry. As expected, for a given event, $E^{\text{entry}}_{\mu,\text{IC79}} \leq E^{\text{entry}}_{\mu,\text{IC86}}$.

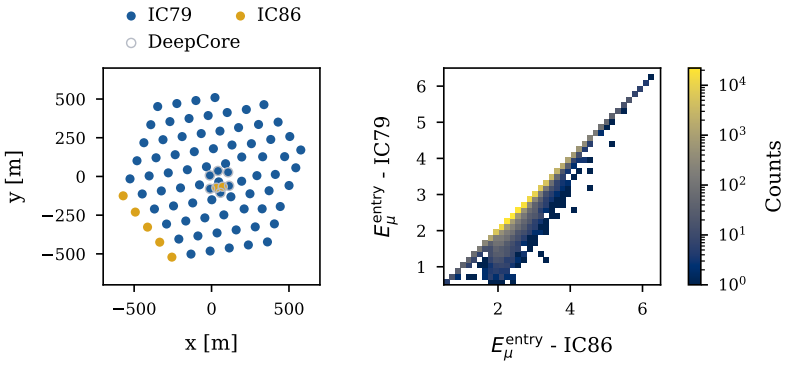


Figure 4.15: **Left:** Disposition of the strings in the IceCube coordinate system. The yellow dots mark the last seven strings added, which changed the detector from the IC79 to the IC86 configuration. For this work, only the five strings added to the edge of the detector are relevant, as the other two are part of the DeepCore detector (dots outlined in grey), which is excluded from the analysis. **Right:** The muon energy on detector entry for the same simulated events in the IC79 detector and in the IC86 detector. The color scale represents the number of events per bin. Approximately 14% of the simulated events have a lower muon energy in the IC79 configuration.

Therefore, IC86 MC simulations cannot be used to describe the distribution of IC79 data. To circumvent this problem, we generate a sample of IC79 MC simulations by re-applying the processing pipeline described in Section 4.4 to the IC86 simulations, starting from Level 2, after removing all pulses recorded by the last-added five strings. Subsequently, the DNN energy and BDT angular uncertainty reconstructions are applied to the obtained IC79 simulations.

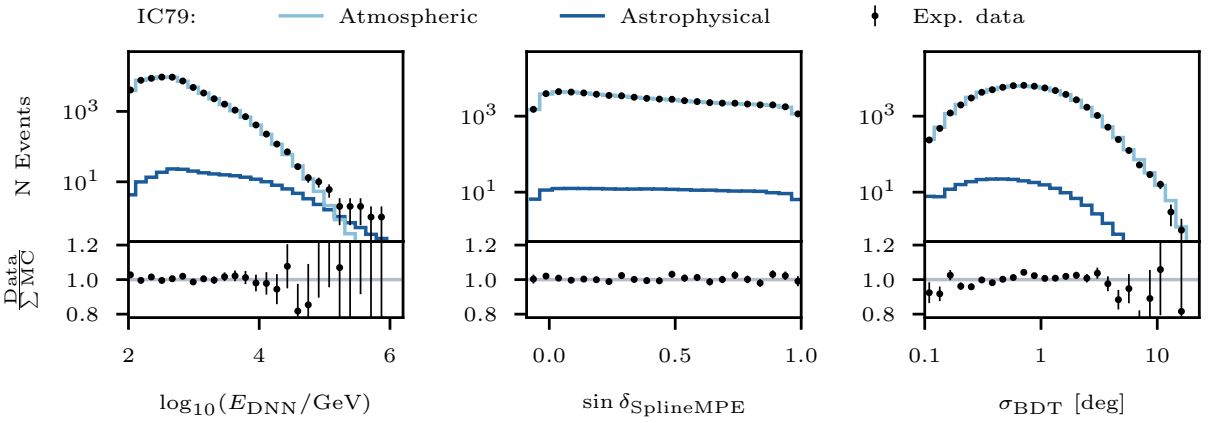


Figure 4.16: Data-MC agreement for the IC79 season in the reconstructed muon observables: the DNN energy, the SplineMPE declination, and the $\sigma_{\text{BDT}}$ angular uncertainty. See Figure 4.14 for more details.

The agreement of data with MC simulations for the IC79 detector configuration is shown in Figure 4.16. Since a well satisfactory agreement is also reached for this data sample, we can include it in the point-source analysis described in Chapter 5, which is performed on the combined IC79 + IC86 dataset.

### 4.7.3 *Neutrino detection efficiency*

An important figure of merit in evaluating the sensitivity of a data sample to a neutrino signal is the detection efficiency. The number of neutrinos in an energy range $\Delta E$ that IceCube detects from a given neutrino flux, in a certain time interval $\Delta T$, and from a solid angle in the sky $\Delta\Omega$, is a function of the detector *effective area* $A_{\text{eff}}$

$$N_\nu = \int_{\Delta T} \mathrm{d}t \int_{\Delta\Omega} \mathrm{d}\Omega \int_{\delta E} \mathrm{d}E A_{\text{eff}}(E,\delta) \frac{\mathrm{d}^3\phi_\nu}{\mathrm{d}t\mathrm{d}\Omega\mathrm{d}E} \tag{4.17}$$

$A_{\text{eff}}$ varies depending on the incoming neutrino energy and declination, while the dependence on the right ascension is negligible due to IceCube's location at the South Pole. Furthermore, it encompasses information on the geometrical acceptance of the detector, the effects related to the flavor- and declination-dependent neutrino propagation through the Earth, and the interaction probability. As $\nu$ and $\bar{\nu}$ are indistinguishable in the detector, the effective area accounts for both.

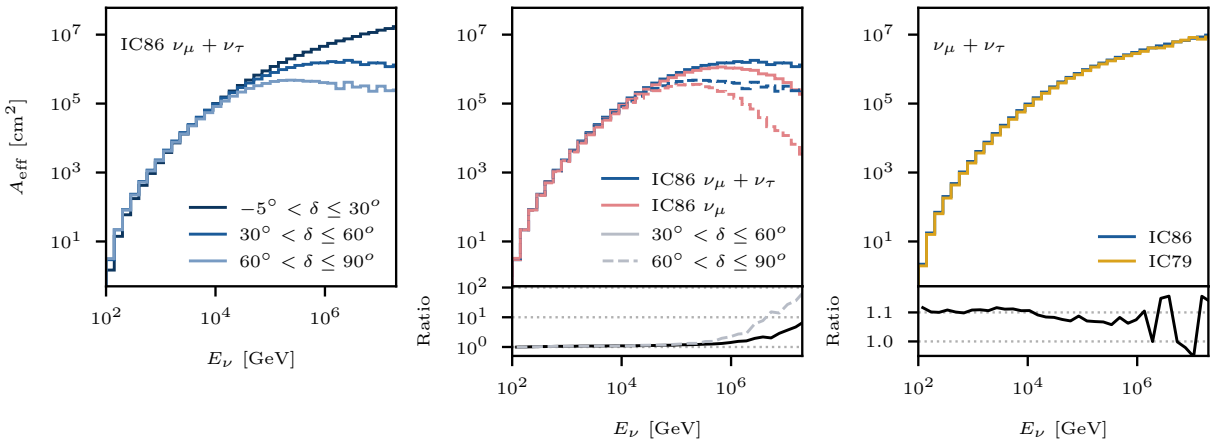


Figure 4.17: Simulated effective area of the up-going muon sample as a function of the neutrino energy. **Left:** Effective area of the IC86 detector shown for three different declination bands in the Northern sky. Towards the pole, the absorption of $\nu_\mu$ neutrinos in the Earth slows down the increase of the effective area with increasing neutrino energy. **Center:** Above 30° declination, the effective area to $\nu_\mu$ and $\nu_\tau$ (blue) is $10 - 100$ times higher than the effective area to $\nu_\mu$ only (blue) at PeV energies and beyond (lower panel). **Right:** Effective area comparison between IC86 and the down-selected IC79 sample. The larger IC86 detector volume translates into a $\sim 10\%$ larger effective area (lower panel).

The effective area of the IC86 data sample is shown in the left panel of Figure 4.17 for three different solid angles. The central panel of the same figure illustrates how the contribution from the regenerated $\nu_\tau$ flux improves the detector acceptance at high energies and declinations. Finally, in the right panel of Figure 4.17, the effective areas of the IC79 and IC86 detectors integrated over the entire Northern hemisphere $(-5^\circ < \delta < 90^\circ)$ are compared. The larger IC86 detector volume translates into a $\sim 10\%$ larger effective area.

## 4.8 Realtime issue of neutrino alerts

Many astrophysical sources exhibit significant time variability in the electromagnetic spectrum. Therefore, timely or coincident observations are crucial to identifying transient phenomena. With an uptime $> 99\%$ and the possibility to constantly observe the entire sky, Icecube is the ideal instrument to prompt follow-up observations of other observatories.

Since 2016, IceCube has deployed a real-time alert system for communicating the detection of well-reconstructed, high-energy neutrinos that have a high probability of being of astrophysical origin. When one of these events is detected, it is necessary to reconstruct its properties quickly using fast algorithms. The overall quality regarding angular resolution, energy, and topology is evaluated. If the event passes all the selection criteria,[86] a notice is sent to the Gamma-ray Coordinated Network[87] (GCN) via the Astrophysical Multi-Messenger Observatory Network[88] (AMON) within approximately 33 seconds. Consequently, follow-up observations from other instruments are triggered. The first directional reconstruction uses the "fast" configuration of the SplineMPE algorithm, which needs fewer steps in optimization compared to the "max" configuration used for the up-going muon track selection (see Subsection 4.5.1).[89]

After the GCN notice is sent out, *alert* events are reconstructed more precisely using slower, more sophisticated algorithms[90] different from those used for the up-going neutrino sample for point-source searches (see Subsection 4.5.1 and Section 4.6). This refined event information is then circulated as an update to the initial GCN notice. Track-like alerts with refined reconstructed properties are collected in the IceCube Event Catalog of Alert Tracks (IceCat)[91].

Alert events that pass the event selection criteria described in Section 4.4 will be included in the sample of up-going muon tracks used to search for neutrino point-like sources in the analysis described in Chapter 5 and Section 8.2. As for all other events in the sample, their direction and energy observables are reconstructed using the "max" SplineMPE algorithm in Subsection 4.5.1 and the DNN energy estimator in Subsection 4.6.2.

[86] Blaufuss et al., "The Next Generation of IceCube Real-time Neutrino Alerts"

[87] https://gcn.gsfc.nasa.gov/

[88] Smith et al., "The Astrophysical Multimessenger Observatory Network (AMON)"

[89] The main features of the "max" SplineMPE algorithm that are not included in the "fast" configuration are an accurate noise modeling and the convolution of the MPE likelihood with an energy-dependent Gaussian function (Abbasi et al., "A muon-track reconstruction exploiting stochastic losses for large-scale Cherenkov detectors").

[90] Aartsen et al., "Energy reconstruction methods in the IceCube neutrino telescope"

[91] Abbasi et al., "IceCat-1: The IceCube Event Catalog of Alert Tracks" and Abbasi et al., "Erratum: "IceCat-1: The IceCube Event Catalog of Alert Tracks" (2023, ApJS, 269, 25)"

# 5 Methods to Search for Neutrino Point-like Sources

Soon after its completion in 2011, IceCube fulfilled its primary scientific mission of observing a diffuse flux of high-energy astrophysical neutrinos.[1] Since then, major efforts have been devoted to searching for the sources of this flux. Over the years, the increased amount of recorded data has improved the sensitivity of IceCube to astrophysical signals from point sources, lowering the flux threshold for discovery by over an order of magnitude, as shown in the right panel of Figure 5.1. In a background-dominated experiment, the linear growth of the number of signal events in time is penalized by background fluctuations, which are expected to grow proportionally to the inverse of the square root of the exposure time. In a background-free experiment, *e.g.*, with perfect angular resolution or at high energies where the atmospheric background vanishes, the sensitivity improvement is only limited by the linear signal growth. Hence, it scales proportionally to the inverse of the exposure time.

[1] IceCube Collaboration, "Evidence for High-Energy Extraterrestrial Neutrinos at the IceCube Detector".

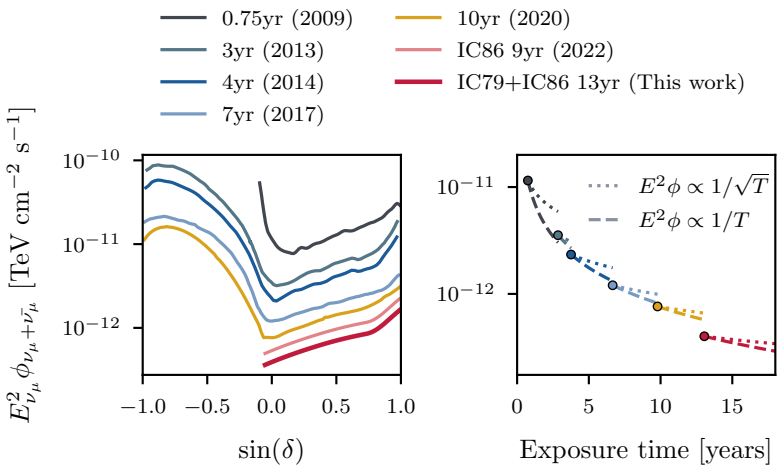


Figure 5.1: Improvement over the years of the average $\nu_\mu$ flux that IceCube needs for a $5\sigma$ discovery (pre-trial) assuming $E^{-2}$ neutrino emission. **Left:** Discovery potential as a function of the source declination. Each color represents a different point-source analysis. The lowest flux shown as a thicker red line is produced in this work, as described in more detail in this chapter. **Right:** Discovery potential at $\delta = 0°$ as a function of increasing exposure time $T$. Each dot represents a different analysis. The dotted and dashed lines represent the evolution of the discovery potential, assuming it scales as $\sqrt{1/T}$ and $1/T$, respectively. For clarity, the 9-year (2022) analysis is omitted. This work extends the 9-year analysis to 13 years of exposure while sharing the same selection, reconstructions, and methods with it. See the text for more details and the following hyperlinks for references: 0.75yr (2009), 3yr (2013), 4yr (2014), 7yr (2017), 10yr (2020), 9yr (2022).

Figure 5.1 shows the evolution over time of the $5\sigma$ discovery threshold of IceCube to an $E^{-2}$ muon neutrino spectrum. Several factors have contributed to improving the discovery potential beyond the extreme case of a background-free experiment, including

the completion of the 86-string detector, refinements in the event selection and reconstruction procedures, and improved analysis methods.

In this chapter, we provide a review of the unbinned maximum likelihood method[2] that is widely used in neutrino astronomy to search for point-like neutrino emission[3]. The more accurate likelihood modeling that was introduced in a previous work[4,5] provides a robust characterization of the source energy spectrum by ensuring mostly unbiased fit parameters. Afterward, we discuss the performance of the likelihood analysis on 13 years of up-going muon tracks, the data sample introduced in Section 4.7, which includes one year of data taken with the 79-string detector configuration (IC79) and 12 years of data from the complete IceCube detector (IC86). The last section outlines the procedure for producing a significance map of neutrino emission in the Northern sky. The results of the point-source analysis on 13 years of IceCube data described in this chapter are discussed in Section 8.2.

[2] Braun et al., "Methods for point source analysis in high energy neutrino telescopes"

[3] See, for example, any of the references in Figure 5.1, but also, *e.g.*, Adrián-Martínez et al., "First Search for Point Sources of High-energy Cosmic Neutrinos with the ANTARES Neutrino Telescope".

[4] Abbasi et al., "Evidence for neutrino emission from the nearby active galaxy NGC 1068".

[5] Glauch, "The Origin of High-Energy Cosmic Particles: IceCube Neutrinos and the Blazar Case".

## 5.1 Hypothesis test

Point-like sources are expected to produce clusters of astrophysical events over the atmospheric and diffuse astrophysical backgrounds. Hence, given the sample of the observed events, the point-source analysis compares the likelihood of a background-only hypothesis to the likelihood of a signal + background hypothesis and tries to discriminate the two.

Given an hypothesis defined by a set of parameters $\boldsymbol{\theta}$, the unbinned likelihood of the observed data $\boldsymbol{x}$ is

$$\mathcal{L}(\boldsymbol{\theta}|\boldsymbol{x}) = \prod_i f(x_i|\boldsymbol{\theta}). \tag{5.1}$$

$f(x_i|\boldsymbol{\theta})$ is the probability density function (PDF) of the $i$-th observation $x_i$ given the hypothesis. The product is taken over all observations $x_i$.

The two alternative hypotheses we compare in the point-source analysis are:

- $H_0 : \boldsymbol{\theta} = \boldsymbol{\theta}_\mathrm{b}$ – The observed data solely consists of background events induced by the atmospheric or the astrophysical diffuse neutrino fluxes.[6] Throughout the thesis, we will refer to $H_0$ as the *null* or *background-only* hypothesis.

- $H_1 : \boldsymbol{\theta} = \boldsymbol{\theta}_\mathrm{s}$ – The observed data consists of both background and signal events, where the latter are induced by the interaction of astrophysical neutrinos originating from a point-like neutrino source, located at $\boldsymbol{r}_\mathrm{src} = (\alpha_\mathrm{src}, \delta_\mathrm{src})$[7]. The source spectrum is described by an unbroken power law $\phi(E) = \phi_0 \times E^{-\gamma}$. We will refer to $H_1$ as the *alternative* or *signal* hypothesis.

[6] The background of atmospheric muons is suppressed through Earth absorption when looking at up-going muon tracks only. See Section 4.4.

[7] $\alpha_\mathrm{src}$ and $\delta_\mathrm{src}$ are the source right ascension and declination in equatorial coordinates, respectively.

Assumptions about the source spectral shape are not necessarily limited to the unbroken power law. However, in Section 8.2, we will discuss the results of point-source analyses based on the power-law hypothesis. Hence, we limit the discussion to this spectrum here as well.

The comparison between the two hypotheses is formalized as the ratio of the respective likelihoods

$$\Lambda = \frac{\sup_{\theta \in \boldsymbol{\theta}_\mathrm{b}} \mathcal{L}(\theta|\boldsymbol{x})}{\sup_{\theta \in \boldsymbol{\theta}_\mathrm{s}} \mathcal{L}(\theta|\boldsymbol{x})}, \tag{5.2}$$

where the supremum is taken over all parameters $\theta$ describing each hypothesis.

The background-only hypothesis fixes the atmospheric and astrophysical diffuse event rates; hence, there are no free parameters in $\boldsymbol{\theta}_\mathrm{b}$. Given a source located at $\boldsymbol{r}_\mathrm{src}$, the signal hypothesis is described by the set of parameters are $\boldsymbol{\theta}_\mathrm{s} = (\alpha_\mathrm{src}, \delta_\mathrm{src}, \phi_0, \gamma)$, where $\phi_0$ and $\gamma$ are fitted to the data. The flux normalization $\phi_0$ is related to the expected number of signal events in the detector $n_\mathrm{s}$ over the exposure time $T$ via the event rate equation:[8]

[8] See Subsection 4.7.3.

$$n_\mathrm{s} = T \int_0^\infty dE_\nu A_\mathrm{eff}(E_\nu, \delta_\mathrm{src}) \times \phi_0(E_\nu). \tag{5.3}$$

Similarly, given a background flux, one can derive the expected number of background events in the detector $n_\mathrm{b}$. Note that Equation 5.3 is the same as Equation 4.17, where the solid angle $\Delta\Omega$ is a $\delta$-function because of the point-like nature of the source. The likelihood function is commonly represented as a mixture model consisting of a signal PDF $f(\boldsymbol{x}|\boldsymbol{\theta}_\mathrm{s})$ and a background PDF $f(\boldsymbol{x}|\boldsymbol{\theta}_\mathrm{b})$, each weighted by the expected frequency of background and signal events.[9] The total number of events in a sample is expected to follow a Poisson distribution $N \sim Poisson(n_\mathrm{s} + n_\mathrm{b})$. This term extends the likelihood function to account for fluctuations in the number of events. Therefore, the extended point-source likelihood reads

[9] Braun et al., "Methods for point source analysis in high energy neutrino telescopes".

$$\begin{aligned}\mathcal{L}(\boldsymbol{\theta}|\boldsymbol{x}) = &\frac{(n_\mathrm{s} + n_\mathrm{b})^N}{N!} e^{-(n_\mathrm{s}+n_\mathrm{b})} \\ &\times \prod_i^N \left\{ \frac{n_\mathrm{s}}{n_\mathrm{s}+n_\mathrm{b}} f_\mathrm{s}\left(x_i|\boldsymbol{\theta}_\mathrm{s}\right) + \frac{n_\mathrm{b}}{n_\mathrm{s}+n_\mathrm{b}} f_\mathrm{b}\left(x_i|\boldsymbol{\theta}_\mathrm{b}\right) \right\}.\end{aligned} \tag{5.4}$$

For $n_\mathrm{s} = 0$, the signal hypothesis reduces to the background-only one.[10] Hence, the two hypotheses are nested, and Wilks' theorem is valid. According to Wilks' theorem, for a large sample size $N \to \infty$, the negative logarithm of the likelihood-ratio in Equation 5.2 assuming the null-hypothesis to be true asymptotically approaches a $\chi^2$-distribution with number of degrees of freedom ($n_\mathrm{dof}$) given by the difference between the number of free parameters in $H_1$ and $H_0$[11]:

[10] Assuming $n_\mathrm{b} \sim N$ in the background-only hypothesis.

[11] Wilks, "The Large-Sample Distribution of the Likelihood Ratio for Testing Composite Hypotheses". See also Appendix C.6.

$$TS = -2 \log \Lambda \to \chi^2_2, \tag{5.5}$$

where $\chi^2_2$ is the $\chi^2$-distribution with $n_\mathrm{dof} = 2$. Equation 5.5 gives the expression for the *test-statistic TS* of the point-source analysis.

Putting together Equation 5.5 and Equation 5.4, and recalling that $n_s = 0$ in the background-only hypothesis, we can rewrite the $TS$ expression as

$$TS = 2\sum_{i}^{N} \log\left\{\frac{\hat{n}_s}{N}\left(\frac{f_s\left(x_i|\boldsymbol{\theta}_s\right)}{f_b\left(x_i\,|\,\boldsymbol{\theta}_b\right)} - 1\right) + 1\right\}, \tag{5.6}$$

which depends on the ratio of the signal and background PDFs. Here, $\hat{n}_s$ and $\hat{\gamma}$ denote the optimized values of the two parameters, which maximize the $TS$. Note that in Equation 5.6, we have also used the fact that background events from the atmospheric flux dominate our data sample. Hence, $n_b \sim N$, and the ratio of the leading Poisson terms in the two likelihoods is $\sim 1$.

We perform a two-dataset likelihood analysis by including IC79 and IC86 neutrino data. Although the data processing is the same for both samples, the distribution of their observables is different. This difference is primarily due to a mismatch in the reconstructed muon energy caused by the five missing strings in the InIce Array of the IC79 detector configuration, as discussed in Subsection 4.7.2. Therefore, the $TS$ in Equation 5.6 needs to be evaluated separately for each sample $j$, which has its own dataset-specific PDFs. The sum of the single dataset contributions gives the total $TS$:

$$TS = 2\sum_{j}\sum_{i}^{N} \log\left\{\frac{\hat{n}_s^j}{N}\left(\frac{f_s^j\left(x_i|\boldsymbol{\theta}_s\right)}{f_b^j\left(x_i\,|\,\boldsymbol{\theta}_b\right)} - 1\right) + 1\right\}. \tag{5.7}$$

The expected total number of signal events $\hat{n}_s$ splits into a contribution from each dataset $\hat{n}_s^j$ based on the corresponding detector event rate equation

$$\begin{aligned}\hat{n}_s^j &= \hat{n}_s \times \frac{T^j \int_0^\infty dE_\nu A_{\text{eff}}^j(E_\nu, \delta_{\text{src}}) \times \phi_0(E_\nu)}{\sum_j T^j \int_0^\infty dE_\nu A_{\text{eff}}^j(E_\nu, \delta_{\text{src}}) \times \phi_0(E_\nu)} \\ &\equiv \hat{n}_s \times K_j(\delta_{\text{src}}, \gamma).\end{aligned} \tag{5.8}$$

Each $\hat{n}_s^j$ is a fraction $K_j(\delta_{\text{src}}, \gamma)$ of the total number of expected signal events in the sample, with $\sum_j K_j(\delta_{\text{src}}, \gamma) = 1$. Therefore, the total $TS$ in Equation 5.7 remains a function of two parameters only: the total number of signal events and the spectral index.

## 5.2 Signal and background PDFs

The two fundamental observables in searches for astrophysical neutrino sources are the events' energy and direction. An estimate of the directional reconstruction quality provides additional information. These observables characterize each recorded event $x_i$, and the signal and background PDFs in Equation 5.4 describe their distribution under the signal and background-only hypothesis, respectively.

For each event in the up-going tracks sample used in this work,[12] the muon energy $E_\mu$, its direction $\boldsymbol{r}_\mu = (\alpha_\mu, \delta_\mu)$, and the uncertainty on the reconstructed muon direction $\sigma_\mu$ are estimated. $\sigma_\mu$ (given

[12] See Section 4.4 and Section 4.7 for details about the dataset.

by the BDT estimator described in Subsection 4.5.2) relates to the total angular uncertainty $\sigma$ between the parent neutrino and the true muon—which is used in the likelihood—once the energy-dependent kinematic angle between the two is considered (see Equation 4.13):

$$\sigma = \sqrt{\sigma^2_{\mu,\mathrm{BDT}} + \psi^2_{\nu\mu,\mathrm{kin}}}. \tag{5.9}$$

The background-only hypothesis assumes an isotropic background flux composed of atmospheric and astrophysical neutrinos. Once these two background rates are determined by the choice of atmospheric and astrophysical flux models, $\boldsymbol{\theta}_\mathrm{b}$ is fixed, and the background PDF does not depend on any free parameters. Moreover, the background PDF is uniform in right ascension due to IceCube's location at the Geographic South Pole. Hence, it only depends on the events declination and reads as follows:

$$f_\mathrm{b}\left(x|\boldsymbol{\theta}_\mathrm{b}\right) = \frac{1}{2\pi} f_\mathrm{b}\left(E_\mu, \sin\delta_\mu, \sigma|\boldsymbol{\theta}_\mathrm{b}\right). \tag{5.10}$$

Using the law of total probability, we can separate the term describing the angular uncertainty:

$$\frac{1}{2\pi} f_\mathrm{b}\left(E_\mu, \sin\delta_\mu, \sigma|\boldsymbol{\theta}_\mathrm{b}\right) = \frac{1}{2\pi} f_\mathrm{b}\left(E_\mu, \sin\delta_\mu|\boldsymbol{\theta}_\mathrm{b}\right) \cdot f_\mathrm{b}\left(\sigma|E_\mu, \sin\delta_\mu, \boldsymbol{\theta}_\mathrm{b}\right). \tag{5.11}$$

The signal PDF depends on the source hypothesis, including the source location. The spectral index $\gamma$ is treated as a free parameter, and the signal PDF conditionally depends on it. The flux normalization, translated into the expected number of signal events in the detector $n_\mathrm{s}$, enters the relative strength of signal and background in Equation 5.4, and is not part of the definition of $f_\mathrm{s}\left(x|\boldsymbol{\theta}_\mathrm{s}\right)$, which reads:

$$\begin{aligned} f_\mathrm{s}\left(x|\boldsymbol{\theta}_\mathrm{s}\right) &= f_\mathrm{s}\left(E_\mu, \boldsymbol{r}_\mu, \sigma|\boldsymbol{r}_\mathrm{src}, \gamma\right) \\ &= \frac{1}{2\pi\sin\psi} f_\mathrm{s}\left(E_\mu, \psi, \sigma|\delta_\mathrm{src}, \gamma\right). \end{aligned} \tag{5.12}$$

Events from a point-like source are expected to cluster around the source location. Hence, in Equation 5.12, the relevant spatial observable is the angular distance between source and reconstruction $\psi = \sphericalangle(\boldsymbol{r}_\mathrm{src}, \boldsymbol{r}_\mu) \equiv \sphericalangle(\boldsymbol{r}_\nu, \boldsymbol{r}_\mu)$, which absorbs the dependence on the source's right ascension.[13] A conditional dependence on the source declination is left due to IceCube's anisotropic acceptance as a function of the incoming neutrino energy and declination. The $1/(2\pi\sin\psi)$ factor ensures the normalization of $f_\mathrm{s}$ on the sphere.

[13] In the last equivalence, we replaced the direction of the source with the direction of the neutrino it produces.

Similarly to the background PDF, we can split the signal PDF into spatial, energy, and angular uncertainty terms:

$$\begin{aligned} &\frac{1}{2\pi\sin\psi} f_\mathrm{s}\left(E_\mu, \psi, \sigma|\delta_\mathrm{src}, \gamma\right) = \\ &\qquad \frac{1}{2\pi\sin\psi} f_\mathrm{s}\left(\psi|E_\mu, \sigma, \gamma\right) \cdot f_\mathrm{s}\left(E_\mu|\delta_\mathrm{src}, \gamma\right) \cdot f_\mathrm{s}\left(\sigma|E_\mu, \delta_\mathrm{src}, \gamma\right) \end{aligned} \tag{5.13}$$

The angular uncertainty PDF term depends only weakly on the source spectral index $\gamma$, as shown in the left panel of Figure 5.2. If we neglect this dependence, the angular uncertainty PDF in Equation 5.13 only depends on the reconstructed track energy and source location. The right panel of Figure 5.2 shows that the probability distribution of the angular uncertainty changes minimally when the source declination is replaced by the reconstructed muon declination. These two considerations lead to the approximation

$$f_s\left(\sigma|E_\mu, \delta_{src}, \gamma\right) \sim f_b\left(\sigma|E_\mu, \sin\delta_\mu, \boldsymbol{\theta}_b\right). \tag{5.14}$$

Hence, the signal and background contributions from the angular uncertainty distributions cancel out in the *TS* in Equation 5.6. While keeping all terms in the likelihood to ensure the most accurate description of the events would be preferable, this approximation reduces the likelihood's dimensions.

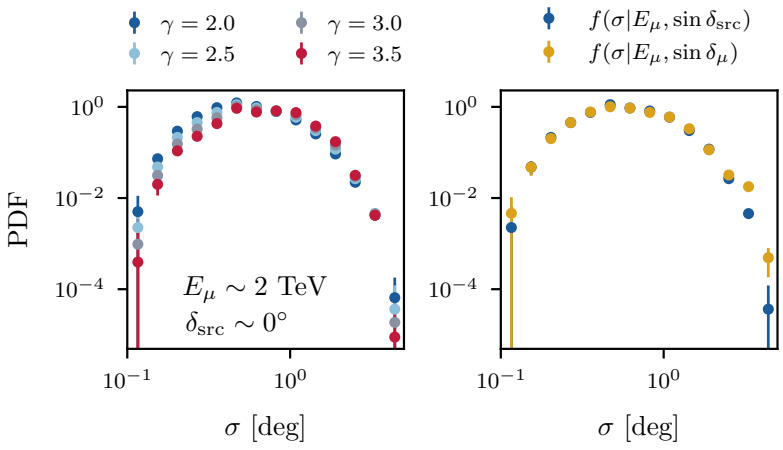


Figure 5.2: Probability distribution of the angular uncertainty between the neutrino and the reconstructed track. As an example, the distribution is shown at source declination $\delta_{src} \sim 0°$ and reconstructed energy $E_\mu$ 2 TeV. **Left:** The angular uncertainty term in the signal PDF for different spectral indices, shown as different colors. **Right:** Comparison between the angular uncertainty term in the signal PDF, depending on the source declination $\delta_{src} \sim 0°$, and in the background PDF, depending on the reconstructed muon declination $\delta_\mu \sim 0°$. Differences are minimal; hence, the approximate equality of the two terms holds, and they cancel out in the PDF ratio.

As a result, we are left with a two-dimensional background PDF in the reconstructed energy-declination parameter space

$$f_b\left(x|\boldsymbol{\theta}_b\right) = \frac{1}{2\pi} f_b\left(E_\mu, \sin\delta_\mu|\boldsymbol{\theta}_b\right), \tag{5.15}$$

and a signal PDF that is split into a spatial ($\mathcal{S}$) and energy ($\mathcal{E}$) term

$$f_s\left(x|\delta_{src}, \gamma\right) = \mathcal{S}\left(\psi|E_\mu, \sigma, \gamma\right) \cdot \mathcal{E}\left(E_\mu|\delta_{src}, \gamma\right). \tag{5.16}$$

### 5.2.1 *Analytical versus non-parametric description*

In the assumption that events coming from a point-like source should be distributed around the source location, a simple and reasonable analytical approximation for the spatial part of the signal PDF is a two-dimensional Gaussian distribution around the direction of the source[14,15,16]

$$\mathcal{S}\left(\psi|E_\mu, \sigma, \gamma\right) \sim \mathcal{S}\left(\psi|\sigma\right) = \frac{1}{2\pi\sigma^2} e^{\frac{-\psi^2}{2\pi\sigma^2}}. \tag{5.17}$$

[14] Braun et al., "Methods for point source analysis in high energy neutrino telescopes".

[15] Aartsen et al., "All-sky Search for Time-integrated Neutrino Emission from Astrophysical Sources with 7 yr of IceCube Data".

[16] Aartsen et al., "Time-Integrated Neutrino Source Searches with 10 Years of IceCube Data".

However, this approximation neglects the dependence of $\mathcal{S}$ on the spectral index $\gamma$ and on the reconstructed energy $E_\mu$.[17] The limited accuracy of the Gaussian approximation introduces biases in the fit parameters $\hat{n}_s$ and $\hat{\gamma}$.

In general, the optimized values that maximize the likelihood ($\hat{n}_s$ and $\hat{\gamma}$ in our case) are known as *maximum likelihood estimators* (MLEs). One property of MLEs is their *consistency*, meaning that they converge to their true value as soon as the sample size tends to infinity.[18] Therefore, consistency is a desirable MLE property when one wants to characterize the source spectrum based on the best-fit values of $\hat{n}_s$ and $\hat{\gamma}$. However, model misspecifications can produce biases in the MLEs, caused by incorrect assumptions about the data distribution.

One way of improving the PDF modeling is by inferring the distributions from Monte Carlo (MC) simulations using non-parametric, numerical methods. Recent works[19] have introduced PDF inference via *kernel density estimation* (KDE), a non-parametric technique used to estimate the probability density function of a random variable. KDEs do not rely on any assumption about data distribution, thus allowing for more flexibility in the modeling. For each spectral index $\gamma$, a large set of MC events is weighted according to an $E^{-\gamma}$ neutrino energy spectrum. The conditional spatial and energy PDFs in Equation 5.16 are then modeled through a KDE approximation of the corresponding MC distributions, yielding multi-dimensional KDEs for each spectral index $\gamma$. In this work, KDEs for the signal likelihood are constructed for $\gamma \in [0.52, 4.52]$ in steps of 0.05. Penalized B-splines[20] are used to store the multidimensional signal spatial ($\mathcal{S}(\gamma)$) and energy ($\mathcal{E}(\gamma)$) PDFs, including the $\gamma$ dimension. The KDE PDF construction is done separately for the IC79 and IC86 samples for the reasons mentioned above[21].

Figure 5.3 shows the result of the signal spatial PDF modeling with KDEs for the IC86 dataset. The PDF includes the conditional dependence on the spectral index and the explicit conditional dependence on the reconstructed muon energy. Compared to the Reyleigh approximation,[22] the KDE functions describe the expected spatial distribution of signal events more accurately for both hard and soft spectra. Especially at energies $< 10$ TeV, the KDE approximation can reproduce the long tail of events reconstructed further from the source location. Furthermore, thanks to the weighting of the PDF according to the source spectrum, the PDFs can account for the different probabilities of obtaining low-energy events, which are expected to have lower reconstruction quality estimates $\sigma_\mu$ and, therefore, to be reconstructed at larger angular distances. While hard spectra and high-energy events are generally well described by the bivariate Gaussian approximation, the characterization of the neutrino signal from sources emitting soft energy spectra, with most of the events reconstructed at TeV energies, largely benefits from the improved modeling of the PDFs. As discussed in Chapter 3, the most significant extragalactic neutrino source detected to date, NGC 1068, shows a soft neutrino spectrum with spectral index $\gamma \simeq 3.2$.[23] Therefore, a

[17] The angular uncertainty $\sigma$ introduces a partial dependence on the reconstructed energy through the inclusion of the kinematic angle.

[18] Casella and Berger, "Statistical Inference".

[19] Abbasi et al., "Evidence for neutrino emission from the nearby active galaxy NGC 1068".

[20] Whitehorn, van Santen, and Lafebre, "Penalized splines for smooth representation of high-dimensional Monte Carlo datasets"

[21] A full description of the KDE generation pipeline using the *Meerkat* package (Poluektov, "Kernel density estimation of a multidimensional efficiency profile") can be found in chapter 7 of Glauch, "The Origin of High-Energy Cosmic Particles: IceCube Neutrinos and the Blazar Case".

[22] The projection on the angular distance of the two-dimensional Gaussian in Equation 5.17.

[23] Abbasi et al., "Evidence for neutrino emission from the nearby active galaxy NGC 1068".

robust inference of the spectral properties given the assumed spectral shape is fundamental to reliably characterize the source spectrum. In Subsection 5.3.1, we discuss the ability of the analysis to recover the signal injection in terms of the number of signal events and spectral index.

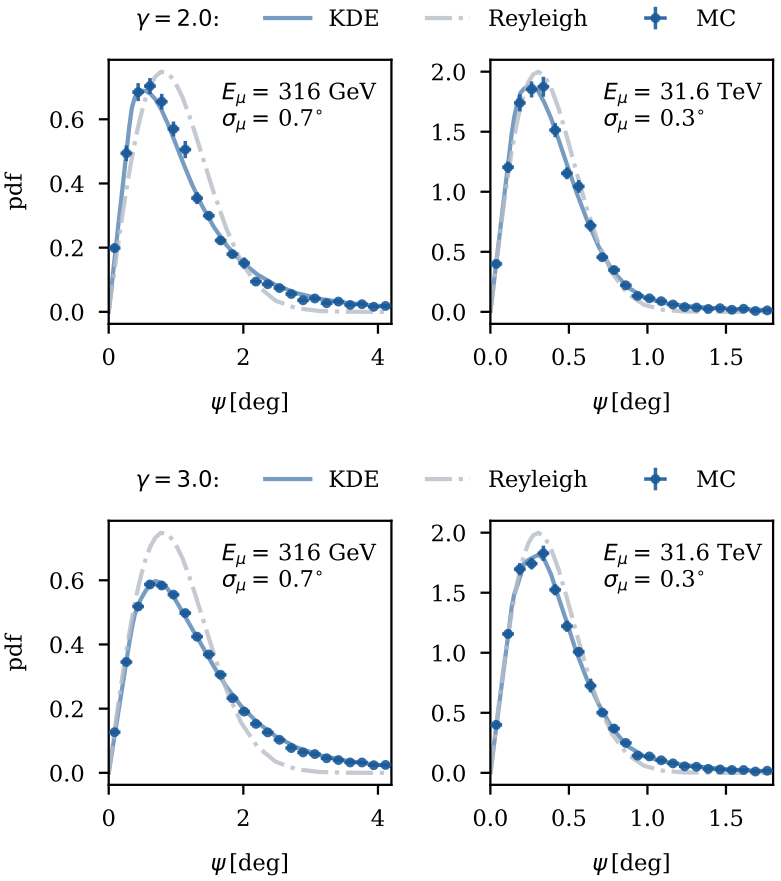


Figure 5.3: Spatial terms of the signal likelihood assuming $\gamma = 2.0$ (top) and $\gamma = 3.0$ (bottom). The distribution of the angular distance $\psi$ between the neutrino and the reconstructed muon from MC simulations of the IC86 dataset (blue points) is compared to the KDE-based PDF (solid blue line) and the Rayleigh analytical approximation (dash-dotted grey line). The conditional observables—reconstructed muon energy and reconstruction quality estimator—are given in each panel. The same plot for the IC79 season can be found in Section C.2.

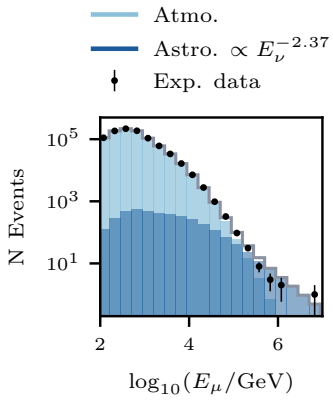


Figure 5.4: Distribution of reconstructed muon energies. The experimental data are shown as black dots with error bars corresponding to the 68% statistical uncertainty. The number of events per bin from the atmospheric and astrophysical diffuse flux expected from MC simulations is shown in light and dark blue, respectively. The sum of the two simulated background components is shown as a grey line.

[24] For example, towards the pole, where the IceCube's effective area to high energy neutrinos decreases due to Earth absorption and (see Figure 4.17), or at high energy, where the neutrino flux diminishes (see Figure 5.4).

The background PDF can, in principle, be modeled directly from the distribution of experimental data in energy and declination. At the end of the data selection process, atmospheric neutrinos dominate the sample of up-going muon tracks at all declinations (see Figure 4.8). The contribution of a single point source is negligible when constructing the background PDF. However, statistical fluctuations in the data distributions become relevant in some regions of the parameter space[24]. To address this inconvenience, the background PDF is also inferred from a large-scale sample of MC simulations, which provides better parameter space coverage. Constructing a reliable PDF based on MC requires excellent agreement between the data distribution and the simulations in the energy-declination space. At energies below a few tens of TeV, where the abundant atmospheric background dominates, we match the event rate in simulations to that observed in the data, fixing the atmospheric flux for the background-only hypothesis. In the energy range where the

astrophysical diffuse flux becomes relevant (see Figure 5.4), we assume an event rate based on the latest measurement based on muon track, resulting in $\phi^{100\text{TeV}} = 1.44 \times 10^{-18}$ GeV$^{-1}$ cm$^{-2}$ s$^{-1}$ sr$^{-1}$ and $\gamma_{\text{astro}} = 2.37$.[25] The excellent agreement in energy and declination separately has been demonstrated in Figure 4.14 and Figure 4.16 for IC86 and IC79 data, respectively. Figure 5.5 shows the two-dimensional distribution of data and weighted MC simulations, along with the ratio of the two. The agreement is almost perfect where a large amount of data is available. At the same time, data suffer from large statistical fluctuations at high energies, and the MC distribution is less constrained. However, we demonstrate in Appendix C.4 that the point-source analysis is insensitive to mismodeling of the astrophysical diffuse background component due to its subdominant contribution compared to the atmospheric background.

[25] Abbasi et al., "Improved Characterization of the Astrophysical Muon-neutrino Flux with 9.5 Years of IceCube Data"

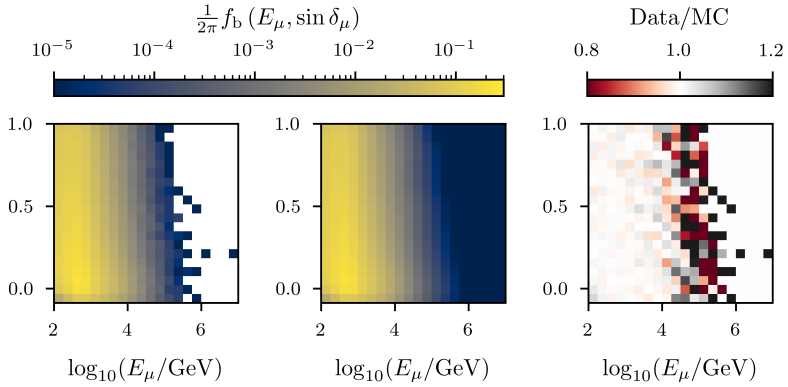


Figure 5.5: Two-dimensional density distribution of the IC86 data in energy and declination. **Left:** Distribution of the experimental data. **Center:** Weighted distribution of MC simulations. The MC distribution weights are adjusted to match the experimental data below a few tens of TeV, where the amount of data constrains the event rates with statistical accuracy. The high-energy tail of the distribution is weighted according to the latest IceCube's measurement of the astrophysical diffuse neutrino flux. See text for more details. **Right:** Agreement between data and MC simulations showed as the data/MC ratio. For the agreement in energy and declination separately, see Figure 4.14 and Figure 4.16 for the IC86 and IC79 datasets, respectively.

## 5.3 *Analysis performance*

The point-source analysis's power to detect a signal and its accuracy in characterizing the source energy spectrum are two fundamental parameters that should be studied on MC simulations before analyzing the experimental data. Due to the IceCube detector's energy- and declination-dependent effective area, the performance of the analysis can vary based on the location and energy spectrum of a point source. In this section, we report on studies of the analysis' performance in the Northern sky assuming two benchmark spectral indices for the power-law energy spectrum of the signal hypothesis: a hard spectral index $\gamma = 2.0$ and a soft one $\gamma = 3.2$, which represent two extreme cases. In particular, $\gamma = 3.2$ is the measured spectral index of the neutrino emission from NGC 1068,[26] the most significant source in the Northern sky, which will be tested again with more data in this work.[27]

[26] Abbasi et al., "Evidence for neutrino emission from the nearby active galaxy NGC 1068".

[27] The results are presented in Section 8.2.

### 5.3.1 Recovery of the injected signal

Maximum likelihood estimators are known for their consistency, meaning that as the sample size increases, the estimated parameters tend to converge to the true values, provided the likelihood function accurately represents the underlying data. This property is crucial for reliably determining the physical parameters of detected neutrino sources. We test the consistency of the signal strength and spectral index parameters on MC simulations for the exposure time of 13 years of data. We simulate point-source signals of various strengths $n_s^{inj}$ according to a power-law energy spectrum with spectral index $\gamma^{inj}$. The best-fit values from the likelihood maximization, $\hat{n}_s$ and $\hat{\gamma}$, are then compared to the injection. Figure 5.6 and Figure 5.7 show the recovery of the injected source parameters for an injection with $\gamma = 2.0$ and $\gamma = 3.2$, respectively, at two exemplary declinations.

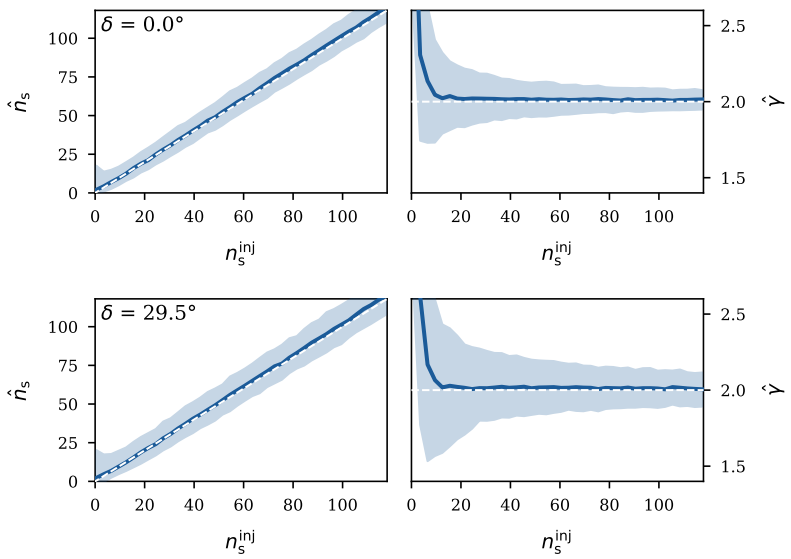


Figure 5.6: Fitted versus injected signal for a $\gamma^{inj} = 2.0$ source spectrum and two exemplary declinations, as indicated in each figure. The left plot shows the recovery of the mean number of signal events, while the right plot illustrates how well we can recover the injected spectral index. The solid line represents the median $\hat{n}_s$ and $\hat{\gamma}$ at each $n_s^{inj}$. The shaded bands show the 68% central quantiles. The ideal unbiased recovery of the parameters is shown as a dashed white line.

When a strong enough signal is injected, the source parameters converge against the true values. The performance in terms of the recovery of the injection is equally accurate across the entire Northern sky, with some biases remaining only close to the pole. Small remaining biases are likely due to remaining imperfections in the modeling, *e.g.*, the missing angular uncertainty term in the likelihood (see Section 5.1). However, the biases are smaller than the statistical uncertainty in most of the Northern sky. The trend of the biases as a function of the declination is illustrated in Figure 5.8, where two exemplary signal strengths $n_s^{inj} = 13$ and $n_s^{inj} = 91$ are injected for $\gamma^{inj} = 2.0$ and $\gamma^{inj} = 3.2$, respectively.

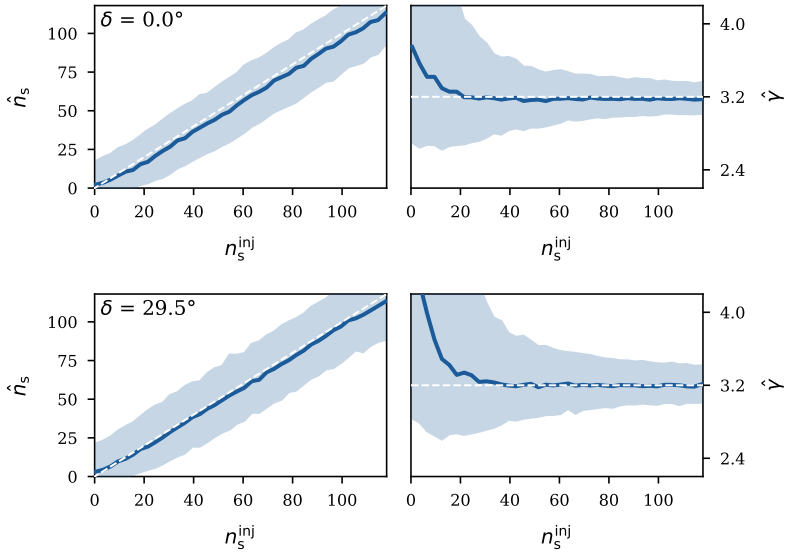


Figure 5.7: Fitted versus injected signal for a $\gamma^{inj} = 3.2$ source spectrum and two exemplary declinations, as indicated in each figure. The left plot shows the recovery of the mean number of signal events, while the right plot illustrates how well we can recover the injected spectral index. The solid line represents the median $\hat{n}_s$ and $\hat{\gamma}$ at each $n_s^{inj}$. The shaded bands show the 68% central quantiles. The ideal unbiased recovery of the parameters is shown as a dashed white line.

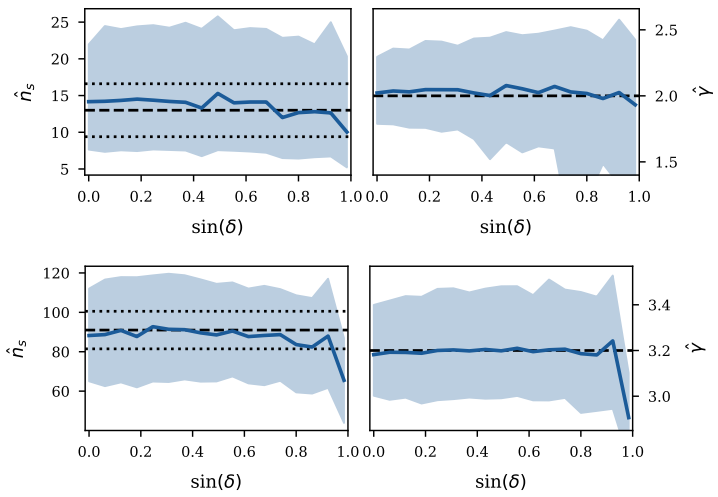


Figure 5.8: Recovery of the injected signal strength and spectral index as a function of the simulated source declination. The solid line represents the median $\hat{n}_s$ and $\hat{\gamma}$ at each $n_s^{inj}$. The shaded bands show the 68% central quantiles. The ideal unbiased recovery of the parameters is shown as a horizontal dashed white line.

### 5.3.2 *Sensitivity and discovery potential*

The outcome of the point-source analysis is the maximized test-statistic value in Equation 5.7 with the corresponding MLEs, $\hat{n}_s$ and $\hat{\gamma}$. The compatibility between the experimentally observed $TS_{exp}$ and the background-only hypothesis can be estimated by computing the p-value

$$p = \int_{TS_{exp}}^{\infty} f(TS|H_0)\mathrm{d}TS, \tag{5.18}$$

where $f(TS|H_0)$ is the probability distribution of the test-statistic assuming the null hypothesis to be true. Thereby, the smaller the p-value, the higher the confidence for rejecting the background-only hypothesis. The $TS$ distribution under the null hypothesis is obtained from simulations by performing the likelihood-ratio test on

pseudo-datasets generated according to the background-only hypothesis without any point-like source signal. As an example, Figure 5.9 shows the background *TS* distributions at some declinations across the sky.

Two standard figures of merit are used in IceCube to quantify the analysis capability to identify a point-source signal:

- The *sensitivity* is the average point-source flux needed to exceed the median value of the background test-statistic distribution in 90% of the cases. In other words, it quantifies the 90% C.L. upper limit on the neutrino flux the analysis can set when the observed *TS* equals the background median.
- The $5\,\sigma$ *discovery potential* defines the average point-source flux needed to exceed the $5\,\sigma$ quantile of the background test statistic distribution in 50% of the cases. The p-value corresponding to a $5\,\sigma$ significance corresponds to $\simeq 2.9 \times 10^{-7}$.

The computation of the $5\,\sigma$ discovery potential requires the knowledge of the background *TS* down to its $5\,\sigma$ quantile. According to Wilks' theorem in Equation 5.5, the distributions in Figure 5.9 should follow a $\chi^2$ with two degrees of freedom. However, the condition of a large sample required by Wilks' theorem is not always fulfilled in the entire observable space, causing deviations from the expected shape. For this reason, we parametrize the background *TS* distributions by fitting a more flexible truncated Γ-distribution to it:

$$f(TS) \underset{TS\geq\eta}{=} \Gamma(TS|a,b,\eta) \underset{TS\geq\eta}{=} (\xi/C_0)\cdot\Gamma(TS|a,b), \tag{5.19}$$

where $\eta$ is the lower threshold for the integration of the distribution, $a$ and $b$ are the shape and scale parameters of the Γ-distribution, respectively, $\xi$ is the fraction of pseudo experiments having a value larger than $\eta$, and $C_0 = \int_\eta^\infty \Gamma(TS|a,b)$ is a normalization constant. To ensure that the fit of the tail is not affected by the distortion of the distribution close to zero, we adopt the truncation threshold $\eta = 3.0$. The fitted gamma functions are shown together with the *TS* distributions in Figure 5.9.

Due to the IceCube detector's energy- and declination-dependent effective area (see Subsection 4.7.3), the sensitivity to an astrophysical point-source signal varies depending on the signal hypothesis, *i.e.*, depending on the assumed source declination and spectral index $\gamma$. In this work, we have extended the up-going muon tracks sample for point-source searches from 9 to 13 years of data by including one year of data recorded by the IC79 detector and three new years of data recorded by the IC86 complete detector.[28] Thanks to the increased exposure time compared to the previous work that used the same data selection and analysis methods,[29] both the sensitivity and $5\,\sigma$ discovery potential of the analysis improve by $20-25\%$ depending on the spectral index, as illustrated in Figure 5.10. The improvement is larger for the hard spectral index case, for which the background increase in time is slower than for soft spectra.

[28] See Section 4.7 for a review of the dataset properties.

[29] Abbasi et al., "Evidence for neutrino emission from the nearby active galaxy NGC 1068".

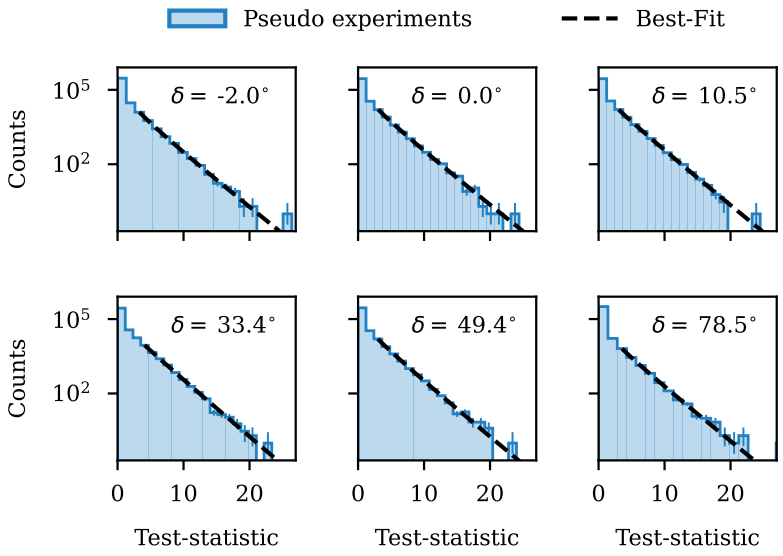


Figure 5.9: Distribution of 350,000 test-statistic values obtained assuming the background-only hypothesis to be true at various declinations across the Northern sky. The tail of the distribution at $TS > 3$ is fitted with a truncated $\Gamma$-distribution to extrapolate the behavior at high $TS$ values. The number of trials returning $TS = 0$ is approximately 45%.

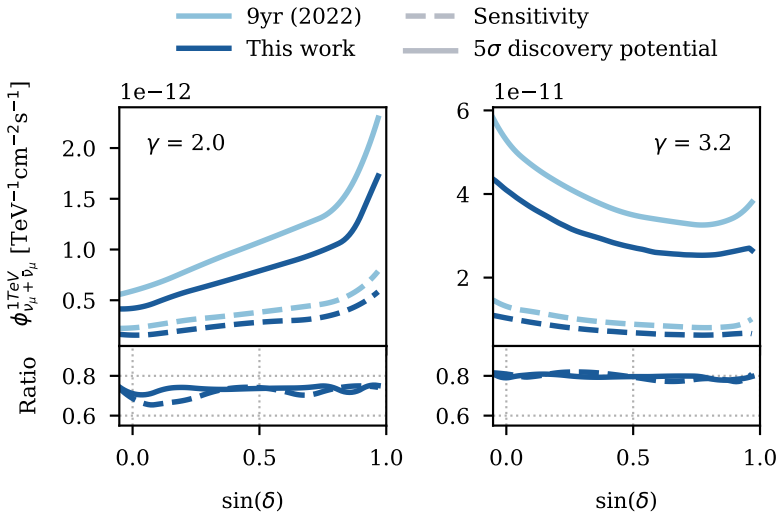


Figure 5.10: Sensitivity (dashed) and $5\sigma$ discovery potential (solid) across the Northern hemisphere for point-source signals with spectral indices $\gamma = 2.0$ (left) and $\gamma = 3.2$ (right). The same quantities are shown for the 13 years of data used in this work (in blue) and for 9 years of data analyzed by previous work (in light blue) that used the same analysis methods and sample (Abbasi et al., "Evidence for neutrino emission from the nearby active galaxy NGC 1068"). The lower panel of each plot shows the relative improvement of this analysis compared to the previous one.

The energy dependence of the analysis' sensitivity and $5\sigma$ discovery potential can be understood by constructing the two quantities in neutrino energy bins. This results in the so-called *differential sensitivity/discovery potential*, which are shown in Figure 5.11 using two bins per energy decade.

The effect of Earth absorption at high energies becomes evident for declination $\delta \gtrsim 30°$, where both the sensitivity and discovery fluxes of the analysis increase rapidly, as seen in the top panels of Figure 5.11. The lower panels show the same quantity expressed in terms of the mean number of detected signal events in 13 years of data. From this perspective, the difference across declinations is less prominent. However, a much larger flux is needed to detect a handful of signal events at high energies and declinations due to the

reduced detection efficiency. From the lower panels of Figure 5.11, we also notice that, for sources emitting mainly in the TeV energy region (soft spectra), we need to detect approximately 100 events for a $5\sigma$ discovery.[30] On the other hand, for sources emitting $\gtrsim 100$ TeV neutrinos, detecting only $\sim 10$ signal events results in the same significance due to the reduced background rate at high energies.

[30] Note that here we refer to a *local* significance as we are not accounting for possible penalty factors due to multiple testing. See *e.g.*, Section 5.4 for a discussion about *trial factors* in the sky scan search.

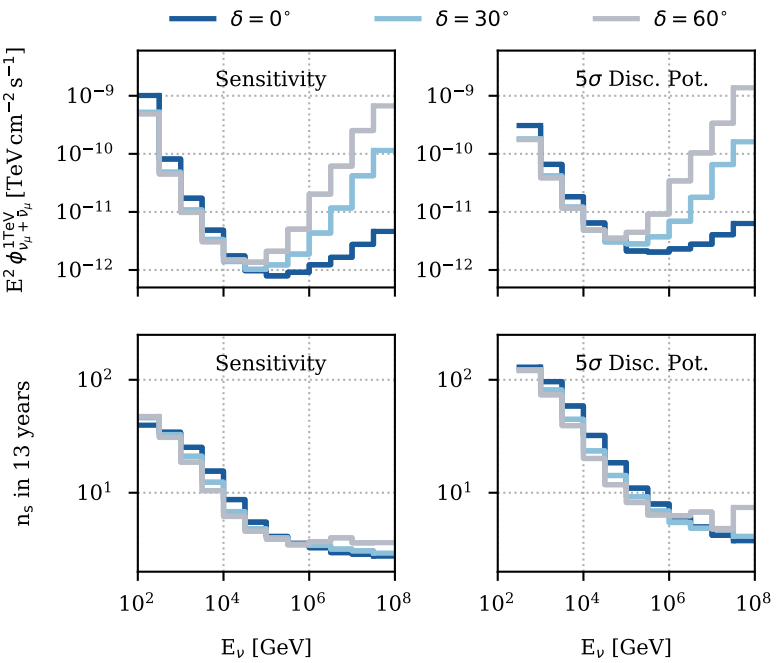


Figure 5.11: Differential sensitivity and $5\sigma$ discovery potential neutrino fluxes (top) and mean number of signal events in 13 years of data (bottom) as a function of the neutrino energy. Three different declinations are displayed in different colors. In each bin, we assume a power-law energy spectrum with spectral index $\gamma = 2.0$.

### *Systematic uncertainties*

In Subsection 4.3.1, we mentioned that the knowledge of the Antarctic ice properties is crucial to characterize the Cherenkov photon propagation through the detector. While enormous efforts are constantly devoted to improving our understanding of the ice,[31] uncertainties in its modeling produce systematic uncertainties in the analysis. However, previous works have demonstrated that the impact of these uncertainties on the angular resolution and significance of a point-source signal is negligible compared to the dominant statistical uncertainty[32].[33]

Additionally, we checked the robustness of our analysis against potential mismodeling of the astrophysical diffuse background component, which is part of the background-only hypothesis in the point-source analysis. As discussed in Section 5.1, while the observed event rate determines the atmospheric background, the expected rate of diffuse astrophysical neutrinos is based on the latest IceCube measurement.[34] We assessed the effect of background mismodeling by studying the uncertainty's impact on the tails of the background *TS* distribution. Background *TS* distributions simulated using different

[31] Abbasi et al., "In situ estimation of ice crystal properties at the South Pole using LED calibration data from the IceCube Neutrino Observatory".

[32] Abbasi et al., "Evidence for neutrino emission from the nearby active galaxy NGC 1068".

[33] Glauch, "The Origin of High-Energy Cosmic Particles: IceCube Neutrinos and the Blazar Case".

[34] Abbasi et al., "Improved Characterization of the Astrophysical Muon-neutrino Flux with 9.5 Years of IceCube Data".

diffuse neutrino flux spectra, varied within the published uncertainties, are detailed in Appendix C.4. The analysis response shows no significant change. Thus, we could conclude that the uncertainty of the diffuse flux measurement has a negligible effect on the analysis.

Finally, we checked the impact of an unmodeled background contribution from Galactic Plane (GP) neutrinos. This additional check is motivated by the $4.5\,\sigma$ evidence for neutrino emission from the GP recently reported by IceCube.[35] The measured GP neutrinos contribute significantly to the total astrophysical flux at energies $\lesssim 10$ TeV (see Figure 2.6). However, this background is anisotropic, aligning with the GP spatial profile. An unmodeled background could lead to overestimating a signal's significance for sources aligned with the GP. We evaluated the impact of this possible systematic mismodeling on the analysis' discovery potential. The effect is marginal across the whole hemisphere, with the largest decrease in discovery potential being $\lesssim 5\%$ for sources with soft spectra ($\gamma \gtrsim 3.0$) located where the GP model adopted for the study[36] predicts the maximal neutrino emission in the Northern sky, *i.e.*, at the closest point to the Galactic Center.[37] The full study of the systematic uncertainty due to an unmodeled GP background component is reported in Appendix C.4.1.

[35] Icecube Collaboration, "Observation of high-energy neutrinos from the Galactic plane".

[36] Schwefer, Mertsch, and Wiebusch, "Diffuse Emission of Galactic High-energy Neutrinos from a Global Fit of Cosmic Rays".

[37] The Galactic Center is located at 266.4° right ascension and -29.0° declination.

## 5.4 *Significance map of the Northern sky*

The search for the most significant clustering of astrophysical events in the sky, known as the *sky scan*, does not rely on any assumptions about the location of potential neutrino sources. The sky is divided into a grid of equally sized pixels using HealPix,[38] with each pixel's center tested as a source position. The *TS* in Equation 5.7 is maximized at each pixel, yielding best-fit values $\hat{n}_s$ and $\hat{\gamma}$. Although the data selection includes events with reconstructed declinations ranging from -5° to 90°, we scan the Northern sky within a declination range $-3^\circ < \delta < 81^\circ$. The band from $-5^\circ$ to $-3^\circ$ is excluded because the KDE used to parametrize the signal spatial PDF ($\mathcal{S}(\psi)$ in Figure 5.3) cannot be symmetric when the source is located close to the boundary. The pole area is also excluded due to the reduced performance of the angular reconstruction for low-energy, nearly vertical events, for which only optical modules from a few detector lines are involved in the detection (see Section 4.3). The analysis aims to identify the most significant spot in the sky (also known as the *hottest spot*). However, this does not necessarily correspond to the highest *TS* due to the declination dependence of *TS* values. The declination dependence can be absorbed by converting all observed *TS* values into p-values (Equation 5.18). By interpolating the parameters of the $\Gamma$-distribution fitted at $\sim 350$ declinations across the hemisphere, we can calculate the p-value for any *TS* observed at any declination. The splines to interpolate the $\Gamma$-distribution parameters across the sky can be found in Section C.3.

A first, coarser scan is conducted on a grid of $\sim 400,000$ pixels, each with an area of about $0.2 \times 0.2$ square degrees.[39] From the

[38] Górski et al., "HEALPix: A Framework for High-Resolution Discretization and Fast Analysis of Data Distributed on the Sphere".

[39] HealPix *Nside* parameter 256.

coarse scan, we identify the 20 most significant spots.[40] A finer scan is then performed within a 0.75° radius around these spots, using pixels of approximately $0.03 \times 0.03$ square degrees.[41] The second scan, which is finer than the minimum angular uncertainty on the single event (0.1°), ensures the accurate localization of the hottest spot within the angular resolution of the data sample.

When performing a sky scan, we assume a point-like neutrino source and perform a maximum likelihood-ratio analysis at each pixel location. Therefore, we must account for the multiple potential sources tested in a single scan. Since not all pixels in the skymap grid are statistically independent, the actual number of independently tested point-like sources, $N$, is usually smaller. Thus, we estimate the *trial factor* $N$ directly from simulations. A distribution of hottest spot p-values is constructed from MC simulations of sky scans generated under the background-only hypothesis.[42] The fraction of background-only p-values smaller than the observed one provides the corrected *post-trial* p-value, $p_{\text{post}}$, which represents the global significance of the hottest spot.

In this thesis, we present results from three sky scans: one with spectral index left as a free parameter and two assuming fixed spectra indices of 2.0 and 2.5. Predicted cosmic-ray spectra in the shock acceleration scenario (see Section 2.3) motivate the choice of $\gamma = 2.0$. The spectral index $\gamma = 2.5$ corresponds to the latest measurements of the astrophysical diffuse neutrino flux.[43] Exemplary background *TS* distributions for the fixed spectral index cases and the interpolation splines of the $\Gamma$-distribution parameters across the hemisphere are provided in Appendix C.3.

[40] The spots with the lowest local p-values. See Section 7.1 for the definition of a hotspot used in this work.

[41] HealPix *Nside* parameter 2048.

[42] The entire procedure of coarse and subsequent finer scans is repeated.

[43] Naab et al., "Measurement of the astrophysical diffuse neutrino flux in a combined fit of IceCube's high energy neutrino data".

# 6 Point-source Searches with IceCube Public Data

In 2020, the IceCube Collaboration published the results of an all-sky time-integrated search for neutrino point sources. The search was based on a selection of ten years of track-like events produced by muons created in muon-neutrino interactions in the ice.[1] The result revealed a first hint of neutrino emission from NGC 1068, at 2.9 $\sigma$.[2] In January 2021, IceCube released these data to the public.[3] Hereafter, we will refer to the IceCube publication as *Aartsen et al. PRL 124, 2020*.

This chapter introduces a novel open-source software interface that enables users to search for neutrino sources using IceCube public data. We discuss the data release and its limitations and explain how it can be used to search for point-like astrophysical neutrino emission. We implement the likelihood-ratio test for point-source searches described in Section 5.1. We follow the implementation used in *Aartsen et al. PRL 124, 2020* and approximate the spatial distribution of signal events with a bivariate Gaussian centered at the source location.[4] To validate our implementation, we investigate the performance of the analysis and compare it with published results. Besides time-integrated searches, the new analysis tool allows the search for neutrino transient emission in public data using an unsupervised learning algorithm. We analyze the neutrino flare from the blazar TXS 0506+056[5] and compare the result to that published by IceCube.[6]

This work was presented at the 38th International Cosmic Ray Conference[7] on behalf of the IceCube Collaboration and published as a proceeding.[8] The author of this dissertation is the primary developer of the software interface described here, together with the co-authors of the published proceedings.

## 6.1 The SkyLLH analysis framework

Searching for the sources of high-energy cosmic particles requires sophisticated analysis techniques, frequently involving hypothesis tests with unbinned log-likelihood functions, as we discussed in Chapter 5. SkyLLH[9,10] is an open-source, Python-based software tool designed to build these likelihood functions for celestial event data and perform likelihood-ratio tests. Developed within the IceCube

[1] Aartsen et al., "Time-Integrated Neutrino Source Searches with 10 Years of IceCube Data".
[2] Ibid.
[3] IceCube Collaboration, "IceCube Data for Neutrino Point-Source Searches Years 2008-2018".

[4] Note that this approach does not involve the non-parametric inference of the probability density functions through kernel density estimation that has been described in Section 5.1.

[5] IceCube Collaboration et al., "Neutrino emission from the direction of the blazar TXS 0506+056 prior to the IceCube-170922A alert".
[6] IceCube Collaboration, "IceCube Data for Neutrino Point-Source Searches Years 2008-2018".
[7] https://www.icrc2023.org/
[8] Bellenghi, M. Karl, and Wolf, "Extending SkyLLH software for neutrino point source analyses with 10 years of IceCube public data".

[9] Wolf, "SkyLLH - A generalized Python-based tool for log-likelihood analyses in multi-messenger astronomy".
[10] Kontrimas and Wolf, "The SkyLLH framework for IceCube point-source search".

collaboration, it supports statistical data analyses for point-like neutrino source searches. Remarkably, SkyLLH has been used for the search that resulted in a $4.2\sigma$ evidence for neutrino emission from the Seyfert II galaxy NGC 1068.[11] Moreover, the point-source analysis detailed in Chapter 5, with results presented in Section 8.2, is also implemented using SkyLLH.

The SkyLLH software framework is designed to follow the mathematical structure of the log-likelihood ratio formalism in Equation 5.7. Hence, base Python classes define interfaces for probability density functions (PDFs), signal-over-background (S/B) PDF ratios, log-likelihood ratios, and test-statistic functions. The `Analysis` class integrates all components of a point-source analysis into a single object. In addition to classes and functions for evaluating the log-likelihood function, SkyLLH provides utility classes for data handling.[12] Once the `Analysis` object is constructed, the user can choose to analyze the experimental data via the `unblind` method or to generate a pseudo-experiment with background and signal events via the `do_trial` method of the `Analysis` class. SkyLLH's documentation provides a tutorial that guides the user through the main analysis steps. It gives examples for loading the public data, creating the `Analysis` object for a single point source assuming a power-law energy spectrum, generating pseudo-experiments for sensitivity and significance calculations.[13] Following the tutorial, the user can reproduce the results published in *Aartsen et al. PRL 124, 2020*.[14] SkyLLH's design supports combined data analysis of multiple datasets or detectors by taking the product of all datasets' likelihood functions. Therefore, the public data could be combined with data from other experiments.

[11] Abbasi et al., "Evidence for neutrino emission from the nearby active galaxy NGC 1068".

[12] For instance, the `Dataset` class allows users to define a dataset with observed data and simulations stored on disc and to load them into memory.

[13] See Subsection 5.3.2 for a definition of sensitivity flux in the point-source analysis.

[14] https://icecube.github.io/skyllh/master/html/tutorials/publicdata_ps.html

## 6.2 *The public release of ten years of neutrino data*

In the past, IceCube performed all-sky searches for steady and flaring neutrino point-like sources using ten years of point-source data.[15,16] This selection of 1,134,450 events detected from the entire sky was made public in 2021.[17] Although selected as candidate neutrino events, the data sample is dominated by cosmic-ray-induced atmospheric muons in the Southern sky. Harsh cuts to reduce this contamination effectively reduce the selection to only very high energy events, from tens of TeV up. Atmospheric muons are instead absorbed in the Northern hemisphere when crossing the Earth. Therefore, detected events from the Northern sky are primarily produced in neutrino interactions, and events with sub-TeV energies survive the selection.

The data spans the time range from April 2008 to July 2018, covering five different data acquisition periods (seasons) corresponding to different detector configurations: IC40 (2008), IC59 (2009), IC79 (2010), IC86 2011, and IC86 2012–2017[18], where the last two digits indicate the number of detector strings deployed in the ice at the time of the data acquisition (see Section 4.3). The release encompasses events recorded with their reconstructed muon observables $\boldsymbol{x} = (E_\mu, \boldsymbol{r}_\mu, \sigma, t_\mu)$: the energy $E_\mu$, the direction in right ascension $\alpha$

[15] Aartsen et al., "Time-Integrated Neutrino Source Searches with 10 Years of IceCube Data".

[16] Abbasi et al., "Search for Multi-flare Neutrino Emissions in 10 yr of IceCube Data from a Catalog of Sources".

[17] IceCube Collaboration, "IceCube Data for Neutrino Point-Source Searches Years 2008-2018".

[18] Different selection, software, and detector calibration procedure were used for each season until they were standardized for the IC86 detector from 2012 on.

and declination $\delta$, $\boldsymbol{r}_\mu = (\alpha_\mu, \delta_\mu)$, the uncertainty on the reconstructed muon direction $\sigma$, as well as the observation time $t_\mu$. Similarly to the sample of up-going muon tracks used for the point-source analysis in Chapter 5, the SplineMPE algorithm is used to reconstruct the muon direction. However, the energy and angular uncertainty observables are inferred using the *Truncated Energy* and *Paraboloid* algorithms instead of the more advanced machine-learning-based reconstructions, which are currently optimized for the Northern sky only.[19] The angular uncertainty $\sigma$ published in the release already includes a correction to account for the kinematic angle between the parent neutrino and the reconstructed muon, relevant at neutrino energies $\lesssim 1$ TeV (see Equation 4.13). The kinematic angle correction is included in the so-called *pull correction*, which IceCube applies to the Paraboloid estimate, $\sigma_p$. We define the *pull* as the angular distance between the parent neutrino and the reconstructed muon direction divided by the angular uncertainty, $\Delta\psi/\sigma$. Under the assumption that a 2D Gaussian distribution describes the pull for a given neutrino energy, 50% of events with angular uncertainty estimate $\sigma$ should fall within $1.177 \times \sigma$ from the parent neutrino direction, as seen in Figure 6.1. Therefore, if $\sigma_p$ provides the rigth coverage, $\Delta\psi/\sigma_p = 1.177$. However, the left panel of Figure 6.2 shows that $\sigma_p$ does not satisfy this condition. The pull correction shifts the pull to the expected value of 1.177. It is calculated as a function of the reconstructed muon energy on Monte Carlo (MC) simulations, assuming an $E^{-2}$ neutrino energy spectrum. The data release already provides pull-corrected angular uncertainty values, which can directly be used to construct the point-source spatial PDF.

[19] See Section 4.5 and Section 4.6 for a review of the various reconstruction algorithms.

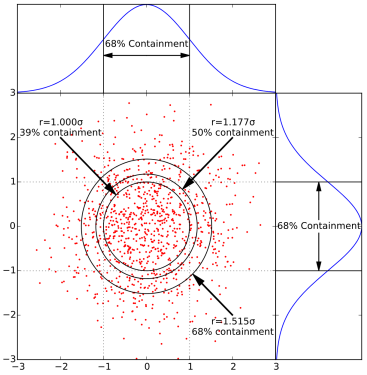


Figure 6.1: Distribution of events sampled from a symmetric 2D Gaussian around a central source position for a certain angular error estimate $\sigma$. Note that $\sigma$ is the standard deviation of each one-dimensional Gaussian, providing the corresponding 68% coverage in 1D. Figure taken from https://docs.icecube.aq/icetray/main/projects/paraboloid/index.html.

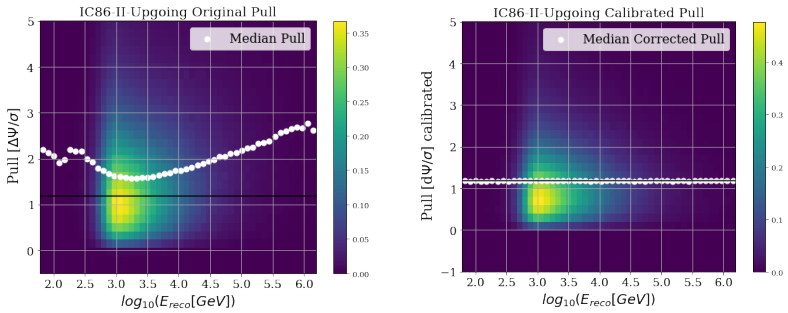


Figure 6.2: Correction applied to the pull (see details in the text) as a function of the reconstructed muon energy. The pull correction is calculated for neutrino energies distributed according to an $E^{-2}$ energy spectrum. The heatmap illustrates the probability density function normalized in each energy bin. The white dots represent the corresponding medians. The solid black line marks the expectation for the correct 50% coverage in 2D. The left and right panels show the distribution before and after the correction. Figure reprinted from Carver, "Time integrated searches for astrophysical neutrino sources using the IceCube detector and gender in physics studies for the Genera Project".

In addition, the release provides tabulated instrument response functions (IRFs), which include binned muon-neutrino effective areas, $A_{\text{eff}}(E_\nu, \delta_\nu)$, and binned reconstruction probabilities in the form $M(E_\mu, \psi, \sigma|\delta_\nu, E_\nu)$. Thus, for a given parent neutrino with declination $\delta_\nu$ and energy $E_\nu$, the three-dimensional matrix $M$ contains the probability of reconstructing the secondary muon with $E_\mu$, $\sigma$, and an angular separation $\psi$ between the parent neutrino and the muon. From here on, $M$ will be referred to as the detector response matrix.[20] It should be noted that the detector response matrix provides only three bins for the incoming neutrino declination, covering the

[20] It is denoted as the *smearing matrix* in the data release.

Southern sky ($-90^\circ < \delta_\nu < -10^\circ$), the horizon ($-10^\circ < \delta_\nu < 10^\circ$), and the Northern sky ($10^\circ < \delta_\nu < 90^\circ$). As we will see in Section 6.5, this summarized information causes some loss in the analysis' sensitivity compared to the published performance of the same dataset. Nevertheless, through the published IRFs, it is possible to construct the PDFs that form the basis of the point-source likelihood defined in Equation 5.4.

## 6.3 A Point-source analysis with public data

In Section 5.1, we introduced the concept of hypothesis testing via likelihood-ratio tests for point-source searches. Here, we want to perform the same hypothesis test using public data: We use the likelihood-ratio test to evaluate which one between the background-only and the background+signal hypotheses is favored given the observed data. The background-only hypothesis assumes that all observed events are produced in atmospheric interactions of cosmic rays or by a diffuse astrophysical neutrino flux. The alternative hypothesis assumes that the data can be explained by the combination of diffuse isotropic backgrounds and an additional flux component produced by a point source located at right ascension $\alpha_{\rm src}$ and declination $\delta_{\rm src}$. In the following, we assume a power-law point-source flux characterized by a spectral index $\gamma$, which is the flux model used by *Aartsen et al. PRL 124, 2020*. However, the possibility of testing arbitrary flux shapes with the public data is currently being implemented within SkyLLH.

In Section 5.1, we described the general form of the point-source likelihood and the joint background+signal PDF that describes the events' distributions. The final expressions for the background and signal PDFs are given by Equation 5.15 and Equation 5.16. This work follows the implementation used to produce the results published in *Aartsen et al. PRL 124, 2020*. For each data sample, the background PDF is modeled directly on the distribution of the experimental data in $E_\mu$ and $\sin\delta_\mu$, under the assumption that experimental data are background-dominated and that the background flux is uniformly distributed in space. This is a safe assumption since $\sim$99% of the diffuse astrophysical neutrino flux is currently unresolved. The signal PDF for the event $\boldsymbol{x}$ can be split into the product of a spatial and an energy term, which we re-write here for clarity:

$$f_{\rm s}\left(\boldsymbol{x}|\delta_{\rm src},\gamma\right) = \mathcal{S}\left(\psi|E_\mu,\sigma,\gamma\right)\cdot\mathcal{E}\left(E_\mu|\delta_{\rm src},\gamma\right) \tag{6.1}$$

The spatial part is modeled using the analytical approximation of a bivariate Gaussian distribution. As discussed in Chapter 5, this approximation does not always accurately describe the point spread function of the detector, especially for soft spectra or low-energy events. Consequently, it produces biases in the fit parameters, as we will see in Section 6.4. However, this does not impact the robustness of experimental p-values.

The signal energy PDF can be constructed from the detector response matrix $M$ and formulated as an integral over all neutrino energies:

$$\mathcal{E}(E_\mu|\delta_{\rm src},\gamma) \equiv \mathcal{E}(E_\mu|\delta_\nu,\gamma) = \int_{E_{\rm min}}^{E_{\rm max}} dE_\nu\, f(E_\mu|E_\nu,\delta_\nu)\cdot w_{\rm flux}(E_\nu|\gamma)\cdot w_{\rm det}(E_\nu|\delta_\nu). \tag{6.2}$$

The integrand is the product of three factors:

- $f(E_\mu|E_\nu,\delta_\nu)$ is the probability density of the reconstructed energy given the parent neutrino energy and declination. It is calculated from the detector response matrix $M$.
- $w_{\rm flux}(E_\nu|\gamma)$ is a *flux weight*, which accounts for the probability of a neutrino energy given a power-law spectrum with spectral index $\gamma$.
- $w_{\rm det}(E_\nu|\delta_\nu)$ is a *detection weight*, which accounts for the probability of detecting a neutrino with energy given its declination. It is calculated from the tabulated effective areas, $A_{\rm eff}(E_\nu,\delta_\nu)$.

The integration limits $E_{\rm min}$ and $E_{\rm max}$ are set to cover a neutrino energy range of $10^2 - 10^9$ GeV, as provided in the IRFs.

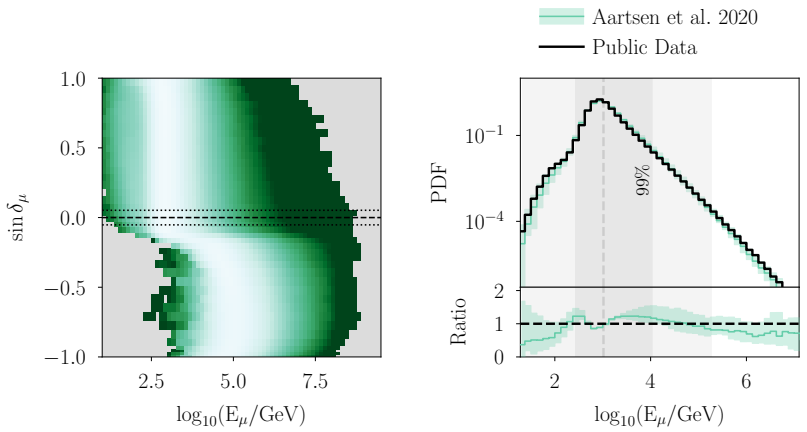


Figure 6.3: Comparison of the signal energy PDFs for the season IC86 2012–2017 and spectral index $\gamma = 3.2$. **Left**: The PDF as used in *Aartsen et al. PRL 124, 2020* (Aartsen et al. 2020 in the legend). The color scale represents the probability density. The black lines delimit $\delta_\mu = (-0.01 \pm 3.00)^\circ$. **Right**: 1D comparison between the internal IceCube PDF (green) at reconstructed muon declination $\delta_\mu = -0.01^\circ$ and the one used in the public data analysis (black) at source declination $\delta_{\rm src} = -0.01^\circ$. The shaded green band represents the variations of the internal energy PDF when considering events reconstructed at declinations enclosed by the dotted black lines in the left-hand plot. The energies of the experimental data fall in the gray shaded area, with the central 99% quantile indicated by the darker grey area. The lower panel shows the ratio between the public PDF and the internal one for all events reconstructed within 3° from the source.

Only the mathematical representation of the signal energy PDF differs from the internal IceCube analysis used in *Aartsen et al. PRL 124, 2020*. Internally, it is constructed as $\mathcal{E}(E_\mu|\delta_\mu,\gamma)$ using the approximation $\delta_{\rm src} \approx \delta_\mu$, which is valid in the assumption that the muon is reconstructed close to parent neutrino/source direction. This approximation is introduced to have signal and background energy PDFs with the same structure, which simplifies the S/B ratio in the test-statistic (*TS*, see Equation 5.6). The modification introduced in the public data analysis (Equation 6.2) is necessary to cope with the absence of the reconstructed muon declination $\delta_\mu$ in the detector response matrix. In fact, $M$ provides the binned angular separation of the reconstructed muon from the original neutrino but not the individual reconstructed muon coordinates.

The difference between the *internal* and *public* energy PDFs is illustrated in Figure 6.3 for the dataset IC86 2012–2017, for a source at the location of NGC 1068 ($\delta = -0.01°$) and with its best-fit spectral index $\gamma = 3.2$, as measured in *Aartsen et al. PRL 124, 2020*.

## 6.4 Recovery of the fit paramenters

The modeling of the signal spatial PDF with a bivariate Gaussian provides a good description of the data in many cases. However, inaccuracies in the PDF description of data can cause biases in the fit parameters of the likelihood, namely the number of signal events in the detector $n_s$ and the spectral index $\gamma$. Here, we study the capability of the public data analysis to recover an injected power-law energy spectrum. The procedure is similar to the one described in Subsection 5.3.1: point-source signals of various strengths $n_s^{inj}$ are injected according to a power-law energy spectrum with spectral index $\gamma^{inj}$. The best-fit values resulting from the maximization of the *TS* in Equation 5.7, $\hat{n}_s$ and $\hat{\gamma}$, are then compared to the injection. Figure 6.4 and Figure 6.5 show the recovery of the injection at three exemplary source declinations and assuming hard and soft spectral emission.

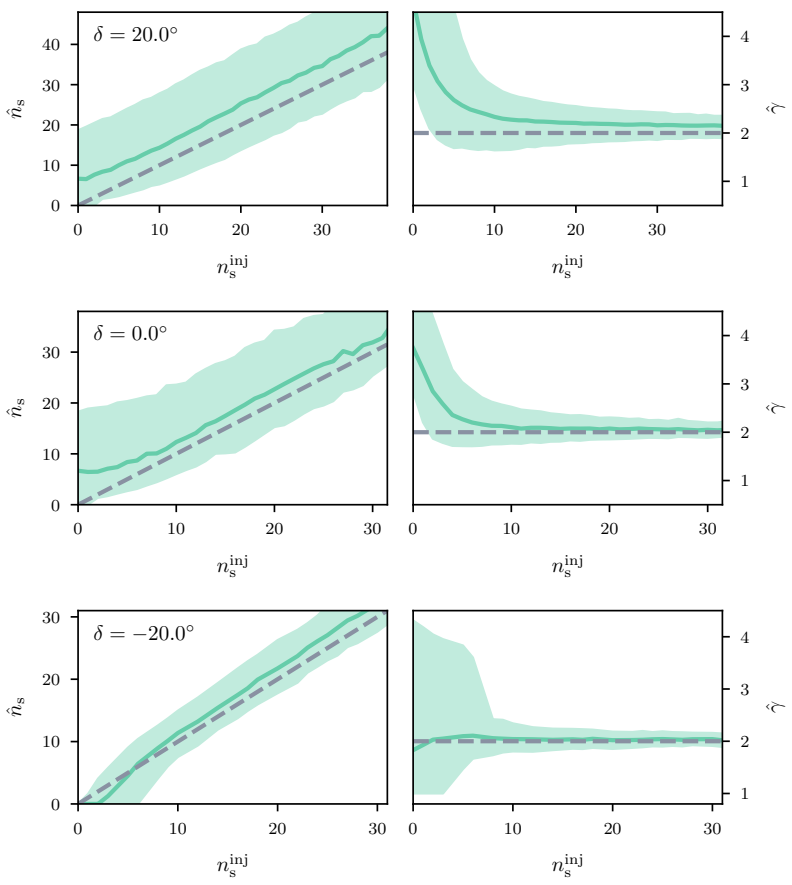


Figure 6.4: Fitted versus injected signal for a $\gamma^{inj} = 2.0$ source spectrum and three exemplary declinations, as indicated in each figure. The left plot shows the recovery of the mean number of signal events, while the right plot illustrates how well we can recover the injected spectral index. The solid lines represent the median $\hat{n}_s$ and $\hat{\gamma}$ at each $n_s^{inj}$. The shaded bands show the 68% central quantiles. The ideal unbiased recovery of the parameters is shown as a dashed grey line.

The mismodeling of the Gaussian PDF is especially severe for soft spectral indices, as seen in Figure 6.5. In these cases, the tails of the spectral index-independent Gaussian cannot reproduce the tail of events reconstructed at larger distances from the source (see Figure 5.3). Consequently, those events are ignored by the spatial likelihood, and the total number of signal events is underestimated. However, signals from hard power-law spectra are more accurately recovered, with biases smaller than the statistical uncertainty (shown by the shaded bands in Figure 6.4 and Figure 6.5). Overall, the observed parameter biases are consistent with what has been observed by IceCube when using the same Gaussian spatial approximation.[21]

[21] See the supplementary material of Abbasi et al., "Evidence for neutrino emission from the nearby active galaxy NGC 1068"

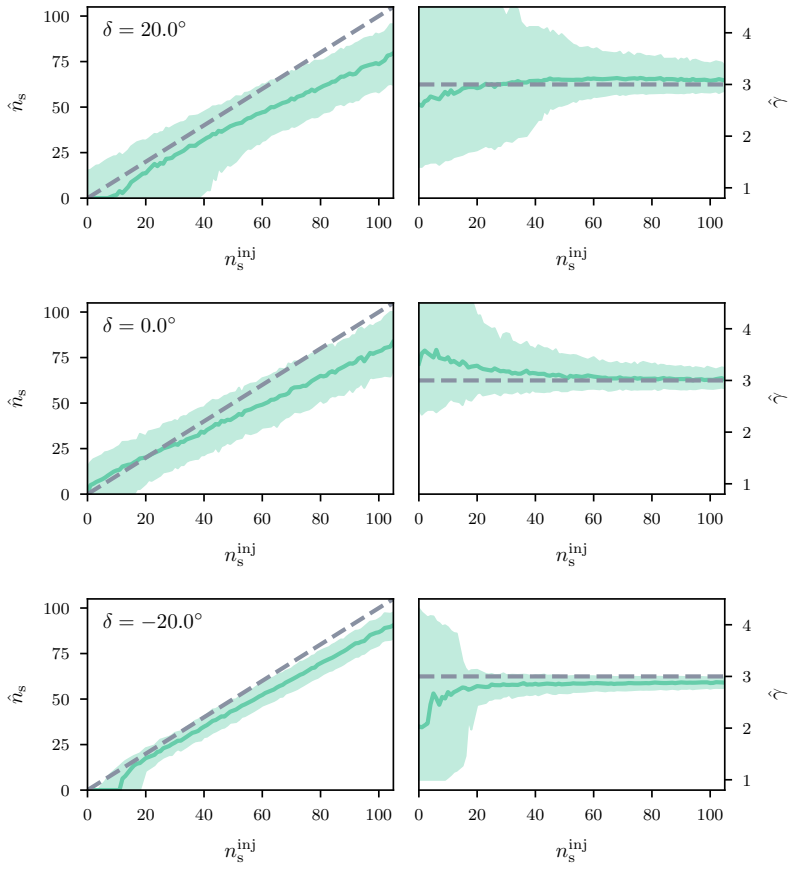


Figure 6.5: Fitted versus injected signal for a $\gamma^{inj} = 2.0$ source spectrum and three exemplary declinations, as indicated in each figure. The left plot shows the recovery of the mean number of signal events, while the right plot illustrates how well we can recover the injected spectral index. The solid line represents the median $\hat{n}_s$ and $\hat{\gamma}$ at each $n_s^{inj}$. The shaded bands show the 68% central quantiles. The ideal unbiased recovery of the parameters is shown as a dashed grey line.

## 6.5 *Sensitivity to an astrophysical signal*

To test how accurately the analysis published in *Aartsen et al. PRL 124, 2020* can be replicated using the public data release and the software developed in this work, we compare their respective sensitivities to an $E^{-2}$ flux of astrophysical neutrinos produced by a point-like source. The result of this comparison is illustrated in the left panel of Figure 6.6, where the sensitivity flux is shown as a function of the declination for the public data (black dashed) and the internal IceCube analysis (green).

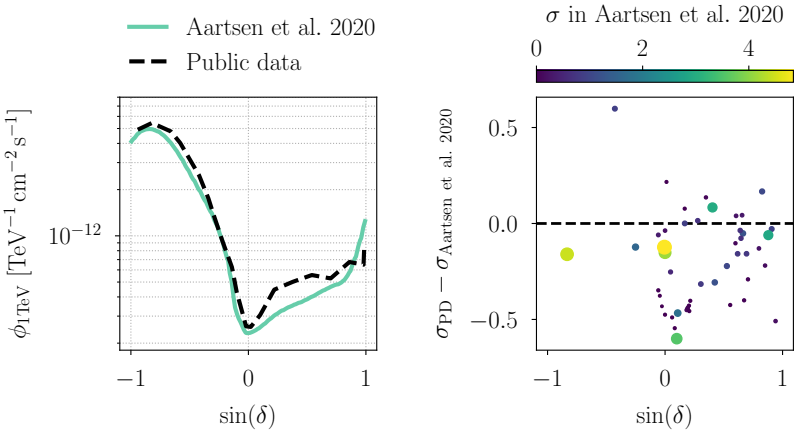


Figure 6.6: **Left:** Comparison of sensitivity to an astrophysical neutrino flux as a function of the position in the sky assuming an $E^{-2}$ neutrino spectrum. The sensitivity published in *Aartsen et al. PRL 124, 2020* (green solid line) and the public data (PD) analysis presented in this work (dashed black line). **Right:** Shift of local significance in Gaussian-equivalent standard deviations as a function of the declination compared to the published results. The dots represent the objects in the list of candidate sources analyzed by IceCube and the two most significant locations in the northern and southern sky. The color scale, as well as the size of the dots, represent the published local significance. The green point with the largest shift to lower significances (at the very bottom of the panel) corresponds to TXS 0506+056.

The right panel of Figure 6.6 displays the local significance difference in Gaussian-equivalent standard deviations at the location of the source candidates analyzed in *Aartsen et al. PRL 124, 2020*. For most tested sources, the significance is weaker when using the public data (PD), but it is reproduced within ∼0.5 Gaussian-equivalent standard deviations. Overall, the public data analysis is slightly less sensitive due to the coarse binning of the detector response matrix, which contains only three bins for the parent neutrino direction.

As a final reproducibility check, we measured the muon-neutrino flux $\phi(E_\nu) = \phi_{1\mathrm{TeV}}\,(E_\nu/1\mathrm{TeV})^{-\gamma}$ from NGC 1068 with the public data analysis presented in this work and find the best-fit values for the flux parameters to be $\hat{n}_\mathrm{s} = 60 \pm 15$, and $\hat{\gamma} = 3.2^{+0.4}_{-0.2}$. The statistical uncertainties are estimated from the 1D profile likelihood assuming Wilks' theorem.[22] The observed mean number of signal events $\hat{n}_s$ can be converted into a neutrino flux normalization by integrating the effective area at the source location multiplied by the power-law energy flux over the neutrino energy range and the observation period. This yields $\phi_{1\mathrm{TeV}} = 3.3 \times 10^{-11}\,\mathrm{TeV}^{-1}\,\mathrm{cm}^{-2}\,\mathrm{s}^{-1}$. All these values are compatible with the ones published by IceCube, which are $\hat{n}_\mathrm{s} = 50$, $\hat{\gamma} = 3.2$ and $\phi_{1\mathrm{TeV}} \sim 3 \times 10^{-11}\,\mathrm{TeV}^{-1}\,\mathrm{cm}^{-2}\,\mathrm{s}^{-1}$ (as inferred from Figure 4 of *Aartsen et al. PRL 124, 2020*). The likelihood scan around the best-fit flux parameters with the $1\,\sigma$ and $2\,\sigma$ confidence levels derived from Wilks' theorem is illustrated in Figure 6.7. The comparison with the published likelihood contours shows that the two results largely overlap.

[22] Wilks, "The Large-Sample Distribution of the Likelihood Ratio for Testing Composite Hypotheses"

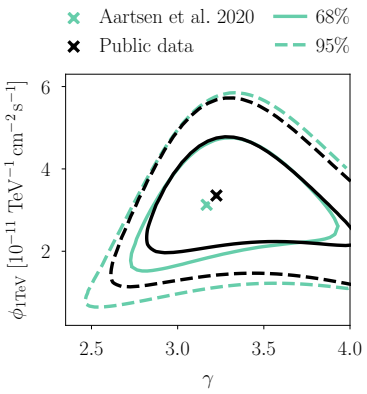


Figure 6.7: Likelihood profile of the flux parameters—$\phi_{1\mathrm{TeV}}$ and $\gamma$—of NGC 1068. The cross marks the best-fit values, while the solid and dashed lines indicate the 68% and 95% confidence level contours according to Wilks' theorem. IceCube results published in *Aartsen et al. PRL 124, 2020* are reported in green, while the analysis of the public data is shown in black. The two results show good agreement.

## 6.6 *Time-dependent neutrino emission profiles*

So far, all the comparisons we showed assumed steady neutrino emission as done in *Aartsen et al. PRL 124, 2020*. However, within the SkyLLH software interface, searching the public data for transient neutrino emission from point-like sources is also possible. Besides classes for spatial and energy PDFs, SkyLLH also provides classes that implement time PDFs. Hence, the signal PDF in Equation 6.1

can be modified to include a time PDF, $\mathcal{T}$:

$$f_s\left(\boldsymbol{x}|\delta_{src},\gamma\right) = \mathcal{S}\left(\psi|E_\mu,\sigma,\gamma\right)\cdot\mathcal{E}\left(E_\mu|\delta_{src},\gamma\right)\cdot\mathcal{T}(t_\mu|t_0,\sigma_T). \tag{6.3}$$

The current software version includes a box-shaped time PDF (assuming constant emission between a starting and end time) and a Gaussian-shaped time PDF centered at $t_0$ with width $\sigma_T$. Using the box-shaped time profile with start and stop times, respectively, of $t_{start} = 56927.86$ (MJD) and $t_{stop} = 57116.76$ (MJD) we can reproduce the fit of the neutrino flare from TXS 0506+056 that was published together with the data release.[23] We find best-fit parameters for the flare of the blazar TXS 0506+056 are $\hat{n}_s = 11.7$ and $\hat{\gamma} = 2.2$, which agree with the published values, namely $\hat{n}_s = 11.9$ and $\hat{\gamma} = 2.2$.

[23] IceCube Collaboration, "IceCube Data for Neutrino Point-Source Searches Years 2008-2018".

In neutrino astronomy, we commonly want to search for flares that happened at an unknown time in IceCube's history. For this purpose, SkyLLH supports the fitting of the parameters of a Gaussian-shaped time PDF (*i.e.*, $t_0$ and $\sigma_T$) using the unsupervised learning algorithm "Expectation Maximization (EM)".[24] The EM fitting algorithm is applied to the time sequence of the events, where each event is weighted with its signal-over-background PDF ratio of the spatial and energy PDFs, as in Equation 5.6. We create the time PDF with the best-fit time parameters and subsequently optimize the likelihood function with the signal PDF in Equation 6.3. Since the PDF ratio values depend on $\gamma$, we repeat these steps for several $\gamma$ values ranging from 1 to 5 and take the maximal *TS* from all EM fits as the final *TS* value.

[24] Dempster et al., "Maximum Likelihood from Incomplete Data via the EM Algorithm".

The EM method has been used with IceCube internal data by a previous work,[25] which showed that the published best-fit flare parameters and p-value for TXS 0506+056 could be reproduced.[26,27,28] We do the same test on the public data samples using the EM algorithm. We find that the best-fit parameters for the time-dependent neutrino fluence from TXS 0506+056 are $\hat{n}_s = 7.6$ and $\hat{\gamma} = 2.2$, centered at $\hat{t}_0 = 56972.6$ (MJD) with $\hat{\sigma}_T = 27.9$ days. In a published IceCube work that used the same data,[29] the flare parameters were $\hat{t}_0 = 57000 \pm 30$ (MJD), $\hat{\sigma}_T = 62 \pm 27$ days, $\hat{n}_s = 10^{+5.2}_{-4.2}$, and $\hat{\gamma} = 2.2 \pm 0.3$. However, it should be noted that the flare fitting algorithm and the signal energy PDF (see Section 6.3) and, therefore, the signal-over-background PDF-ratio weights are not directly comparable in the two cases. We estimate the significance of the observed flare and find a p-value of ∼5.8%, which is larger than the published $\sim 3\,\sigma$ significance.[30] However, as discussed in Section 6.5, a reduced p-value compared to previous works is expected at the location of TXS 0506+056.

[25] M. S. Karl, "Unraveling the origin of high-energy neutrino sources: follow-up searches of IceCube alert events".

[26] IceCube Collaboration et al., "Neutrino emission from the direction of the blazar TXS 0506+056 prior to the IceCube-170922A alert".

[27] IceCube Collaboration, "IceCube Data for Neutrino Point-Source Searches Years 2008-2018".

[28] Abbasi et al., "Search for Multi-flare Neutrino Emissions in 10 yr of IceCube Data from a Catalog of Sources".

[29] Ibid.

[30] Here we refer to the *local* p-value, with no corrections for multiple testing.

Despite the reduced significance, all flare properties are recovered within the uncertainties except for the flare width, which is smaller when using the EM method in the public data framework. This demonstrates the feasibility of neutrino flare searches with SkyLLH using ten years of public IceCube data.

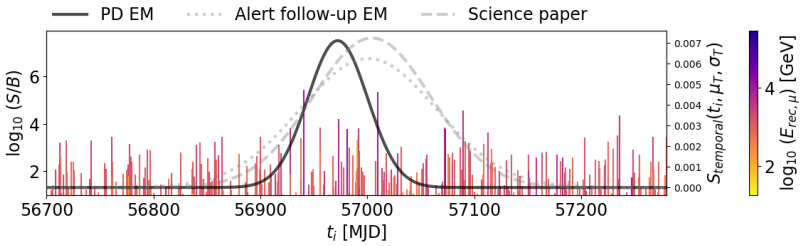


Figure 6.8: Time-independent weight of individual events during the 2014-2015 neutrino flare from the blazar TXS 0506+056. The weights are estimated in the SkyLLH framework for public data analyses. Each vertical line represents an event observed at the time indicated in Modified Julian Date format (MJD). The height of each line indicates the event weight: the product of the event's spatial term and energy term in the unbinned likelihood analysis (as indicated on the left y-axis), assuming the best-fit spectral index $\gamma = 2.2$. The color scale represents the reconstructed muon track energy. The Gaussian curves display the best-fit flare time window for different analyses: Figure courtesy of M. Karl.

## 6.7 *Applications and outlook*

In this chapter, we introduced a newly developed extension of the open-source software SkyLLH to perform time-integrated and time-dependent neutrino point-source searches based on ten years of public IceCube data[31]. This new interface allows users to reproduce reasonably well the results published by IceCube.[32,33] In this work, we have implemented the point-source analysis assuming power-law energy spectra and demonstrated its performance as a starting point. Thanks to the interest from the community, new features are now under development, including support for point-source analyses assuming arbitrary source flux shapes and multi-source searches (*stacking* analyses[34]).

The following publications have used our open-source SkyLLH interface for public data to produce scientific results:

- Peer-reviewed – Bellenghi, Padovani, et al., "Correlating High-energy IceCube Neutrinos with 5BZCAT Blazars and RFC Sources", *Astrophysical Journal Letters* (2023)
- Conference proceedings – Barbano et al., "Investigating high-energy neutrinos from blazars with a maximum-likelihood analysis of the IceCube observatory data", *Proceedings of 38th International Cosmic Ray Conference — PoS* (2023)
- Peer-reviewed – M. Karl, Padovani, and Giommi, "The spectra of IceCube Neutrino (SIN) candidate sources - IV. Spectral energy distributions and multiwavelength variability", *Monthly Notices of the Royal Astronomical Society* (2023)
- Accepted for publication in *A&A*, peer-reviewed – Rodrigues et al., "The Spectra of IceCube Neutrino (SIN) candidate sources – V. Modeling and interpretation of multiwavelength and neutrino data", *arXiv e-prints* (2024)

[31] https://github.com/icecube/skyllh/tree/master/skyllh/analyses/i3/publicdata_ps, https://icecube.github.io/skyllh/master/html/tutorials/publicdata_ps.html.

[32] Aartsen et al., "Time-Integrated Neutrino Source Searches with 10 Years of IceCube Data".

[33] Abbasi et al., "Search for Multi-flare Neutrino Emissions in 10 yr of IceCube Data from a Catalog of Sources".

[34] Huber, Krings, et al., "Results of IceCube searches for neutrinos from blazars using seven years of through-going muon data".

# 7 Methods to Unveil Populations of Weaker Sources

In Chapter 5, we described the unbinned likelihood-ratio test used for conducting a point-source analysis and presented its performance. In particular, we detailed the method for performing a search for the strongest emission in the sky, see Section 5.4. In this chapter, we describe three analyses that complement the point-source analysis by searching for an excess of multiple signals originating from multiple faint neutrino sources. First, we describe the methods of the so-called *hotspot population analysis* (HPA), which uses Poisson statistics to assess whether a population of rather weak sources is necessary to explain the number of hotspots observed in a neutrino sky map. Second, we present the population binomial test, which can be used to search for a cumulative excess from a predefined list of candidate sources. Finally, we describe the statistical method used in a recent study to correlate blazars with neutrinos in the IceCube's Southern sky.[1]

All of the methods described in this section have in common that they assess the significance of a population of local p-values obtained from the point-source analysis.

[1] Buson et al., "Beginning a Journey Across the Universe: The Discovery of Extragalactic Neutrino Factories".

## 7.1 Neutrino hotspots as a population of sources

From a very general perspective, the HPA takes a set of values and searches for a significant excess of small or large values within the set. This makes the approach applicable to many different types of population studies. In the context of this work, the analysis evaluates the set of local p-values populating a sky map obtained by scanning the Northern sky for neutrino emission from point-like sources (see Section 5.4). A statistically relevant excess of p-values individually lying above a minimum local significance threshold may be the signature of a population of subdominant sources. The method described below is based on that presented in previous studies.[2,3] As part of this work, we introduce a new signal simulation strategy. As we will see in Subsection 7.1.2 and Subsection 7.1.4, it allows us to more accurately assess the neutrino flux that produces the hotspots observed in a sky map.

[2] Aartsen et al., "All-sky Search for Time-integrated Neutrino Emission from Astrophysical Sources with 7 yr of IceCube Data".

[3] Aartsen et al., "Search for steady point-like sources in the astrophysical muon neutrino flux with 8 years of IceCube data".

The analysis strategy entails counting the number of hotspots in a sky map that exceed some significance threshold, and then comparing this number to what would be expected from the background alone. The background in question here is the combined diffuse atmospheric and astrophysical neutrino flux. The astrophysical signal from point-like sources is expected to appear as an excess above the background and produce several p-values smaller than one in the point-source analysis.[4] The important metric is the number of hotspots that are more significant than the threshold $x_{thr}$ out of a total of $N$ selected hotspots. This can be quantified as

[4] Further details about the point-source analysis can be found in Section 5.1.

$$n(x_{\text{thr}}) = \sum_{i=1}^{N} \Theta(x_i - x_{thr}), \tag{7.1}$$

where $\Theta(x)$ is the Heaviside function and the sum is evaluated for each hotspot $i$. Note also that the metric $n(x_{\text{thr}})$ is by definition a monotonically decreasing distribution.

If the hotspots are statistically independent, their count distribution is Poissonian, which allows us to estimate the significance of an excess of hotspots above a certain threshold using the Poisson p-value

$$p_{\text{Poisson}}(\lambda(x_{\text{thr}})) = \mathrm{e}^{-\lambda(x_{\text{thr}})} \sum_{k=n(x_{\text{thr}})}^{\infty} \frac{\lambda(x_{\text{thr}})^k}{k!}, \tag{7.2}$$

which is used as the test-statistic of the analysis. Here, $\lambda(x_{\text{thr}}) = Nx_{\text{thr}}$ represents the expected number of hotspots from the background at a threshold $x_{\text{thr}}$, and $k = n(x_{\text{thr}})$ is the observed number of hotspots at $x_{\text{thr}}$. Note that we use the $-\log_{10} p$ as significance thresholds for this analysis. Therefore, from now on, $x_{\text{thr}} = -\log_{10} p_{\text{thr}}$.

### *What is a "hotspot"?*

The input for this analysis is the output sky map of the point-source analysis. This Northern sky map is divided into a grid of approximately 0.2 by 0.2 square degree pixels. With the bin centers as candidate source coordinates, the signal likelihood is maximized, and the $-\log_{10} p$ is calculated at each grid point. The choice of how to define a *hotspot* in the skymap must ensure that the selected hotspots will be statistically independent to use Poisson statistics for the analysis. We define a hotspot as a pixel in the sky map that:

- has the lowest p-value among its eight closest neighboring pixels and
- is at least $1^\circ$ away from any other hotspot in the sky.

Therefore, if two hotspots are closer than $1^\circ$, only the most significant one is selected, while the other is assumed to be correlated with the more significant one and thereby discarded. Choosing a minimum distance $\Psi_{\text{min}} = 1^\circ$ ensures the selection of independent and, therefore, Poisson-distributed hotspots. For example, Figure 7.1 shows

the count distributions obtained from 1,000 simulated background sky maps at six different thresholds. We evaluate the compatibility of each observed distribution with a Poisson distribution by performing a Kolmogorov-Smirnov (KS) test.[5] The agreement is satisfactory, with p-values larger than 10% at all thresholds, as illustrated in Figure 7.2. Distributions at other thresholds can be found in Section B.1.

[5] Arnold and Emerson, "Nonparametric Goodness-of-Fit Tests for Discrete Null Distributions".

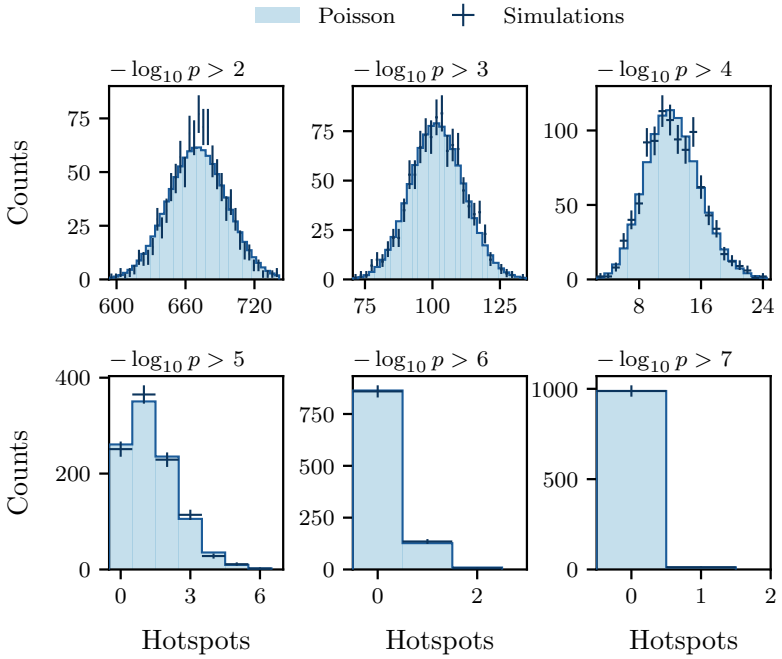


Figure 7.1: The count distribution of hotspots obtained from 1,000 simulated sky maps (dark error bars) is compared to the Poissonian distribution centered at its mean value (light blue histogram). In each panel, a different $-\log_{10} p_{\text{thr}}$ is considered.

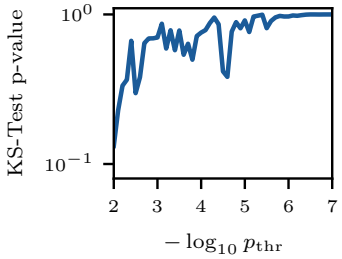


Figure 7.2: KS test p-values assessing the compatibility of the observed hotspot counts with a Poisson distribution. The distribution at the first threshold, $-\log_{10} p_{\text{thr}}$ =2.0, shows the greatest deviation from the null hypothesis of perfect agreement. However, all p-values are above 10%, indicating good overall agreement.

### 7.1.1 *Parametrization of the background expectation*

The number of expected hotspots from background $\lambda(-\log_{10} p_{\text{thr}})$ is estimated from Monte Carlo simulations for many thresholds in the range $-\log_{10} p_{\text{thr}} = [2.0, 7.0]$ in steps of 0.1. We simulate 1,000 background (atmospheric and diffuse astrophysical) sky maps and perform the hotspot search as per Equation 7.1. The mean of the distribution at a given threshold (see Figure 7.1) is taken as the expected hotspot count at that threshold.

A non-smoothing spline combined with a linear fit is used to interpolate between the 51 values for $\lambda(-\log_{10} p_{\text{thr}})$ as a function of the threshold to extrapolate the background expectation at any threshold. Smoothing the interpolation is not possible because of the slight deviation from the Poisson behavior at small $-\log_{10} p_{\text{thr}}$, visible in Figure 7.2.

The interpolation spline is shown in Figure 7.3. The unsmoothed linear interpolation is replaced by the linear fit at $-\log_{10} p_{\text{thr}} = 5.5$, *i. e.*, where the difference between the two parametrizations is minimal. The interpolation parametrizes the low $-\log_{10} p_{\text{thr}}$ region, while the fit is used for the high-threshold regime. The advantage of the linear fit is that it reduces the effect of statistical fluctuations in the

high-threshold regime. In $6 < -\log_{10} p_{\text{thr}} < 7$, where the statistical fluctuations begin to affect the experimental expectation significantly, the relative difference between the non-smoothing spline and the fit line reaches a non-negligible difference of $\sim 15\%$.

The typical output of the HPA is displayed in Figure 7.4 for a background simulation. The lower panel of the figure shows the Poisson p-value $p_{\text{Poisson}}$ at each $-\log_{10} p_{\text{thr}}$. The test-statistic of the experiment will be the minimum $p_{\text{Poisson}}$ out of the scan. The number of hotspots and corresponding $-\log_{10} p_{\text{thr}}$ at the minimum $p_{\text{Poisson}}$ are the best-fit parameters of the analysis. Since the analysis requires the scan of several significance thresholds, the experimental result (pre-trial $p_{\text{Poisson}}$) must be corrected for the multiple hypothesis testing, *i.e.*, for the *look elsewhere effect*. As the tests are all highly correlated, the trial-corrected p-value (or post-trial p-value) has to be estimated from simulations.

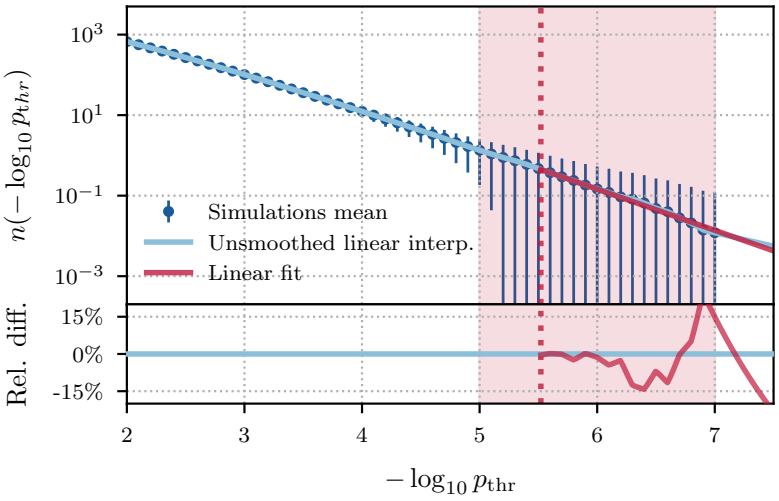


Figure 7.3: Parametrization of the expected number of hotspots from the background as a function of the significance threshold. **Top:** The blue dots represent the mean of the count distributions obtained from simulations, with statistical uncertainties. The unsmoothed linear interpolation of the mean values results in the solid, light blue line. In the high-threshold region, highlighted by the shaded area, a linear fit (solid, red line) is performed to estimate the expected number of hotspots. The dashed red line indicates the threshold value at which the fit replaces the interpolation. **Bottom:** Relative difference between the two parametrizations.

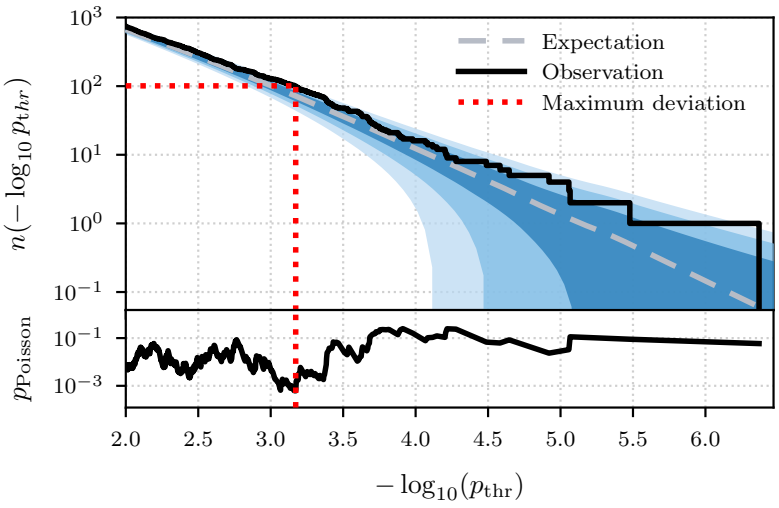


Figure 7.4: Example analysis output on a background pseudo-experiment. **Top:** The dashed grey line represents the background expectation, with the shaded blue areas indicating the $1\,\sigma$, $2\,\sigma$, and $3\,\sigma$ uncertainties. The solid black line shows the observed number of hotspots. The dotted red line highlights the maximum deviation from the background expectation. **Bottom:** Poisson p-value of the observed number of hotspots above each threshold.

### 7.1.2 Simulations and analysis performance

In principle, each HPA simulation (trial) requires the computation of a sky map. However, performing an unbinned likelihood maximization in the whole Northern sky necessitates $\sim$ 100 CPU hours, thus making the computation of $\mathcal{O}(10^{4-5})$ sky maps not feasible. Following the approach previously employed in analogous studies,[6] the problem is addressed as outlined below.

[6] Reimann, "Search for the sources of the astrophysical high-energy muon-neutrino flux with the IceCube neutrino observatory".

#### Simulations of background sky maps

The Poissonian behavior of the hotspot counts is a helpful feature for the simulation of background sky maps as well. First, we extract the hotspots with $-\log_{10} p > 2.0$ from 2,000 background sky maps and combine them in a large set of $-\log_{10} p$ (approximately 1.34 million). As expected in the background-only scenario, these p-values are uniformly distributed.[7] We can generate a single background pseudo-experiment by randomly sampling $N$ values from the aforementioned *pool* of background hotspots, where $N$ is the mean of the Poisson distribution for $-\log_{10} p_{\text{thr}} = 2$ (see the upper left panel of Figure 7.1). By construction, the simulations will contain the correct number of background hotspots with the correct frequency of significance, including statistical fluctuations.

[7] Consequently, the $-\log_{10} p$ are exponentially distributed.

Following this procedure, we construct the background test-statistic distribution, namely the distribution of the minimum Poisson p-values from the background pseudo-experiments. We perform the HPA on 2,000 background sky maps (the same used for constructing the pool of background hotspots). The resulting 2,000 test-statistic values distribution is presented in Figure 7.5.

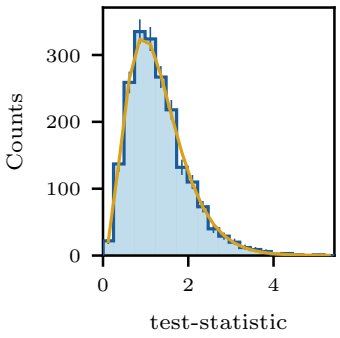


Figure 7.5: Distribution of test-statistics obtained by searching the hotspots in 2,000 simulated background sky maps. The yellow line represents the gamma distribution fitted to the distribution of *TS* values.

The distribution can be conveniently parametrized by a gamma distribution defined as

$$f(x|k,\theta) = \frac{1}{\theta^k \Gamma(k)} x^{k-1} \mathrm{e}^{-x/\theta}, \tag{7.3}$$

where $k$ and $\theta$ are the shape and scale parameters of the function, respectively. From the fit, we obtain $k = 3.68$ and $\theta = 0.35$. The median of the distribution is 1.16. To verify the compatibility of the distribution with the fitted gamma shown in Figure 7.5, we perform a Kolmogorv-Smirnov test, which yields in excellent agreement, with a p-value of 0.46. The gamma distribution can be used to calculate the $5\sigma$ quantile of the background *TS* distribution, which is necessary for the discovery potential calculation.

#### Simulations of sky maps with injected signal

To simulate a sky map with hotspots produced by astrophysical point sources, we take the following steps:

1. Generate a background pseudo-experiment as described in the previous paragraph;

2. Define a population of $N$ sources as $N$ declinations and $N$ corresponding fluxes;

3. By using the detector effective area at the source declination ($\delta$), convert the fluxes into a mean number of injected neutrinos, $\mu_{\text{inj}}$, for each source;

4. Draw the number of events to inject at the source position, $n_{\text{inj}}$, from a Poisson distribution with expectation value $\mu_{\text{inj}}$;

5. Based on $\delta$ and $n_{\text{inj}}$, select a $-\log_{10} p$ from a large pool of single point-source trials (the generation of the signal pool is described later);

6. If the selected $-\log_{10} p$ is greater than the minimum threshold of 2.0, it is a signal hotspot to be added to the population generated in the first step.

The last part of the hotspot selection procedure is the angular cut, which preserves the minimum angular distance $\Psi_{\text{min}} = 1^\circ$. The simulation of the cut is performed as part of step 6. before adding the hotspot to the population:

- For each signal p-value, draw a random number $r$ between 0 and 1 from a uniform distribution.

- If $r > M\,\Omega_{\text{HS}}/\Omega_{\text{hemi}}$, add the p-value to the population. $M$ is the number of hotspots already in the population, $\Omega_{\text{HS}} = \pi\Psi^2_{\text{min}}$ is the solid angle occupied by a hotspot, and $\Omega_{\text{hemi}}$ is the solid angle covered in the point-source scan of the Northern hemisphere from -3° to 81° declination.

- If $r <= M\,\Omega_{\text{HS}}/\Omega_{\text{hemi}}$, the hotspot is considered to be too close to another one. In this case, randomly select a hotspot from the ones already in the population and compare its $-\log_{10} p$ with the new candidate's one: the greater one is kept in the population, while the other is discarded.

This procedure accounts for the increasing probability of finding two hotspots too close to each other as the number of hotspots in the set grows. Finally, the maximum number of hotspots that can belong to a population is limited to the mean of the distribution of background $-\log_{10} p > 2.0$ plus three standard deviations. This is motivated by the fact that the population of background hotspots already includes the astrophysical diffuse neutrino background, which serves as our natural upper limit on the neutrino signal in the sky.

**Generation of a pool of signal hotspots**

The aforementioned "signal" hotspots can be generated as single point-source trials. We generate a large number of point-source simulations by injecting various signal strengths at several declinations, chosen uniformly in $\sin(\delta)$, with $\delta = [-3^\circ, 81^\circ]$. Each trial is recorded with information about the true number of injected events,

$n_{inj}$, and the local p-value obtained from the unbinned likelihood-ratio test. This procedure generates a large pool of hotspots generated according to a power-law neutrino spectrum $\propto E_\nu^{-\gamma}$.

We simulate background and signal events and perform the point-source analysis by scanning a disc of radius $1^\circ$ and centered at the injection location.[8] We select the minimum p-value from the scan as the candidate hotspot and save it in the pool for signal injections. While the procedure could be expedited by simply recording the $-\log_{10} p$ at the injection location (source), the disc scan produces a more realistic simulation of weak signals, with a more prominent effect when the hotspots are dominated by low-energy events ($\lesssim 1$ TeV) and their localization is less accurate (see Figure 4.9). The left panel of Figure 7.6 depicts the disc scan performed after the injection of 5 signal events sampled from a neutrino spectrum $\propto E_\nu^{-2.0}$ at declination $\delta \sim 10^\circ$. For reference, this signal is at the sensitivity level of the point-source analysis for a spectral index $\gamma = 2.0$ (see Figure 5.11). However, the minimum p-value is often localized $0.1^\circ - 0.2^\circ$ from the injection location (the yellow star in the figure). The ratio between the p-value at the injection pixel and the minimum p-value from the scan is shown in the left panel of the same figure. On average, for small signals, the p-value at the injection pixel can be up to a factor of $\sim 8$ larger than the minimum p-value, depending on the spectral index of the injected neutrino spectrum, $\gamma$, and on the signal strength, $n_{\rm inj}$. The average ratio between the two p-values remains greater than one even for $5\sigma$ equivalent sources (which need a mean number of signal events of $\sim 15$ and $\sim 70$ for $\gamma = 2.0$ and $\gamma = 3.2$, respectively).

[8] As we work in spherical coordinates, the *radius* represents an angular distance of $1^\circ$.

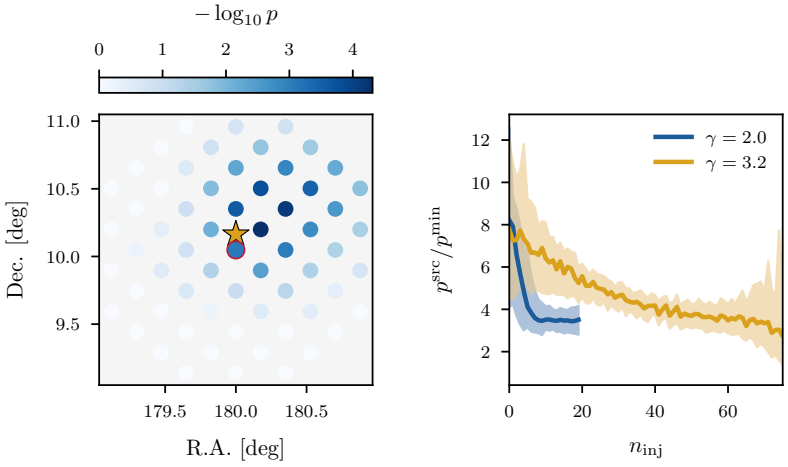


Figure 7.6: **Left:** Example disc scan to select a candidate signal hotspot. The disc is divided into equivalent pixels of $\sim 0.2 \times 0.2$ square deg. Each pixel is displayed as a dot, with the color scale representing their significance. The yellow star marks the source location. The pixel outlined in red includes the source location within its area. The most significant $-\log_{10} p$ (the darkest one) is 17 times smaller than the source one. **Right:** The ratio between the p-value at the source pixel and the minimum p-value from the scan as a function of signal strength. The point-source simulations are for two different injected power-law spectral indices, shown in different colors. Source locations are simulated between $0^\circ$ and $30^\circ$ in declination. The bands represent the central 68% quantile of the distributions. The $\gamma = 2.0$ curve is interrupted because sources with over 20 events are already well beyond the $5\sigma$ discovery threshold of the point-source analysis.

Figure 7.7 shows that by selecting the hotspots out of the disc scan, the variance of $-\log_{10} p$ for a given signal strength is reduced by up to 15% when the underlying signal spectrum is hard, *e.g.*, $(E_\nu/1\text{TeV})^{-2.0}$. Conversely, for a soft spectral index, *e.g.* $(E_\nu/1\text{TeV})^{-3.2}$, the variance stays roughly the same. However, in both cases, the flux at 1 TeV resulting in $-\log_{10} p > 2.0$ reduces by $\gtrsim 30\%$.

This procedure to choose the signal-like hotspots is more likely to select background fluctuations. Nevertheless, the same occurs when the hotspot search is conducted on the experimental sky map.

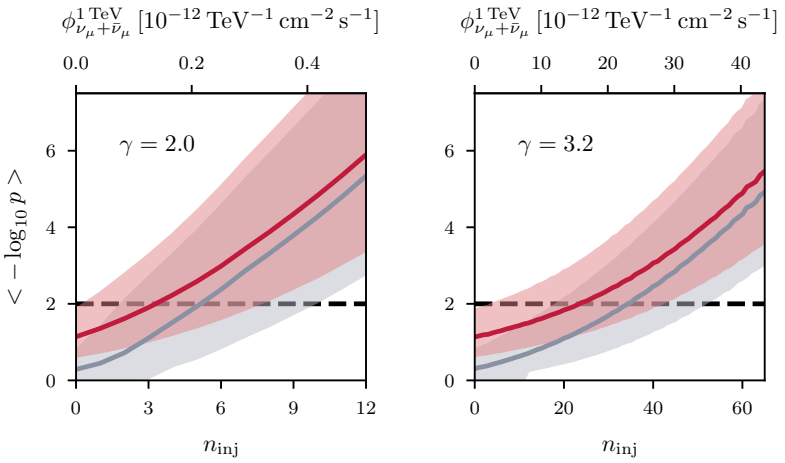


Figure 7.7: Median local $-\log_{10} p$ of the hotspots as a function of the signal strength, expressed both as the number of injected signal events (bottom $x$ axis) and flux normalization at 1 TeV (top $x$ axis). The curves represent averages across all declinations, as the hotspots are generated uniformly across the hemisphere. The p-value at the source location is shown in grey, while the red distribution shows the minimum p-values from the disc scan. **Left:** Simulated neutrino spectrum with a hard spectral index, $\gamma = 2$; **Right:** Soft spectral index, $\gamma = 3.2$.

### 7.1.3 *Study of the analysis performance*

The signal generation procedure described in this section is employed for the first time in the context of this analysis. Regarding analysis performance, it results in a more accurate and less conservative estimate of the analysis sensitivity. The effect is driven by the smaller average signal strength required to detect a signal above the background.[9]

The simplest scenario for evaluating the sensitivity of the analysis is that of a population of sources with equal neutrino fluxes at Earth. While being rather unrealistic, this population makes comparisons between different implementations easier. For example, Figure 7.8 displays the *TS* distributions for the sensitivity and $5\,\sigma$ discovery potential fluxes of a population of 64 equal strength sources. Complementarily, Figure 7.9 shows the sensitivity and $5\,\sigma$ discovery potential flux per source as a function of the number of sources simulated in the population. The implementation that injects signal hotspots from a pool of single point-source p-values at the source location is compared to the new one using the minimum p-values out of a $1^\circ$ scan around the source location. The new implementation reduces the estimated sensitivity flux by up to $\sim$ 20% in the small population regime. If the experimental sky map turns out to be compatible with the background hypothesis, this translates into up to 20% more stringent upper limits. Besides, from Figure 7.9, we observe a bending in the flux-per-source curves when they approach the astrophysical diffuse flux limit, *i.e.*, the large population regime. This effect has previously been understood as due to underestimating the total astrophysical diffuse flux being injected in the simulations.[10] In Sub-

[9] See Subsection 5.3.2 for a general definition of sensitivity and discovery potential.

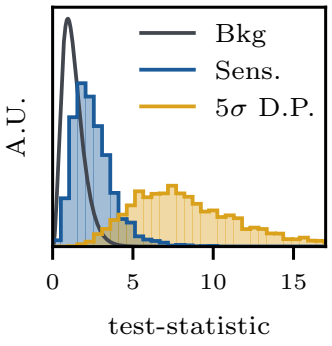


Figure 7.8: Test-statistic distributions corresponding to the flux per source for detecting 64 sources at the sensitivity level (blue histogram) and $5\,\sigma$ (yellow histogram). The simulated spectral index is $\gamma = 2.0$ and the two *TS* distributions are obtained for 2.1 and 4.3 neutrinos per source, respectively. The solid black line shows the background, approximated by the gamma distribution from Figure 7.5. Note that the distributions have been scaled up for clarity.

[10] Reimann, "Search for the sources of the astrophysical high-energy muon-neutrino flux with the IceCube neutrino observatory".

section 7.1.4, we propose a simple yet effective method to properly account for this additional flux.

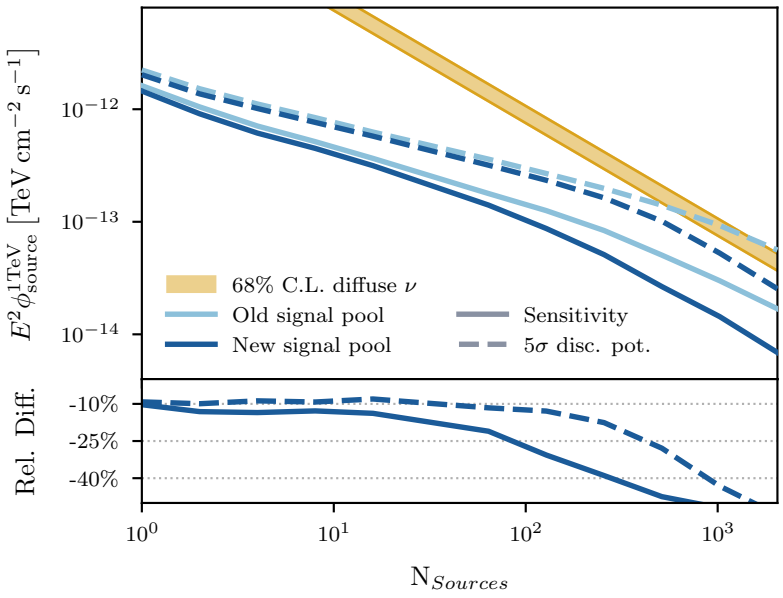


Figure 7.9: The sensitivity (dashed) and discovery potential (solid) $E_\nu^{-2}$ fluxes per source are shown as a function of the number of simulated sources in the sky. The light blue lines are obtained by injecting hotspots as the p-value at the simulated point-source location. The dark blue fluxes use signal hotspots defined as the minimum p-value from the disc scan described in the text. The best-fit astrophysical diffuse flux per source within $1\,\sigma$ uncertainty is shown as a yellow band. Its spectral index is 2.28, as per Stettner et al., "Measurement of the diffuse astrophysical muon-neutrino spectrum with ten years of IceCube data".

Before discussing the estimation of the astrophysical signal in the simulated sky maps, we examine the typical response of the HPA to different types of signals by performing controlled injection simulations. We simulate populations of hotspots containing $\sim 3\,\sigma$ sources (*i.e.*, with $-\log_{10} p \sim 2.9$) and perform the HPA. Figure 7.10 presents the cumulative distribution of the recovered sources' significance.

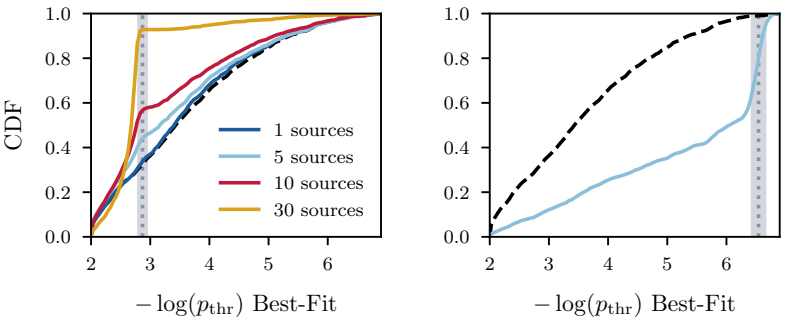


Figure 7.10: Response of the HPA to controlled signal injections shown as the cumulative distribution of the best-fit $-\log_{10} p_{\text{thr}}$ based on 2,000 trials. **Left:** Simulations of populations of $\sim 3\,\sigma$ sources, with each color representing a different number of injected sources. The dashed black line shows the background case. **Right:** Similar to the left panel, b but simulating only one population consisting of a single $\sim 5\,\sigma$ source. In both panels, the dotted grey line indicates the mean $-\log_{10} p$ of the injected sources, with the band representing the spread of the Gaussian distribution from which they are sampled.

The test shows that the HPA is not sensitive to a single source with a local significance of $3\,\sigma$. It needs approximately ten sources of that significance to recover the injected $-\log_{10} p$ in a reasonable fraction of the pseudo-experiments. In fact, random clusterings of background events are expected to produce $\sim 124 \pm 11$ hotspots (see Figure 7.3), where the uncertainty corresponds to one standard deviation. The Poisson p-value corresponding to such a signal would be $\sim 3\%$, before any correction for multiple testing. The right panel of Figure 7.10 shows the same study but when we simulate one single

source with a local significance of $5\sigma$. In this scenario, the analysis expects only 0.04 hotspots; therefore, one single source at that significance is enough to recover the injection in most simulations. In this case, the analysis *TS* would be $\sim 4\%$.

### 7.1.4 *Influence of the astrophysical diffuse neutrino flux on simulations*

Simulated background sky maps for the HPA already contain the total astrophysical diffuse flux, which is included as a background component of the point-source analysis. Concerning the signal hypothesis, the single point-source analysis assumes that the observed events originate from the combination of atmospheric and astrophysical diffuse fluxes with a clustering of astrophysical events originating from a point-like source. Thus, HPA pseudo-experiments with injected signals have two astrophysical diffuse fluxes: one from the background hotspots and an additional fraction in each signal hotspot. To properly assess the amount of astrophysical flux injected in each simulation, the background level in a sky map should be adjusted dynamically based on the injected point-source flux, ensuring that the total astrophysical flux does not exceed the measured value. However, this requires simulating an enormous number of background sky maps to parametrize the expected hotspot counts as a function of the fraction of astrophysical diffuse flux injected as point-like signals.

To quantify the impact of the diffuse astrophysical flux on the HPA, we simulated 100 background sky maps without astrophysical background and 100 with twice the usual background. Figure 7.11 compares the hotspot counts in these scenarios to the standard case, showing significant differences exceeding 3 standard deviations up to $-\log_{10} p_{\text{thr}} \simeq 3.2$.

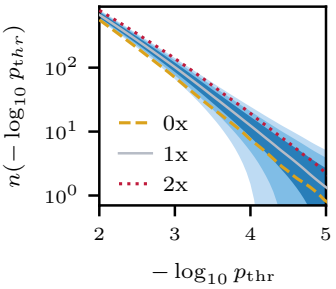


Figure 7.11: Hotspot counts obtained from background sky maps, including the best-fit diffuse astrophysical flux (grey solid), are compared to the counts obtained when no astrophysical component is included in the background (dashed yellow) and when we inject twice the best-fit astrophysical flux (dotted red). The blue bands represent the $1\sigma$, $2\sigma$, and $3\sigma$ Poisson uncertainties on the grey, solid line.

[11] Aartsen et al., "Search for steady point-like sources in the astrophysical muon neutrino flux with 8 years of IceCube data".

Previous work[11] resorted to removing the astrophysical diffuse background from the point-source simulations to generate signal hotspots. However, this approach leads to a modification of the signal hypothesis tested in the point-source analysis. Hence, we try to solve the issue by quantifying the amount of additional flux injected in each HPA simulation.

In the Northern sky, the assumption that the detected astrophysical diffuse background is isotropic holds.[12] Under this assumption, we can use Equation 4.17 to calculate the average number of muon-neutrino events from the all-flavor diffuse flux, $\phi^{\text{Astro}}(E) = 1.44 \times (E/100\ \text{TeV})^{-2.28} \times 10^{-18}\ \text{GeV}^{-1}\ \text{cm}^{-2}\ \text{s}^{-1}\ \text{sr}^{-1}$, contribute to a hotspot. First, we divide $\phi^{\text{Astro}}(E)$ by 3 to account only for the muon-neutrino flux, assuming an equal flavor ratio at Earth (see Subsection 2.2.2). Then, we calculate the average number of neutrinos contributing to a hotspot as $\phi^{\text{Astro}}(E)\,\Omega_{\text{PSF}}/3$, where $\Omega_{\text{PSF}} = \pi\Psi^2_{\text{PSF}}$. We use $\Psi_{\text{PSF}} = 1.7^\circ$, which is the angular distance corresponding approximately to the 68% quantile of the point-source point spread function[13] for events with muon energy $\sim$ 10 TeV and

[12] In Subsection C.4.1, we showed that a possible anisotropic contribution from the Galactic Plane on 13 years of up-going muon tracks is still negligible, see Subsection C.4.1

[13] For a description of the PSF of the point-source analysis used in this work, see Section 5.1.

averaged over angular errors from 0.1° to 0.6°. We obtain that each signal hotspot is produced by ∼0.3 neutrinos of astrophysical origin, adding to the ones injected as a point-source signal.

This approach does not alter the simulation pipeline. The only difference is that a slightly increased flux is associated with each source. Since 0.3 neutrinos over 9 years are below the IceCube sensitivity, the effect of the additional flux is only visible when a large number of sources, $\mathcal{O}(100)$, are simulated in the sky. This value of 0.3 is averaged over the entire Northern sky, so it may not be exact when injecting a few $(1-10)$ sources but provides a reasonable estimate when injecting $\mathcal{O}(100)$ sources, where the contribution becomes significant for the analysis. Figure 7.12 shows the effect of the proper assessment of the total injected flux: the bending of the sensitivity and discovery potential curves in Figure 7.9 disappears, and the estimation of the fluxes becomes reliable also for large populations of simulated sources.

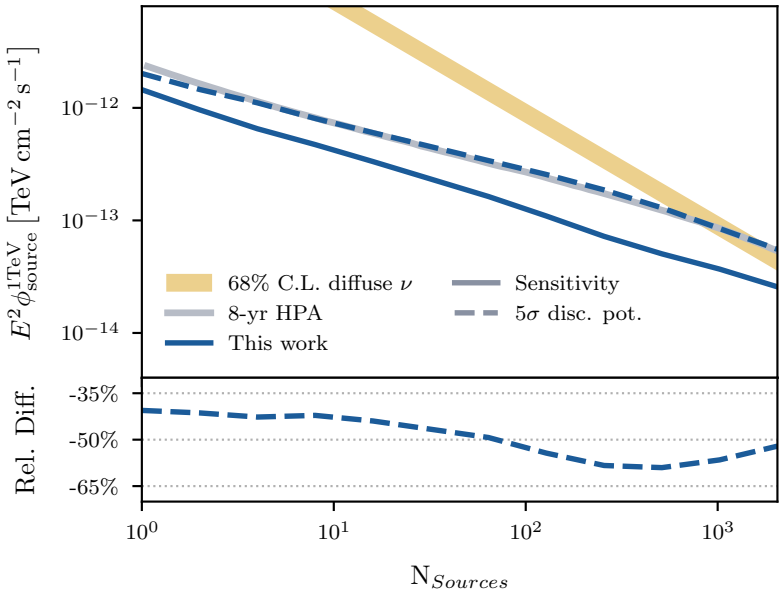


Figure 7.12: The final sensitivity and $5\,\sigma$ discovery potential fluxes per source for populations of equal strength at Earth sources are shown as a function of the population size in solid and dashed blue, respectively. For comparison, we show the sensitivity flux per source of the 8-year HPA (Aartsen et al., "Search for steady point-like sources in the astrophysical muon neutrino flux with 8 years of IceCube data"). The astrophysical diffuse flux is shown with its $1\,\sigma$ uncertainty in yellow. The lower panel shows the improvement in the sensitivity estimate of this analysis over the 8-year HPA.

In the context of this work, we perform the HPA on the sky map obtained from the point-source search performed on 9 years of upgoing muon-neutrino events.[14] Previously, the same analysis was conducted using 8 years of Northern sky events.[15] Both the 8-year and 9-year samples were constructed following the same selection criteria. Still, the 8-year sample included data from incomplete detector configurations (IC59 and IC79) and six years of IC86 data.[16] In contrast, this analysis uses 9 years of IC86 data, resulting in approximately 30% more muon-neutrino events in the 9-year dataset. Our sensitivity is comparable to the $5\,\sigma$ discovery potential of the previous 8-year analysis, as shown in Figure 7.12. Approximately 20% of this improvement is attributed to the increased sensitivity due to the larger neutrino data sample. The remaining $20\% - 40\%$ (depending

[14] Abbasi et al., "Evidence for neutrino emission from the nearby active galaxy NGC 1068".

[15] Reimann, "Search for the sources of the astrophysical high-energy muon-neutrino flux with the IceCube neutrino observatory".

[16] See Chapter 4 for a description of the detector configurations.

on the population size) is due to enhanced simulation strategies, including the new signal pool construction and consistent calculation of the injected astrophysical flux in simulations. It is also important to note that the 8-yr point-source analysis had a Gaussian prior term on the spectral index centered at $\gamma = 2.19$ in its likelihood. Thus, the two studies in Figure 7.12 are not exactly comparable. However, the sensitivity and discovery potential in the figure are estimated for a spectral index of 2.0, likely boosting the results of the previous analysis with the hard spectrum prior and thus making the estimated improvement of the new HPA conservative.

The results from the hotspot population analysis are discussed in Section 8.1. Next, we will explore another methodological approach to detect subdominant neutrino sources in a less biased manner by examining neutrino emissions from a predefined list of candidate astrophysical sources.

## 7.2 *Neutrino emission from a catalog of subdominant sources: a binomial test*

Given a list of $N$ candidate neutrino emitters, this approach evaluates a subset of sources that show positive results in the single point-source analysis. The test examines the sources' pre-trial p-values ($p_{\text{local}}$) to identify any excess of small p-values beyond what is expected from random background fluctuations. Therefore, this test is a special case of the HPA: Instead of having an unknown number of potential sources, we focus on a list of predefined sources, usually selected based on a prior belief that they are neutrino emitters. The probability of observing $k$ or more sources with p-values smaller than $p_k$ out of a total of $N$ sources is described by binomial statistics:

$$p_{\text{binom}} = \sum_{i=k}^{N} P_{\text{binom}}\left(i|p_k, N\right) = \sum_{i=k}^{N} \binom{N}{i} p_k^i \left(1-p_k\right)^{N-i}. \tag{7.4}$$

$p_{\text{binom}}$ is calculated for each $p_k$, *i.e.*, the p-value obtained from the point-source analysis at each source in the list. The pair ($k$, $p_k$) yielding the minimum $p_{\text{binom}}$ represents the best-fit result of the binomial test. The binomial p-value must be corrected for scanning $N$ p-value thresholds $p_k$. We apply the correction by comparing the observed p-value $p_{\text{binom}}^{\text{obs}}$ to the distribution of minimum $p_{\text{binom}}$ obtained from background simulations of the entire catalog. The trial-corrected significance is given by the fraction of simulated background $p_{\text{binom}}$ values smaller than the observed one. It is important to test all $N$ source locations on the same simulated neutrino sample to account for possible spatial correlations between nearby sources.

The price one has to pay for such a simple and robust test is that, given a best-fit number of sources contributing to a significant binomial excess, the specific objects responsible for an observed signal are not identified. One cannot distinguish between sources genuinely produced by an astrophysical signal and those boosted by

background fluctuations. Instead, the result indicates the compatibility of the entire list of target sources with the background-only hypothesis.

In this thesis, the binomial test has been used on two lists of candidate neutrino emitters: a list of 110 gamma-ray detected objects and a list of 47 X-ray bright Seyfert galaxies. The selection strategies for these lists and the outcomes of the searches are discussed in Subsection 8.2.2 and Subsection 8.2.3, respectively.

## 7.3 *Spatial correlation of neutrino hotspots with source catalogs*

The last analysis strategy to identify populations of sub-dominant neutrino sources in the sky that we need to introduce uses the method employed by Buson et al., "Beginning a Journey Across the Universe: The Discovery of Extragalactic Neutrino Factories", hereafter referred to as *Buson et al. ApJL 933, 2022*. Their study performs a spatial correlation analysis to explore possible associations between the sources listed in the 5th edition of the Roma-BZCAT Multifrequency Catalogue of Blazars[17] (5BZCAT) and the Southern neutrino sky, using 7 years of muon tracks recorded by the IceCube detector.[18] The authors observed a substantial deviation from the expected chance coincidence correlation, reaching the $\sim 4.5\,\sigma$ level,[19] leading to their claim of discovering *extragalactic neutrino factories*. As part of our research, we reproduce the result obtained by *Buson et al. ApJL 933, 2022* and conduct several additional tests to verify their claim. As we shall see in Section 8.3, where the results are presented, our findings do not support the discovery claimed by the published work. Here, we outline the methods used in the original paper and describe their adaptation for this work. The outcome of this search has been published in *Bellenghi et al. ApJL 955, 2023*,[20] and the following discussion closely follows our publication.

[17] Massaro et al., "The 5th edition of the Roma-BZCAT. A short presentation".

[18] Aartsen et al., "All-sky Search for Time-integrated Neutrino Emission from Astrophysical Sources with 7 yr of IceCube Data".

[19] Buson et al., "Erratum: "Beginning a Journey Across the Universe: The Discovery of Extragalactic Neutrino Factories" (2022, ApJL, 933, L43)".

[20] Bellenghi, Padovani, et al., "Correlating High-energy IceCube Neutrinos with 5BZCAT Blazars and RFC Sources".

### 7.3.1 *The blazar samples*

The 5BZCAT catalog includes coordinates and multi-frequency data for 3,561 sources, either confirmed blazars or exhibiting blazar-like characteristics. Upon its initial release, this catalog likely represented the most comprehensive collection, incorporating most well-documented literature sources. However, it is an inhomogeneous sample, collecting sources detected in various frequency bands and surveys. Moreover, it is not flux-limited, *i.e.*, it does not encompass all objects above a certain flux threshold in a given frequency band. As shown in the left panel of Figure 7.13, the 5BZCAT catalog exhibits significant undersampling in the Southern hemisphere due to a radio-optical identification bias towards the Northern sky.[21]

To assess the impact of using a flux-limited and uniformly distributed sample compared to an inhomogeneous one, we repeat our tests using a subset of the very-long baseline radio interferometry

[21] Massaro et al., "The 5th edition of the Roma-BZCAT. A short presentation".

[22] http://astrogeo.org/rfc/

(VLBI)-based Radio Fundamental Catalogue.[22] (RFC) This sample comprises 3,411 AGN, mostly blazars, with an average 8 GHz VLBI flux density $\geq$ 150 mJy. It was meticulously selected by A. Plavin et al., "Observational Evidence for the Origin of High-energy Neutrinos in Parsec-scale Nuclei of Radio-bright Active Galaxies" to ensure completeness above this limit. The distribution of the RFC sources in the sky is displayed in the right panel of Figure 7.13.

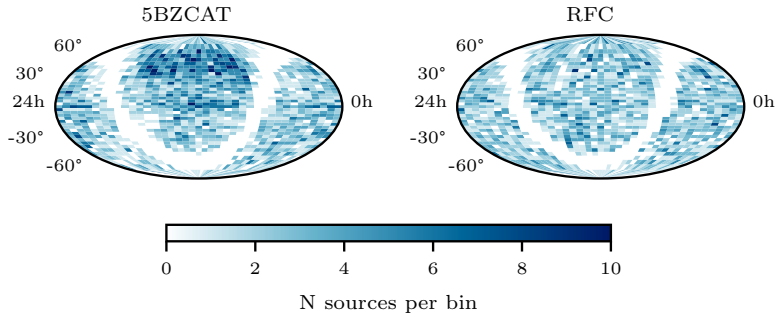


Figure 7.13: 5BZCAT (left) and RFC (right) sources uniformly binned in equatorial coordinates. Spatial non-uniformities in the 5BZCAT with a bias towards the Northern sky are evident.

The declination distribution of sources in the two catalogs is compared to the expected uniform distribution (excluding the galactic plane at galactic latitude $|b_{II}| < 10°$) in Figure 7.14. Aside from the 5BZCAT undersampling in the Northern sky, there are notable excesses at $\delta \sim 0°$ and $\delta \sim 40°$. KS and Wilcoxon-Mann-Whitney (WMW) tests reject the compatibility of the 5BZCAT declination distribution with the uniform distribution at more than $8\,\sigma$. In contrast, although not perfect, the RFC sources display better spatial uniformity (p-values from the compatibility tests are at the percent level).

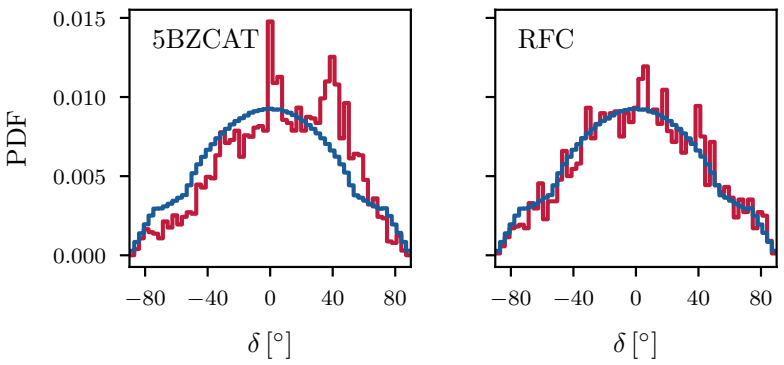


Figure 7.14: The declination distribution of the sources in the 5BZCAT (left) and in the RFC (right) catalogs in red are compared to the cosine distribution in blue. Note that the expected uniform distribution is not a perfect cosine because sources from the galactic plane are removed.

We use the RFC *2020_b* version, which has already been used to test for an association between the RFC and IceCube neutrinos by other works.[23,24] For both catalogs and for consistently with *Buson et al. ApJL 933, 2022*, we exclude from the correlation analysis

[23] A. V. Plavin et al., "Directional Association of TeV to PeV Astrophysical Neutrinos with Radio Blazars".

[24] Abbasi et al., "Search for Correlations of High-energy Neutrinos Detected in IceCube with Radio-bright AGN and Gamma-Ray Emission from Blazars".

sources overlapping with the Galactic plane ($|b_{II}| < 10°$). Additionally, to match the coverage of the neutrino sky map, only sources with $|\delta| < 85°$ are considered. Finally, when using the 5BZCAT, we omit the 92 objects classified as "BL Lac candidates".

### 7.3.2 *Statistical method*

*Buson et al. ApJL 933, 2022* correlates the 5BZCAT blazars with the neutrino sky map resulting from a point-source scan of the sky using 7 years of IceCube data.[25] This map is provided as a list of pre-trial local p-values on a grid of equivalent pixels of $\sim(0.11°)^2$ constructed using a HEALPix[26] projection with resolution parameter $Nside = 512$. Following *Buson et al. ApJL 933, 2022*, we denote the $-\log_{10} p_{\rm local}$ mapping the neutrino sky as $L$ to avoid confusion with the p-values of the correlation analyses. As already described in Section 5.1, the $L$ values are based on a maximum likelihood ratio comparing a background and a signal hypothesis. The former assumes that the neutrino emission is due to atmospheric background and diffuse astrophysical fluxes, while the latter includes an additional component from the source clustering around it. Larger values of $L$ indicate a lower compatibility of the neutrino data with the background-only hypothesis.

[25] Available at https://icecube.wisc.edu/data-releases/2020/02/all-sky-point-source-icecube-data-years-2012-2015/.

[26] Górski et al., "HEALPix: A Framework for High-Resolution Discretization and Fast Analysis of Data Distributed on the Sphere".

The goal is to search for a spatial correlation between the blazars and the IceCube neutrinos using the hotspots in the neutrino sky map. The relevant metric of this analysis is the number of hotspots in the sky associated with at least one source based on proximity criteria. As in Section 7.1, the hotspots are defined as independent pixels with local significance $L$ above a threshold $L_{\rm min}$ and are independent when they are at least $1°$ away from each other.[27]

[27] For the 7-year sky map this has been demonstrated for hotspots with $L > 3$ in Coenders, "High-energy cosmic ray accelerators: searches with IceCube neutrinos. Probing seven years of IceCube muon data for time-integrated emission of point-like neutrino sources".

The test-statistics of the correlation analysis is the number of hotspots ($\mathrm{HS}_\nu$) with $\mathrm{L} > L_{\rm min}$ having at least one source closer than an association radius $r_{\rm assoc}$:

$$TS = n(L_{\rm min}, r_{\rm assoc}) = \sum_{\{\mathrm{HS}_\nu : \mathrm{L} > \mathrm{L}_{\rm min}\}} \Theta\left(\sum_{\rm src} \Theta\left(r_{\rm assoc} - \sphericalangle(\mathrm{HS}_\nu, \mathrm{source})\right)\right) \tag{7.5}$$

where the first sum is over all neutrino hotspots belonging to the set with $L > L_{\rm min}$, and the second sum is over all sources. $\Theta(x)$ is the Heaviside function, which is 1 when the angular distance between the hotspot and the source is smaller than the tested association radius $r_{\rm assoc}$.

A set of $L_{\rm min}$ and $r_{\rm assoc}$ values are defined a priori, and the number of hotspot-blazar coincidences is computed for each combination. For each pair of ($L_{\rm min}$, $r_{\rm assoc}$), the p-value of the correlation is defined as the chance probability of getting the observed $TS$ (Equation 7.5). We derive it by performing the correlation analysis on pseudo-experiments generated by randomizing the position of the sources, thereby creating a simulated catalog in each trial. Following *Buson et al. ApJL 933, 2022*, we limit the scrambling of the source

locations to a maximum angular distance of 10° from their original position. The p-value is then given by the fraction of pseudo-experiments yielding a *TS* smaller than the observed one. The best-fit parameters are the ones yielding the smallest p-value. The best p-value is then corrected for the "look-elsewhere effect", *i.e.*, for having tested all possible combinations of $L_{\rm min}$ and $r_{\rm assoc}$. This final step is done by performing the entire analysis procedure on several pseudo-experiments. The number of correlations is computed for all combinations of parameters, and the best pre-trial p-value is recorded. The final trial-corrected p-value is obtained as the fraction of pseudo-experiments yielding a pre-trial p-value smaller than the observed one.

The authors scanned the $L_{\rm min}$ parameter in [3.5, 4.0, 4.5] and the $r_{\rm assoc}$ parameter between 0.4° and 0.7° in steps of 0.05°. They found 44, 19, and 9 hotspots above the three $L_{\rm min}$ thresholds, respectively. The largest deviation from the chance coincidence corresponds to ten correlations at $L_{\rm min} = 4.0$ and $r_{\rm assoc} = 0.55°$, meaning that 10 out of 19 neutrino hotspots with $-\log_{10} p_{\rm local} > 4.0$ have at least one blazar closer than 0.55°. The chance origin of this coincidence is excluded at $5\,\sigma$ before accounting for all trials. We reproduced the result using the same analysis parameters, as shown in the left panel of Figure 7.15.

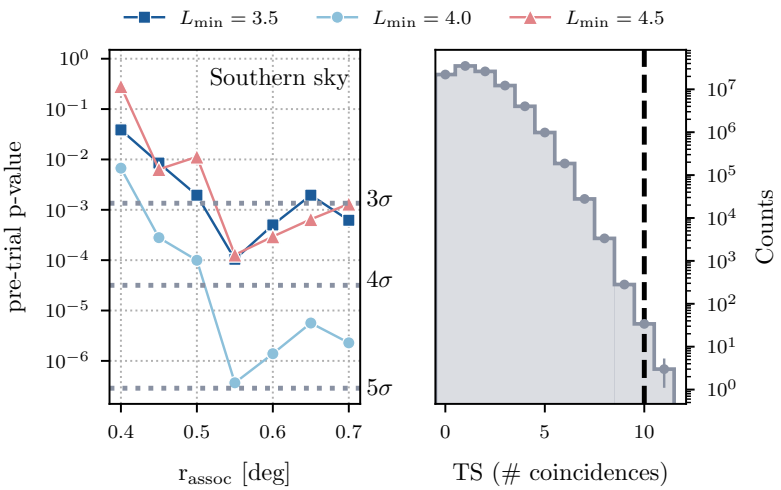


Figure 7.15: **Left:** Local p-value for the 5BZCAT – neutrino hotspot spatial correlation as a function of the association radius ($r_{\rm assoc}$) and for various minimum significance thresholds $L_{\rm min}$ in the 7-year Southern sky. The most significant correlation is found for $L_{\rm min} = 4.0$ and $r_{\rm assoc} = 0.55°$, corresponding to a significance of approximately $5\,\sigma$. **Right:** The *TS* distribution obtained from over $10^8$ pseudo-experiments with randomized source positions assuming the best-fit analysis parameters. The observed *TS* is marked as a dashed black line. The p-value is obtained as the fraction of pseudo-experiments with $TS \geq 10$.

The right panel of Figure 7.15 shows the distribution of the number of coincidences obtained from pseudo-experiments with randomized source positions assuming the best-fit parameters. The ten associated blazars are the same as in *Buson et al. ApJL 933, 2022*, *i.e.*, five FSRQs, three BL Lacs, and two blazars of uncertain type. The mean angular separation between the sources and their associated hotspots is $\langle\psi\rangle \sim 0.40°$, and the mean redshift is 1.3. By definition, all of them are radio-detected, while only three are gamma-ray sources.

In *Buson et al. ApJL 933, 2022*, they state that limiting the randomization of the source positions in pseudo-experiments reproduces the catalog's original structure (and non-uniformity) in the simulated ones. While this attempt to preserve the morphology of the catalog is a reasonable choice when dealing with a non-uniform sample, it is interesting to study its effect on the analysis. Figure 7.16 shows the distributions of 10,000 pseudo-experiments generated for the best-fit parameters, $L_{\text{min}} = 4.0$ and $r_{\text{assoc}} = 0.55°$, when the scrambling of the sources' position is limited to a maximum of 10° and when it is not. The distribution produced without any constraints on the scrambling exhibits a longer tail, meaning that the p-value would be larger (and hence less significant) for a given observed TS value.

We can use a Poisson distribution to interpolate the distributions in Figure 7.16 and infer the p-value at $TS = 10$. The Poisson expectation value is set at the mean of the *TS* distribution. We find that the p-value corresponding to a *TS* of 10 increases from $5.3 \times 10^{-7}$ to $1.7 \times 10^{-6}$ when no maximum shift from the original position is imposed. As a result, the pre-trial significance decreases from $4.9\,\sigma$ to $4.6\,\sigma$. While the choice made by the authors affects the statistical significance of their result in a non-conservative direction, we acknowledge that the effect is small and does not change the overall outcome of their work.

Remarkably, for the more uniform RFC catalog, the effect of this choice diminishes greatly and almost disappears as it should, as can be seen in Figure 7.17.

The results of the various tests performed to validate the claim of the discovery of blazars as PeV neutrino sources are presented in Section 8.3. For consistency with what has been done by the authors, we stick to the choice of generating pseudo-experiments by randomizing the sources' locations within 10° from their original positions.

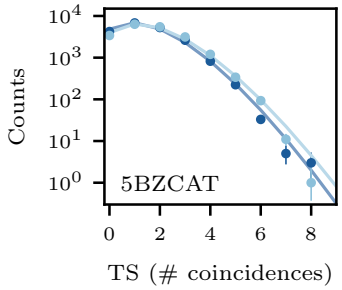


Figure 7.16: *TS* distributions degenerated by performing the correlation analysis on randomized 5BZCAT positions for the analysis parameters $L_{\text{min}} = 4.0$ and $r_{\text{assoc}} = 0.55°$. The dark histogram shows the case where the randomization is limited to a maximum angular distance of 10° from the original location. The light histogram depicts the same distribution when this limit is not imposed. The dark and light solid lines indicate the Poisson distributions with expectation values equal to the mean of the two *TS* distributions, respectively.

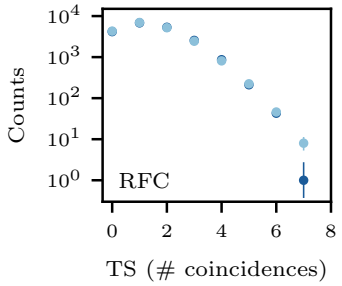


Figure 7.17: Same as Figure 7.16, but for the more uniform RFC catalog.

# 8 Results from Searches for Steady Neutrino Emission

This chapter summarizes all results from the analyses described in previous chapters. We start with the search for an accumulation of hotspots in the Northern neutrino sky map obtained using 9 years of data.[1] The second section is devoted to the point-source analysis of 13 years of IceCube data in the Northern sky.[2] Finally, the third section covers the results of various tests aimed at validating the claim of association between blazars and neutrino hotspots from a neutrino sky map based on 7 years of IceCube data.[3] It is important to note that while the first two sections report results produced by analyzing IceCube internal data, the last is solely based on public IceCube data and information.[4]

[1] IC86 2011-2019, see Section 4.7 for a description of the data sample.

[2] IC79 2010 and IC86 2011-2022, see again Section 4.7 for a description of the datasets.

[3] Buson et al., "Beginning a Journey Across the Universe: The Discovery of Extragalactic Neutrino Factories".

[4] See Chapter 6.

## 8.1 Search for an emergent population of hotspots

With a blind search for neutrino emission using 9 years of muon tracks induced by interactions of neutrinos originating in the Northern sky, we found the most significant spot to be spatially consistent with the location of NGC 1068, a nearby Seyfert 2 galaxy.[5] After producing a full scan of the sky, aside from searching for the most significant excess, we aim to determine whether a population of subdominant sources exists. These sources may collectively contribute to a detectable signal through the accumulation of minor fluctuations, which are otherwise too weak to be interesting individually. The hotspot population analysis (HPA) offers the methodology to test the hypothesis of such an excess over the background expectation, as detailed in Section 7.1.

[5] Abbasi et al., "Evidence for neutrino emission from the nearby active galaxy NGC 1068".

As a reminder, the data used for the test are the p-values smaller than 1% ($-\log_{10} p_{\text{local}} > 2.0$) populating the sky map obtained by performing the point-source analysis at each point in the sky using 9 years of NorthernTracks.[6] The minimum threshold of 1% and the minimum angular separation of $1^\circ$ ensure that the selected hotspots are statistically independent so that the expected number of hotspot counts follows the Poisson statistics (see Figure 7.1).

[6] This analysis only includes IC86 data from 2011 to 2019. The results of the point-source analysis on this dataset, including the sky map, have been published in Abbasi et al., "Evidence for neutrino emission from the nearby active galaxy NGC 1068".

We scan the $-\log_{10} p_{\text{local}}$ of all selected hotspots and use them as thresholds ($-\log_{10} p_{\text{thr}}$) for the analysis. We compare the number of hotspots observed with significance above each threshold to the expected hotspots induced by random clusterings of background

(atmospheric and diffuse astrophysical) events. Figure 8.1 displays the result. The maximum deviation from the Poisson expectation is found for one source at $-\log_{10} p_{\text{thr}} = 6.75$, which is NGC 1068. On average, background fluctuations produce 0.025 hotspots with a significance larger than the one of NGC 1068 in 9 years of observations. The corresponding Poisson p-value is 2.4% ($\sim 2\,\sigma$).

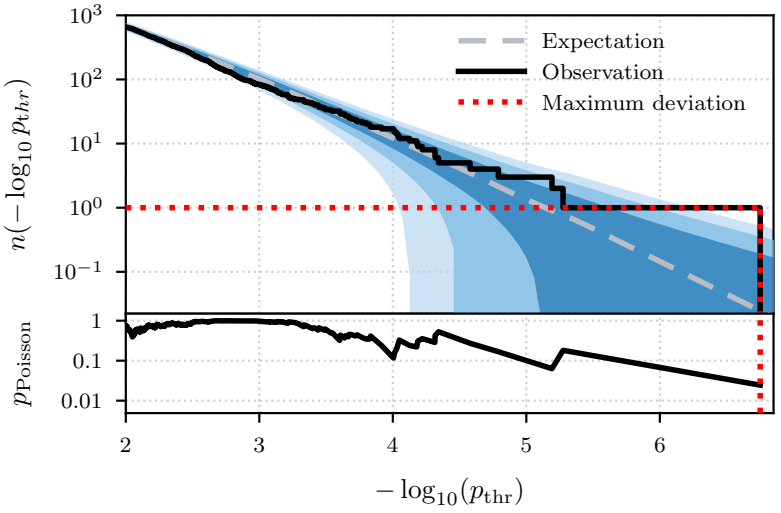


Figure 8.1: Results from the hotspot population analysis on the 9-yr Northern neutrino sky. In the upper panel, the observed hotspot counts as a function of the local p-value threshold ($-\log_{10} p_{\text{thr}}$) (solid, black line) are compared to the counts expected under the background-only hypothesis (dashed grey line) with 1, 2, and 3 Poisson standard deviations shown as blue shaded areas. The lower panel shows the Poisson p-value of the observation at each $-\log_{10} p_{\text{thr}}$. The dotted red lines indicate the maximum deviation from the background-only expectation.

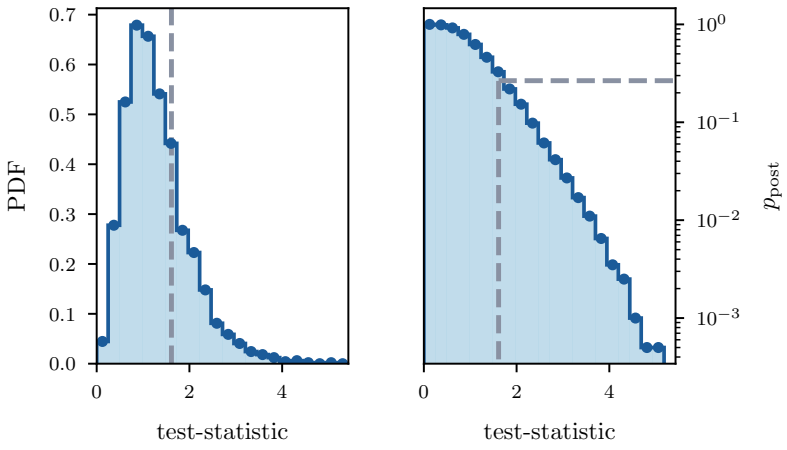


Figure 8.2: The left panel shows the distribution of Poisson p-values from 2000 pseudo-experiments, assuming the background-only hypothesis to be true. The distribution displayed in the right panel shows the fraction of pseudo-experiments returning a result more significant than the observed one as a function of the observed $-\log_{10} p_{\text{Poisson}}$. In both panels, the vertical dashed line marks the experimental result. In the right panel, the horizontal dashed line marks the corresponding post-trial background p-value.

Due to performing multiple tests, *i.e.*, scanning multiple significance thresholds, we need to penalize the significance of the outcome. Since the thresholds are incremental, the tests are highly correlated, which reduces the number of effectively independent tests. We estimate the trial-corrected significance based on background-only pseudo-experiments. The post-trial p-value is given by the fraction of background trials returning a minimum Poisson p-value smaller

than the observed one. In this analysis, a pre-trial p-value of 2.4% reduces to 26.6%, as shown in Figure 8.2, indicating a trial factor of $\sim$ 13 for testing 655 thresholds (corresponding to the total number of hotspots with $-\log_{10} p_{\text{local}} > 2.0$). The result is fully compatible with the background-only hypothesis.

From Figure 8.1, we observe an under-fluctuation compared to the parametrized background expectation[7] at the $2\,\sigma$ level around $-\log_{10} p_{\text{local}} = 3$. We have demonstrated in Subsection 7.1.4 that a severe underestimation of the astrophysical diffuse background would have a sizeable impact on the HPA. Therefore, it is reasonable to test whether an extreme scenario where the diffuse astrophysical background component does not produce any background hotspots could explain our observation. The result is illustrated in Figure 8.3, where the observation is compared to the background expectation computed on simulated skymaps that do not include the astrophysical diffuse flux as a background component of the point-source analysis.[8] The largest deviation is found for $-\log_{10} p_{\text{thr}} = 2.04$, where we observe 621 hotspots when $\sim$ 507 are expected. The corresponding pre-trial Poisson p-value is $6 \times 10^{-7}$, which translates into $4.9\,\sigma$. Therefore, we strongly reject the hypothesis that the astrophysical diffuse neutrino flux does not contribute to the total number of hotspots with $-\log_{10} p_{\text{local}} > 2.0$ observed in the sky map.

[7] See Section 7.1 for details about the background parametrization in the HPA.

[8] We use the diffuse neutrino flux from Stettner et al., "Measurement of the diffuse astrophysical muon-neutrino spectrum with ten years of IceCube data"

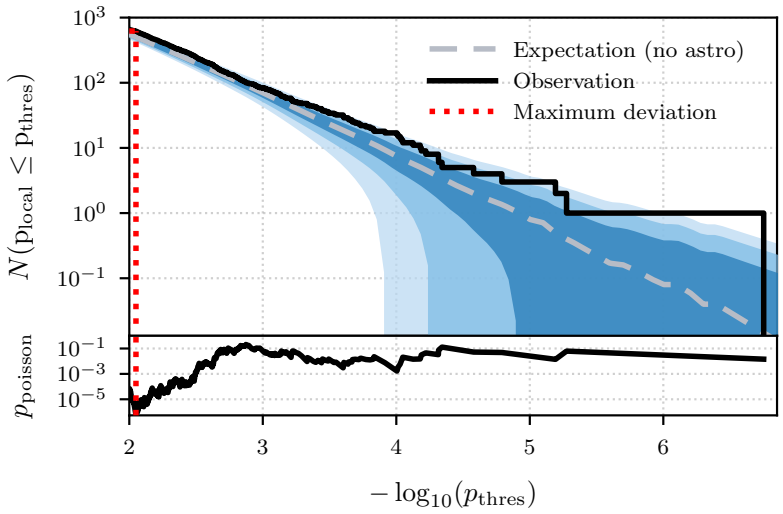


Figure 8.3: The observed hotspot counts are compared to a background expectation without the astrophysical diffuse component (see Figure 7.11). The maximum deviation is found for the total number of hotspots in the skymap, and we reject this background hypothesis at $4.9\,\sigma$.

### 8.1.1 *Neutrino Emission from a Population of Standard Candles*

Given the background-compatible result obtained from this analysis, we can constrain the total contribution to the IceCube diffuse flux from a population of hotspots. Specifically, we constrain the source luminosity of a population of neutrino standard candles at several source densities ($\rho_0$) simulated using the open-source Python

package FIRESONG.[9] We assume the cosmological evolution model based on the history of star formation rates by Madau and Dickinson[10] and allow a maximum redshift of 5. For each simulated source density $\rho_0$, the 90% C.L. upper limit on the neutrino luminosity of standard candles is defined as the luminosity corresponding to a neutrino flux that the HPA would detect with a minimum Poisson p-value smaller than the observed one in 90% of the trials. The result is shown in Figure 8.4. We can constrain the diffuse muon neutrino flux up to $\rho_0 \sim 10^{-9}$ Mpc$^{-3}$. A low local source density of $10^{-11}$ Mpc$^{-3}$, corresponding to approximately 100 standard candles in the universe, produces at most 10% of the equivalent diffuse neutrino luminosity observed by IceCube. Thanks to the increased amount of data and the improved simulation strategy developed in this work, our limit is approximately 50% more stringent than constraints set by the previous HPA.[11]

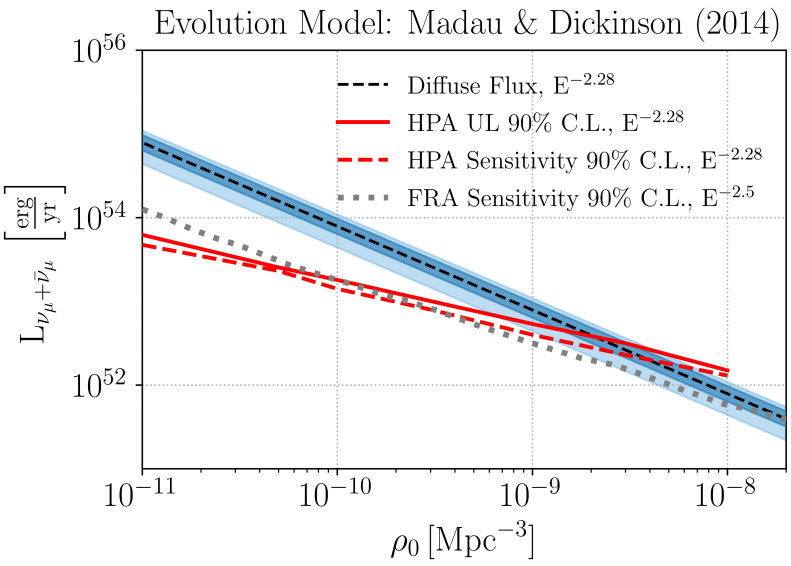


Figure 8.4: Upper limit on the luminosity per source from a population of steady neutrino standard candles based on the hotspot population analysis (HPA). The 90% C.L. sensitivity (dashed red) and upper limits (solid red) are plotted as a function of the local source density. The cosmological evolution model used is Madau and Dickinson, "Cosmic Star-Formation History". The luminosity corresponding to the astrophysical diffuse neutrino flux measured by IceCube is displayed as a dashed black line with its 1 $\sigma$ and 2 $\sigma$ uncertainties as blue bands. For comparison, we also show the sensitivity of the Fast Response Analysis (FRA) (Pizzuto et al., "Realtime follow-up of astrophysical transients with the IceCube Neutrino Observatory"), which searched for neutrino emission in the direction of IceCube's highest energy events (see Section 4.8), as a dotted grey line. The two analyses show similar sensitivities to an astrophysical signal, with the HPA being more sensitive in a scenario where fewer, more luminous objects emerge from the background.

The hotspot associated with NGC 1068 produces the most significant deviation from the background-only hypothesis in the HPA. The strength of this model-independent and discovery-oriented analysis is that it does not rely on any specific assumption regarding the physical properties of the source population it might find. However, in the case of a null result, the absence of underlying physics assumptions makes it hard to constrain specific astrophysical scenarios.

We proceed with a different strategy, and as part of the point-source analysis presented in the next section, we test the scenario where sources sharing similar physical properties to NGC 1068 might constitute a population of neutrino sources.

[9] Tung et al., "FIRESONG: A python package to simulate populations of extragalactic neutrino sources".
[10] Madau and Dickinson, "Cosmic Star-Formation History".
[11] Aartsen et al., "Search for steady point-like sources in the astrophysical muon neutrino flux with 8 years of IceCube data".

## 8.2 Search for neutrino emission in the Northern sky

**Disclaimer:** The results presented in this section are preliminary. While we do not anticipate significant changes in their interpretation, readers should be aware that future publications on this topic may report small differences due to refinements in precision. The analysis was designed and conducted by a team of analyzers at TUM, led by the author of this dissertation, who was also one of the analyzers. Aside from parts of the technical implementation of the analysis, this author developed the selection of candidate neutrino sources among X-ray bright Seyfert galaxies.

We present a comprehensive search for neutrino emission in the Northern sky. All searches reported in this section are based on the unbinned maximum likelihood method for point-source searches detailed in Chapter 5.

After adding three more years of up-going neutrino events from the complete detector configuration and one year of IC79 detector data,[12] we present results of several analyses searching for point-like neutrino emissions from single sources and populations. We examine the neutrino emission from a list of gamma-ray sources as done by previous studies,[13,14] and introduce a new list of X-ray bright AGN as promising neutrino source candidates. We list the target searches here briefly:

[12] The dataset has been described in Section 4.4 and Section 4.7.

[13] Aartsen et al., "Time-Integrated Neutrino Source Searches with 10 Years of IceCube Data".
[14] Abbasi et al., "Evidence for neutrino emission from the nearby active galaxy NGC 1068".

- A **scan of the Northern sky** ($-3^\circ \leq \delta \leq 81^\circ$). The goal is to perform a point-source analysis at each point in the sky and find the strongest deviation from the background-only hypothesis. The sky scan procedure was described in Section 5.4. We perform three sky scans assuming three different spectral hypotheses: one optimizes the spectral index of an unbroken power-law neutrino energy spectrum for maximum likelihood, while the other two fix the power-law index to 2.0 and 2.5, respectively. The final result is the hottest spot out of the three sky scans.

- A **catalog search on a list of 110 gamma-ray sources**. Consistently with previous work,[15] we search each source individually for neutrino emission, assuming an unbroken power-law spectrum with a floating spectral index. We discuss the source with the highest significance. This test allows us to re-evaluate the neutrino emission from NGC 1068, with 50% more data.

[15] Ibid.

- A **binomial population study.**[16] **on the list of 110 gamma-ray sources** Once again, we test the three spectral hypotheses of the sky scans and report the best result.

[16] This statistical analysis method has been described in Section 7.2.

- A **catalog search on a new list of 47 X-ray bright, non-blazar AGN**, introduced for the first time in this work. The detection of astrophysical neutrinos from NGC 1068 inspires the selection. In addition to the unbroken power-law hypothesis, we investigate the possibility that the X-ray bright corona of AGN is a neutrino

source[17] by testing the disc-corona model presented by two phenomenological studies.[18] We then report on the source with the highest significance. As the power-law assumption yielded the best results for this analysis, we limit the discussion to this spectral model.

- A **binomial population study on the list of 47 X-ray bright AGN**. The unbroken power-law and the disc-corona emission models are tested. Once again, only results based on the power-law assumption, which yields the most significant outcome, are discussed.

Even though results are reported for the power-law spectral assumption only, trial correction factors calculated in the following always correctly penalize the significance of the experimental results for having tested multiple spectral hypotheses.

### 8.2.1 *The hottest spot in the Northern sky*

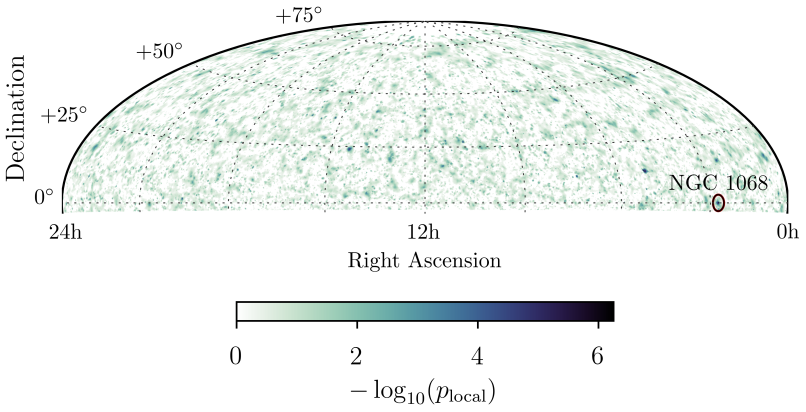


Figure 8.5: Hammer-Aitoff projection of the sky map from the maximum likelihood search for neutrino point-like sources in the Northern sky. The spectral index of the power-law energy spectrum is a free parameter in the likelihood-ratio test. The color scale indicates the negative logarithm of the local p-value ($-\log_{10} p_{\text{local}}$) at each point. Darker colors represent stronger deviations from the background-only assumption. The black circle marks the location of NGC 1068, spatially consistent with the most significant spot found.

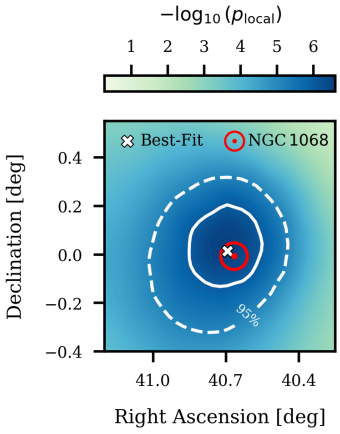


Figure 8.6: Zoomed-in sky scan around the most significant location in the Northern sky, marked by a white cross. A red dot marks the position of NGC 1068, with the red circle representing the optical size of the galaxy hosting the AGN. The 68% and 95% confidence regions are outlined in white. The color scale corresponds to that of Figure 8.5.

Scanning the sky, we find that the most significant spot is in the sky map with floating spectral index $\gamma$. It is spatially consistent with the nearby Seyfert 2 galaxy NGC 1068 (see Chapter 3), highlighted in Figure 8.5. The two likelihood maps calculated with fixed power-law spectral indices can be found in Appendix C.5. A more detailed scan of the most significant spot in the sky is shown in Figure 8.6. The confidence region for the hotspot localization is obtained from Monte Carlo (MC) re-simulations of the best-fit flux at the location of NGC 1068, assuming it is the hotspot source. The distance between the galaxy and the best-fit location from the scan is 0.04°. The hotspot parameters are summarized in Table 8.1, along with the results from the sky scans with fixed spectral indices.

The result of this search is the hotspot with the minimum p-value out of the three scans. However, to identify the smallest p-value correctly, we must correct each of the three hottest spots for having tested $\sim 400,000$ locations as potential neutrino sources. The correction factor is estimated directly from simulations to account

[17] See Chapter 3 for a discussion on the X-ray corona as the neutrino source in NGC 1068.

[18] Kheirandish, Murase, and Kimura, "High-energy Neutrinos from Magnetized Coronae of Active Galactic Nuclei and Prospects for Identification of Seyfert Galaxies and Quasars in Neutrino Telescopes".

for the statistical correlation among nearby pixels. For each spectral hypothesis, we simulated 2000 pseudo-experiments under the background-only hypothesis. From each background sky map, we selected the smallest p-value. We then compared the distribution of these 2000 p-values produced by background-only fluctuations with the experimental observation to determine the post-trial significance of the hottest spot of each sky map. We find that the floating $\gamma$ hypothesis has the smallest post-trial p-value of 7.6% ($1.4\,\sigma$), implying a large trial factor of approximately 294,000, as expected for this type of search.

| Spectral hypothesis | R.A. | Dec. | $\hat{n}_s$ | $\hat{\gamma}$ | Local significance |
|---|---|---|---|---|---|
| Floating $\gamma$ | $40.69^\circ$ | $0.02^\circ$ | 102.6 | 3.4 | $5.0\,\sigma$ |
| $\gamma = 2.0$ | $77.01^\circ$ | $12.98^\circ$ | 16.8 | – | $4.9\,\sigma$ |
| $\gamma = 2.5$ | $161.48^\circ$ | $27.32^\circ$ | 34.3 | – | $4.5\,\sigma$ |

Table 8.1: Coordinates (R.A. and Dec.), best-fit flux parameters ($\hat{n}_s$ and $\hat{\gamma}$), and local significance of the hottest spots in the sky scans obtained under three spectral hypotheses.

The sky scan is a powerful tool to identify the strongest overfluctuations in the sky without including any prior knowledge about specific candidate neutrino sources. However, it comes with a very large trial factor that will inevitably suppress the statistical significance of potentially interesting findings. An alternative strategy to reduce the number of trials is to define an independent analysis that tests a shorter list of candidate sources selected a priori. In the context of this work, we searched for neutrino emission from two predefined lists of objects. The selection criteria and the results of these searches are summarized in the following subsections.

### *8.2.2 NGC 1068 and the list of gamma-ray emitters*

The first list of candidate neutrino sources has been previously employed in several IceCube works.[19,20,21] It consists of 110 known gamma-ray sources, whose selection is motivated by the possible connection between the gamma-ray and neutrino luminosities of cosmic accelerators (see Section 2.2). The number of 110 candidates addresses the trial factor, as a $5\,\sigma$ pre-trial detection becomes $4\,\sigma$ after accounting for 110 tests. The catalog construction involves weighting the integrated gamma-ray flux above 1 GeV of all 4FGL sources in the declination range $-3^\circ \leq \delta \leq 81^\circ$ with the IceCube sensitivity at the source declination. The top 5% BL Lacs and FSRQs from this ranking are then added, along with all six starburst galaxies at allowed declinations, which are predicted to emit neutrinos via proton-proton interaction.[22] One Galactic source, MGRO J1908+06, is also included, as its expected neutrino emission assuming $\phi_\nu \propto \phi_\gamma$ is compatible with the differential sensitivity in Figure 5.11.

The same search detailed here was done on 9 years of up-going track-like events and found that NGC 1068 was the hottest source in this list. The hypothesis of a background-only origin of the observed data was rejected at $4.2\,\sigma$[23]. With 13 years of data, we searched again

[19] Aartsen et al., "Time-Integrated Neutrino Source Searches with 10 Years of IceCube Data".

[20] Abbasi et al., "Search for Multi-flare Neutrino Emissions in 10 yr of IceCube Data from a Catalog of Sources".

[21] Abbasi et al., "Evidence for neutrino emission from the nearby active galaxy NGC 1068".

[22] Murase, Ahlers, and Lacki, "Testing the hadronuclear origin of PeV neutrinos observed with IceCube".

[23] Abbasi et al., "Evidence for neutrino emission from the nearby active galaxy NGC 1068"

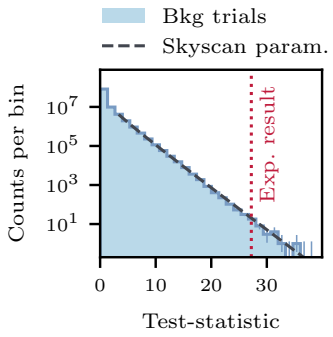


Figure 8.7: The distribution of the *TS* under the background-only hypothesis at the declination of NGC 1068 ($\delta = -0.01°$) is shown as a blue histogram. It is compared to the interpolated parametrization of the background *TS* distribution used to produce the sky scan (dashed grey line). The experimental TS value is marked as a dotted red line.

[24] Casella and Berger, "Statistical Inference", p. 229.

and found NGC 1068 to still be the most significant object in the catalog. The result is not surprising, as it is also spatially consistent with the hottest spot from the sky scan.

Its pre-trial p-value is $2.6 \times 10^{-7}$, translating into a local significance of $5.0\,\sigma$ in Gaussian-equivalent standard deviations. The background *TS* distribution at the declination of NGC 1068 is shown in Figure 8.7, alongside the experimental *TS* value of 27.2. For independent trials, the binomial probability of observing at least one trial with a p-value smaller than the observed one under the background-only hypothesis is analytically defined as[24]

$$p_{\text{post}} = 1 - (1 - p_{\text{local}})^N. \tag{8.1}$$

With $N = 110$, Equation 8.1 leads to a post-trial (global) p-value of $2.8 \times 10^{-5}$, corresponding to a significance of $4.0\,\sigma$.

The best-fit neutrino flux and its statistical uncertainty are visualized as a 2D likelihood scan in the flux parameters—the flux normalization at 1 TeV $\phi^{1\text{TeV}}_{\nu_\mu+\bar{\nu}_\mu}$ and the spectral index $\gamma$—in the left panel of Figure 8.8.

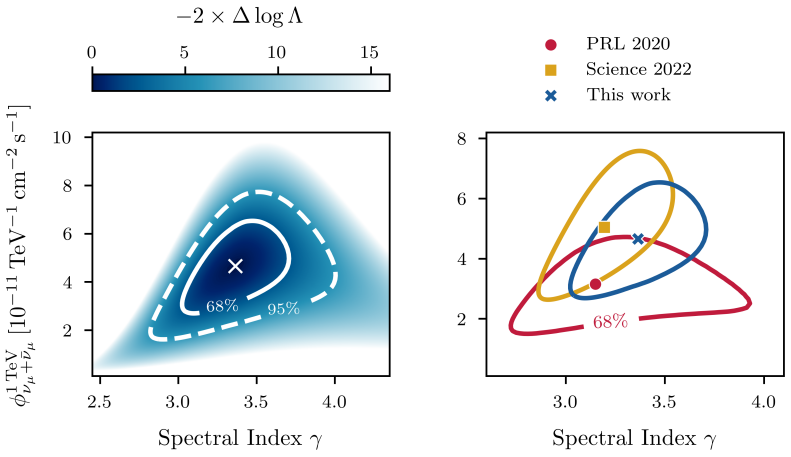


Figure 8.8: **Left:** 2D profile likelihood for the flux parameters of NGC 1068. the color scale corresponds to the difference $-2(\log\Lambda - \log\Lambda^{\text{max}})$, where $\Lambda$ is the likelihood-ratio evaluated at each pair of flux parameters and $\Lambda^{\text{max}}$ is the likelihood-ratio at the best-fit flux parameters. The cross indicates the best-fit values, while the white contours show the 68% (solid) and 95% (dashed) confidence levels, derived from Wilk's theorem assuming two degrees of freedom. **Right:** Comparison between various measurements of the neutrino flux of NGC 1068 performed in different IceCube analyses: *Aartsen et al. PRL 124, 2020* in red, *IceCube Coll. Science 378.6619, 2022* in yellow, and this work in blue. All confidence levels include statistical uncertainties only.

The 68% and 95% statistical uncertainties are estimated using Wilks' theorem after ensuring its validity on MC simulations (see Appendix C.6). The best-fit flux parameters are $\hat{n}_s = 102 \pm 25$ and $\hat{\gamma} = 3.4 \pm 0.2$, where the $1\,\sigma$ statistical uncertainties on each parameter are obtained from the one-dimensional profile likelihood. The mean number of signal events $\hat{n}_s$ can be converted into a flux normalization via the event rate equation

$$n_s = T \int_0^\infty dE_\nu A_{\text{eff}}(E_\nu, \delta_{\text{src}}) \times \phi_{\nu_\mu+\bar{\nu}_\mu}(E_\nu), \tag{8.2}$$

where $T$ is the exposure time, $\phi_{\nu_\mu+\bar{\nu}_\mu}(E_\nu) = \phi^{1\text{ TeV}}_{\nu_\mu+\bar{\nu}_\mu} \times (E_\nu/1\text{ TeV})^{-\gamma}$, and $A_{\text{eff}}(E_\nu, \delta_{\text{src}})$ is the IceCube's effective area[25] for detecting neutrinos with energy $E_\nu$, from the source declination $\delta_{\text{src}}$.

[25] See Subsection 4.7.3.

The best-fit flux normalization at 1 TeV with its statistical uncertainty is then $\phi^{1\ \mathrm{TeV}}_{\nu_\mu+\bar{\nu}_\mu} = 4.7^{+1.1}_{-1.3} \times 10^{-11}\ \mathrm{TeV}^{-1}\,\mathrm{cm}^{-2}\,\mathrm{s}^{-1}$. The impact of systematic uncertainties on the ice structure, the optical module efficiency, and mis-modeling of the astrophysical background component are negligible in this analysis, as discussed in Section 5.3 and Appendix C.4. Considering statistical uncertainties, the source's flux is unchanged compared to previous measurements: The $1\,\sigma$ likelihood confidence regions shown in the right panel of Figure 8.8 are consistent with each other. However, the spectral index of the power-law slightly softens in the latest measurement, moving from 3.2 to 3.4. The softening of the spectrum is caused by the relatively low reconstructed energies of the newly detected signal-like events, mostly with $\hat{E}_\mu$ between 100 GeV and 3 TeV.

The distribution of the experimental data in squared angular distance and reconstructed muon energy is shown in Figure 8.9. In both observables, an excess over the background only expectation is visible. Most of the signal excess is at reconstructed muon energies smaller than 1 TeV. It is important to stress that a binned likelihood analysis (or a goodness-of-fit test) on these histograms will not produce the same result as obtained from the unbinned likelihood approach used in this work. There are two main reasons for this: 1. None of the shown distributions includes information about the quality of the angular reconstruction,[26] and 2. The likelihood approach implements the joint spatial and energy distribution of the events.

[26] The $\sigma_{\mathrm{BDT}}$ variable described in Subsection 4.5.2.

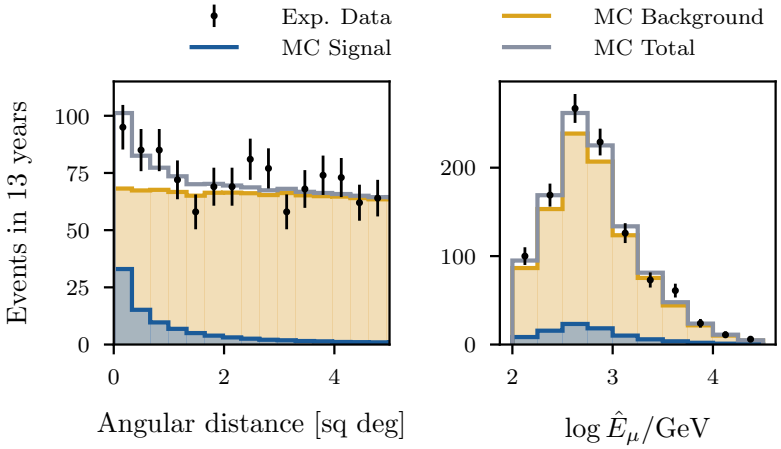


Figure 8.9: The angular distance squared (left) and energy distribution (right) of the experimental data (black dots) around the location of NGC 1068 are shown. MC resimulations of the best-fit flux (blue) and the background (yellow) are summed (grey) and compared to the experimental data distribution.

To extract the sensitive neutrino energy range of this spectral measurement, we construct a mapping of the reconstructed energy of the muons contributing to the excess into the corresponding probable parent neutrino energy. This mapping was done by selecting simulated neutrino events in a declination band of $\pm 2^\circ$ around the source's declination with reconstructed properties similar to those of the detected muons.[27] Each simulated event is weighted by the *TS* of the corresponding detected event, and the 68% (95%) central quantile

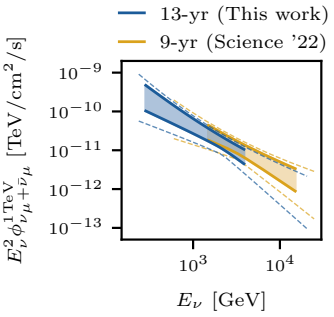


Figure 8.10: The $\nu_\mu + \bar{\nu}_\mu$ spectrum of NGC 1068 is shown as measured in the 9-yr analysis (yellow) and this work, using 13 years of data (blue). The solid contours indicate the 68% C.L. flux in the 68% C.L energy range. The dashed contours are for the 95% C.L. flux and energy uncertainties.

[27] We selected simulated events with reconstructed energy and angular uncertainty differing from the detected ones by 10% at maximum.

of the obtained neutrino energy distribution gives the estimated $1\sigma$ ($2\sigma$) energy range. The sensitive energy intervals are $[0.3,\ 2.8]$ TeV at 68% C.L. and $[0.2,\ 20.6]$ TeV at 95% C.L.. They are slightly shifted compared to the energy ranges obtained by the previous analysis,[28] $[1.5,\ 15]$ TeV at 68% C.L. and $[0.6,\ 24.8]$ TeV at 95% C.L.. However, the two measurements remain compatible, as visible in Figure 8.10.

[28] Abbasi et al., "Evidence for neutrino emission from the nearby active galaxy NGC 1068".

Assuming all three neutrino flavors contribute equally, as expected for neutrino oscillations over cosmic distances, the total flux is given by our measured muon-neutrino flux multiplied by 3. With a source luminosity distance of 10.1 Mpc,[29] and assuming isotropic neutrino emission, the equivalent neutrino luminosity is $L_\nu = 10^{43.1\pm0.1}$ erg/s in $[0.3,\ 2.8]$ TeV, where the uncertainty is statistical only.

[29] See Section 3.1.

This analysis cannot rule out the possibility that the shift of the neutrino flux to softer spectra is due to a time-variable spectrum. Dedicated time-dependent analyses[30] will settle the matter in the future. Statistical fluctuations and/or time variability could also explain the slight decrease in the significance of the neutrino emission from NGC 1068 compared to previous work. Another possibility is that the power-law spectrum assumed in this work does not accurately describe the true spectral shape of the neutrino emission in the observed energy range. Therefore, a more accurate spectral characterization, particularly below 100 GeV, should be a primary focus of future measurements.

[30] Abbasi et al., "A Time-Variability Test for Candidate Neutrino Sources Observed with IceCube"

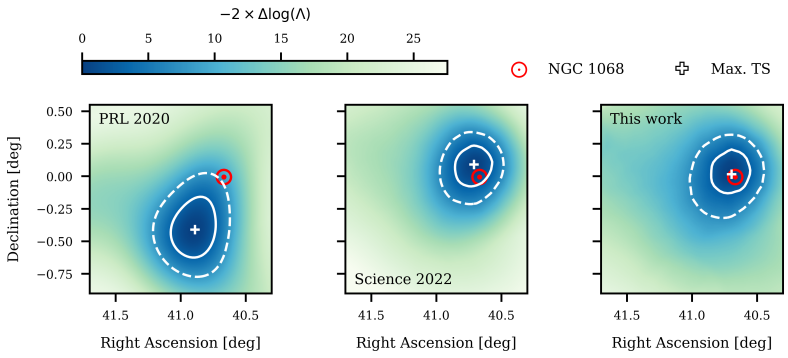


Figure 8.11: Profile likelihood scan around the location of NGC 1068. These figures are similar to Figure 8.6, but the color scale corresponds to the difference $-2(\log\Lambda - \log\Lambda^{\max})$, where $\Lambda$ is the likelihood-ratio evaluated at each location in the sky and $\Lambda^{\max}$ is the likelihood-ratio at the hottest spot. **Left:** The result of *Aartsen et al. PRL 124, 2020*; **Center:** The result of *IceCube Coll. Science 378.6619, 2022*; **Right:** The result of this work from the analysis of 13 years of data. Note that the central and left panels use the same concept of an MC-based likelihood, but this work combines two IceCube detector configurations, IC79 and IC86 (see Section 4.7 for details).

As a final remark on the new measurement of the neutrino signal from NGC 1068, it is worth noting that the localization of the signal has also improved over repeated measurements. This is visualized in Figure 8.11, where the most significant neutrino emission shifts toward the source location thanks to improved detector calibration and analysis methods (left panel to central panel) and increased statistics (central panel to right panel).

NGC 1068 is the most significant source in the list of gamma-ray sources. What about the remaining 109? We performed a binomial test to study the distribution of the local p-values obtained at the

location of each source. In this case, we tested three unbroken power-law spectra again: one with a floating spectral index and two with fixed spectral indices of 2.0 and 2.5.

For each list of $N = 110$, we compute the binomial p-value (hereafter indicated as $p_{\text{binom}}$ to avoid confusion) of observing $k$ out of 110 sources with $p_{\text{local}} \leq p_{\text{local}}^k$ (see Section 7.2). From each scan, we select the minimum $p_{\text{binom}}$ and correct it for having tested 110 local p-values as significance thresholds. Finally, the minimum $p_{\text{binom}}$ out of the three must be penalized for testing three spectral shapes for the neutrino emission. We find that the minimum $p_{\text{binom}}$ occurred under the floating spectral index hypothesis for 3 sources out of 110, contributing to a $3.0\,\sigma$ excess: NGC 1068, TXS 0506+056, and PKS 1424+240. The result is visualized in Figure 8.12, where the lower panel shows $p_{\text{binom}}$ when looking at one, two, three, ..., $N$ objects in the list, sorted by increasing $p_{\text{local}}$.

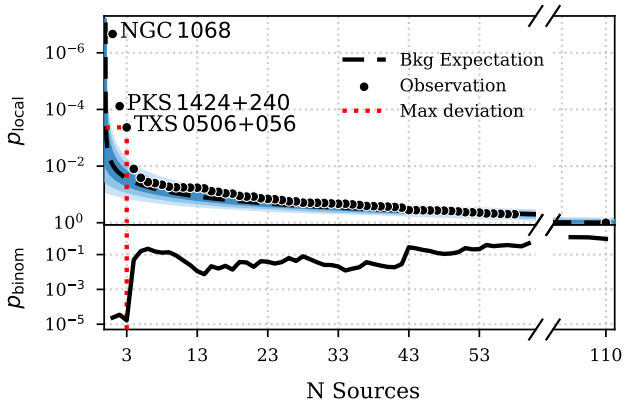


Figure 8.12: Binomial excess from the list of 110 gamma-ray sources, sorted by increasing $p_{\text{local}}$. **Upper panel:** $p_{\text{local}}$ threshold for the test as a function of the number of sources tested. The dashed black line indicates the mean background expectation estimated from MC simulations, with Poissonian uncertainties ($1\,\sigma$, $2\,\sigma$, $3\,\sigma$) as blue bands. **Lower panel:** $p_{\text{binom}}$ for each subset of sources considered in the scan. A red dotted line indicates the maximum deviation from the background. The three objects contributing to the binomial excess are highlighted.

The same three objects contributed to the most significant excess in the previous search.[31] Coherently with the expectation, the statistical significance decreases from $3.4\,\sigma$ to $3.0\,\sigma$. The last source contributing to the excess is TXS 0506+056, a blazar from which one neutrino flare and one single high energy event were detected.[32,33] Our time-integrated analysis of this object will inevitably detect its emission with lower significance as the accumulated background increases with exposure. Hence, as long as TXS 0506+056 drives it, the significance of the binomial excess will decrease over time. No new objects from this list of gamma-ray sources seem to contribute to a population signal, most likely pointing to a gamma ray–neutrino connection being less trivial than a simple linear correlation.

[31] Abbasi et al., "Evidence for neutrino emission from the nearby active galaxy NGC 1068".

[32] IceCube Collaboration et al., "Neutrino emission from the direction of the blazar TXS 0506+056 prior to the IceCube-170922A alert".

[33] IceCube Collaboration et al., "Multimessenger observations of a flaring blazar coincident with high-energy neutrino IceCube-170922A".

### *8.2.3 Neutrinos from X-ray bright Seyfert galaxies*

Currently, only three neutrino source candidates have been detected by IceCube with some statistical confidence ($\gtrsim 3\,\sigma$). They have strikingly different natures: our own non-active galaxy, the Milky Way; the flaring blazar TXS 0506+056; and the non-jetted AGN NGC 1068. The two extragalactic objects produce a small part ($\sim 1\%$) of the total

diffuse astrophysical neutrino flux. Whether they belong to a population of sources that share similar astronomical features and could explain a larger fraction of the diffuse neutrino emission remains an open question.

Here, we test the hypothesis that AGN sharing characteristics similar to the Seyfert 2 NGC 1068 may be a population of neutrino sources. As discussed in Chapter 3, observational and theoretical considerations restrict the likely origin of the neutrinos from NGC 1068 to the region close to its accretion disc around the SMBH. Let us briefly summarize again the key points leading to this conclusion:

- No other possible source within the galaxy/AGN can reach the measured neutrino power, except for the disc-corona system;
- No accompanying gamma rays have been detected at the neutrino energies (TeV) by MAGIC[34] and HAWC,[35] and the GeV photon flux is approximately two orders of magnitude lower than the neutrino one;[36]
- The AGN corona can naturally provide the necessary UV photon targets for neutrino production and the X-ray photons to reprocess the TeV radiation to MeV energies;
- The existence of "gamma-ray hidden" neutrino sources could naturally explain the $\mathcal{O}(10)$ TeV diffuse neutrino flux observed by IceCube[37] without violating the *Fermi*-LAT GeV gamma-ray background (see Subsection 2.2.2).

Therefore, we investigate the possibility that the X-ray bright corona of AGN is a neutrino source by using X-rays as tracers of neutrino production. Leveraging invaluable scientific connections with experts in the X-ray and astronomy fields, we produce a new selection of bright X-ray sources and search them individually for point-like neutrino emission. Additionally, we investigate the collective signal contribution of the selected sources employing the binomial analysis method, as shown previously for the list of gamma-ray emitters.

### *Selection criteria*

Indications of compelling deviations from the background have been reported for two other X-ray bright, non-blazar, AGN by IceCube: NGC 4151 ($2.9\,\sigma$)[38] and CGCG 420−015 ($2.3\,\sigma$)[39]. Moreover, NGC 4151 and CGCG 420−015 out of a list of 27 X-ray bright Seyfert galaxies contributed to a binomial excess of $2.7\,\sigma$.[40] Following these hints, we select a list of X-ray bright Seyfert galaxies with updated criteria.

We use the BAT Spectroscopic Survey (BASS)[41] *Swift*/BAT 70-month catalog,[42] an all-sky survey of AGN detected in the 14-195 keV band. Out of the 838 AGN it comprises, we select sources in the declination range, $-3^\circ < \delta < 81^\circ$, classified as Seyfert galaxies in the more recent *Swift*/BAT 105-month catalog.[43,44] Assuming a linear correlation between the neutrino and the X-ray fluxes and considering the sensitivity improvement of the current analysis over the

[34] Acciari et al., "Constraints on Gamma-Ray and Neutrino Emission from NGC 1068 with the MAGIC Telescopes".

[35] Willox and HAWC Collaboration, "HAWC Follow-up on IceCube evidence from NGC 1068".

[36] Ajello et al., "The Fourth Catalog of Active Galactic Nuclei Detected by the Fermi Large Area Telescope: Data Release 3".

[37] Murase, Guetta, and Ahlers, "Hidden Cosmic-Ray Accelerators as an Origin of TeV-PeV Cosmic Neutrinos".

[38] Goswami, "Search for high-energy neutrino emission from hard X-ray AGN with IceCube"

[39] Glauch et al., "Searching for High-Energy Neutrino Emission from Seyfert Galaxies in the Northern Sky with IceCube"

[40] Ibid.

[41] https://www.bass-survey.com/index.html.

[42] Ricci et al., "BAT AGN Spectroscopic Survey. V. X-Ray Properties of the Swift/BAT 70-month AGN Catalog".

[43] Oh et al., "The 105-Month Swift-BAT All-sky Hard X-Ray Survey".

[44] As the X-ray flux of the sources is not given in this updated catalog version, we could not use it for the selection.

previous version based on 9 years of data,[45] this analysis will be sensitive to neutrinos produced by any source with at least 20% of the X-ray flux of NGC 1068. Hence, we select all sources with at least 20% of the X-ray flux ($F_X$) of NGC 1068.

We select the objects with the highest $F_X$ corrected for the absorption in matter surrounding the accreting system along the line of sight. This absorption is typically parametrized by the neutral hydrogen column density ($N_H$, see Chapter 3). This so-called *intrinsic* X-ray flux ($F_X^{intr}$) is provided in the BASS catalog.

[45] See Subsection 5.3.2

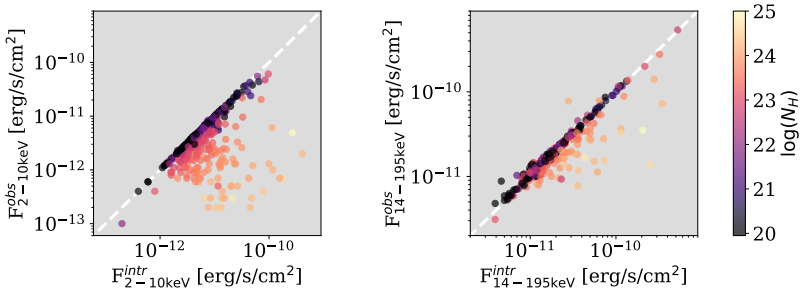


Figure 8.13: Correlation between the observed and intrinsic X-ray fluxes of Northern Seyfert galaxies with different obscuration levels ($\log N_H$, color scale) in the BASS catalog. Absorption strongly affects the correlation for softer X-ray fluxes (left). The conversion from observed to intrinsic flux relies on models of the torus surrounding the SMBH, which suffer from large uncertainties (see Ricci et al., "BAT AGN Spectroscopic Survey. V. X-Ray Properties of the Swift/-BAT 70-month AGN Catalog"). In contrast, the higher penetration power of X-ray fluxes above 10 keV makes the absorption negligible up to $\log N_H \simeq 23.5$ (right).

Specifically, we choose to use the hard X-ray component of the spectrum in the 20 to 50 keV band: While harder radiation has higher penetration power through obscuring material, as shown in Figure 8.13, we want to ensure robustness to a possible bias against objects with an early thermal turnover in the X-ray spectrum. This cutoff, typically observed between 100 and 300 keV, is related to the maximum energy that thermal electrons in the corona can impart to the UV disc photons through inverse Compton scattering. As discussed in Subsection 2.3.3, when the photons' energy approaches the thermal energy of the electrons, the Compton scattering is balanced by pair-production processes. Hence, the cutoff should appear where the thermalization of the photons to the electron temperature occurs. For some AGN, an early cutoff below 100 keV has been observed, indicating a lower temperature corona[46]. In Section 3.2, we have discussed that a $\sim 1-10$ TeV neutrino flux, as observed from NGC 1068, implies parent proton energies of $\sim 25-250$ TeV. The photon energy threshold for pion production with these protons lies in the *soft* X-ray spectrum. Therefore, a selection of neutrino source candidates among X-ray emitters should not be penalized by the cutoff of the *hard* X-ray spectrum. We deem a maximum X-ray energy of 50 keV to be a safe choice in this perspective, as it has been shown that less than 10% of AGN are expected to have a cutoff below 50 keV[47].

Finally, Figure 8.14 demonstrates that the intrinsic $20-50$ keV X-ray flux is linearly correlated to the $14-195$ keV flux, thus proving that the estimation of $F_X^{intr}$ is robust against uncertainties in the modeling of absorption, also in this smaller energy range.

[46] Fabian, Lohfink, Belmont, et al., "Properties of AGN coronae in the NuSTAR era - II. Hybrid plasma" addressed this issue by proposing a *hybrid corona*, containing a mixture of thermal and non-thermal particles.

[47] ibid.

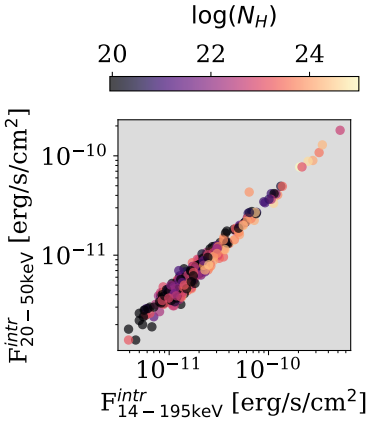


Figure 8.14: Linear correlation between the $20-50$ keV and the $14-195$ keV X-ray fluxes. Both fluxes similarly robust against absorption in the surroundings of the AGN; see Figure 8.13. Note that the BASS catalog does not report an observed (absorbed) $20-50$ keV flux.

The selection retains 47 Seyfert galaxies, excluding NGC 1068. Of these, 23 show narrow emission lines only, indicating high optical obscuration of the broad-line region. Therefore, they are classified as Seyfert 2 (or 1.9) in the BASS catalog. The remaining 25, with less obscured optical spectra, are classified as Seyfert 1 (or Seyfert 1.2 or Seyfert 1.5). For further details on the properties of Seyfert galaxies, see Chapter 3. It is noteworthy that $\sim 10$ radio galaxies survive the selection cuts. Although Seyfert galaxies are usually known to be radio-quiet, this property is not intrinsic to the nature of these objects. Rather, it is due to the weakness of the IR/optical emission compared to the radio emission from a jet or its lobes. For relatively nearby ($z < 0.1$) jetted AGN that are not blazars (their jet is not pointing directly toward us), the IR/optical emission may still be detected. In fact, similarities between the spectra of galaxies identified by Karl Seyfert[48] and, *e.g.*, the well-known radio source Cygnus A (present in our list), were observed as early as 1954[49]. In summary, our selection criteria effectively retain nearby X-ray bright sources, which, although possibly jetted, are not blazars. It should also be noted that no significant neutrino emission has been yet associated with blazars aside TXS 0506+056, and the role of the jet in connection to high-energy neutrino emission remains unclear.[50]

[48] Seyfert, "Nuclear Emission in Spiral Nebulae."

[49] Baade and Minkowski, "On the Identification of Radio Sources."

[50] As we will see later in this chapter, the recent claim of the discovery of neutrino emission from blazars (Buson et al., "Erratum: "Beginning a Journey Across the Universe: The Discovery of Extragalactic Neutrino Factories" (2022, ApJL, 933, L43)") is severely questioned by our results presented in Section 8.3.

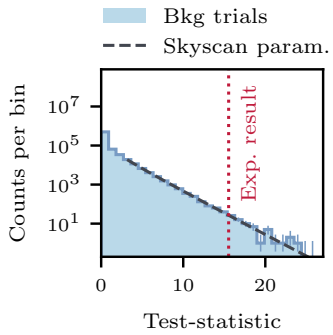


Figure 8.15: Distribution of the *TS* under the background-only hypothesis at the declination of NGC 7469 ($\delta = 8.87°$) in blue. The dashed grey line displays the interpolated parametrization of the background *TS* distribution used to produce the sky scan. The experimental *TS* value is marked as a dotted red line.

[51] We use Equation 8.1 to correct for 47 independent tests within a single spectral hypothesis. However, the total trial factor, including the penalty for testing two spectra, is estimated directly from MC simulations under the background-only hypothesis to account for correlations.

[52] Glauch et al., "Searching for High-Energy Neutrino Emission from Seyfert Galaxies in the Northern Sky with IceCube".

[53] Goswami, "Search for high-energy neutrino emission from hard X-ray AGN with IceCube".

### *Hard neutrino emission from NGC 7469 and excess from the population*

First, we search for the source with the strongest neutrino emission in the list. The Seyfert 1 NGC 7469, at redshift 0.016, shows the most prominent deviation from the background when testing the unbroken single power-law emission. Its *TS* distribution under the null hypothesis is shown in Figure 8.15. The local significance is $3.7\,\sigma$ ($p_{\text{local}} = 9.8 \times 10^{-5}$), which, after accounting for all the hypotheses tested, translates into a trial-corrected significance of $2.4\,\sigma$[51].

The best-fit spectral parameters are $\phi^{1\text{TeV}}_{\nu_\mu+\bar{\nu}_\mu} = 2.0^{+1.7}_{-1.8} \times 10^{-13}$ $\text{TeV}^{-1}\,\text{cm}^{-2}\,\text{s}^{-1}$ and $\gamma = 1.9^{+0.4}_{-0.5}$, where the uncertainties have been estimated from the one-dimensional profile likelihood. The second and third sources with the smallest local significances are NGC 4151 ($3.1\,\sigma$) and CGCG 420−015 ($2.7\,\sigma$), the two Seyferts for which neutrino emission with global significance between $2\,\sigma$ and $3\,\sigma$ was previously reported.[52,53] The best-fit flux parameters and local significance for the entire list of sources can be found in Appendix C.7. The two-dimensional likelihood scans for the flux parameters of NGC 7469, NGC 4151, and CGCG 420−015 are shown in Figure 8.16, together with the one of NGC 1068.

The hard neutrino spectrum of NGC 7469 strikingly differs from the softer ones of NGC 1068 ($\gamma = 3.4$), NGC 4151 ($\gamma = 2.7$), and CGCG 420−015 ($\gamma = 2.7$). By looking at the scan around its location in Figure 8.17, we notice not only that the hotspot is very well localized but also that two high-energy neutrino events (alerts, see Section 4.8)—IC220424A and IC230416A—included in the data sample

used for the analysis are very close to the source. Upon further investigation, we found that these two events drive the *TS* completely: When they are removed from the data sample, the significance of the emission from NGC 7469 vanishes.

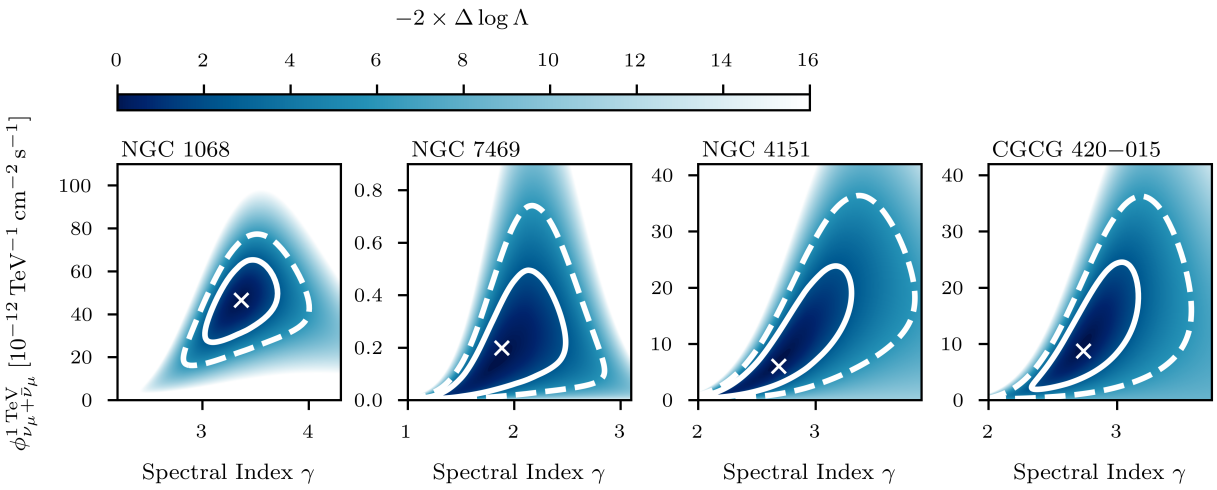


Figure 8.16: 2D profile likelihoods for the flux parameters of the four X-ray bright Seyfert galaxies showing the smallest local p-values when searched for point-like neutrino emission individually. The scan of NGC 1068 is the same of Figure 8.8, however the flux normalization $\phi^{1\mathrm{TeV}}_{\nu_\mu+\bar{\nu}_\mu}$ is reported in units of $10^{-12}\,\mathrm{TeV}^{-1}\,\mathrm{cm}^{-2}\,\mathrm{s}^{-1}$, as it is for the other sources.

In Figure 8.18, the dependence on single events of the *TS* at the location of NGC 7469 is compared to the one at NGC 1068. A soft signal in the TeV energy range, like the one from NGC 1068, needs a large clustering of events for the analysis to be sensitive to it, which makes the *TS* quite robust against the contribution of each event. Conversely, 100 TeV–1 PeV events have a much higher probability of being astrophysical as it is unlikely to detect atmospheric neutrinos at those energies. Hence, the detection of $\mathcal{O}(1)$ event with energy $\gtrsim$ 100 TeV tends to result in a significant detection. On the other hand, the likelihood-ratio test ultimately relies on one (or few) signal events, and the measured neutrino flux normalization suffers from a large relative uncertainty.

As a final remark, as all events in the neutrino sample used for this analysis, the two alert events are also reconstructed using the SplineMPE algorithm (see Section 4.4). GCN notices[54] issued by IceCube apply this angular reconstruction as well (although with different settings, see Section 4.8). The chance coincidence probability for the two alert events to be associated with NGC 7469 has been recently studied in a work external to the IceCube Collaboration.[55] Although this is an a posteriori evaluation triggered by the observation of these two high-energy events, their analysis excludes the chance coincidence at the $3.3\,\sigma$ level. Additionally, they conclude that the non-detection of a TeV excess from this source in previous IceCube works implies that the spectral index of a power-law energy spectrum has to be hard. Our result confirms the indication of high-energy neutrino emission from NGC 7469, compatible with hard spectral emission, via an independent and completely blind analysis.

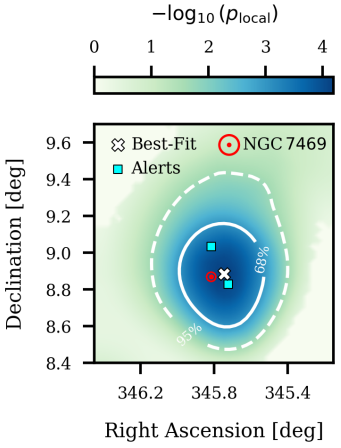


Figure 8.17: Zoomed-in sky scan around the location of NGC 7469. As in Figure 8.6, we highlight the source location and the best-fit position and confidence regions for the neutrino emission. Additionally, the positions of two alert events are marked as cyan crosses.

[54] https://gcn.nasa.gov/notices

[55] Sommani, Franckowiak, et al., "Two 100 TeV neutrinos coincident with the Seyfert galaxy NGC 7469".

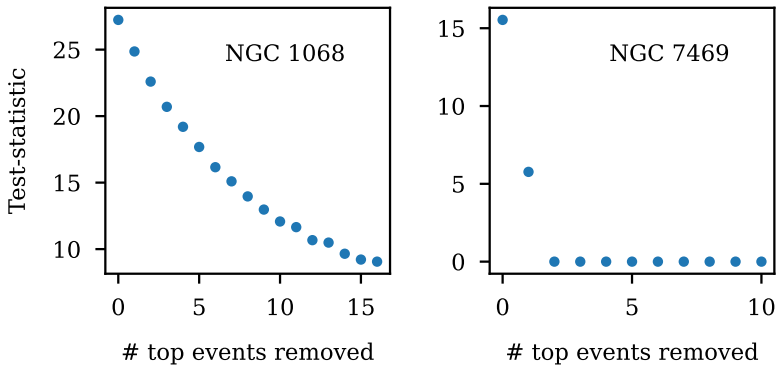


Figure 8.18: *TS* dependence on the single events contributing to the maximum likelihood-ratio for (left) NGC 1068 and (right) NGC 7469. The x-axis shows the number of events, sorted by decreasing contribution to the *TS*, subsequently removed from the data sample. The y-axis reports the corresponding experimental *TS* value.

The binomial test is the second and last test performed on the 47 X-ray bright, non-blazar AGN list. Once again, two emission models have been tested, but as the unbroken power-law spectrum results in the highest significance, we report only on that result.

The minimum $p_{\text{binom}}$ of $1.7 \times 10^{-5}$ ($4.2\,\sigma$) is found for $k = 11$ sources out of 47. Figure 8.19 visualizes the excess in the same way as Figure 8.12. However, the excess remains firmly above the background expectation source after source for more than half of the list. Conversely, the binomial excess seen in the list of gamma-ray sources aligns with the background expectation as soon as we look at more than three sources. Notably, the second most significant point from the scan is found for $k = 27$ sources with a $p_{\text{binom}}$ almost identical to the minimum.

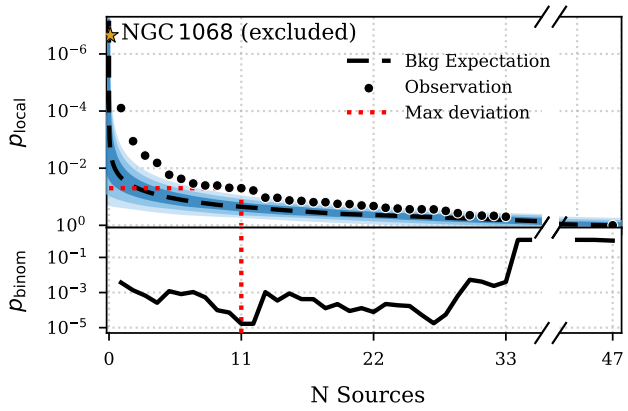


Figure 8.19: Binomial excess from the list of 47 X-ray Seyfert galaxies, sorted by increasing $p_{\text{local}}$. **Upper panel:** $p_{\text{local}}$ threshold for the test as a function of the number of sources tested. The dashed black line indicates the mean background expectation estimated from MC simulations, with Poissonian uncertainties ($1\,\sigma$, $2\,\sigma$, $3\,\sigma$) as blue bands. **Lower panel:** $p_{\text{binom}}$ for each subset of sources considered in the scan. A red dotted line indicates the maximum deviation from the background. 11 sources contribute to the binomial excess. NGC 1068 is marked here as source zero, as it does not participate in the test but is part of the population.

After accounting for all trial factors (scan of 47 thresholds and test of two spectral shapes), the significance lowers to $p^{\text{post}}_{\text{binom}} = 5.5 \times 10^{-4}$, corresponding to $3.3\,\sigma$. Therefore, we have found **evidence for neutrino emission from a population of X-ray bright, non-blazar AGN**. NGC 1068 is not included in the test to have an unbiased and blind statistical significance for the observation. However, it belongs to the same class of sources, and for the sake of completeness, we report the

pre-trial significance of the binomial test when including it. We find a $4.5\,\sigma$ excess (pre-trial) from the same 11 sources plus NGC 1068. The trend of $p_{\text{binom}}$ modified by the addition of NGC 1068 is shown in Figure 8.20. Interestingly, adding such a significant object to the list does not change the conclusion: A large fraction of the selected sources produce p-values in the point-source analysis smaller than expected from background-only.

From MC simulations of the background-only hypothesis, we estimate that, on average, this analysis would detect $\sim 5$ sources out of 47 with a minimum $p_{\text{local}} < 5\%$.[56] As mentioned in Section 7.2, the population test performed here does not distinguish between sources boosted by background fluctuations and p-values produced by astrophysical signals. However, we do gain an indication that this population of hard X-ray bright, non-blazar AGN shows a $3.3\,\sigma$ incompatibility with the background-only hypothesis.

Table 8.2 reports the result of the point-source analysis on the 12 sources contributing to the excess in the binomial test. The full table including all 48 sources can be found in Appendix C.7.

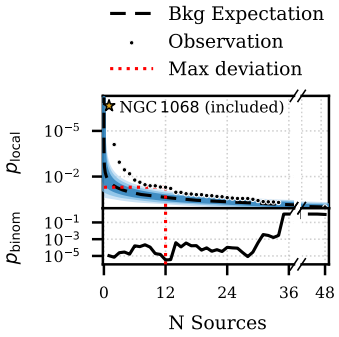


Figure 8.20: Everything here is as in Figure 8.19, except that NGC 1068 is now included in the binomial test. The maximum deviation from the background is then found for 12 sources out of 48, and the population contributing to the excess does not change.

[56] The best-fit significance threshold found by the binomial test.

| Source Name | R.A. (deg) | Dec. (deg) | $z$ | $\log N_H$ | $F^{\text{intr}}_{20-50\,\text{keV}}$ ($\times 10^{-11}\text{erg}^{-1}\text{cm}^{-2}\text{s}^{-1}$) | $\hat{n}_s$ | $\hat{\gamma}$ | $TS$ | $p_{\text{local}}$ |
|---|---|---|---|---|---|---|---|---|---|
| NGC 1068 | 40.67 | -0.01 | 0.003 | 25.00 | 7.72 | 102.2 | 3.4 | 27.1 | $2.2\times10^{-7}$ ($5.0\,\sigma$) |
| NGC 7469 | 345.82 | 8.87 | 0.016 | 20.53 | 2.69 | 5.5 | 1.9 | 15.5 | $9.8\times10^{-5}$ ($3.7\,\sigma$) |
| NGC 4151 | 182.64 | 39.41 | 0.003 | 22.71 | 18.09 | 27.6 | 2.7 | 10.8 | $1.1\times10^{-3}$ ($3.1\,\sigma$) |
| CGCG 420−015 | 73.36 | 4.06 | 0.029 | 24.08 | 1.77 | 35.3 | 2.7 | 8.4 | $3.6\times10^{-3}$ ($2.7\,\sigma$) |
| Cygnus A | 299.87 | 40.73 | 0.056 | 23.38 | 4.93 | 3.4 | 1.6 | 7.4 | $6.5\times10^{-3}$ ($2.5\,\sigma$) |
| LEDA 166445 | 42.68 | 54.70 | 0.015 | 24.01 | 1.61 | 57.1 | 4.4 | 5.2 | 0.02 ($2.1\,\sigma$) |
| NGC 4992 | 197.27 | 11.63 | 0.025 | 23.69 | 2.34 | 27.3 | 2.9 | 5.0 | 0.02 ($2.0\,\sigma$) |
| NGC 1194 | 45.95 | -1.10 | 0.014 | 24.18 | 3.87 | 43.2 | 4.4 | 4.1 | 0.03 ($1.8\,\sigma$) |
| Mrk 1498 | 247.02 | 51.78 | 0.055 | 23.23 | 1.86 | 39.9 | 3.6 | 3.7 | 0.04 ($1.7\,\sigma$) |
| MCG+4−48−2 | 307.15 | 25.73 | 0.014 | 23.86 | 4.32 | 36.7 | 3.2 | 4.1 | 0.04 ($1.7\,\sigma$) |
| NGC 3079 | 150.49 | 55.68 | 0.004 | 24.56 | 3.33 | 33.8 | 3.6 | 3.3 | 0.05 ($1.7\,\sigma$) |
| Mrk 417 | 162.38 | 22.96 | 0.033 | 23.90 | 1.73 | 4.4 | 1.9 | 3.5 | 0.05 ($1.6\,\sigma$) |

Table 8.2: Coordinates (R.A. and Dec.), redshift ($z$), logarithm of the hydrogen column density (in $\text{cm}^{-2}$), intrinsic X-ray flux used for the selection, best-fit flux parameters ($\hat{n}_s$ and $\hat{\gamma}$), *TS* value, and local significance of the top 11 (12 including NGC 1068) sources out of 47 (48) contributing to the binomial excess in Figure 8.19 (Figure 8.20).

### 8.2.4 *Implications for the diffuse neutrino background*

The best-fit neutrino fluxes with the $1\,\sigma$ uncertainties (in units of $\text{TeV}^{-1}\,\text{cm}^{-2}\,\text{s}^{-1}$) for the top four sources in the list of gamma-ray emitters are summarized here:

- NGC 1068:
  $\phi^{1\text{TeV}}_{\nu_\mu+\bar{\nu}_\mu} = 4.7^{+1.1}_{-1.3}\times10^{-11}$ and $\hat{\gamma} = 3.4\pm0.2$
- NGC 7469:
  $\phi^{1\text{TeV}}_{\nu_\mu+\bar{\nu}_\mu} = 2.0^{+1.7}_{-1.8}\times10^{-13}$ and $\hat{\gamma} = 1.9^{+0.4}_{-0.5}$
- NGC 4151:
  $\phi^{1\text{TeV}}_{\nu_\mu+\bar{\nu}_\mu} = 6.0^{+1.1}_{-0.5}\times10^{-12}$ and $\hat{\gamma} = 2.7^{+0.4}_{-0.5}$
- CGCG 420−015:
  $\phi^{1\text{TeV}}_{\nu_\mu+\bar{\nu}_\mu} = 8.7^{+0.9}_{-0.5}\times10^{-12}$ and $\hat{\gamma} = 2.7\pm0.3$

The $1\,\sigma$ statistical uncertainties on each parameter are estimated according to Wilks' theorem.

The multimessenger SEDs of NGC 1068, NGC 7469, NGC 4151, and CGCG 420−015 are shown in Figure 8.21 and Figure 8.22. Similar to NGC 1068, no gamma-ray emission has been associated with NGC 7469 and CGCG 420−015. Out of the analysis of *Fermi*-LAT data, a recent study[57] reported the detection of $0.1 - 100$ GeV gamma rays from NGC 4151 at $5.5\,\sigma$. This Seyfert galaxy is known to host a UFO,[58,59] and the authors of the study argue that it is the probable source of the observed non-thermal emission. They provide a hadronic acceleration model that can produce the observed gamma-ray flux. The model also predicts the associated per-flavor neutrino flux at 1TeV to be $\phi_{\nu+\bar{\nu}} \simeq 5 \times 10^{-15}\,\mathrm{TeV}^{-1}\,\mathrm{cm}^{-2}\,\mathrm{s}^{-1}$. This is three orders of magnitude smaller than the muon-neutrino flux measured in this work, $\phi^{1\,\mathrm{TeV}}_{\nu+\bar{\nu}} = 6.0 \times 10^{-12}\,\mathrm{TeV}^{-1}\,\mathrm{cm}^{-2}\,\mathrm{s}^{-1}$. This discrepancy suggests that most of the neutrino emission detected from NGC 4151 may originate from the X-ray corona, while only a negligible contribution comes from the UFO.

[57] Peretti et al., "Gamma-ray emission from the Seyfert galaxy NGC 4151 and multimessenger implications for ultra-fast outflows".

[58] Ultrafast outflow, see Subsection 2.3.3.

[59] Tombesi et al., "Evidence for ultra-fast outflows in radio-quiet AGNs. I. Detection and statistical incidence of Fe K-shell absorption lines".

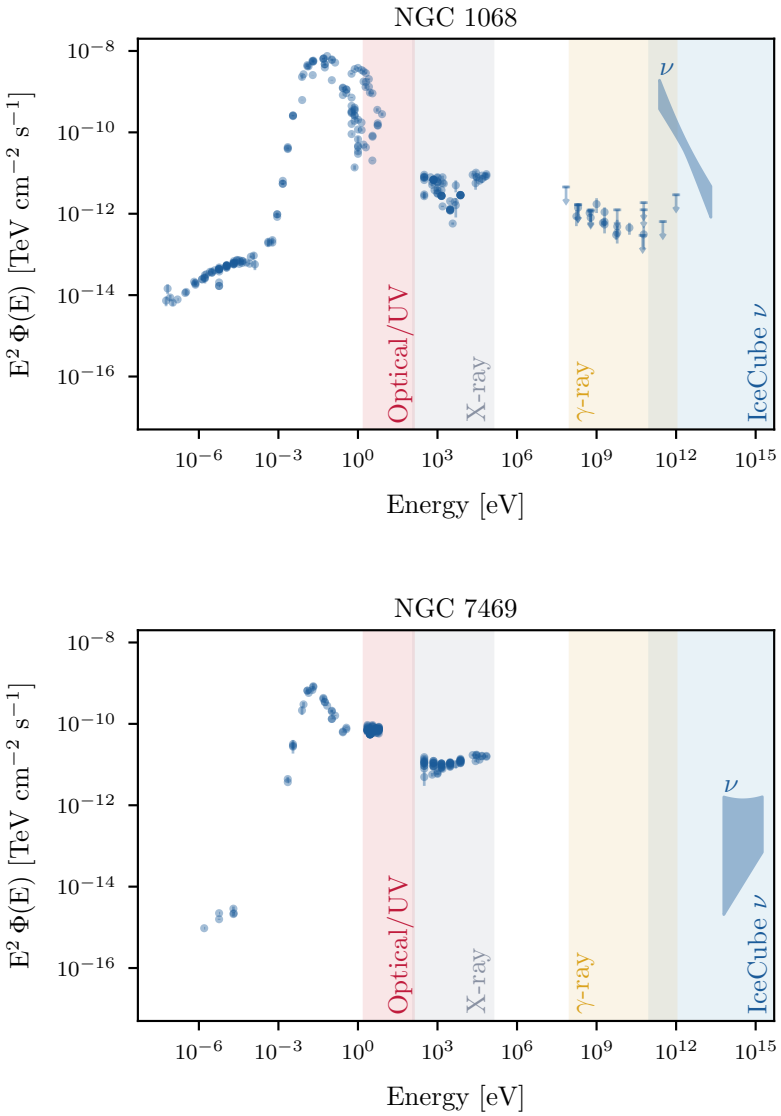


Figure 8.21: Multimessenger SED of NGC 1068 (top) and NGC 7469 (bottom). Highlighted are the various energy bands for different electromagnetic emissions. The all-flavor neutrino flux is obtained by multiplying the best-fit muon-neutrino flux by a factor of 3. The neutrino spectrum is shown as the 68% C.L. flux contour in the 95% C.L. energy range. The multiwavelength electromagnetic data are from https://tools.ssdc.asi.it/SED/, accessed May 17, 2024.

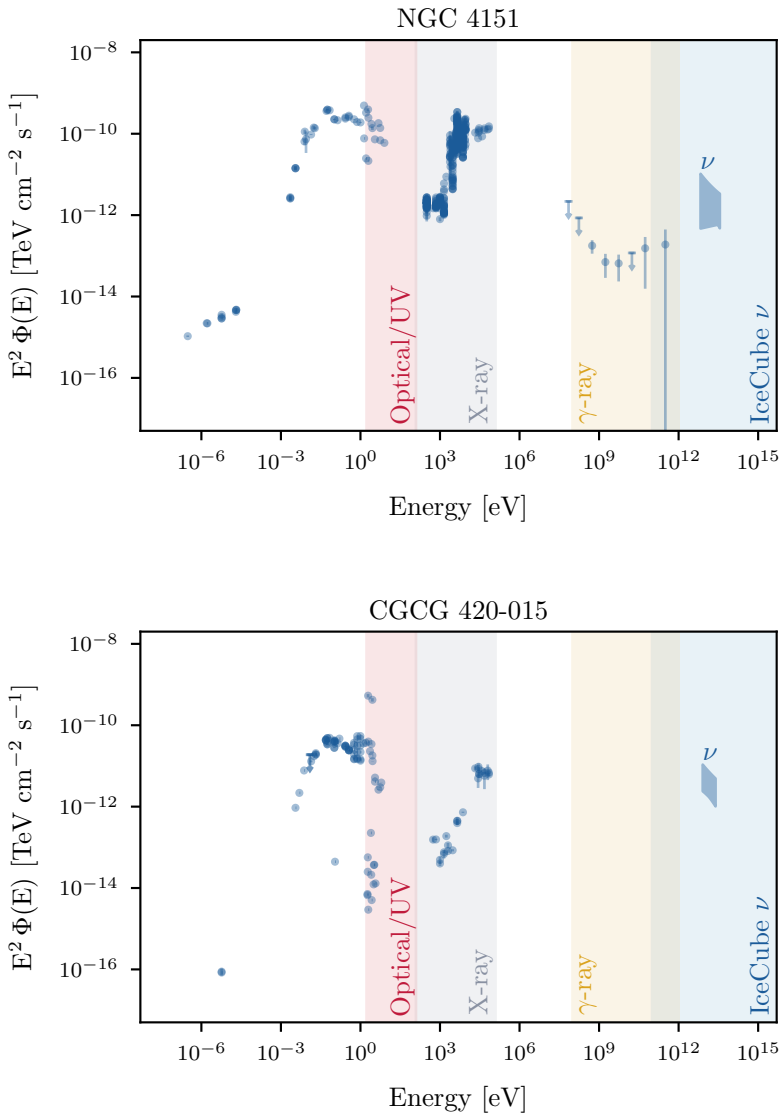


Figure 8.22: Multimessenger SED of NGC 1068 (top) and NGC 7469 (bottom). See description of Figure 8.21.

At the end of this work, the question about the implications of the new results on the diffuse neutrino flux produced by non-jetted AGN arises. An update to our prediction discussed in Section 3.3 will be the subject of a future publication. However, we can take the results from Section 3.3 and include the new measurements for a qualitative comparison. The resulting picture is shown in Figure 8.23, where the diffuse neutrino background from AGN is shown as a black solid line. Non-jetted AGN produces the first hump of the spectrum, proportional to the cosmic X-ray background. The second peak represents a model of the collective emission from blazars.[60]

While the measured spectra of NGC 4151 and CGCG 420−015 seem to fall well within the predicted energy range for this class of sources, we detected two very high energy events from NGC 7469. As a result, NGC 7469 shows a much harder spectral shape than the other three sources. The spectrum of NGC 1068 has shifted to slightly lower energies, although remaining statistically compatible

[60] Padovani, Petropoulou, et al., "A simplified view of blazars: the neutrino background".

with the previous measurement. Furthermore, NGC 7469 and NGC 4151 are Seyfert galaxies of type 1 and therefore less obscured (with $\log N_H < 21$ and $\log N_H \lesssim 23$, respectively) compared to the Seyfert 2 galaxies NGC 1068 and CGCG 420−015, which are Compton-thick AGN ($\log N_H > 24$). The different obscuration levels suggest that the gas column density is unrelated to neutrino production.

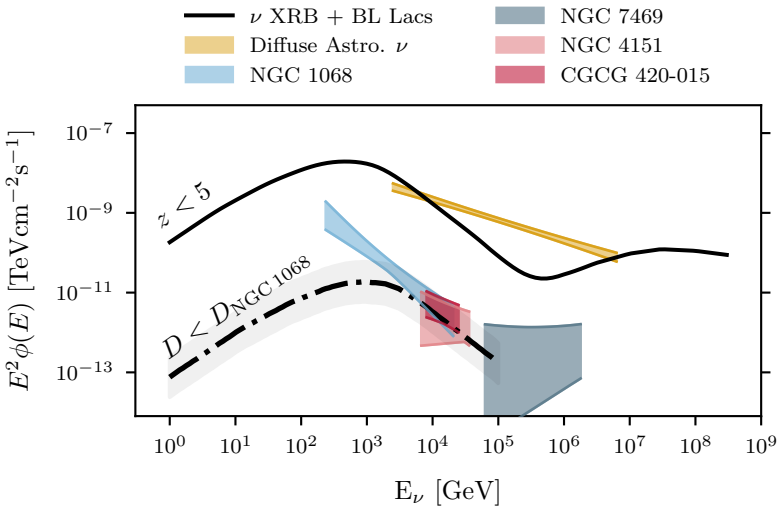


Figure 8.23: Updated version of Figure 3.11. The black solid line represents the diffuse neutrino emission from AGN. Two components contribute to it: A model-independent prediction of neutrino emission from non-jetted X-ray AGN and a blazar emission model (Padovani, Petropoulou, et al., "A simplified view of blazars: the neutrino background"). The astrophysical diffuse neutrino flux is shown as a yellow-shaded area. Other shaded areas represent the best-fit fluxes with their 68% C.L. uncertainty band in the 95% C.L. energy range for the top four sources identified in the list of 47 X-ray bright, non-blazar AGN. All fluxes are reported for all three neutrino flavors, obtained by multiplying by a factor of 3 the best-fit fluxes from this work, under the assumed flavor ratio $(\nu_e : \nu_\mu : \nu_\tau) = (1 : 1 : 1)$, see Subsection 2.2.2.

In Section 3.3, we calibrated the scaling between the X-ray and neutrino powers based on the ratio between the intrinsic X-ray and neutrino energy densities at 1 keV and 4 TeV, respectively. The neutrino flux measurement of NGC 1068 remained compatible with previous results in an energy range that includes 4 TeV. Hence, the scaling factor remains approximately the same, *i.e.*, $\sim 40$. We can compute the same scaling factors for NGC 7469, NGC 4151, and CGCG 420−015[61]. Given the best-fit neutrino spectra associated with these three sources, we find very variable ratios, ranging from $\sim 5$ to $\sim 190$ for NGC 4151 and NGC 7469 respectively. This result suggests that the assumption that all non-jetted, X-ray bright AGN share the neutrino emission mechanism as NGC 1068 is too simplistic[62].

In an attempt to provide an overall interpretation, we can draw three main conclusions:

1. A more detailed measurement of the spectral shape of NGC 1068 at $\lesssim 100$ GeV is a missing necessary input for studies of neutrino production mechanisms. Although the fit of the unbroken power-law energy spectrum resulted in the highest significant results presented in this work, recent models of the neutrino emission from NGC 1068 predict peaked spectral shapes.[63,64,65] Moreover, simple considerations on the source's energetics suggest that the spectrum should have a turnover to a rather hard slope at low energies, see Subsection 3.3.1.

[61] The X-ray energy densities are estimated from the X-ray fluxes in $2 - 10$ keV and spectral indices in J. Wang et al., "Revisiting the Short-term X-ray Spectral Variability of NGC 4151 with Chandra" for NGC 4151, Tanimoto et al., "NuSTAR Observations of 52 Compton-thick Active Galactic Nuclei Selected by the Swift/Burst Alert Telescope All-sky Hard X-Ray Survey" for CGCG 420−015, and https://www.bass-survey.com/dr1.html for NGC 7469.

[62] The same conclusion has already been suggested by Padovani, Gilli, et al., "The neutrino background from non-jetted active galactic nuclei" based on preliminary measurements of the neutrino flux from NGC 4151 and CGCG 420−015.

[63] Inoue et al., "On High-energy Particles in Accretion Disk Coronae of Supermassive Black Holes: Implications for MeV Gamma-rays and High-energy Neutrinos from AGN Cores".

[64] Murase, "Hidden Hearts of Neutrino Active Galaxies".

[65] Fiorillo et al., "TeV Neutrinos and Hard X-Rays from Relativistic Reconnection in the Corona of NGC 1068".

2. The assumption that all non-jetted AGN behave like NGC 1068 in terms of their neutrino properties is challenged by both the very hard spectrum of NGC 7469 as well as the variable scaling factors between X-ray and neutrino powers of NGC 4151, CGCG 420−015, and NGC 7469. In other words, if these objects share a neutrino production mechanism, this mechanism is not such that a constant scaling factor directly relates the neutrino and X-ray fluxes.

3. The presence of both type 1 and type 2 Seyfert galaxies among the most significant sources in our list seems to support a unified view of these objects,[66] where the obscuration levels along the line of sight are merely due to our viewing angle and not to any intrinsic fundamental differences that might affect possible neutrino emission.

[66] Urry and Padovani, "Unified Schemes for Radio-Loud Active Galactic Nuclei".

Our results indicate that X-ray bright, non-blazar AGN might be non-negligible contributors. However, more neutrino and electromagnetic observations are needed to corroborate the reported evidence and make more conclusive statements about the composition of the high-energy neutrino flux. What about the blazar contribution to neutrinos beyond PeV energies?

## *8.3 Are blazars responsible for unassociated hotspots?*

**Disclaimer:** The results summarized in this section are based on publicly available IceCube data (see Chapter 6) and information only. The discussion follows closely the published work *Bellenghi et al. ApJL 955, 2023*.[67]. The author of this dissertation developed the software tool for the analysis of IceCube public data, conducted the analysis, interpreted the results, and contributed to the writing of the manuscript as the primary author.

[67] Bellenghi, Padovani, et al., "Correlating High-energy IceCube Neutrinos with 5BZ-CAT Blazars and RFC Sources" Analysis code available at https://github.com/chiarabellenghi/Correlation_Analysis.

AGN are excellent candidates as high-energy neutrino sources. Among them, blazars are especially promising due to their dominant non-thermal emission and almost ubiquitous association with high-energy gamma rays (see Subsection 2.3.3). The first association between the blazar TXS 0506+056 and a high-energy neutrino detected by IceCube in September 2017 ($E_\nu \sim 290$ TeV) immediately sparked great interest for these astrophysical accelerators to be neutrino producers. The possibility that blazars constitute the dominant class of high-energy neutrino sources had been already suggested in several studies prior to the September 2017 event.[68,69,70] Since then, numerous investigations have delved into this topic to find statistically robust associations, albeit with mostly inconclusive ($\lesssim 3\sigma$) results.[71,72]

[68] Padovani, Resconi, Giommi, et al., "Extreme blazars as counterparts of IceCube astrophysical neutrinos"

[69] Lucarelli et al., "AGILE Detection of a Candidate Gamma-Ray Precursor to the ICECUBE-160731 Neutrino Event"

[70] Huber, Krings, et al., "Results of IceCube searches for neutrinos from blazars using seven years of through-going muon data"

[71] See Giommi and Padovani, "Astrophysical Neutrinos and Blazars" for a review

[72] Abbasi et al., "Search for Correlations of High-energy Neutrinos Detected in IceCube with Radio-bright AGN and Gamma-Ray Emission from Blazars".

A recently published work—*Buson et al. ApJL 933, 2022*[73]—sought to answer the very same question by testing the spatial correlation between the neutrino hotspots from the Southern sky of the 7-yr neutrino sky map[74] and the sources in the 5th edition of the Roma-

[73] Buson et al., "Beginning a Journey Across the Universe: The Discovery of Extragalactic Neutrino Factories".

[74] Aartsen et al., "All-sky Search for Time-integrated Neutrino Emission from Astrophysical Sources with 7 yr of IceCube Data".

BZCAT Multifrequency Catalogue of Blazars[75] (5BZCAT, see Subsection 7.3.1). To test this hypothesis, they count how many sources in the 5BZCAT have at least one neutrino hotspot with local significance $L > L_{\text{min}}$[76] within an association radius $r_{\text{assoc}}$ and compare this number with what is expected by chance coincidences only. Ranges of values for the analysis parameters—$L_{\text{min}}$ and $r_{\text{assoc}}$—are defined a priori and scanned to find the combination that yields the highest significance for the correlation. The details of the analysis have been discussed in Section 7.3.

*Buson et al. ApJL 933, 2022* found that ten neutrino hotspots with $L \geq 4.0$ are closer than $0.55^\circ$ to ten blazars in the 5BZCAT: five FSRQs, three BL Lacs, and two blazars of uncertain type. The mean angular separation between sources and hotspots is $\langle \psi \rangle \sim 0.40^\circ$. The mean redshift is 1.3. The chance coincidence for this number of associations to happen is excluded at $4.6\,\sigma$, making it the strongest correlation between neutrinos and a population of blazars ever claimed.

The authors' choice of using the Southern neutrino sky for their correlation is motivated by the difference in the covered energy ranges between the Northern and Southern skies in the published IceCube data. The absorption in the Earth of the highest-energy neutrinos reduces the detection efficiency of IceCube for energies above 1 PeV at declinations $\delta \gtrsim 30^\circ$ (see Figure 4.13 and Figure 4.17). Hence, in the Northern sky, the range of reconstructed energies goes from a few tens of GeV to approximately 1 PeV, with most events reconstructed at 1 TeV. The Southern sky, instead, covers a broader spectrum of energies, going up to 10 PeV. On the other hand, the Southern hemisphere is dominated by the background of muons produced at high multiplicity in atmospheric interactions and boosted in the direction of the shower,[77] thus resembling high-energy tracks. This effect dramatically reduces the background discrimination power of any selection cuts (see Section 4.4). However, these muon bundles are absorbed above $\delta = -5^\circ$. These considerations leave the horizon ($-5^\circ \lesssim \delta \lesssim 30^\circ$) as the region where IceCube is the most sensitive to an astrophysical flux of neutrinos.

As part of this thesis, we investigated this result further. First, we extended the analysis to study the correlation of 5BZCAT sources with hotspots in the Northern sky of the same sky map used in *Buson et al. ApJL 933, 2022*. As extragalactic signals are expected to be isotropically distributed in the sky, a correlation should also be found in the Northern hemisphere, especially at the horizon, where IceCube is most sensitive. As a second test, we correlated sources in the Radio Fundamental Catalog (RFC, see Subsection 7.3.1) with both the Northern and the Southern neutrino sky. Unlike the 5BZCAT, the RFC is flux-limited, and its sources are uniformly distributed in the sky. Finally, we calculated the neutrino sky map based on 10 years of data and performed all the previous searches again. This final test provides insight into the impact of an improved, larger neutrino sample on the published correlation.

[75] Massaro et al., "The 5th edition of the Roma-BZCAT. A short presentation".

[76] $L = -\log_{10} p_{\text{local}}$ out of the 7-year neutrino sky map.

[77] Coenders, "High-energy cosmic ray accelerators: searches with IceCube neutrinos. Probing seven years of IceCube muon data for time-integrated emission of point-like neutrino sources".

### 8.3.1 Correlation with the 10-year neutrino sample

The public release of 10 years of IceCube events has been described in Section 6.2. It includes data recorded between April 2008 and July 2018, and the number of events has increased by approximately 60% compared to the previous 7-year sample. The IceCube collaboration has previously used this neutrino data sample for an all-sky time-integrated search for neutrino point sources.[78] A machine-readable version of the sky map produced for that search is not publicly available, but using the SkyLLH interface for IceCube's public point-source data presented in Chapter 6, we can produce our own sky map using an unbinned maximum likelihood method, as prescribed in Section 6.3.

[78] Aartsen et al., "Time-Integrated Neutrino Source Searches with 10 Years of IceCube Data".

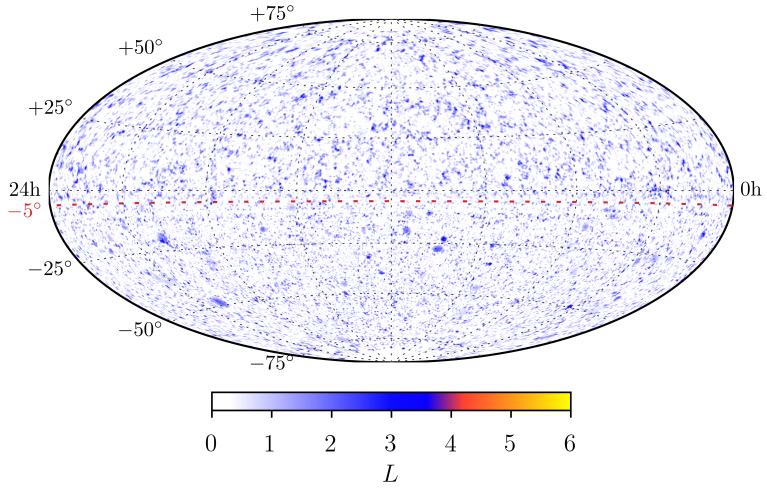


Figure 8.24: Sky map of the point-source likelihood search in the Northern and Southern Hemispheres. The map is shown in equatorial coordinates on a Hammer-Aitoff projection. The color scale indicates the $L$ values obtained from the maximum likelihood-ratio analysis performed at each pixel in the sky. The dashed red line indicates the Northern and Southern sky separation at $\delta = -5°$.

The sky map is shown in Figure 8.24, with a dashed red line separating the Northern and Southern skies at $\delta = -5°$. It is necessary to stress here that, due to limitations of the public data release format,[79] the neutrino p-value map presented here should not be considered as an exact reproduction of the one published by IceCube. Instead, it should be understood as the outcome of a maximum-likelihood search for neutrino sources, which finds results statistically compatible with the IceCube's results.[80]

[79] The impact on several aspects of the analysis has been discussed in Chapter 6.

[80] Aartsen et al., "Time-Integrated Neutrino Source Searches with 10 Years of IceCube Data".

To find blazar–hotspot correlations using this sky map, we decide to re-define the correlation parameters $L_{\text{min}}$ and $r_{\text{assoc}}$. In Section 6.5, we have shown that the sensitivity of the point-source analysis using the public data sample is reduced by up to 50% compared to the one published by the IceCube collaboration, see Figure 6.6. To compensate for this loss of sensitivity to an astrophysical signal, we start scanning the $L_{\text{min}}$ parameter from a lower significance threshold of 3.0 (instead of 3.5) up to 4.5, in steps of 0.5.

To choose the optimal $r_{\text{assoc}}$ range to scan, we perform a dedicated study on the capability of our analysis to localize a point-like source. We simulate an $E^{-2}$ neutrino spectrum at various locations in the sky and with various signal strengths. For each simulation,

we search the associated hotspot in a circle of 1° centered at the signal injection location and calculate the angular distance hotspot and simulated source. To locate the hotspot, we divide the area around the source into pixels of $\sim 0.1 \times 0.1$ square degrees, perform the point-source analysis, obtain the *TS* at each pixel, and convert it into a local significance $L$ (the procedure is outlined in Section 5.4). The pixel with the maximum $L$ is taken as the hotspot for that trial.[81] We repeat this procedure approximately 10,000 times, and Figure 8.25 depicts the distributions of angular distances between a source and its hotspot for the Northern and Southern sky.

[81] The hotspot search is similar to the one described in Subsection 7.1.2 to simulate hotspots produced by injected neutrino events. An example is illustrated in the left panel of Figure 7.6.

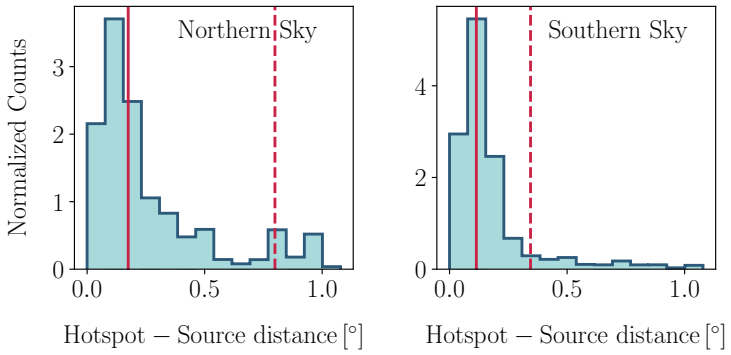


Figure 8.25: Distributions of the angular separation between the location of a simulated point-source emitting an $E^{-2}$ neutrino spectrum and the associated hotspot with $L > 3.0$. The solid and dashed red lines in both panels mark the median and the 90% quantile of the distribution, respectively.

In the Northern sky, 50% (90%) of the hotspots with $L > 3.0$ are localized within 0.17° (0.80°) from the source. In the Southern sky, the same quantiles are at 0.13° and 0.35°. Differences between the two distributions are due to different energy ranges and data selection procedures. In the Northern sky, the long tail of the angular separation distribution at high values is caused by the poor directional reconstruction quality of events with low reconstructed muon energy. The average separation between the parent neutrino and the reconstructed muon is approximately 0.9°,[82] and the uncertainty on the reconstructed declination peaks at $\gtrsim 1°$ for events with neutrino energies below 1 TeV.[83] A smaller association region corresponds to a reduced chance probability of associating a hotspot with a source. Hence, to always include at least 50% of the distribution and maximally reduce the background coincidences, we scan $r_{\text{assoc}}$ from 0.20° to 0.70° (the maximum values used by *Buson et al. ApJL 933, 2022*) in steps of 0.05°. The same strategy is applied to the Northern sky of the 7-year sample.

[82] Carver, "Time integrated searches for astrophysical neutrino sources using the IceCube detector and gender in physics studies for the Genera Project".

[83] As shown in Figure 3 of IceCube Collaboration, "IceCube Data for Neutrino Point-Source Searches Years 2008-2018".

### 8.3.2 *Results and discussion*

#### *5BZCAT – 7-year hotspots correlation*

The two upper panels of Figure 8.26 illustrate the results of the spatial correlation analysis between the 5BZCAT and the hotspots from the 7-yr point-source sky map. Pre-trial p-values are shown as a function of the association radius ($r_{\text{assoc}}$) for various hotspots significance thresholds $L_{\text{min}}$. The left panel displays the result when the

analysis is extended to the Northern neutrino sky. Here, 112, 43, 18, and 7 neutrino hotspots have $L > L_{\rm min}$, with $L_{\rm min}$ ranging from 3.0 to 4.5 in steps of 0.5. Note that, together with the additional threshold of 3.0, we also scan $r_{\rm assoc}$ starting from 0.2°, based on the source localization study on the 10-yr neutrino sample. The strongest fluctuation corresponds to a local p-value of $\sim 1\%$. After accounting for having tested 44 combinations of the correlation parameters, it reduces to $\sim 10\%$, therefore well compatible with a chance correlation. This result is shown with the local $5\,\sigma$ finding of *Buson et al. ApJL 933, 2022*, displayed in the right panel for comparison.

### *RFC – 7-year hotspots correlation*

The result of the spatial correlation analysis between the RFC and the hotspots from the 7-yr point-source sky map is shown in the two lower panels of Figure 8.26. Here, for the Southern sky (right), we use the same $L_{\rm min}$ and $r_{\rm assoc}$ thresholds as in *Buson et al. ApJL 933, 2022* to make the comparison to the 5BZACT result straightforward. The smallest pre-trial p-value is $1.4 \times 10^{-4}$, which becomes $6.9 \times 10^{-4}$ ($3.2\,\sigma$) post-trial. The correlation parameters yielding the smallest p-value are $L_{\rm min} = 4.5$ and $r_{\rm assoc} = 0.55°$. The p-value curve as a function of the association radius matches exactly the one in the right panel of Figure 8.26, which is not surprising as the sources being associated are precisely the same, five blazars: four FSRQs and one blazar of uncertain type, with $\langle \psi \rangle \sim 0.41°$, and mean redshift 1.8. Only one of them is a gamma-ray source. However, similar to the 5BZCAT case, in the 7-year Northern sky (Figure 8.26, left), the result is compatible with the chance coincidence hypothesis, as the minimum pre-trial p-value is $\sim 3\%$, increasing to $\sim 17\%$ post-trial.

### *Blazar – 10-year hotspots correlations*

When analyzing the Northern sky of the 10-year neutrino sky map, we find 149, 58, 18, and 7 hotspots with $L$ above 3.0, 3.5, 4.0, and 4.5, respectively. In the Northern sky, the number of hotspots with $L$ above the same set of thresholds is 95, 36, 7, and 2.

Figure 8.27 displays the results of the correlation analysis with 5BZCAT blazars performed in the two hemispheres. None of them is statistically significant, with minimum pre-trial p-values of $\sim 25\%$ ($\sim 75\%$ post-trial) and $\sim 3\%$ ($\sim 19\%$ post-trial) in the Northern and Southern sky, respectively. As for the 7-year sample, the analysis is repeated using the RFC catalog. Again, the outcomes are compatible with a chance coincidence, resulting in minimum pre-trial p-values of $\sim 32\%$ ($\sim 80\%$ post-trial) and $\sim 7\%$ ($\sim 34\%$ post-trial) in the Northern and Southern sky, respectively.

The post-trial p-values from all the analyses described in this section are summarized in Table 8.3.

| | Northern Sky | | Southern Sky | |
|---|---|---|---|---|
| | 7-yr $\nu$ | 10-yr $\nu$ | 7-yr $\nu$ | 10-yr $\nu$ |
| 5BZCAT | 0.10 | 0.19 | $2.5\times10^{-6}$ | 0.75 |
| RFC | 0.17 | 0.34 | $4.4\times10^{-4}$ | 0.80 |

Table 8.3: Post-trial p-values for the different correlation analyses performed in this work.

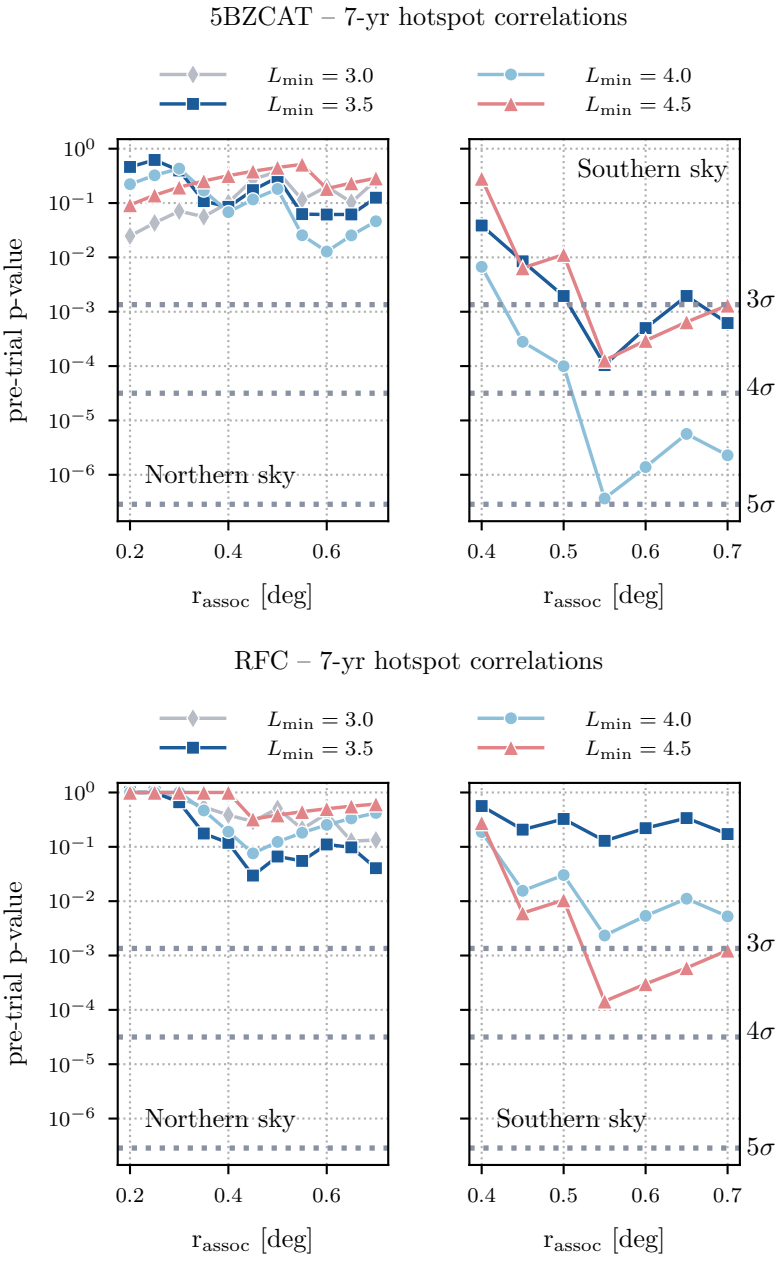


Figure 8.26: Pre-trial p-value for the blazar – neutrino hotspot spatial correlation as a function of the association radius ($r_{\rm assoc}$) and for various minimum significance thresholds for the hotspots $L_{\rm min}$ for the 7-year sample. The upper (lower) figure shows the result of the correlation analysis when using the 5BZCAT (RFC). The analysis is performed in both the Northern (left) and the Southern sky (right). The dotted grey lines in each panel mark the number of Gaussian-equivalent standard deviations. The right panel shows that we were able to replicate the results presented in *Buson et al. ApJL 933, 2022* and is the same as in Figure 7.15.

The robustness of the claim of discovery of a neutrino-blazar correlation with the 5BZCAT catalog is strongly questioned by the results presented in this section. The significance of the correlation vanishes when the same analysis strategy is applied to the Northern sky of the same neutrino sample. Moreover, when using a larger and more sensitive neutrino dataset, the correlation disappears completely also in the Southern hemisphere.

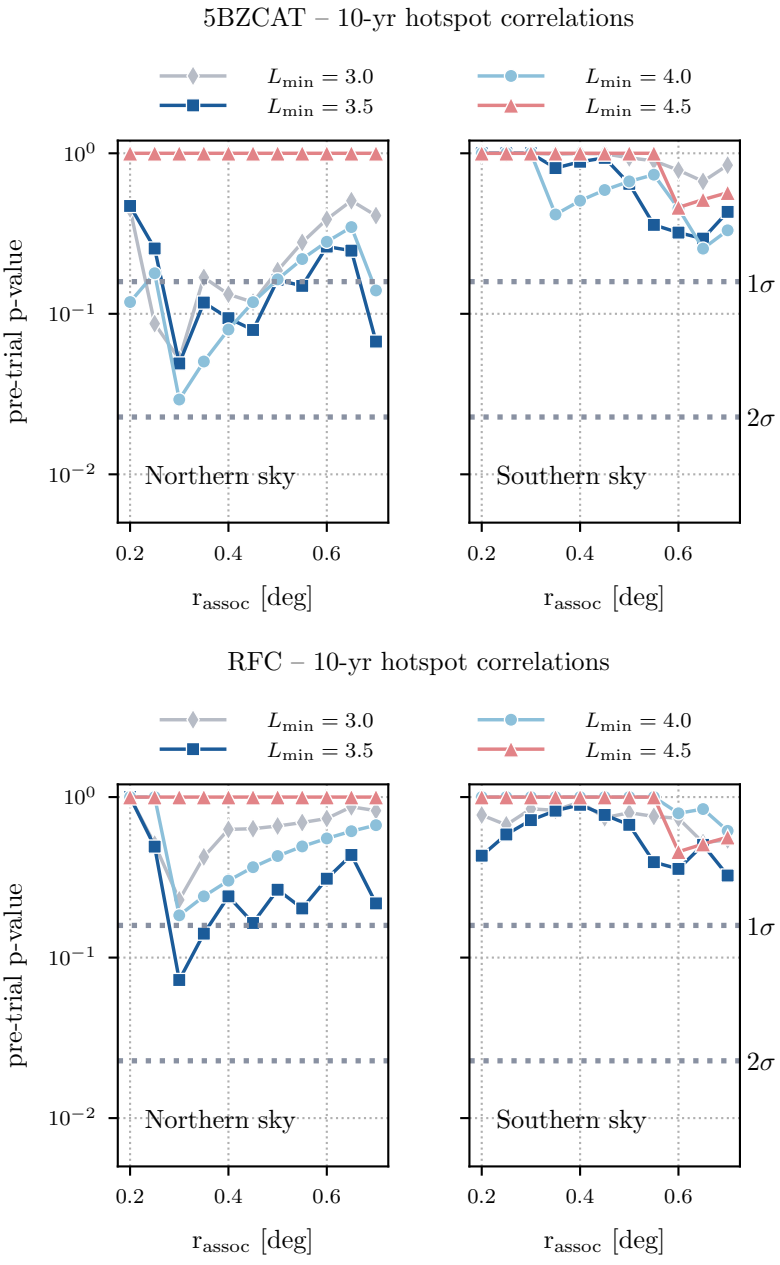


Figure 8.27: Pre-trial p-value for the blazar – neutrino hotspot spatial correlation as a function of the association radius ($r_{\rm assoc}$) and for various minimum significance thresholds for the hotspots $L_{\rm min}$ for the 10-year sample. The upper (lower) figure shows the result of the correlation analysis when using the 5BZCAT (RFC). The analysis is performed in both the Northern (left) and the Southern sky (right). The dotted grey lines in each panel mark the number of Gaussian-equivalent standard deviations.

Focusing deeper on the claimed associations in the 7-year Southern neutrino sky, we find some more concerning points: The mean offset between source and hotspots for the ten associations is 0.4°,

roughly 3 times larger than the median localization capability of the point-source analysis used to analyze 10 years of data. 7 out of 10 hotspots are found at an angular distance larger than the median. A simple way to determine whether this is a reasonable outcome in the signal hypothesis is to use the distribution in the right panel of Figure 8.25 and compute the binomial probability of frequency of the observed distances, which is $\sim 2 \times 10^{-6}$. Considering that the 7-year neutrino sample has a slightly worse angular resolution than the 10-year sample, we can assume an extreme case and worsen the localization capability shown in Figure 8.25 by a factor of 2. The binomial probability of finding 7 out of 10 associated hotspots farther than $0.4^\circ$ from their sources remains extremely small ($\sim 10^{-3}$). According to our study, this makes the observed correlation inconsistent with a hypothetical signal.

The second most interesting result is the correlation of the RFC catalog with hotspots from the Southern sky of the 7-year neutrino sample, at a significance of $3.2\,\sigma$. We test whether finding 4 out of 5 associated hotspots more than $0.41^\circ$ away from their sources is reasonable under the signal assumption. We find a binomial probability of $5 \times 10^{-4}$ using the right panel of Figure 8.25 and $7 \times 10^{-3}$ in the scenario where the resolution is worsened by a factor of 2.

As a final remark, we note that our analysis does not select the hotspot associated by IceCube to TXS 0506+056 because its significance $L$ is below our threshold of 3.0 ($L = 2.7$). However, the IceCube collaboration reports it with a local significance of $L = 3.7$ based on a point-source analysis conducted on the same dataset. We discussed the possible reasons for this mismatch in Section 6.5. We perform an a posteriori check to ensure that the absence of this hotspot in the list of candidates does not impact the results in a sizeable way. Therefore, we repeat both correlation analyses in the Northern sky of the 10-year neutrino sample by manually adding a hotspot with $L_{\text{min}} = 3.7$ at the location of TXS 0506+056. After performing the correlation analysis with both catalogs again, we find that the best $L_{\text{min}}$ changes from 4.0 to 3.5 when using the 5BZCAT, while it stays at 3.5 for the RFC. The pre-trial p-value of the correlation slightly decreases, going from 2.9% to 1.3% for the 5BZCAT and from 7.9% to 1.8% for the RFC, but remaining compatible with the chance coincidence hypothesis.

In conclusion, all analyses performed to test the blazar-neutrino hotspot correlation produced non-significant results. Hence, the findings we aimed to probe in this section appear most likely due to a statistical fluctuation. However, we can not exclude a blazar contribution to the IceCube signal, which is supported by the neutrino association with TXS 0506+056 and the binomial excess produced together with PKS 1424+240 (see Subsection 8.2.2). On the contrary, our results support a scenario where only a small fraction of the gamma-ray and radio-selected blazars are high-energy neutrino emitters, in agreement with several previous works[84,85,86,87] and with the total neutrino prediction in Figure 8.23.

[84] Aartsen et al., "Constraints on Ultrahigh-Energy Cosmic-Ray Sources from a Search for Neutrinos above 10 PeV with IceCube"

[85] Oikonomou, "High-energy neutrino emission from blazars"

[86] Padovani, Boccardi, et al., "PKS 1424+240: yet another masquerading BL Lac object as a possible IceCube neutrino source"

[87] Abbasi et al., "Search for Correlations of High-energy Neutrinos Detected in IceCube with Radio-bright AGN and Gamma-Ray Emission from Blazars".

# 9 Conclusion

In the last decade, cosmic neutrinos have emerged as crucial astrophysical messengers in high-energy astronomy. The detection of $1-10$ TeV neutrinos from the Seyfert galaxy NGC 1068,[1] alongside the non-detection of very-high-energy gamma rays, has given new momentum to theories suggesting that the gamma-ray hidden cores of AGN could be powerful cosmic-ray accelerators.

This dissertation began with the $4.2\,\sigma$ observation of neutrinos from NGC 1068. In Chapter 3, we have reported a multi-wavelength and multi-messenger review study of this galaxy conducted with astronomers, astrophysicists, and theorists. Considering its multi-messenger spectral energy distribution, we have identified all potential neutrino sources within NGC 1068. We identified all potential neutrino sources within NGC 1068 and used order-of-magnitude estimates to derive the maximum neutrino power each component could provide. Our analysis suggests that the most probable neutrino production site is the innermost part of the AGN, close to the supermassive black hole.[2] Within the first few milliparsecs from the SMBH, AGN are known to host a bright X-ray source, the so-called *corona*, which is exceptionally bright in NGC 1068. Photons of X-ray energies offer the optimal target for $p-\gamma$ interactions and consequent production of $\sim$ TeV neutrinos. At the same time, the abundant UV photon field associated with the AGN accretion disc can absorb the accompanying gamma rays, reprocessed to MeV energies. Future proposed missions, like e-ASTROGAM[3] and AMEGO-X,[4] will reach sensitivities sufficient to probe the MeV flux from NGC 1068, testing the proposed theory.

With the proposed correlation between X-ray and neutrino emissions, we estimated the total neutrino flux from all non-jetted AGN, which dominate the X-ray sky. Under the assumption that all AGN share a similar X-ray-to-neutrino power scaling factor, we could convert the observed cosmic X-ray background into a high-energy neutrino background.[5] This model-independent flux estimate is consistent with IceCube measurements and upper limits[6,7] at $\gtrsim 10$ TeV.

Identifying more neutrino sources is essential for understanding the diffuse astrophysical neutrino flux and determining whether non-jetted AGN constitute a population of sources. This dissertation contributed to this goal in several ways.

[1] Abbasi et al., "Evidence for neutrino emission from the nearby active galaxy NGC 1068".

[2] Padovani, Resconi, Ajello, et al., "Supermassive black holes and very high-energy neutrinos: the case of NGC 1068".

[3] de Angelis et al., "Science with e-ASTROGAM. A space mission for MeV-GeV gamma-ray astrophysics".

[4] Caputo et al., "All-sky Medium Energy Gamma-ray Observatory eXplorer mission concept".

[5] Padovani, Gilli, et al., "The neutrino background from non-jetted active galactic nuclei".

[6] Naab et al., "Measurement of the astrophysical diffuse neutrino flux in a combined fit of IceCube's high energy neutrino data".

[7] Goswami, "Search for high-energy neutrino emission from hard X-ray AGN with IceCube".

First, we searched for an excess of neutrino hotspots in the Northern sky using 9 years of internal IceCube data. The hotspot from NGC 1068 is identified as the most significant excess. However, the analysis targets populations of several weaker hotspots and is not as sensitive to single sources. Therefore, the excess is compatible with the background expectation, and we constrain the total flux produced by a population of neutrino standard candles in the Northern sky to be at most 10% of the astrophysical diffuse flux at low local source densities. Thanks to a newly developed strategy for signal simulation, the upper limits we set are approximately 50% more stringent than previously reported ones.

Subsequently, we extended the search for neutrino point sources in the Northern sky to 13 years of IceCube internal data. Besides adding three new years of observations, data acquired in 2010 with the incomplete detector configuration IC79 are included in this analysis for the first time.[8] We reassessed the neutrino emission from NGC 1068 with 50% more data, finding it remains the most significant point-like neutrino source in the sky, with a neutrino flux compatible with previous measurements. Notably, the flux measurement is constrained within $[0.3 - 2.8]$ TeV neutrino energies, a lower energy range compared to previous work. The significance of the signal changes slightly, decreasing from $4.2\,\sigma$ to $4.0\,\sigma$. Time-dependent analyses will be necessary to explore potential time variability as the origin of the shift of the neutrino spectrum to lower energies.

Using the same neutrino data, we investigated the possibility that the X-ray bright corona of AGN is a neutrino source by exploiting X-rays as tracers of neutrino production. We introduced a new list of 47 candidate sources in the Northern sky selected among the brightest Seyfert galaxies in the BASS catalog.[9] Discussions with astronomers and experts in the X-ray field were crucial for defining the selection criteria. The most significant neutrino emission is found from the Seyfert 1 galaxy NGC 7469 at $2.4\,\sigma$. The second and third sources are NGC 4151 and CGCG 420−015, a Seyfert 1 and a Seyfert 2 galaxy for which hints of neutrino emission were reported previously by IceCube.[10,11] Most importantly, we observe a $3.3\,\sigma$ binomial excess from 11 of the selected Seyfert galaxies other than NGC 1068, which is excluded to avoid biases. Although this type of test cannot distinguish which of the identified sources is associated with astrophysical signals and which are boosted by background fluctuations, it gives us a robust indication of a collective excess from a population of hard X-ray bright, non-blazar AGN. Therefore, our recent findings add to the growing evidence that this class of AGN appears as the first emerging population of neutrino sources.

Besides the work done on IceCube internal data, we have presented a novel software tool to perform searches for point-like neutrino emission using ten years of IceCube public data. As part of this work, we developed the interface within the open-source Python-based software tool SkyLLH.[12] In Chapter 6, we have demonstrated the performance of the tool, which can reproduce IceCube published

[8] Bellenghi, Ha Minh, et al., "Extending the IceCube search for neutrino point sources in the Northern sky with additional years of data".

[9] Ricci et al., "BAT AGN Spectroscopic Survey. V. X-Ray Properties of the Swift/BAT 70-month AGN Catalog".

[10] Goswami, "Search for high-energy neutrino emission from hard X-ray AGN with IceCube".

[11] Glauch et al., "Searching for High-Energy Neutrino Emission from Seyfert Galaxies in the Northern Sky with IceCube".

[12] Bellenghi, M. Karl, and Wolf, "Extending SkyLLH software for neutrino point source analyses with 10 years of IceCube public data".

results based on the same dataset with some uncertainty, primarily due to the data release format. Using the new software tool, we have tested an external discovery claim of correlations between blazars in the 5BZCAT catalog and hotspots based on seven years of IceCube public data.[13,14] We have extended the analysis to the larger and more sensitive sample encompassing ten years of observations publicly released by IceCube. We have found that the correlation completely disappears, suggesting that the initially claimed correlation was likely due to a statistical fluctuation. The correlation analysis of the 7-year neutrino sample with the more comprehensive RFC radio catalog yields a significance of $\sim 3\,\sigma$, reduced compared to the published $\sim 5\,\sigma$. This additional result further corroborates the hypothesis of a background fluctuation. However, we can not exclude a blazar contribution to the IceCube diffuse flux, which is supported by the neutrino association with the blazar TXS 0506+056 and the binomial excess to which another blazar—PKS 1424+240—contributes.

[13] Buson et al., "Beginning a Journey Across the Universe: The Discovery of Extragalactic Neutrino Factories".

[14] Buson et al., "Erratum: "Beginning a Journey Across the Universe: The Discovery of Extragalactic Neutrino Factories" (2022, ApJL, 933, L43)".

At the end of this work, we observe the emergence of a new neutrino sky, dominated by emissions from AGN. Our findings challenge the long-standing paradigm that jetted, gamma-ray bright AGN are the primary neutrino sources. Instead, we see evidence that X-ray bright, mostly non-jetted AGN are primary contributors to the diffuse neutrino flux. While jetted AGN of the blazar type are believed to emit neutrinos at PeV energies and beyond, the detection of PeV neutrinos from the non-jetted Seyfert 1 galaxy NGC 7469 challenges a hypothetical dual nature of the diffuse neutrino spectrum, where non-jetted AGN emit mostly $\lesssim 10$ TeV neutrinos.

Ultimately, more data are needed to identify additional sources of cosmic neutrinos. Future expansions of IceCube, such as the Gen2 detector,[15] along with other upcoming neutrino telescopes like GVD,[16] KM3NeT,[17] and P-ONE,[18] will enhance our capabilities. Together, they will provide the community with a planetary neutrino monitoring network, advancing multi-messenger astronomy and opening a window to exploring dense objects in the Universe, such as the cores of active galactic nuclei.

[15] Aartsen et al., "IceCube-Gen2: the window to the extreme Universe".

[16] Avrorin et al., "BAIKAL-GVD: The New-Generation Neutrino Telescope in Lake Baikal".

[17] Margiotta, "The KM3NeT deep-sea neutrino telescope".

[18] Agostini et al., "The Pacific Ocean Neutrino Experiment".

# *Acknowledgements*

If I was able to reach the end of the work presented in this thesis, it is to a big part due to the support and encouragement I received from many incredible people with whom I shared this journey.

First and foremost, I am deeply grateful to my supervisor, Prof. Elisa Resconi, for supporting me throughout these years and always giving me the chance to follow my interests and instincts. Our conversations about science and life have been a continuous source of inspiration.

I am especially thankful to my PhD mentor, Dr. Paolo Padovani, for being my guidance through the twists and turns of astronomy and for reminding me that doing scientific research is fun, especially when I needed it most.

Many thanks to Hans and Theo, for introducing me to the world of neutrino searches in IceCube. The work we did together has been a strong motivation to push one step further. Thanks a lot to all my office mates. In particular, to Martina, Tomas, Martin W., Martin H., and Elena: We have been a great team, and this thesis would not be the way it is without you. Especially to Tomas, thank you for sharing the point source work with me since the very beginning. Your support has been a big source of energy. Big thanks to all the ECP members, for always making our work place a space to share scientific knowledge, laughter and slices of cake. A special mention goes to Christian-with-a-C, for offering me a quiet place when I needed peace, to Kristian-with-a-K, for teaching me how to guide younger students offering himself as the test trial, and to Vincent, for the contagious, messy enthusiasm.

A big shout-out to everyone who shared with me a piece of this Munich journey outside of the office. A special thank you to Elisabetta, my forever flatmate and an extraordinary friend for over ten years, and to Sofia and Gianfranco. You made this place a home.

The strength I needed to move, start a new job, build a new home, and make new friends, came from the deep and robust roots I have in Rome, where my family and my oldest friends are. Thank you for holding me tight.

The final and most heartfelt thank you goes to Andrea, for providing the balance I miss in difficult (and not-so-difficult) times, especially on Sundays.

# A Abbreviations and Glossary

Table A.1: This table provides a list of abbreviations frequently used throughout this thesis.

| Acronym | Meaning |
|---|---|
| XFGL | The Xth generation of the Fermi FGL catalog |
| AGN | Active galactic nucleus |
| BL Lac | BL Lacertae object |
| BZCAT | Multi-frequency catalog of blazars |
| CMB | Cosmic microwave background |
| CR | Cosmic ray |
| CXB | Cosmic X-ray background |
| DNN | Deep neural network |
| DOM | Digital optical module |
| EBL | Extragalactic background light |
| EGB | Extragalactic gamma-ray background |
| FSRQ | Flat spectrum radio quasar |
| HBL | Blazar of type BL Lac with high synchrotron peak frequency |
| IBL | Blazar of type BL Lac with intermediate synchrotron peak frequency |
| IC | Inverse Compton |
| ICXX | IceCube detector data-taking season with XX strings |
| KDE | Kernel density estimation |
| $L_\odot$ | Solar luminosity of $\approx 10^{33.58}$ erg s$^{-1}$ |
| LRT | Likelihood-ratio test |
| $M_\odot$ | Solar mass of $\approx 10^{30.30}$ kg |
| MC | Monte Carlo |
| MLE | Maximum likelihood estimator |
| PDF | Probability density function |
| RFC | Radio fundamental catalog for compact radio objects |
| SB | Starburst |
| SMBH | Supermassive black hole |
| TS | Test-statistic |

# B Supplementary Material for the Hotspot Population Analysis

## B.1 Hotspot counts from background simulations

In this section, we provide some supplementary distributions of the hotspot counts obtained from background simulations. Figure B.1 and Figure B.2 show the distributions obtained when simulating the diffuse atmospheric and astrophysical neutrino fluxes as observed by IceCube.

Figure B.3 and Figure B.4 show the hotspot counts when the background is increased by adding twice as much diffuse astrophysical neutrino flux.

Figure B.5 and Figure B.6 show the hotspot counts when the background consists of the atmospheric neutrino flux only and no astrophysical component is injected.

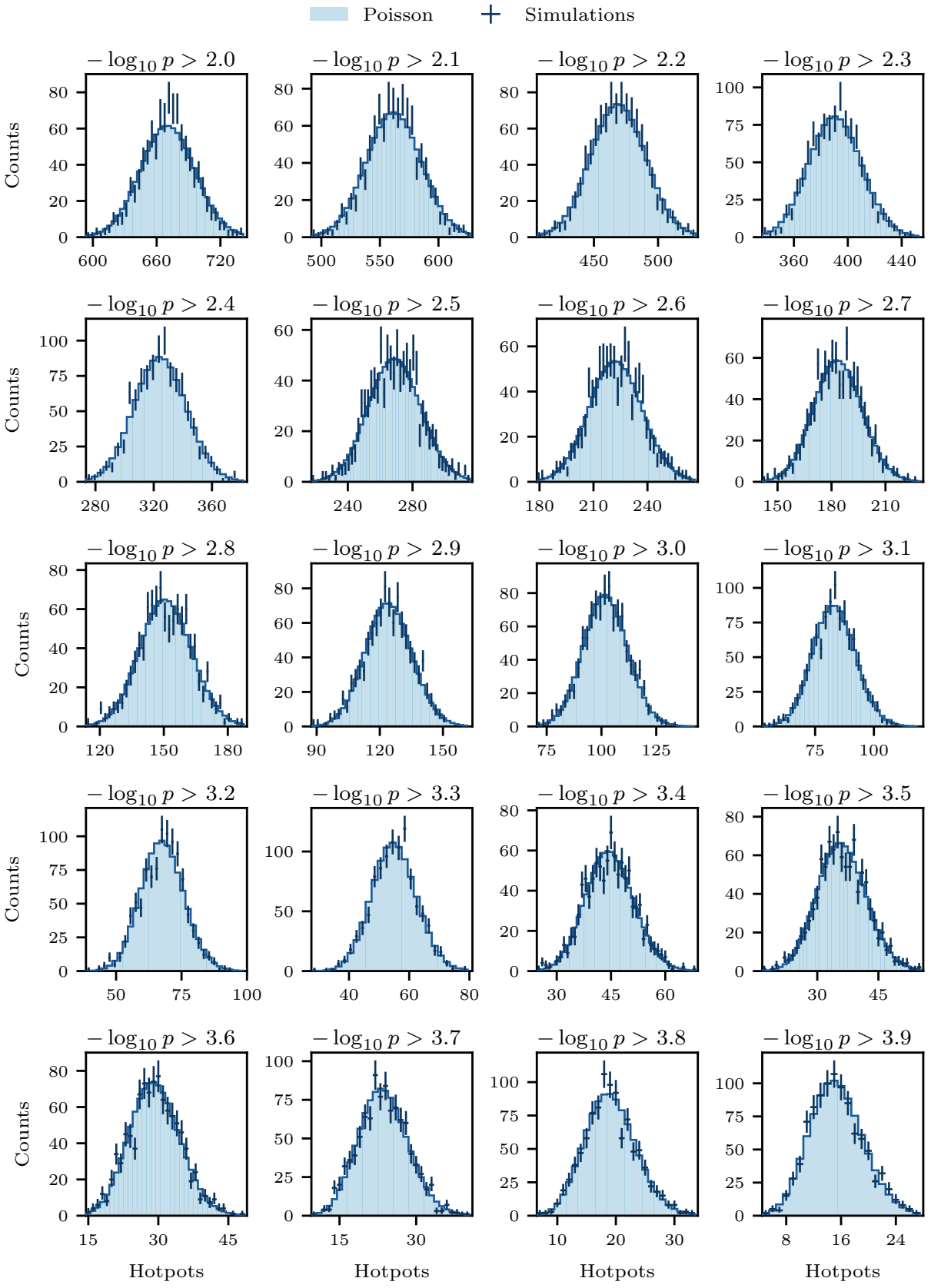


Figure B.1: In each panel, the count distribution of hotspots above $-\log_{10} p_{\text{thr}}$ (dark error bars) from 1,000 simulations is compared to the Poissonian distribution centered at its mean value (light blue histogram). Continues in Figure B.2.

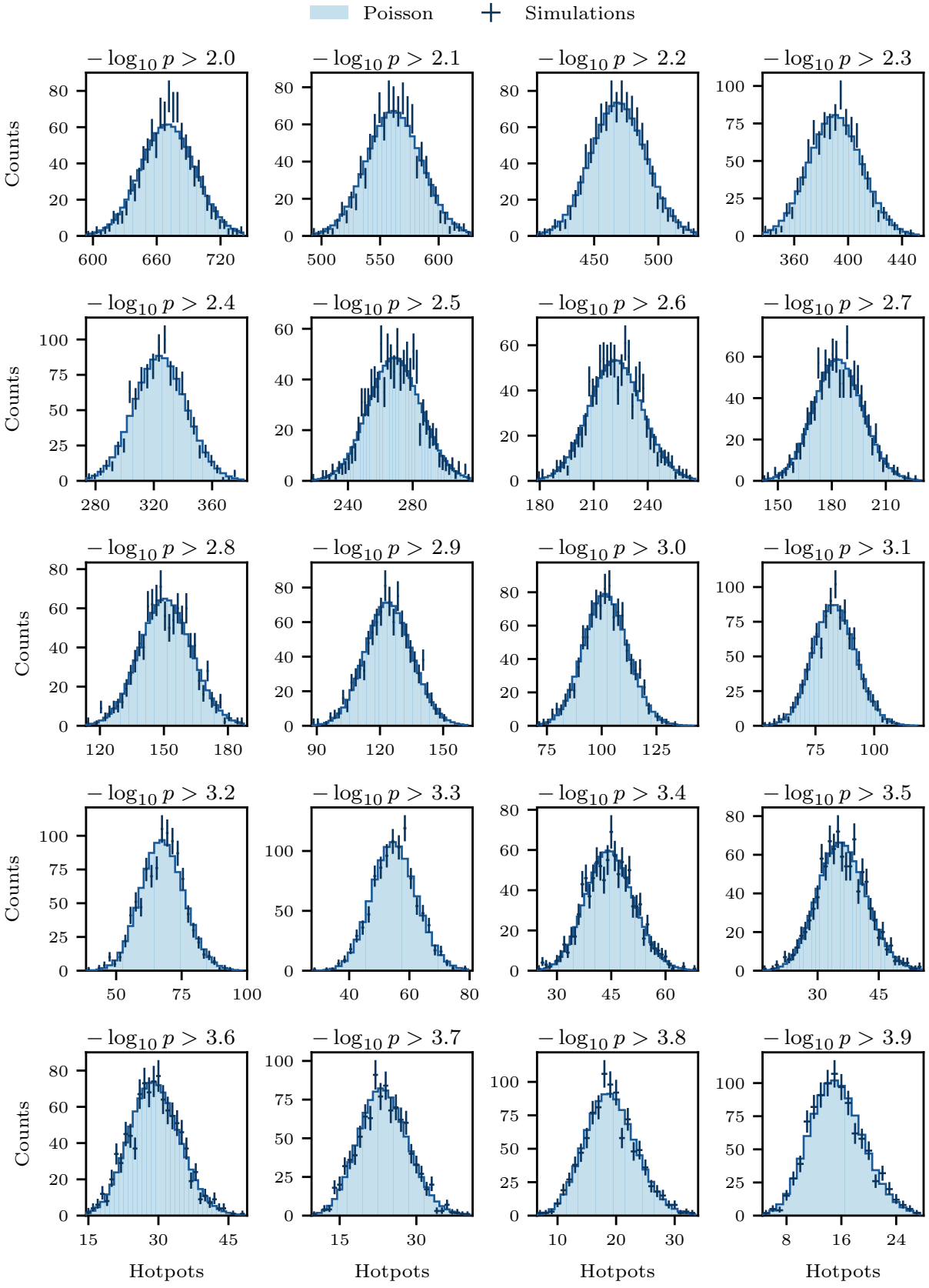


Figure B.2: Continued from Figure B.1.

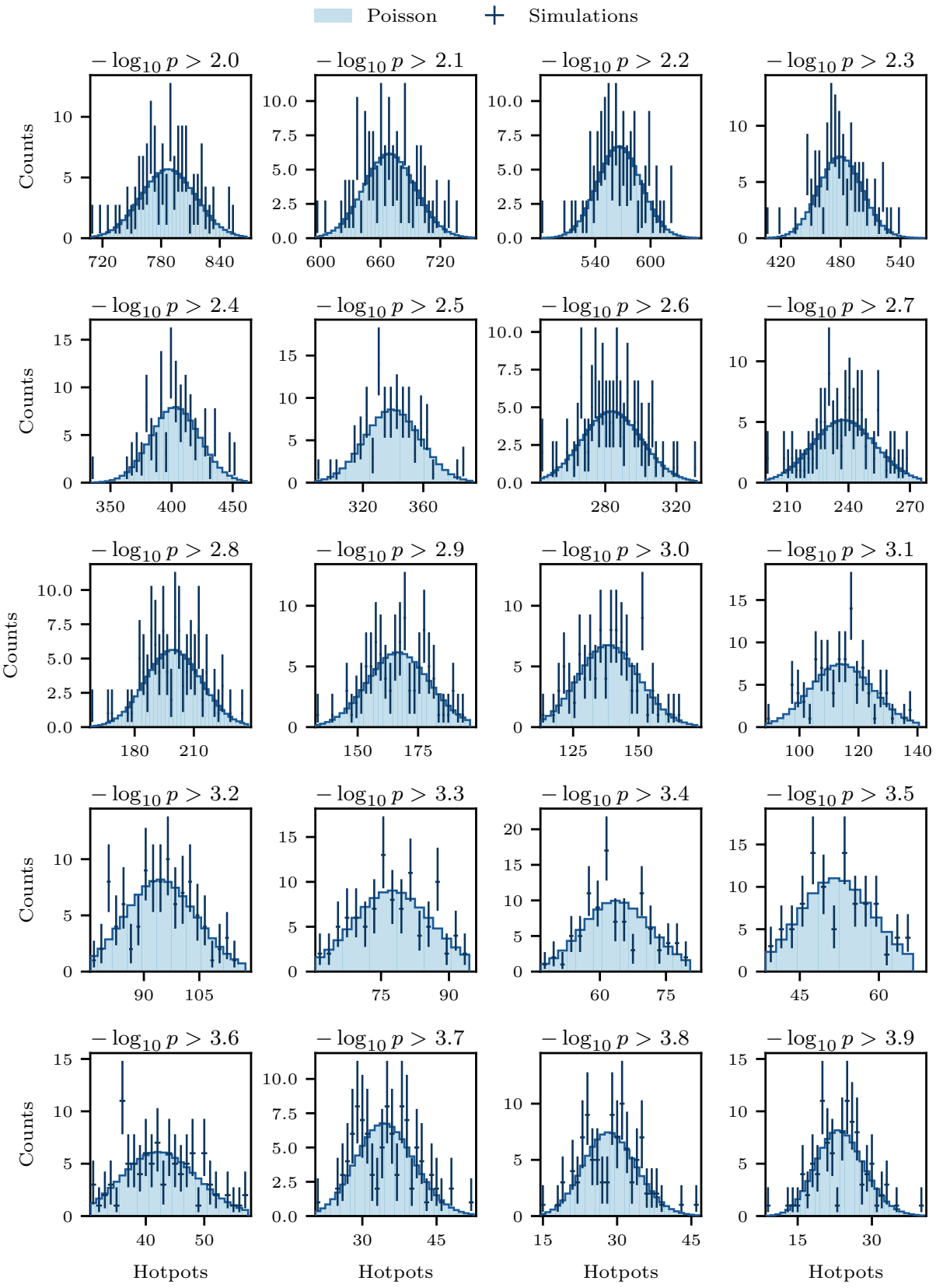


Figure B.3: The same as Figure B.1, but based on 100 simulations and injecting twice the diffuse astrophysical neutrino background. Continues in Figure B.4.

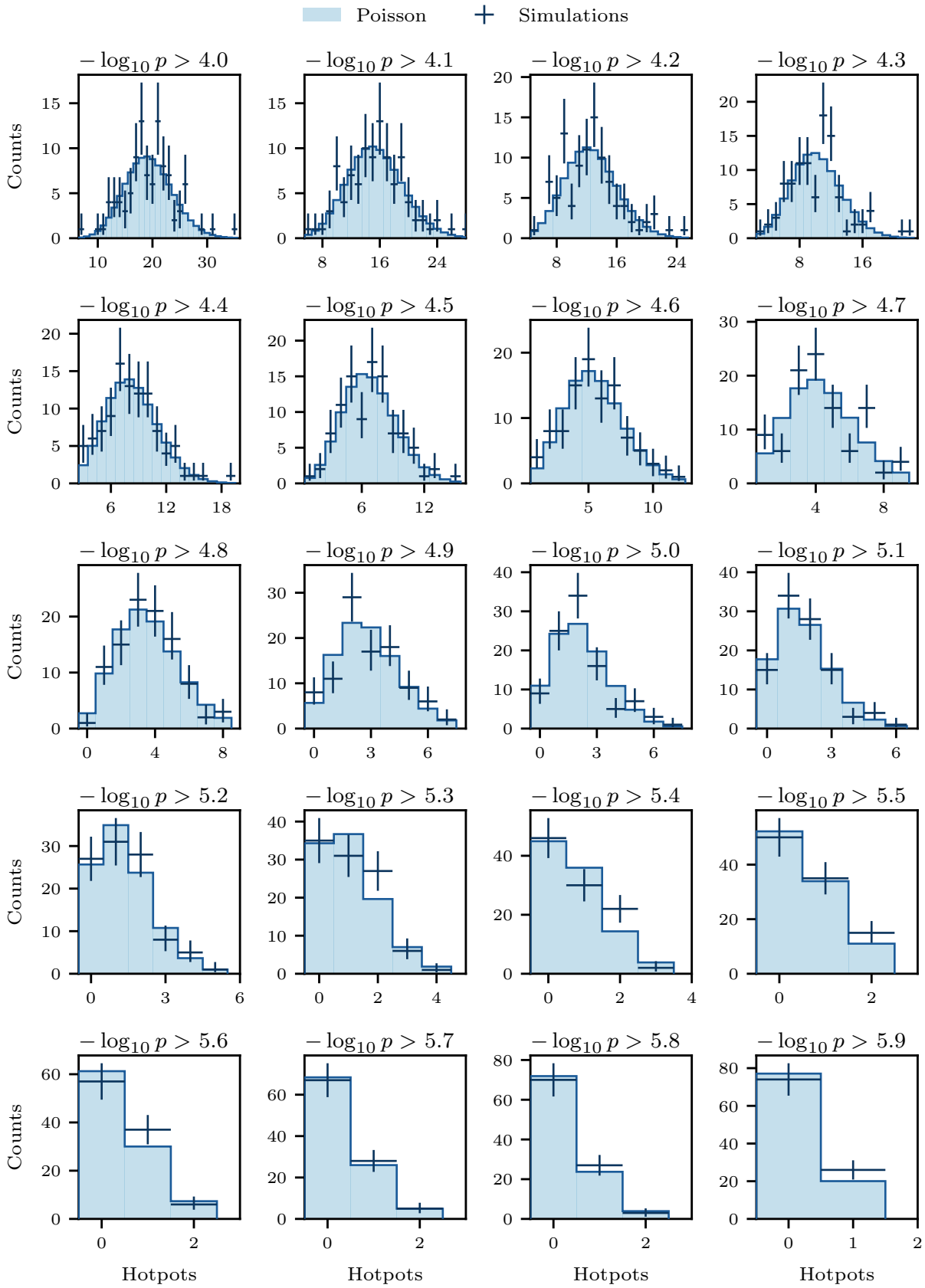


Figure B.4: Continued from Figure B.3.

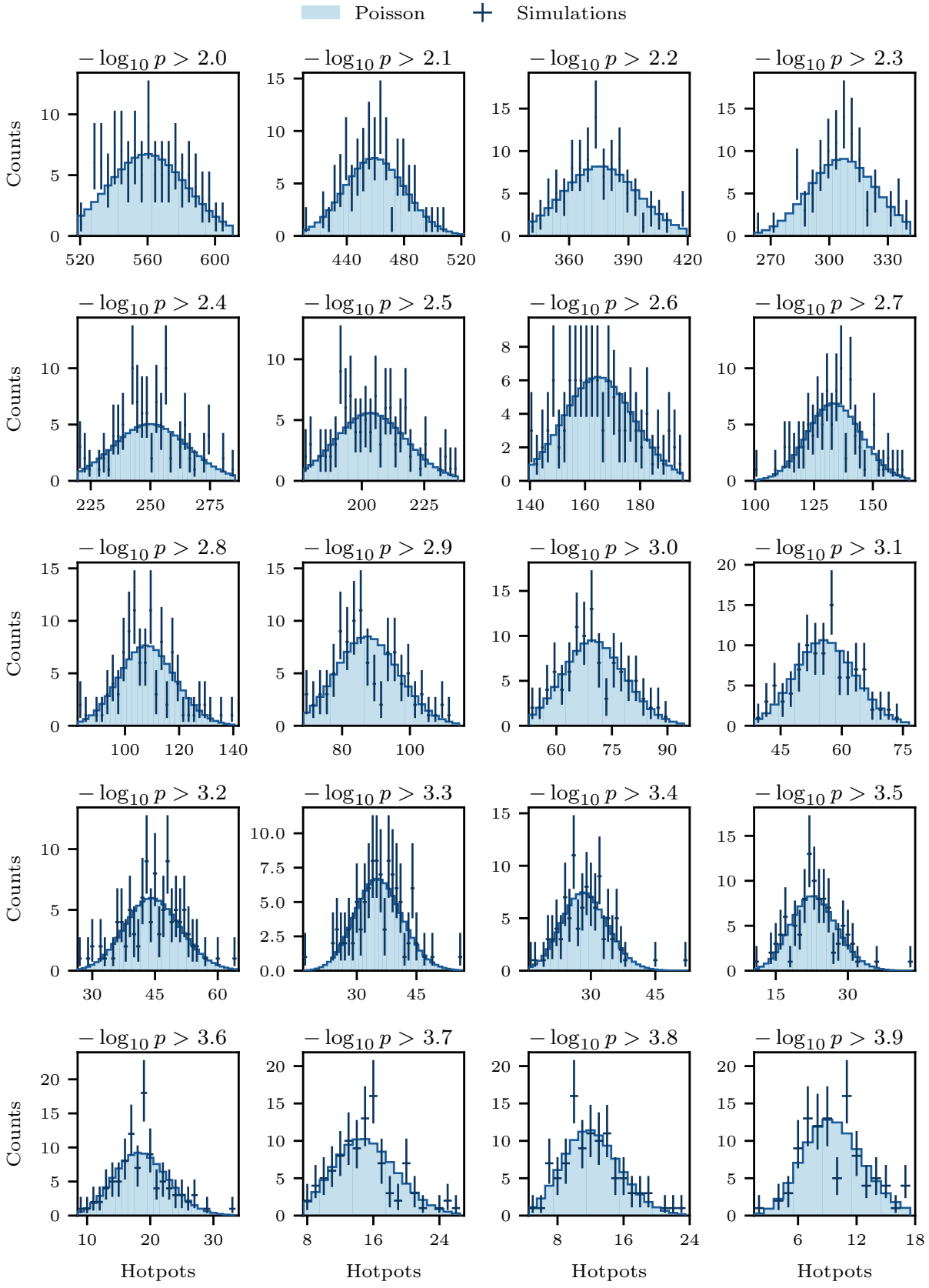


Figure B.5: The same as Figure B.1, but without injecting the diffuse astrophysical neutrino background. Continues in Figure B.6.

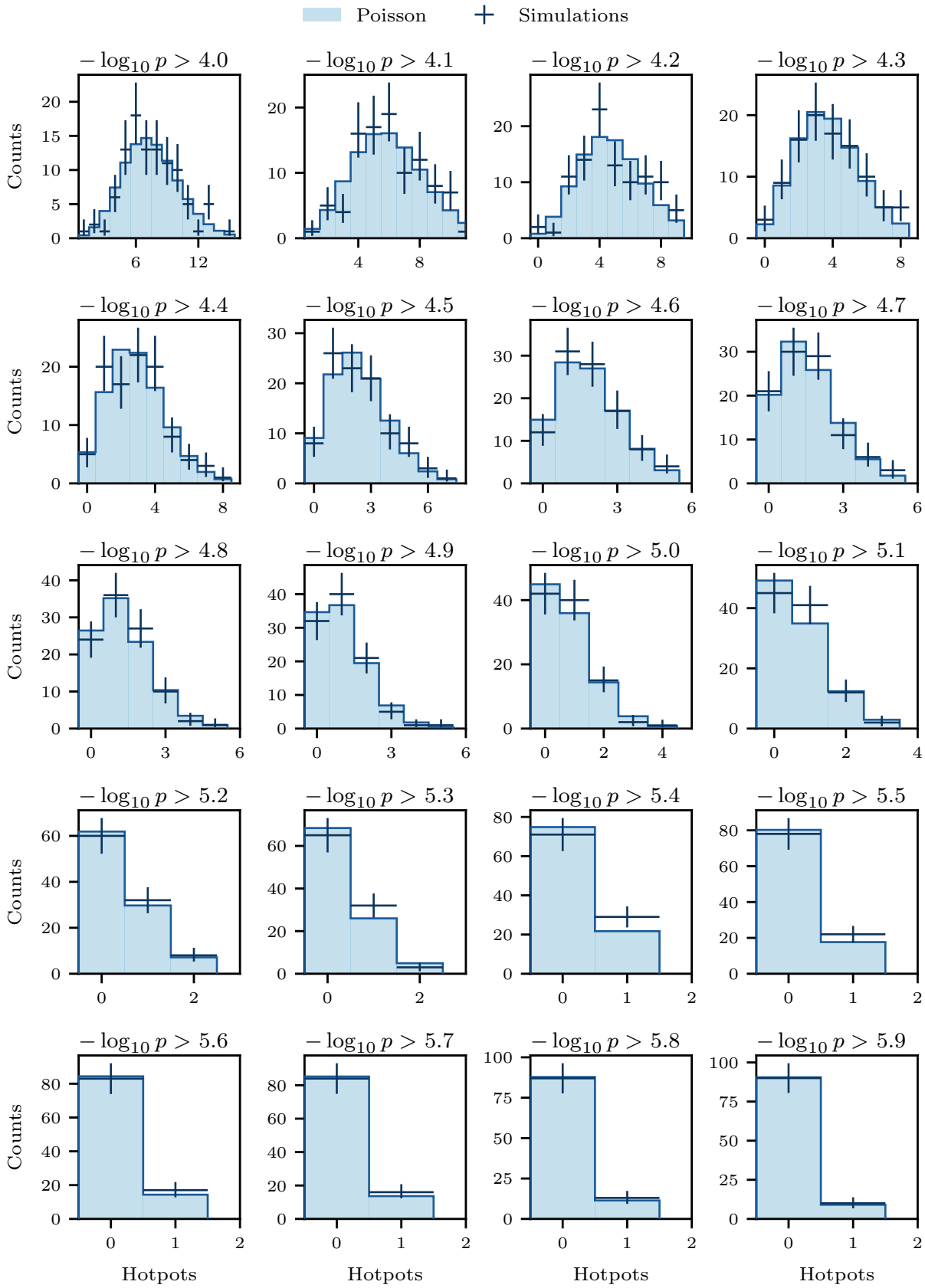


Figure B.6: Continued from Figure B.5.

# C Search for Neutrino Point Sources in the Northern Sky

## C.1 Monte Carlo datasets for the up-going muon tracks selection

The ice model used for all simulations in Table C.1 is *Spice 3.2.1*.

Table C.1: Properties of the Monte Carlo datasets of $\nu_\mu$ and $\nu_\tau$ events. The combination of all datasets is used as a high-statistics simulation sample for the point source analysis. The number of events is given for the final level sample, after the selection criteria (see Section 4.4) have been applied.

| Dataset | Properties |
|---|---|
| 21002 | $\nu_\mu$ simulations<br>*Energy Range*: 100 GeV - 100 PeV ($E^{-2}$ Spectrum)<br># Events: 9,989,091 |
| 21124 | $\nu_\mu$ simulations<br>*Energy Range*: 10 TeV - 500 PeV ($E^{-1}$ Spectrum)<br># Events: 81,208 |
| 21217 | $\nu_\mu$ simulations<br>*Energy Range*: 100 GeV - 100 PeV ($E^{-1.5}$ Spectrum)<br># Events: 2,233,814 |
| 21220 | $\nu_\mu$ simulations<br>*Energy Range*: 100 TeV - 100 PeV ($E^{-1}$ Spectrum)<br># Events: 95,418 |
| 21813 | $\nu_\mu$ simulations<br>*Energy Range*: 100 GeV - 10 TeV ($E^{-2}$ Spectrum)<br># Events: 9,171,860 |
| 21814 | $\nu_\mu$ simulations<br>*Energy Range*: 10 TeV - 1 PeV ($E^{-1.5}$ Spectrum)<br># Events: 6,258,708 |
| 21938 | $\nu_\mu$ simulations<br>*Energy Range*: 1 PeV - 100 PeV ($E^{-1}$ Spectrum)<br># Events: 98,668 |

*Continues on next page*

Table C.1: Properties of the Monte Carlo datasets (continued).

| Dataset | Properties |
|---|---|
| 21219 | $\nu_\tau$ simulations<br>*Energy Range*: 100 GeV - 100 PeV ($E^{-1.5}$ Spectrum)<br># Events: 46,054 |
| 21221 | $\nu_\tau$ simulations<br>*Energy Range*: 100 TeV - 500 PeV ($E^{-1}$ Spectrum)<br># Events: 20,539 |
| 21867 | $\nu_\tau$ simulations<br>*Energy Range*: 100 GeV - 10 TeV ($E^{-2}$ Spectrum)<br># Events: 21,730 |
| 21868 | $\nu_\tau$ simulations<br>*Energy Range*: 10 TeV - 1 PeV ($E^{1.5}$ Spectrum)<br># Events: 35,979 |
| 21939 | $\nu_\tau$ simulations<br>*Energy Range*: 1 PeV - 100 PeV ($E^{-1}$ Spectrum)<br># Events: 2,044 |

## C.2 Signal spatial KDE PDF for the IC79 dataset

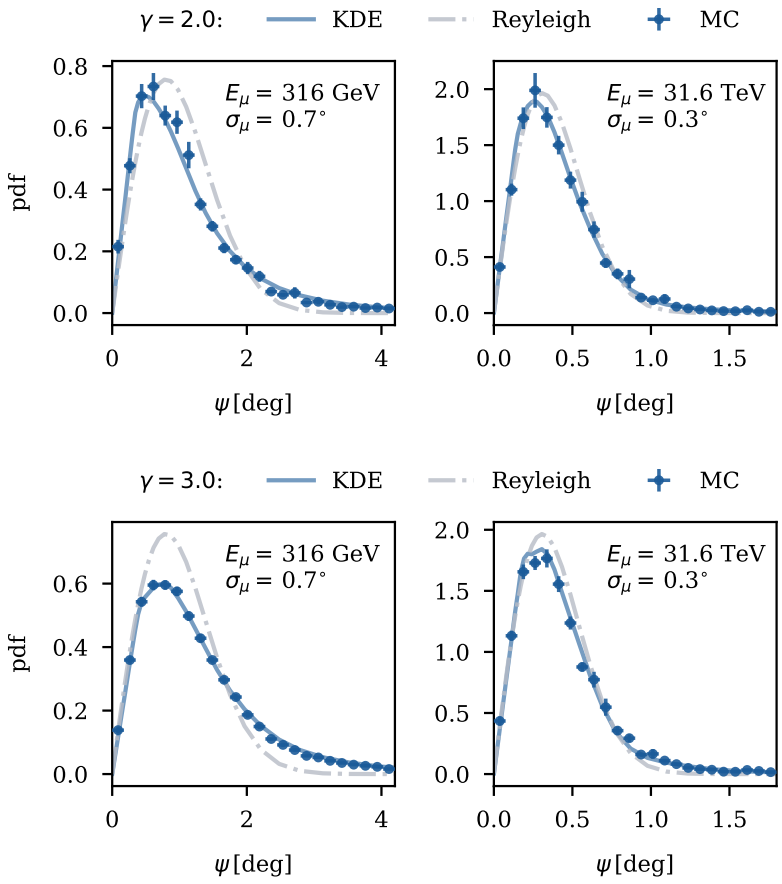


Figure C.1: Spatial terms of the signal likelihood assuming $\gamma = 2.0$ (top) and $\gamma = 3.0$ (bottom). The distribution of the angular distance $\psi$ between the neutrino and the reconstructed muon from MC simulations of the IC79 dataset (blue points) is compared to the KDE-based PDF (solid blue line) and the Rayleigh analytical approximation (dash-dotted grey line). The conditional observables—reconstructed muon energy and reconstruction quality estimator—are given in each panel.

## C.3 Test-statistic distributions under the null hypothesis

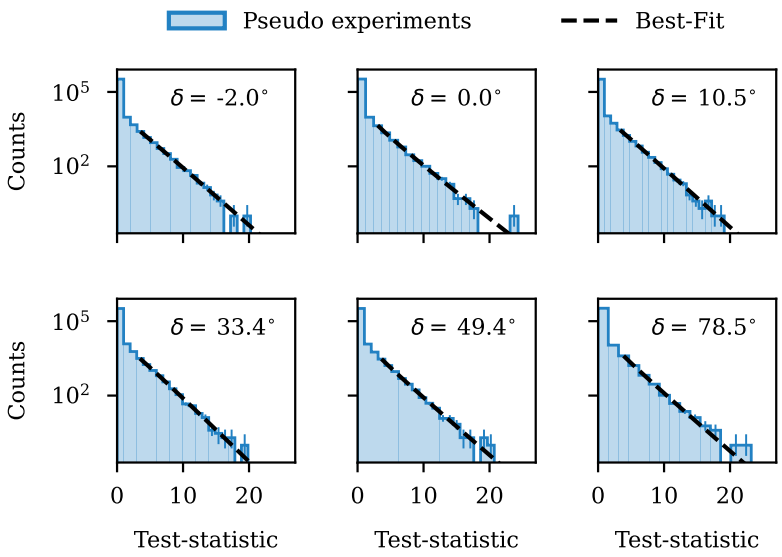


Figure C.2: Distribution of 350,000 test-statistic values obtained assuming the background-only hypothesis to be true and fixed spectral index $\gamma = 2.0$ at various declinations across the Northern sky. The tail of the distribution at $TS > 3$ is fitted with a truncated gamma distribution to extrapolate the behavior at high $TS$ values. The number of trials returning $TS = 0$ is approximately 80%.

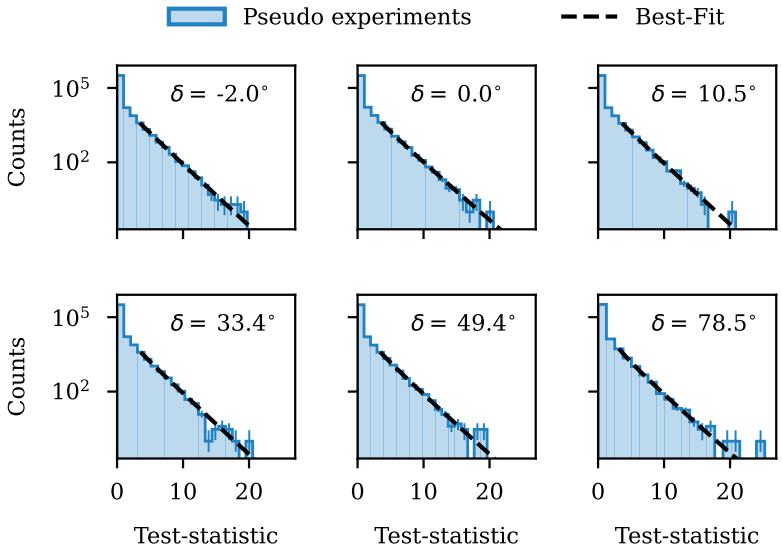


Figure C.3: Distribution of 350,000 test-statistic values obtained assuming the background-only hypothesis to be true and fixed spectral index $\gamma = 2.5$ at various declinations across the Northern sky. The tail of the distribution at $TS > 3$ is fitted with a truncated gamma distribution to extrapolate the behavior at high $TS$ values. The number of trials returning $TS = 0$ is approximately 70%.

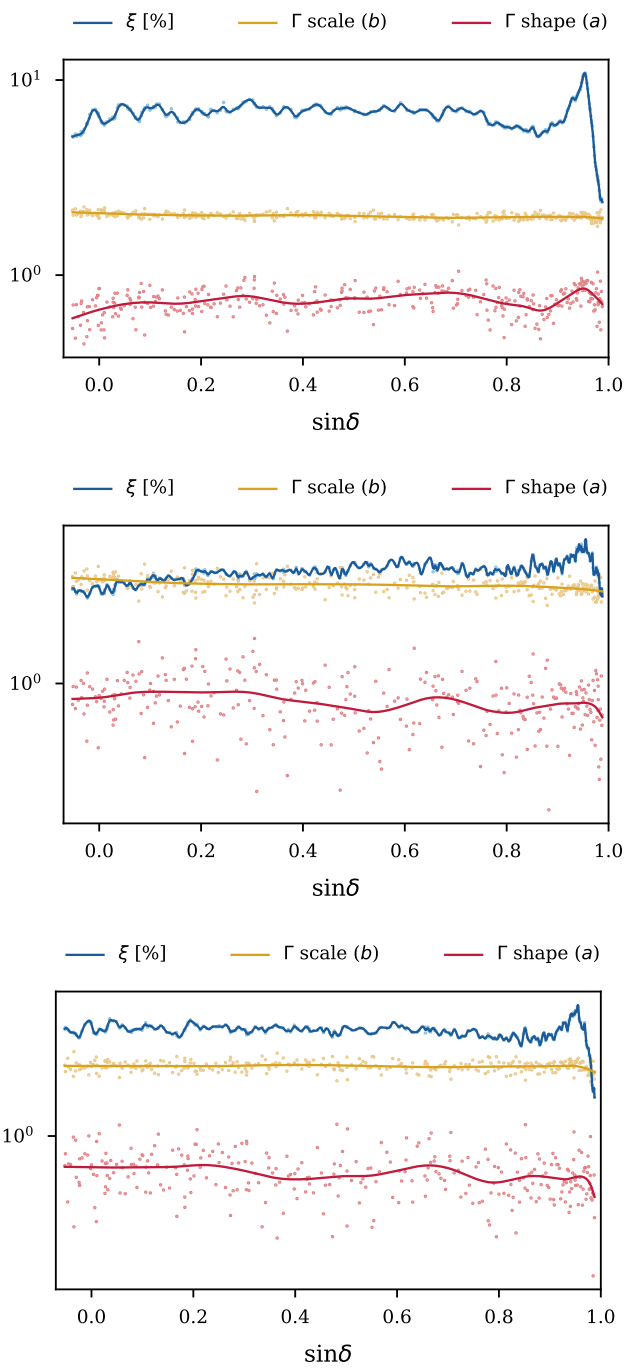


Figure C.4: Colored dots show the parameters of the truncated $\Gamma$-distribution fitted to the background *TS* distributions at approximately 350 declinations. The spectral index $\gamma$ is optimized in the likelihood maximization. The solid lines represent the interpolation splines applied to the measurements. The percentage of *TS* values above the truncation threshold at $TS = 3$ is shown in blue ($\xi$), and the scale and shape parameters of the $\Gamma$-distributions are shown in yellow and red, respectively. The splines are used to extrapolate the parameters at arbitrary declinations in the Northern sky. The middle and lower panel show the same interpolation spline but for the fixed $\gamma = 2.0$ and $\gamma = 2.5$, respectively.

## C.4 Uncertainty on the diffuse astrophysical background

Here, we test the impact of the choice of the astrophysical diffuse flux model on the analysis. The background-only hypothesis of the point-source analysis includes a contribution from an isotropic, diffuse flux of astrophysical origin, which we model according to the latest IceCube measurement[1] (which is our *baseline* astrophysical flux model). However, the measurement comes with a statistical uncertainty that is not included in the modeling of the likelihood function. To quantify the impact on the analysis response of this uncertainty, we can generate pseudo-experiments where we inject events according astrophysical fluxes taken from the 95% likelihood contour in Figure 3 of Abbasi et al., "Improved Characterization of the Astrophysical Muon-neutrino Flux with 9.5 Years of IceCube Data". The resulting background *TS* distributions are shown in Figure C.5. We do not observe any sizeable deviations from the baseline assumption at any declinations besides a small effect at the pole. Hence, we conclude that the point-source analysis is insensitive to this systematic uncertainty in most of the Northern sky.

[1] Abbasi et al., "Improved Characterization of the Astrophysical Muon-neutrino Flux with 9.5 Years of IceCube Data".

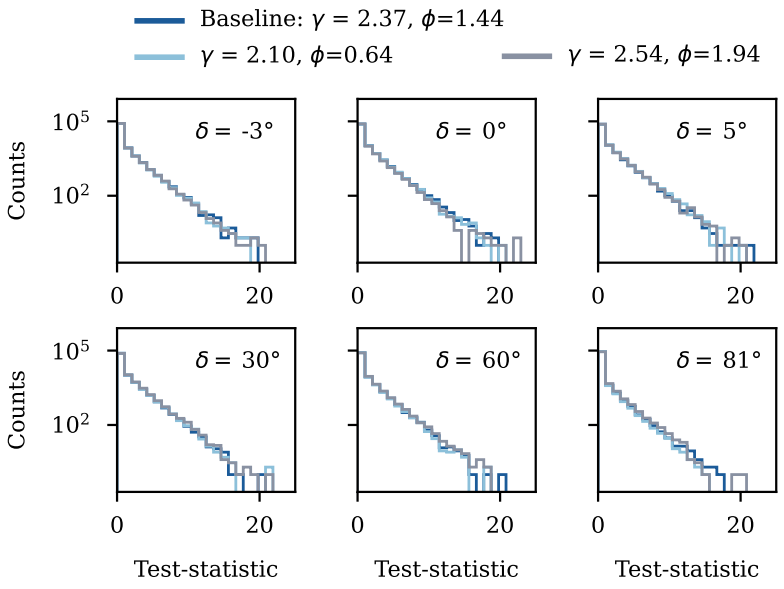


Figure C.5: Background *TS* distributions at various declinations. Each color assumes a different astrophysical diffuse flux component, as indicated in the legend. Flux normalizations $\phi$ are in units of $10^{-18}\mathrm{GeV}^{-1}\ \mathrm{cm}^{-2}\,\mathrm{s}^{-1}$. At all tested declinations, distributions with varied astrophysical backgrounds closely follow the baseline distribution (blue).

### C.4.1 *Systematic effect of the unmodeled diffuse neutrino background from the Galactic Plane*

Following the detection of neutrinos from the Galactic Plane,[2] a fit of the diffuse neutrino flux from the Northern sky resulted in a $2.7\sigma$ preference for the combination of an isotropic (extragalactic) and anisotropic (galactic) fluxes over a diffuse isotropic flux only.[3] This study used the model template for the galactic neutrino emission shown in Figure C.6, for which a flux normalization 2.9 times higher than expected was found.[4]

The analysis was performed using the same up-going muon track selection used for our point-source analysis. However, the background-only hypothesis $H_0$ of the point-source analysis only assumes an isotropic astrophysical background. The impact of having an unmodeled GP background component can be evaluated by performing the baseline[5] point-source analysis on simulated datasets where the astrophysical background consists of:

- An extragalactic isotropic component obtained by subtracting the GP spectrum isotropically as a function of the neutrino energy from the extragalactic diffuse flux.[6]

- A galactic anisotropic component as shown in Figure C.6.

This procedure ensures that the total astrophysical diffuse flux remains conserved and equal to the IceCube measurement but is no longer uniformly distributed in the sky.

When testing sources that lie on the Galactic Plane, the unmodeled GP background produces sizable differences in the background *TS* distributions, shown in Figure C.7. However, the effect becomes negligible when moving further away from the plane. Effectively, the background underestimation translates into the possibility of overestimating the significance of the point-source signal from sources that align with the GP. In Figure C.8, we quantify the possible significance overestimation in terms of sensitivity and $5\sigma$ discovery potential. Both quantities are evaluated at positions where the expected galactic plane flux is maximal, *i.e.*, along the bright GP arms in Figure C.6. Figure C.8 illustrates the outcome of the test. While the sensitivity of the analysis might be overestimated by a factor up to $\sim 20\%$, the discovery potential is way less affected for both hard and soft spectra. The maximum deviation from the baseline discovery potential is approximately 5%. It occurs for sources located right on top of the maximal neutrino emission according to the model adopted for the study,[7] *i.e.*, at the location in the Northern sky that is the closest to the Galactic Center.

[2] Icecube Collaboration, "Observation of high-energy neutrinos from the Galactic plane".

[3] Fuerst et al., "Galactic and Extragalactic Analysis of the Astrophysical Muon Neutrino Flux with 12.3 years of IceCube Track Data".

[4] Ibid.

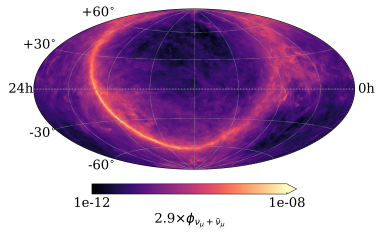


Figure C.6: Model template for the diffuse neutrino emission from the Milky Way (Schwefer, Mertsch, and Wiebusch, "Diffuse Emission of Galactic High-energy Neutrinos from a Global Fit of Cosmic Rays"). The flux normalization (in units of $\mathrm{TeV}^{-1}\,\mathrm{cm}^{-2}\,\mathrm{s}^{-1}$) is scaled by a factor of 2.9 according to the latest IceCube measurement in the Northern sky (see the text for references).

[5] Constructed based on a background-only hypothesis which only contains an isotropic, diffuse, extragalactic background.

[6] Abbasi et al., "Improved Characterization of the Astrophysical Muon-neutrino Flux with 9.5 Years of IceCube Data".

[7] Schwefer, Mertsch, and Wiebusch, "Diffuse Emission of Galactic High-energy Neutrinos from a Global Fit of Cosmic Rays".

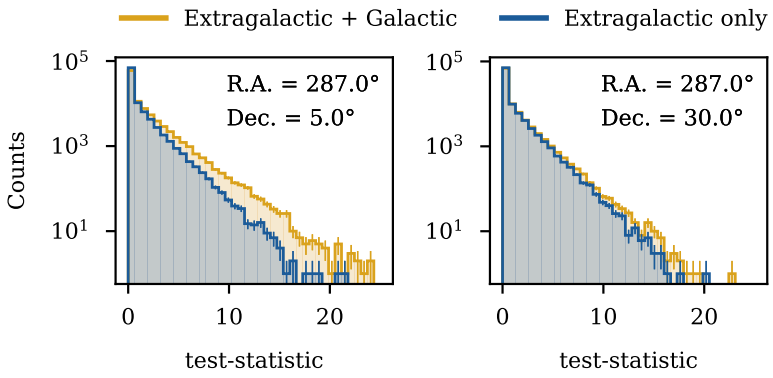


Figure C.7: Background *TS* distribution obtained on simulated samples with a GP contribution. **Left:** The analysis is performed at a location where the GP emission is high according to the template in Figure C.6. **Right:** Moving away from the GP, the effect becomes negligible.

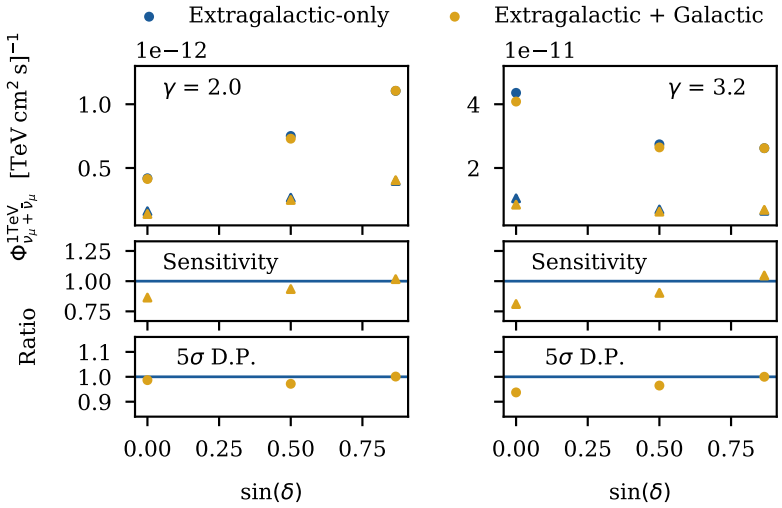


Figure C.8: Sensitivity and discovery potential fluxes as a function of the declination. The baseline isotropic background model (blue) is compared to the anisotropic background caused by a GP flux component (yellow). The systematic effect is studied for both hard ($\gamma = 2$, left) and soft ($\gamma = 3.2$, right) point-source spectra.

Finally, we study the effect of the GP systematic uncertainty on the recovery of the injected signal strength. Figure C.9 and Figure C.10 illustrate the bias in the best-fit number of signal events $\hat{\mu}_{\mathrm{ns}}$ and spectral index $\hat{\gamma}$ as a function of the simulated signal strength $\mu_{\mathrm{inj}}$ assuming both hard and soft spectral shapes. The spectral index fit is substantially unaffected, regardless of the injected spectrum. A small deviation from the baseline behavior is seen for $\hat{\mu}_{\mathrm{ns}}$ at the location of the maximal neutrino emission from the GP, at declination $\delta = 0°$ and right ascension R.A. $= 283°$. However, for both spectra, the systematic effect is subdominant compared to the statistical uncertainty on the measurement of the two parameters, and can be safely neglected.

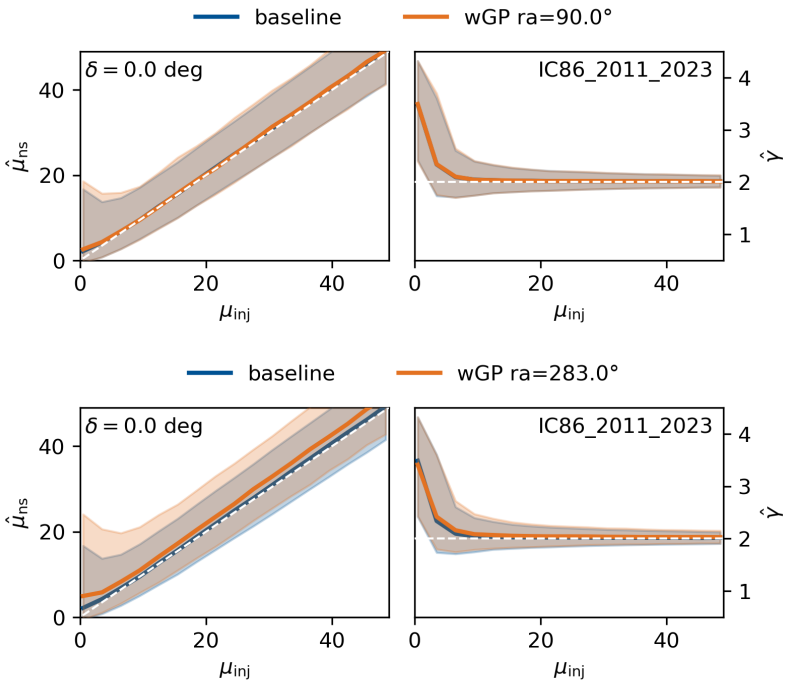


Figure C.9: Fitted versus injected signal for a $\gamma = 2.0$ source spectrum and two different locations. The left and right plots show the recovery of the number of signal events and the spectral index as a function of the number of injected events. The unbiased expectation is shown as a white dashed line. The systematic effect due to the unmodeled GP background flux is shown in orange and compared to the baseline analysis, in blue.

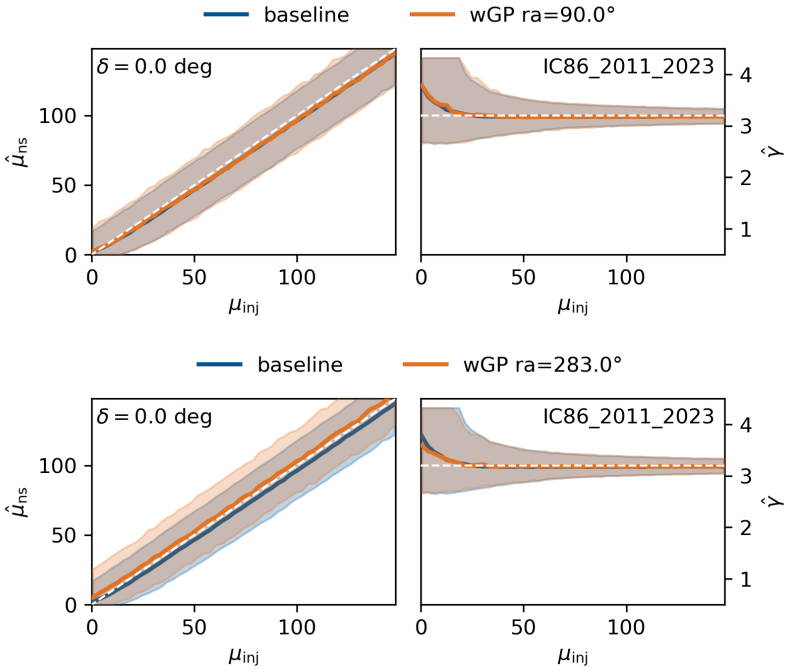


Figure C.10: Same as for Figure C.10, but for a $\gamma = 3.2$ source spectrum.

## C.5 *Neutrino sky maps assuming fixed power-law spectral indices*

Figure C.11 shows the sky scan obtained under the assumption of a fixed spectral index $\gamma = 2.0$ for the unbroken power-law energy spectrum. The hottest spot is found at right ascension 77.01° and declination 12.98°. No gamma-ray or X-ray sources are found near the neutrino excess. One high-energy neutrino event—IC190712A—is found 0.43° from the hotspot.

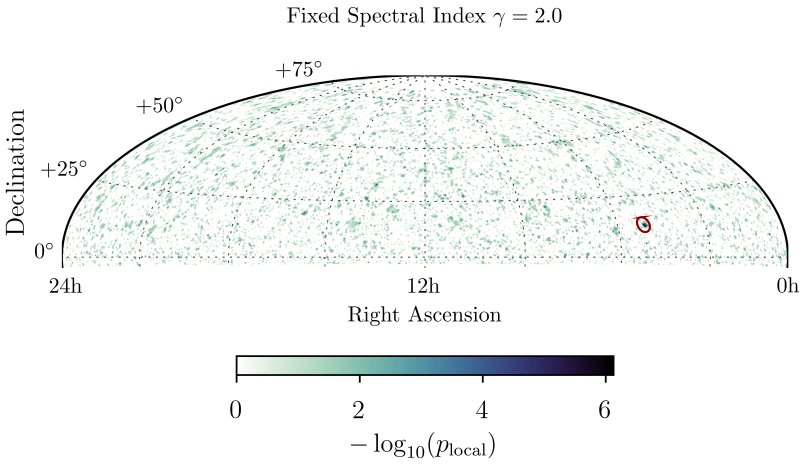


Figure C.11: Hammer-Aitoff projection of the sky map resulting from the maximum likelihood search for neutrino point-like sources in the Northern sky. Here, the spectral index of the power-law energy spectrum is fixed to 2.0. The color scale indicates the negative logarithm of the local p-value ($-\log_{10} p_{\text{local}}$) at each scanned point. Darker colors represent stronger deviations from the background-only assumption. The circle indicates the most significant spot found in the scan.

Figure C.12 shows the sky scan obtained under the assumption of a fixed spectral index $\gamma = 2.5$ for the unbroken power-law energy spectrum. The hottest spot is found at right ascension 161.48° and declination 27.32°. One gamma-ray source—4FGL J1045.3+2751—is found 0.5° from the neutrino hotspot.

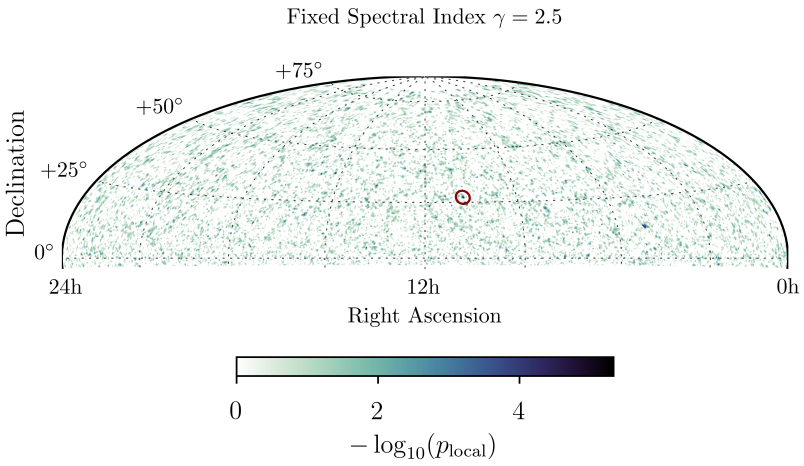


Figure C.12: Hammer-Aitoff projection of the sky map resulting from the maximum likelihood search for neutrino point-like sources in the Northern sky. Here, the spectral index of the power-law energy spectrum is fixed to 2.5. The color scale indicates the negative logarithm of the local p-value ($-\log_{10} p_{\text{local}}$) at each scanned point. Darker colors represent stronger deviations from the background-only assumption. The circle indicates the most significant spot found in the scan.

## C.6 Validation of Wilks' theorem

In this section, we demonstrate on Monte Carlo simulations the validity of Wilks' theorem, which is used in Section 8.2 to estimate the two-dimensional confidence intervals on the best-fit flux parameters of NGC 1068, NGC 7469, NGC 4151, and CGCG 420−015.

**Theorem C.6.1 (Wilks' Theorem)** *For testing an hypothesis $H_0 : \theta = \theta_0$ versus $H_1 = \theta \neq \theta_0$, suppose $x_1, \ldots, x_n$ are independent and identically distributed random variables such that $f(x|\theta)$, $\hat{\theta}$ is the maximum likelihood estimator (MLE) of $\theta$, and $f(x|\theta)$ is sufficiently regular. Then under $H_0$, as $n \to \infty$*

$$TS = -2 \times \log \Lambda \to \chi^2_1 \quad \textit{in distribution},$$

where $\chi^2_1$ is a $\chi^2$ random variable with 1 degree of freedom. While the theorem is given for a hypothesis $H_0$ with one degree of freedom,[8] it can be extended to $N$-degrees of freedom in which case, under the same conditions, the test statistic values are distributed as $\chi^2_N$.[9]

In the point-source analysis described in Section 5.1 we have 2 degrees of freedom as $\theta = \{n_s, \gamma\}$.

$$-2 \times \log \Lambda = -2 \times \log \frac{\mathcal{L}(\hat{n}_s, \hat{\gamma})}{\sup_{n_s,\gamma} \mathcal{L}(n_s, \gamma)}. \tag{C.1}$$

In other words, we build the $TS$ distribution under the hypothesis that the best-fit result obtained from the data analysis is true.

Practically, for each source, we simulate the best-fit flux (according to $\hat{n}_s$ and $\hat{\gamma}$) and compute $-2 \times \log \Lambda$ as in Equation C.1. By definition, $-2 \times \log \Lambda \geq 0$.

Figure C.13 tests the validity of Theorem C.6.1 at the location of the top 12 X-ray bright Seyfert galaxies from the list in Table C.2. The $\chi^2_2$ approximation accurately describes the distributions for most of the sources, except for LEDA 166445 and NGC 1194. For these two objects, $\hat{\gamma}$ is at the boundary of the parameter space that the minimizer is allowed to explore. In this case, the regularity conditions mentioned in Theorem C.6.1 are not fulfilled[10].

[8] Casella and Berger, "Statistical Inference", p. 489.

[9] Wilks, "The Large-Sample Distribution of the Likelihood Ratio for Testing Composite Hypotheses".

[10] For a review of the regularity conditions necessary to prove Theorem C.6.1, we refer the reader to Casella and Berger, "Statistical Inference", p. 516.

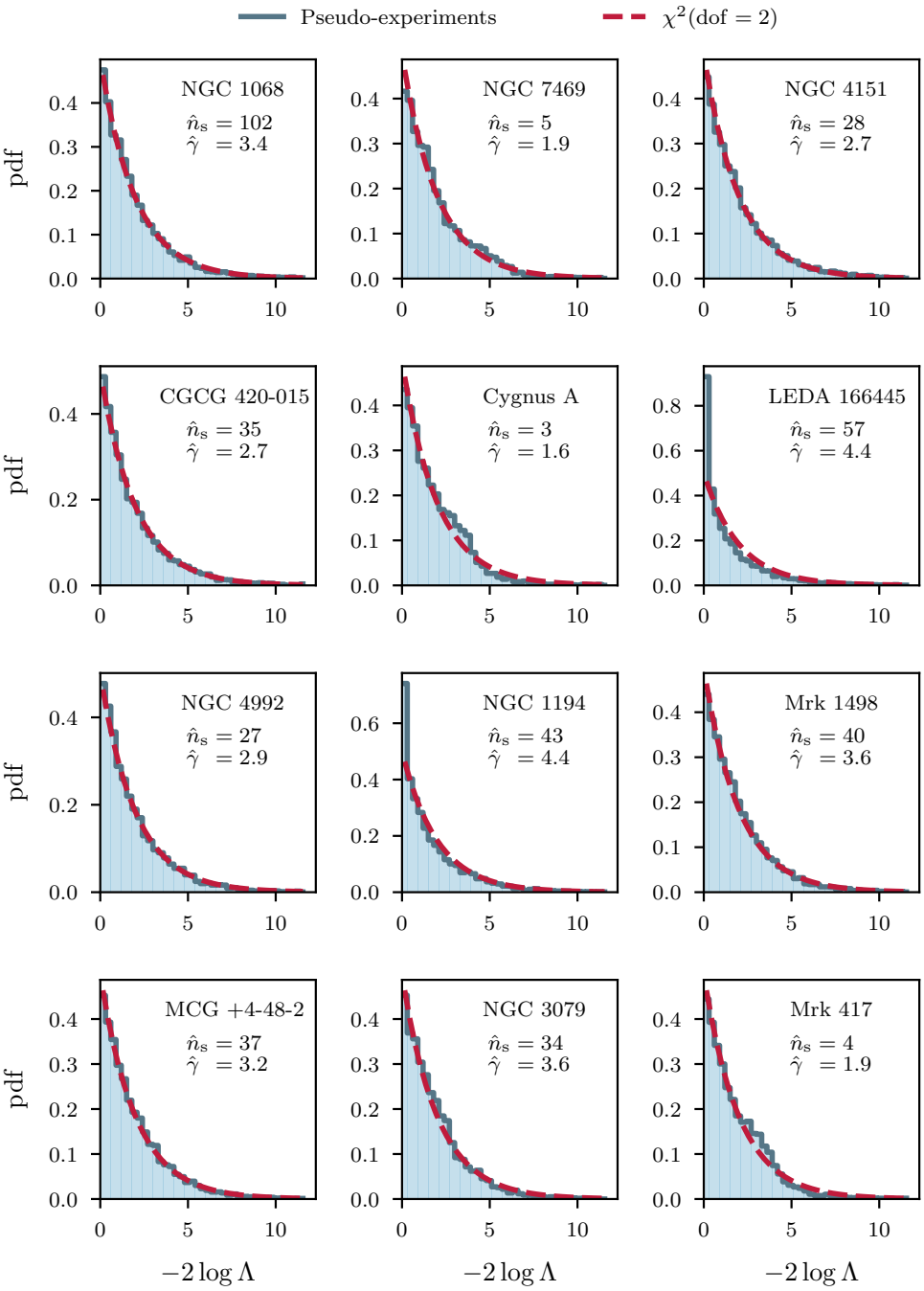


Figure C.13: Validation of Wilks' theorem for the top 12 sources contributing to a $3.3\,\sigma$ binomial excess out of a list of 48 X-ray bright Seyfert. The sources are ordered according to their local significance in the point-source analysis. The $\chi^2$ approximation is valid for almost all 12 sources. However it does not hold for the two sources for which the MLE of the spectral index $\gamma$ is at the boundary of the parameter space, $\gamma \in [0.5, 4.4]$.

## C.7 More results on the Seyfert candidate sources

Table C.2 summarizes the results of the search for neutrino emission from 48 X-ray bright Seyfert galaxies individually. For each source, the right ascension (R.A.), declination (Dec.), redshift (z), hydrogen column density ($N_{\mathrm{H}}$), and hard X-ray flux ($F^{\mathrm{intr}}_{20-50\ \mathrm{keV}}$) are from the BAT 105-month catalog. The best-fit spectral parameters for the power-law ($\hat{n}_{\mathrm{s}}$ and $\hat{\gamma}$), the test-statistic value ($TS$), and the local p-value ($p_{\mathrm{local}}$) result from the point-source analysis.

| Source Name | R.A. (deg) | Dec. (deg) | z | $\log \mathrm{N_H}$ | $F^{\mathrm{intr}}_{20-50\ \mathrm{keV}}$ | $\hat{n}_{\mathrm{s}}$ | $\hat{\gamma}$ | $TS$ | $p_{\mathrm{local}}$ |
|---|---|---|---|---|---|---|---|---|---|
| NGC 1068 | 40.67 | -0.01 | 0.003 | 25.00 | 7.72 | 102.2 | 3.4 | 27.1 | $2.6 \times 10^{-7}$ ($5.0\,\sigma$) |
| NGC 7469 | 345.82 | 8.87 | 0.016 | 20.53 | 2.69 | 5.5 | 1.9 | 15.5 | $9.8 \times 10^{-5}$ ($3.7\,\sigma$) |
| NGC 4151 | 182.64 | 39.41 | 0.003 | 22.71 | 18.09 | 27.6 | 2.7 | 10.8 | $1.1 \times 10^{-3}$ ($3.1\,\sigma$) |
| CGCG 420−015 | 73.36 | 4.06 | 0.029 | 24.08 | 1.77 | 35.3 | 2.7 | 8.4 | $3.6 \times 10^{-3}$ ($2.7\,\sigma$) |
| Cygnus A | 299.87 | 40.73 | 0.056 | 23.38 | 4.93 | 3.4 | 1.6 | 7.4 | $6.5 \times 10^{-3}$ ($2.5\,\sigma$) |
| LEDA 166445 | 42.68 | 54.70 | 0.015 | 24.01 | 1.61 | 57.1 | 4.4 | 5.2 | 0.02 ($2.1\,\sigma$) |
| NGC 4992 | 197.27 | 11.63 | 0.025 | 23.69 | 2.34 | 27.3 | 2.9 | 5.0 | 0.02 ($2.0\,\sigma$) |
| NGC 1194 | 45.95 | -1.10 | 0.014 | 24.18 | 3.87 | 43.2 | 4.4 | 4.1 | 0.03 ($1.8\,\sigma$) |
| Mrk 1498 | 247.02 | 51.78 | 0.055 | 23.23 | 1.86 | 39.9 | 3.6 | 3.7 | 0.04 ($1.7\,\sigma$) |
| MCG+4−48−2 | 307.15 | 25.73 | 0.014 | 23.86 | 4.32 | 36.7 | 3.2 | 4.1 | 0.04 ($1.7\,\sigma$) |
| NGC 3079 | 150.49 | 55.68 | 0.004 | 24.56 | 3.33 | 33.8 | 3.6 | 3.3 | 0.05 ($1.7\,\sigma$) |
| Mrk 417 | 162.38 | 22.96 | 0.033 | 23.90 | 1.73 | 4.4 | 1.9 | 3.5 | 0.05 ($1.6\,\sigma$) |
| Q0241+622 | 41.24 | 62.47 | 0.050 | 20.92 | 3.45 | 17.1 | 2.8 | 3.0 | 0.06 ($1.6\,\sigma$) |
| LEDA 138501 | 32.41 | 52.44 | 0.049 | 20.00 | 1.95 | 34.0 | 4.4 | 1.9 | 0.11 ($1.2\,\sigma$) |
| LEDA 86269 | 71.04 | 28.22 | 0.011 | 22.65 | 1.76 | 39.2 | 4.4 | 2.2 | 0.11 ($1.2\,\sigma$) |
| NGC 5252 | 204.57 | 4.54 | 0.023 | 22.43 | 3.65 | 32.2 | 3.6 | 1.6 | 0.13 ($1.1\,\sigma$) |
| 3C 382 | 278.76 | 32.70 | 0.058 | 20.00 | 2.62 | 32.7 | 4.4 | 1.7 | 0.14 ($1.1\,\sigma$) |
| NGC 4388 | 186.44 | 12.66 | 0.008 | 23.52 | 10.79 | 2.1 | 2.0 | 1.6 | 0.15 ($1.0\,\sigma$) |
| LEDA 168563 | 73.02 | 49.55 | 0.029 | 21.23 | 2.15 | 1.8 | 1.8 | 1.4 | 0.16 ($1.0\,\sigma$) |
| Ark 120 | 79.05 | -0.15 | 0.032 | 20.00 | 2.75 | 26.7 | 4.4 | 1.3 | 0.18 ($0.9\,\sigma$) |
| Z 164−19 | 221.40 | 27.03 | 0.030 | 24.64 | 8.81 | 3.4 | 1.9 | 1.3 | 0.18 ($0.9\,\sigma$) |
| 3C 445 | 335.96 | -2.10 | 0.060 | 23.54 | 2.02 | 14.5 | 4.4 | 0.8 | 0.20 ($0.8\,\sigma$) |
| NGC 5548 | 214.50 | 25.14 | 0.017 | 20.69 | 2.70 | 16.8 | 3.2 | 1.2 | 0.21 ($0.8\,\sigma$) |
| Mrk 6 | 103.05 | 74.43 | 0.019 | 20.76 | 2.15 | 10.0 | 2.8 | 0.9 | 0.24 ($0.7\,\sigma$) |
| NGC 3516 | 166.70 | 72.57 | 0.009 | 20.00 | 4.17 | 33.8 | 4.4 | 1.3 | 0.26 ($0.6\,\sigma$) |
| UGC 11910 | 331.76 | 10.23 | 0.027 | 24.07 | 2.20 | 20.8 | 4.4 | 0.6 | 0.27 ($0.6\,\sigma$) |
| 4C+50.55 | 321.16 | 50.97 | 0.015 | 23.02 | 7.73 | 9.1 | 3.0 | 0.5 | 0.27 ($0.6\,\sigma$) |
| IGR J21277+5656 | 321.94 | 56.94 | 0.015 | 20.00 | 1.67 | 3.7 | 2.4 | 0.5 | 0.28 ($0.6\,\sigma$) |
| Mrk 1040 | 37.06 | 31.31 | 0.017 | 21.09 | 2.37 | 16.4 | 4.4 | 0.4 | 0.31 ($0.5\,\sigma$) |
| 3C 111 | 64.59 | 38.03 | 0.049 | 21.87 | 4.13 | 12.1 | 4.4 | 0.3 | 0.37 ($0.3\,\sigma$) |
| Mrk 1210 | 121.02 | 5.11 | 0.013 | 23.40 | 2.36 | 9.2 | 4.4 | 0.1 | 0.44 ($0.1\,\sigma$) |
| NGC 1142 | 43.80 | -0.18 | 0.029 | 23.76 | 4.05 | 6.2 | 3.7 | 0.1 | 0.46 ($0.1\,\sigma$) |
| NGC 7682 | 352.27 | 3.53 | 0.017 | 24.27 | 1.99 | 1.3 | 2.8 | 0.1 | 0.47 ($0.1\,\sigma$) |
| NGC 7603 | 349.74 | 0.24 | 0.029 | 20.00 | 1.87 | 2.2 | 4.4 | 0.0 | 1.00 ($0.0\,\sigma$) |
| 3C 390.3 | 280.54 | 79.77 | 0.056 | 20.84 | 3.66 | 0.0 | 4.4 | 0.0 | 1.00 ($0.0\,\sigma$) |
| 4C+74.26 | 310.66 | 75.13 | 0.104 | 21.36 | 2.00 | 0.0 | 4.4 | 0.0 | 1.00 ($0.0\,\sigma$) |
| NGC 6240 | 253.25 | 2.40 | 0.025 | 24.25 | 12.89 | 0.0 | 4.4 | 0.0 | 1.00 ($0.0\,\sigma$) |
| NGC 3227 | 155.88 | 19.87 | 0.004 | 20.95 | 4.16 | 0.0 | 4.4 | 0.0 | 1.00 ($0.0\,\sigma$) |
| IRAS 05589+2828 | 90.54 | 28.47 | 0.033 | 20.81 | 2.64 | 0.0 | 4.4 | 0.0 | 1.00 ($0.0\,\sigma$) |
| Mrk 79 | 115.64 | 49.81 | 0.022 | 20.00 | 1.82 | 0.0 | 4.4 | 0.0 | 1.00 ($0.0\,\sigma$) |
| 2MASX J20145928+2523010 | 303.75 | 25.38 | 0.045 | 24.42 | 2.70 | 0.0 | 4.4 | 0.0 | 1.00 ($0.0\,\sigma$) |
| IRAS 05078+1626 | 77.69 | 16.50 | 0.018 | 21.08 | 3.37 | 0.0 | 4.4 | 0.0 | 1.00 ($0.0\,\sigma$) |
| Mrk 110 | 141.30 | 52.29 | 0.035 | 20.00 | 2.12 | 0.0 | 4.4 | 0.0 | 1.00 ($0.0\,\sigma$) |
| NGC 4102 | 181.60 | 52.71 | 0.003 | 24.14 | 2.24 | 0.0 | 2.2 | 0.0 | 1.00 ($0.0\,\sigma$) |
| NGC 7319 | 339.01 | 33.98 | 0.022 | 23.82 | 1.70 | 0.0 | 3.6 | 0.0 | 1.00 ($0.0\,\sigma$) |
| NGC 4051 | 180.79 | 44.53 | 0.002 | 20.00 | 1.75 | 0.0 | 4.4 | 0.0 | 1.00 ($0.0\,\sigma$) |
| UGC 3374 | 88.72 | 46.44 | 0.021 | 20.46 | 4.94 | 0.0 | 4.4 | 0.0 | 1.00 ($0.0\,\sigma$) |
| Mrk 3 | 93.90 | 71.04 | 0.013 | 24.06 | 8.98 | 0.0 | 4.4 | 0.0 | 1.00 ($0.0\,\sigma$) |

Table C.2: Coordinates (R.A. and Dec.), redshift (z), logarithm of the hydrogen column density (in $\mathrm{cm}^{-2}$), intrinsic X-ray flux used for the selection (in units of $10^{-11}\mathrm{erg}^{-1}\mathrm{cm}^{-2}\mathrm{s}^{-1}$), best-fit flux parameters ($\hat{n}_{\mathrm{s}}$ and $\hat{\gamma}$), $TS$ value, and local p-value.

Figure C.14 shows the sky scans around the locations of the top 12 Seyfert galaxies in the list, which contribute to a binomial excess. The localizations' confidence regions differ depending on the flatness of the likelihood space. For NGC 1068, NGC 7469,NGC 4151, and CGCG 420−015, the solid and dashed contours indicate the 68% and 95% C.L. contours, respectively. For all other sources, they indicate the 50% and 68% (when a dashed line is visible) contours, respectively. The likelihood space of NGC 3079 is very flat, and no contour has been drawn in the figure.

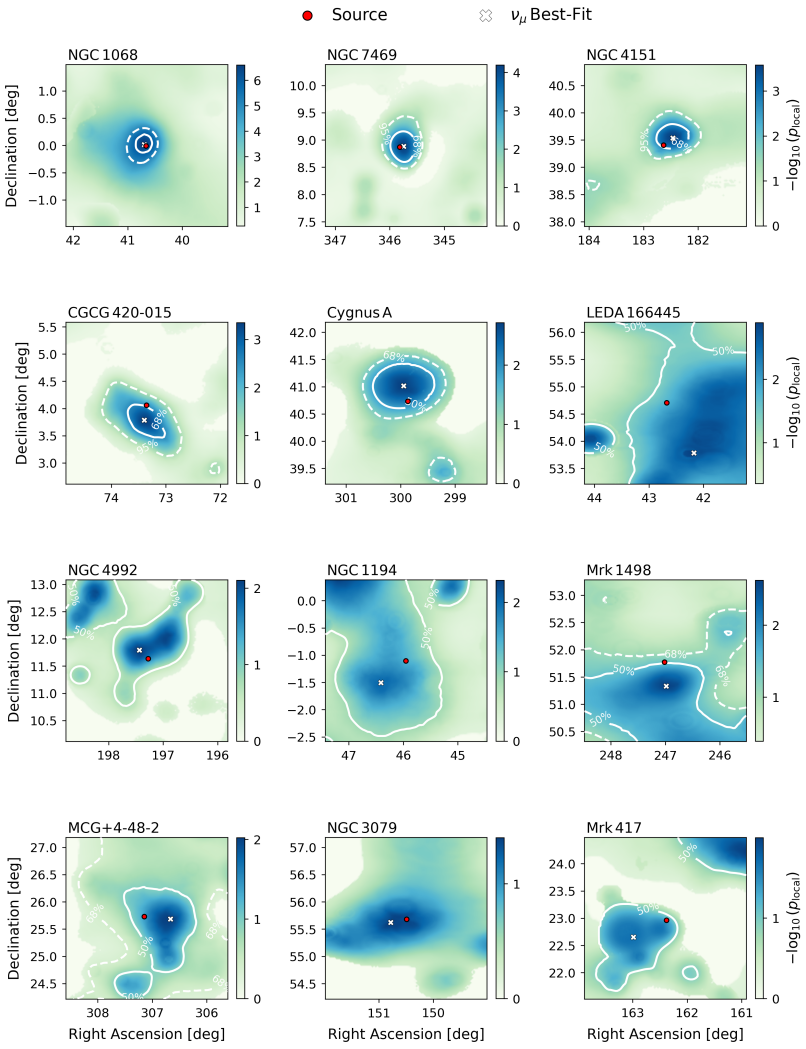


Figure C.14: Likelihood scans around the top 12 sources out of the selection of 48 X-ray bright Seyfert galaxies. The white cross shows the minimum p-value. The white lines mark different likelihood contours (see the text). A red dot indicates the position of the source. All the scans are centered at the source and have the same dimension of $3^\circ \times 3^\circ$.

None of the 48 sources aligns with the maximal Galactic Plane emission, as shown in Figure C.15. Therefore, the possible systematic uncertainty caused by the unmodeled, anisotropic galactic contribution to the astrophysical background is negligible, as discussed in Appendix C.4.1.

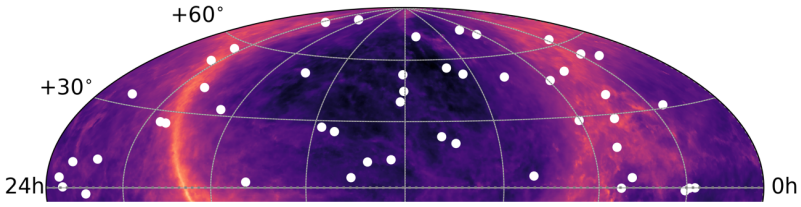


Figure C.15: The location of the 48 Seyfert galaxies is superimposed to a model template for neutrino emission from the Galactic Plane (Schwefer, Mertsch, and Wiebusch, "Diffuse Emission of Galactic High-energy Neutrinos from a Global Fit of Cosmic Rays").

# D SkyLLH Interface for Point-Source Analyses with 10 Years of IceCube Public Data

## D.1 Background test-statistic distributions at various declinations

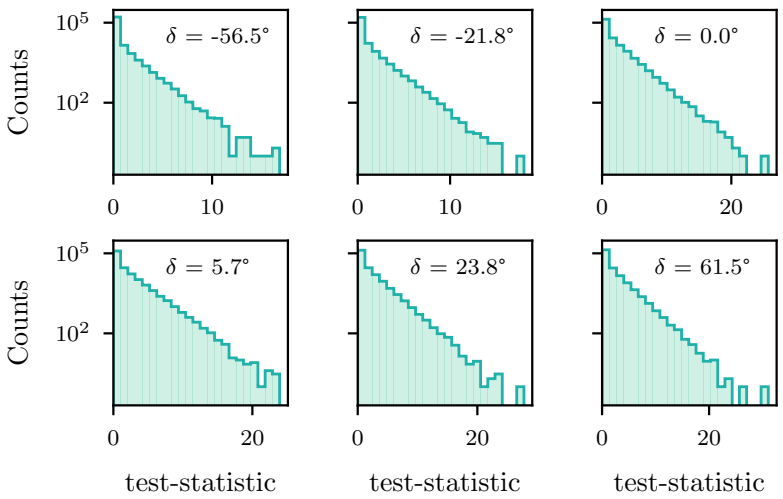


Figure D.1: Exemplary *TS* distributions obtained by generating pseudo-experiments under the assumption that the background-only hypothesis is true. Each panel shows a different declination in the sky. Each distribution is based on approximately 200,000 trials.

## D.2 Signal injection from public detector response matrix

The injection of signal events from a point source emitting a power-law spectrum with fixed spectral index $\gamma$ can be done by using the detector response matrix $M(E_\mu, \psi, \sigma|\delta_\nu, E_\nu)$[1]. In the data release, a detector response matrix is provided for each data sample: IC40 (2008), IC59 (2009), IC79 (2010), IC86 2011, and IC86 2012–2017.

The number of events that need to be injected from each detector configuration is estimated based on the respective dataset weights. The weights depend on the effective area and exposure time of the configuration. For instance, fewer events are injected from the smallest IC40 dataset, which has the smallest effective area due to the 40

[1] It can be done with any spectral shape. We use the power law as an example here.

strings and took data for one year between 2008 and 2009, compared to the IC86 2012-2017 dataset, consisting of six years of the complete detector configuration

For each dataset, we draw the corresponding number of neutrino energies from the power-law distribution. Together with the declination of the source, this fixes a three-dimensional response matrix $M^*(E_\mu, \psi, \sigma)$. $M*$ provides the fractional count of simulated events within the bin relative to all events simulated with the chosen neutrino energy and declination. Hence, this matrix can be used to sample the reconstructed muon energies $E_\mu$ first. These then select a distribution of $\psi$ values from which we sample the angular distances between the muon and the parent neutrino. Finally, the sampled $E_\mu$ and $\psi$ values select a distribution of $\sigma$ values from which we sample the angular uncertainty on each reconstructed muon direction.

Two examples of signal injections are shown in Figure D.2 for a hard spectrum $\gamma = 2$ and a soft one $\gamma = 3$. The injection behaves as expected. When simulating hard spectra, we inject higher-energy events with good pointing and small angular uncertainties on average. Conversely, events produced by a soft spectrum have lower reconstructed energies and are spread over a wider area around the source location.

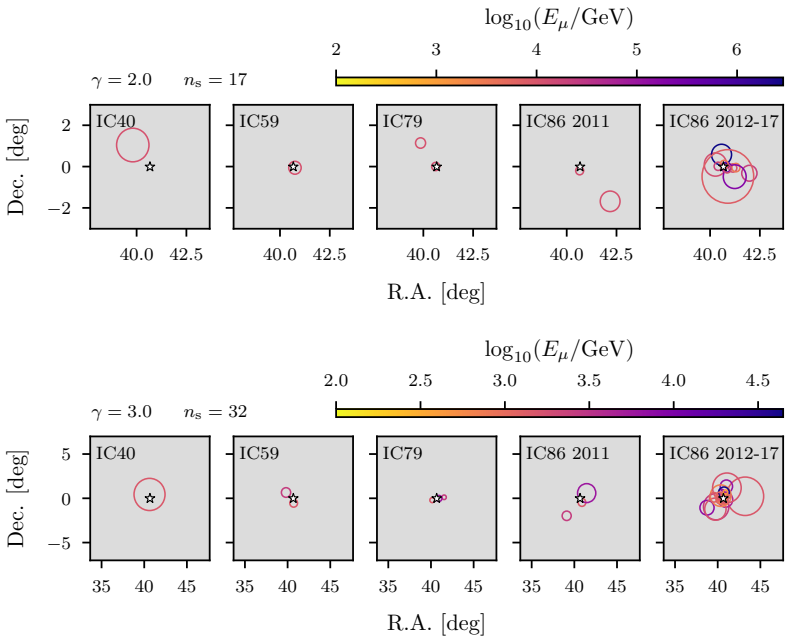


Figure D.2: Simulated signal split among the five different detector configurations according to their respective effective areas and exposure times. The white star marks the position of the simulated source at $\delta = 0°$. In each row, each panel represents one detector configuration. The last season includes six years of data taken with the complete detector configurations. Hence, most of the injected events are sampled from its response matrix. The top row shows an example injection of 17 events according to an $E^{-2}$ point-source spectrum. The bottom row shows the injection of 32 events for an $E^{-3}$ point-source spectrum.

The generation of pseudo-experiments with injected signals, including the maximization of the *TS*, takes approximately 0.2 s/trial.

## *D.3 Energy PDF ratio at the location of TXS 0506+056*

The time-integrated significance of the neutrino emission from TXS 0506+056 cannot be accurately reproduced using the public data release of IceCube. The most likely reason is the discrepancy introduced by the different modeling of the signal energy PDF in the internal and public analyses. Figure D.3 and Figure D.4 compares the signal-over-background (S/B) energy PDF ratio used in the internal IceCube analysis and that implemented for the public data analysis developed in this work. The comparison is shown for three spectral indices close to the best-fit $\gamma = 2.1$ reported in *Aartsen et al. PRL 124, 2020*.

In general, events can get lower energy PDF ratio values in the public data analysis than in the internal analysis. This, in turn, lowers the total S/B ratio of the spatial and energy parts, which enters the definition of the test-statistic in Equation 5.6.

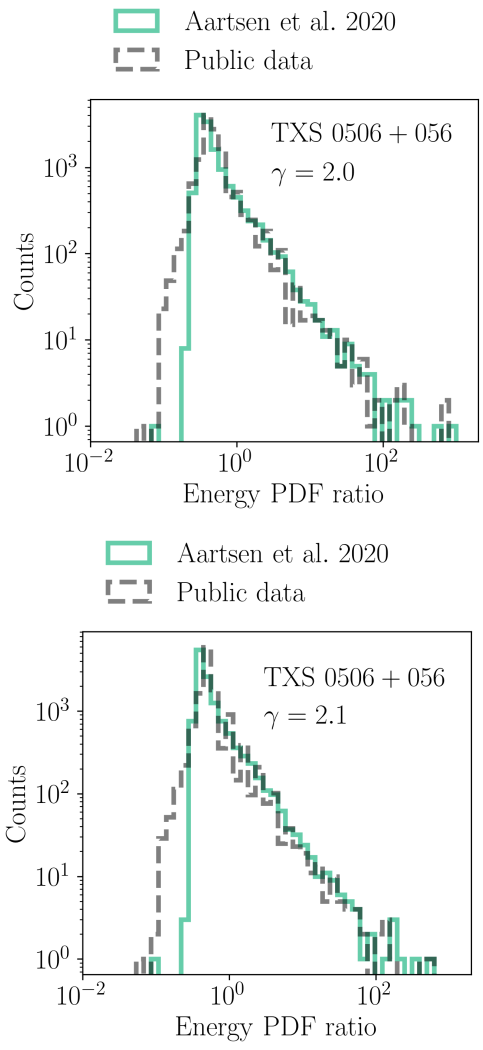


Figure D.3: S/B energy PDF ratio between the internal IceCube analysis used in *Aartsen et al. PRL 124, 2020* (solid green) and the public data analysis implemented in this work (dashed grey). The signal energy PDF is conditional on the source declination. The source tested here is TXS 0506+056, at declination $\delta = 5.7°$. The PDF ratio is shown for $\gamma = 2.0$ and $\gamma = 2.1$.

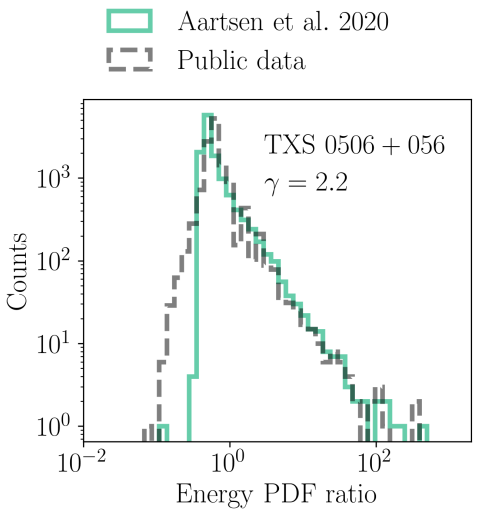


Figure D.4: S/B energy PDF ratio between the internal IceCube analysis used in *Aartsen et al. PRL 124, 2020* (solid green) and the public data analysis implemented in this work (dashed grey). The signal energy PDF is conditional on the source declination. The source tested here is TXS 0506+056, at declination $\delta = 5.7°$. The PDF ratio is shown for $\gamma = 2.2$.

# *Bibliography*

Aartsen, M. G. et al. "All-sky Search for Time-integrated Neutrino Emission from Astrophysical Sources with 7 yr of IceCube Data". *Astrophysical Journal* 835.2, 151 (Feb. 2017) 151. arXiv:1609.04981 [astro-ph.HE] (cit. on pp. 45, 66, 87, 99, 125).

– "Characteristics of the Diffuse Astrophysical Electron and Tau Neutrino Flux with Six Years of IceCube High Energy Cascade Data". *Physical Review Letters* 125.12, 121104 (Sept. 2020) 121104 (cit. on pp. 12, 24, 45).

– "Constraints on Ultrahigh-Energy Cosmic-Ray Sources from a Search for Neutrinos above 10 PeV with IceCube". *Physical Review Letters* 117.24, 241101 (Dec. 2016) 241101. arXiv:1607.05886 [astro-ph.HE] (cit. on p. 38).

– "Constraints on Ultrahigh-Energy Cosmic-Ray Sources from a Search for Neutrinos above 10 PeV with IceCube". *Physical Review Letters* 117.24, 241101 (Dec. 2016) 241101. arXiv:1607.05886 [astro-ph.HE] (cit. on p. 132).

– "Energy reconstruction methods in the IceCube neutrino telescope". *Journal of Instrumentation* 9.3, P03009 (Mar. 2014) P03009. arXiv:1311.4767 [physics.ins-det] (cit. on p. 60).

– "IceCube-Gen2: the window to the extreme Universe". *Journal of Physics G Nuclear Physics* 48.6, 060501 (June 2021) 060501. arXiv:2008.04323 [astro-ph.HE] (cit. on p. 135).

– "In-situ calibration of the single-photoelectron charge response of the IceCube photomultiplier tubes". *Journal of Instrumentation* 15.6 (June 2020) P06032. arXiv:2002.00997 [physics.ins-det] (cit. on p. 46).

– "Measurement of South Pole ice transparency with the IceCube LED calibration system". *Nuclear Instruments and Methods in Physics Research A* 711 (May 2013) 73–89. arXiv:1301.5361 [astro-ph.IM] (cit. on pp. 41, 42, 46, 47).

– "Search for steady point-like sources in the astrophysical muon neutrino flux with 8 years of IceCube data". *European Physical Journal C* 79.3, 234 (Mar. 2019) 234. arXiv:1811.07979 [hep-ph] (cit. on pp. 47, 87, 96, 97, 108).

– "The IceCube Neutrino Observatory: instrumentation and online systems". *Journal of Instrumentation* 12.3 (Mar. 2017) P03012. arXiv:1612.05093 [astro-ph.IM] (cit. on pp. 46–48).

– "Time-Integrated Neutrino Source Searches with 10 Years of IceCube Data". *Physical Review Letters* 124.5, 051103 (Feb. 2020) 051103. arXiv:1910.08488 [astro-ph.HE] (cit. on pp. 66, 77, 78, 86, 109, 111, 127).

Aartsen, M. G. and Aartsen, M. G. "Erratum: Constraints on Ultrahigh-Energy Cosmic-Ray Sources from a Search for Neutrinos Above 10 PeV with IceCube [Phys. Rev. Lett. 117, 241101 (2016)]". *Physical Review Letters* 119.25, 259902 (Dec. 2017) 259902 (cit. on p. 38).

Abbasi, R. et al. "A muon-track reconstruction exploiting stochastic losses for large-scale Cherenkov detectors". *Journal of Instrumentation* 16.8, P08034 (Aug. 2021) P08034. arXiv:2103.16931 [hep-ex] (cit. on pp. 49, 50, 60).
– "A Time-Variability Test for Candidate Neutrino Sources Observed with IceCube". *Proceedings of 37th International Cosmic Ray Conference — PoS(ICRC2021)*. Vol. 395. 2021 p. 1141 (cit. on p. 114).
– "An improved method for measuring muon energy using the truncated mean of dE/dx". *Nuclear Instruments and Methods in Physics Research A* 703 (Mar. 2013) 190–198. arXiv:1208.3430 [physics.data-an] (cit. on p. 53).
– "Erratum: "IceCat-1: The IceCube Event Catalog of Alert Tracks" (2023, ApJS, 269, 25)". *Astrophysical Journal Suppl. Ser.* 272.1, 24 (May 2024) 24 (cit. on p. 60).
– "Evidence for neutrino emission from the nearby active galaxy NGC 1068". *Science* 378.6619 (Nov. 2022) 538–543. arXiv:2211.09972 [astro-ph.HE] (cit. on pp. 11, 13, 18, 19, 23, 24, 26, 47, 51, 52, 54, 55, 62, 67, 69, 72–74, 78, 83, 97, 105, 109, 111, 114, 115, 133).
– "IceCat-1: The IceCube Event Catalog of Alert Tracks". *Astrophysical Journal Suppl. Ser.* 269.1, 25 (Nov. 2023) 25. arXiv:2304.01174 [astro-ph.HE] (cit. on p. 60).
– "IceTop: The surface component of IceCube. The IceCube Collaboration". *Nuclear Instruments and Methods in Physics Research A* 700 (Feb. 2013) 188–220. arXiv:1207.6326 [astro-ph.IM] (cit. on p. 46).
– "Improved Characterization of the Astrophysical Muon-neutrino Flux with 9.5 Years of IceCube Data". *Astrophysical Journal* 928.1, 50 (Mar. 2022) 50. arXiv:2111.10299 [astro-ph.HE] (cit. on pp. 12, 15, 45, 69, 74, 154, 155).
– "Limits on Neutrino Emission from GRB 221009A from MeV to PeV Using the IceCube Neutrino Observatory". *Astrophysical Journal Letters* 946.1, L26 (Mar. 2023) L26. arXiv:2302.05459 [astro-ph.HE] (cit. on p. 18).
– "Measurement of atmospheric neutrino mixing with improved IceCube DeepCore calibration and data processing". *Physical Review D* 108.1, 012014 (July 2023) 012014. arXiv:2304.12236 [hep-ex] (cit. on p. 46).
– "Observation of Seven Astrophysical Tau Neutrino Candidates with IceCube". *Physical Review Letters* 132.15, 151001 (Apr. 2024) 151001. arXiv:2403.02516 [astro-ph.HE] (cit. on p. 43).
– "Search for Correlations of High-energy Neutrinos Detected in IceCube with Radio-bright AGN and Gamma-Ray Emission from Blazars". *Astrophysical Journal* 954.1, 75 (Sept. 2023) 75. arXiv:2304.12675 [astro-ph.HE] (cit. on pp. 100, 125, 132).
– "Search for Multi-flare Neutrino Emissions in 10 yr of IceCube Data from a Catalog of Sources". *Astrophysical Journal Letters* 920.2, L45 (Oct. 2021) L45. arXiv:2109.05818 [astro-ph.HE] (cit. on pp. 78, 85, 86, 111).
Abbasi, R. et al. "In situ estimation of ice crystal properties at the South Pole using LED calibration data from the IceCube Neutrino Observatory". *The Cryosphere* 18.1 (Jan. 2024) 75–102 (cit. on p. 74).
– "Studies of systematic uncertainty effects on IceCube's real-time angular uncertainty". *Proceedings of 37th International Cosmic Ray Conference — PoS(ICRC2021)*. Vol. 395. 2021 p. 1045 (cit. on p. 51).
Abdo, A. A. et al. "Fermi Large Area Telescope First Source Catalog". *Astrophysical Journal Suppl. Ser.* 188.2 (June 2010) 405–436. arXiv:1002.2280 [astro-ph.HE] (cit. on p. 26).

Abdollahi, S. et al. "Fermi Large Area Telescope Fourth Source Catalog". *Astrophysical Journal Suppl. Ser.* 247.1, 33 (Mar. 2020) 33. arXiv:1902.10045 [astro-ph.HE] (cit. on pp. 19, 26).

– "Incremental Fermi Large Area Telescope Fourth Source Catalog". *Astrophysical Journal Suppl. Ser.* 260.2, 53 (June 2022) 53. arXiv:2201.11184 [astro-ph.HE] (cit. on p. 19).

Abraham, J. et al. "Measurement of the energy spectrum of cosmic rays above $10^{18}$ eV using the Pierre Auger Observatory". *Physics Letters B* 685.4-5 (Mar. 2010) 239–246. arXiv:1002.1975 [astro-ph.HE] (cit. on pp. 6, 14).

Acciari, V. A. et al. "Constraints on Gamma-Ray and Neutrino Emission from NGC 1068 with the MAGIC Telescopes". *Astrophysical Journal* 883.2, 135 (Oct. 2019) 135. arXiv:1906.10954 [astro-ph.HE] (cit. on pp. 26, 116).

Ackermann, M. et al. "GeV Observations of Star-forming Galaxies with the Fermi Large Area Telescope". *Astrophysical Journal* 755.2, 164 (Aug. 2012) 164. arXiv:1206.1346 [astro-ph.HE] (cit. on p. 27).

– "The Spectrum of Isotropic Diffuse Gamma-Ray Emission between 100 MeV and 820 GeV". *Astrophysical Journal* 799.1, 86 (Jan. 2015) 86. arXiv:1410.3696 [astro-ph.HE] (cit. on pp. 11, 15).

Adrián-Martínez, S. et al. "First Search for Point Sources of High-energy Cosmic Neutrinos with the ANTARES Neutrino Telescope". *Astrophysical Journal Letters* 743.1, L14 (Dec. 2011) L14. arXiv:1108.0292 [astro-ph.HE] (cit. on p. 62).

Adriani, O. et al. "Direct Measurement of the Cosmic-Ray Proton Spectrum from 50 GeV to 10 TeV with the Calorimetric Electron Telescope on the International Space Station". *Physical Review Letters* 122.18, 181102 (May 2019) 181102. arXiv:1905.04229 [astro-ph.HE] (cit. on p. 6).

– "Time Dependence of the Proton Flux Measured by PAMELA during the 2006 July-2009 December Solar Minimum". *Astrophysical Journal* 765.2, 91 (Mar. 2013) 91. arXiv:1301.4108 [astro-ph.HE] (cit. on p. 6).

Agostini, M. et al. "The Pacific Ocean Neutrino Experiment". *Nature Astronomy* 4 (Sept. 2020) 913–915. arXiv:2005.09493 [astro-ph.HE] (cit. on p. 135).

Aguilar, M. et al. "Precision Measurement of the Proton Flux in Primary Cosmic Rays from Rigidity 1 GV to 1.8 TV with the Alpha Magnetic Spectrometer on the International Space Station". *Physical Review Letters* 114.17, 171103 (May 2015) 171103 (cit. on p. 6).

Aharonian, F. et al. "Observations of selected AGN with HESS". *Astronomy & Astrophysics* 441.2 (Oct. 2005) 465–472. arXiv:astro-ph/0507207 [astro-ph] (cit. on p. 26).

Ahlers, M. and Halzen, F. "Opening a new window onto the universe with IceCube". *Progress in Particle and Nuclear Physics* 102 (Sept. 2018) 73–88. arXiv:1805.11112 [astro-ph.HE] (cit. on p. 15).

Ajello, M. et al. "Gamma Rays from Fast Black-hole Winds". *Astrophysical Journal* 921.2, 144 (Nov. 2021) 144. arXiv:2105.11469 [astro-ph.HE] (cit. on p. 31).

– "The Fourth Catalog of Active Galactic Nuclei Detected by the Fermi Large Area Telescope: Data Release 3". *Astrophysical Journal Suppl. Ser.* 263.2, 24 (Dec. 2022) 24. arXiv:2209.12070 [astro-ph.HE] (cit. on p. 116).

Ajello, M. et al. "The $\gamma$-Ray Emission of Star-forming Galaxies". *Astrophysical Journal* 894.2, 88 (May 2020) 88. arXiv:2003.05493 [astro-ph.GA] (cit. on pp. 19, 26, 27).

Andrés, E. et al. "Observation of high-energy neutrinos using Čerenkov detectors embedded deep in Antarctic ice". *Nature* 410.6827 (Mar. 2001) 441–443 (cit. on p. 39).

Ansoldi, S. et al. "The Blazar TXS 0506+056 Associated with a High-energy Neutrino: Insights into Extragalactic Jets and Cosmic-Ray Acceleration". *Astrophysical Journal Letters* 863.1, L10 (Aug. 2018) L10. arXiv:1807.04300 [astro-ph.HE] (cit. on p. 28).

Antonucci, R. R. J. and Miller, J. S. "Spectropolarimetry and the nature of NGC 1068." *Astrophysical Journal* 297 (Oct. 1985) 621–632 (cit. on p. 25).

Apel, W. D. et al. "Kneelike Structure in the Spectrum of the Heavy Component of Cosmic Rays Observed with KASCADE-Grande". *Physical Review Letters* 107.17, 171104 (Oct. 2011) 171104. arXiv:1107.5885 [astro-ph.HE] (cit. on p. 7).

Arnold, T. and Emerson, J. "Nonparametric Goodness-of-Fit Tests for Discrete Null Distributions". *R Journal* 3 (Dec. 2011) (cit. on p. 89).

Atwood, W. B. et al. "The Large Area Telescope on the Fermi Gamma-Ray Space Telescope Mission". *Astrophysical Journal* 697.2 (June 2009) 1071–1102. arXiv:0902.1089 [astro-ph.IM] (cit. on p. 11).

Avrorin, A. D. et al. "BAIKAL-GVD: The New-Generation Neutrino Telescope in Lake Baikal". *Bulletin of the Russian Academy of Sciences, Physics* 83.8 (Aug. 2019) 921–922 (cit. on p. 135).

Baade, W. and Minkowski, R. "On the Identification of Radio Sources." *Astrophysical Journal* 119 (Jan. 1954) 215 (cit. on p. 118).

Barbano, E. et al. "Investigating high-energy neutrinos from blazars with a maximum-likelihood analysis of the IceCube observatory data". *Proceedings of 38th International Cosmic Ray Conference — PoS* ICRC2023 (2023) 1540 (cit. on p. 86).

Bechtol, K. et al. "Evidence against Star-forming Galaxies as the Dominant Source of Icecube Neutrinos". *Astrophysical Journal* 836.1, 47 (Feb. 2017) 47. arXiv:1511.00688 [astro-ph.HE] (cit. on p. 19).

Bellenghi, C., Karl, M., and Wolf, M. "Extending SkyLLH software for neutrino point source analyses with 10 years of IceCube public data". Vol. ICRC2023. 2023 p. 1061 (cit. on pp. 77, 134).

Bellenghi, C., Ha Minh, M., et al. "Extending the IceCube search for neutrino point sources in the Northern sky with additional years of data". *PoS* ICRC2023 (2023) 1060 (cit. on pp. 57, 134).

Bellenghi, C., Padovani, P., et al. "Correlating High-energy IceCube Neutrinos with 5BZCAT Blazars and RFC Sources". *Astrophysical Journal Letters* 955.2, L32 (Oct. 2023) L32. arXiv:2309.03115 [astro-ph.HE] (cit. on pp. 86, 99, 125).

Berezinskii, V. S., Bulanov, S. V., et al. *Astrophysics of cosmic rays*. 1990 (cit. on p. 34).

Berezinskii, V. S. and Smirnov, A. I. "Cosmic Neutrinos of Ultra High Energies and Detection Possibility". *Astrophysics and Space Science* 32.2 (Feb. 1975) 461–482 (cit. on p. 16).

Berezinsky, V. S. *Proceedings of the International Conference Neutrino '77*. 1977 p. 177 (cit. on pp. 16, 32).

Berezinsky, V. S. et al. "Diffuse radiation from cosmic ray interactions in the galaxy". *Astroparticle Physics* 1.3 (July 1993) 281–287 (cit. on p. 12).

Bird, D. J. et al. "Detection of a Cosmic Ray with Measured Energy Well beyond the Expected Spectral Cutoff due to Cosmic Microwave Radiation". *Astrophysical Journal* 441 (Mar. 1995) 144. arXiv:astro-ph/9410067 [astro-ph] (cit. on p. 5).

Blasi, P. "Origin of very high- and ultra-high-energy cosmic rays". *Comptes Rendus Physique* 15.4 (Apr. 2014) 329–338. arXiv:1403.2967 [astro-ph.HE] (cit. on p. 7).

Blaufuss, E. et al. "The Next Generation of IceCube Real-time Neutrino Alerts". *Proceedings of 36th International Cosmic Ray Conference — PoS(ICRC2019)*. Vol. 358. 2019 p. 1021 (cit. on p. 60).

Bonzini, M. et al. "Star formation properties of sub-mJy radio sources". *Monthly Notices of the Royal Astronomical Society* 453.1 (Oct. 2015) 1079–1094. arXiv:1508.01905 [astro-ph.GA] (cit. on p. 28).

Bose, D. et al. "Galactic and extragalactic sources of very high energy gamma rays". *European Physical Journal Special Topics* 231.1 (Jan. 2022) 27–66. arXiv:2201.06789 [astro-ph.HE] (cit. on p. 10).

Braun, J. et al. "Methods for point source analysis in high energy neutrino telescopes". *Astroparticle Physics* 29.4 (May 2008) 299–305. arXiv:0801.1604 [astro-ph] (cit. on pp. 62, 63, 66).

Bugaev, E. et al. "Propagation of $\tau$-neutrinos and $\tau$-leptons through the Earth and their detection in underwater/ice neutrino telescopes". *Astroparticle Physics* 21.5 (Aug. 2004) 491–509. arXiv:hep-ph/0312295 [hep-ph] (cit. on p. 56).

Buson, S. et al. "Beginning a Journey Across the Universe: The Discovery of Extragalactic Neutrino Factories". *Astrophysical Journal Letters* 933.2, L43 (July 2022) L43. arXiv:2207.06314 [astro-ph.HE] (cit. on pp. 2, 87, 99, 105, 125, 135).

– "Erratum: "Beginning a Journey Across the Universe: The Discovery of Extragalactic Neutrino Factories" (2022, ApJL, 933, L43)". *Astrophysical Journal Letters* 934.2, L38 (Aug. 2022) L38 (cit. on pp. 2, 99, 118, 135).

Caputo, R. et al. "All-sky Medium Energy Gamma-ray Observatory eXplorer mission concept". *Journal of Astronomical Telescopes, Instruments, and Systems* 8, 044003 (Oct. 2022) 044003. arXiv:2208.04990 [astro-ph.IM] (cit. on pp. 34, 133).

Carver, T. "Time integrated searches for astrophysical neutrino sources using the IceCube detector and gender in physics studies for the Genera Project". PhD thesis. University of Geneva, Switzerland, Jan. 2019 (cit. on pp. 79, 128).

Casella, G. and Berger, R. "Statistical Inference". Duxbury advanced series in statistics and decision sciences. Thomson Learning, 2002. ISBN: 9780534243128 (cit. on pp. 67, 112, 159).

Cavagnolo, K. W. et al. "A Relationship Between AGN Jet Power and Radio Power". *Astrophysical Journal* 720.2 (Sept. 2010) 1066–1072. arXiv:1006.5699 [astro-ph.CO] (cit. on p. 28).

Chirkin, D. and Rhode, W. "Propagating leptons through matter with Muon Monte Carlo (MMC)". *arXiv e-prints*, hep-ph/0407075 (July 2004) hep–ph/0407075. arXiv:hep-ph/0407075 [hep-ph] (cit. on pp. 42, 52).

Cicone, C. et al. "The largely unconstrained multiphase nature of outflows in AGN host galaxies". *Nature Astronomy* 2 (Feb. 2018) 176–178. arXiv:1802.10308 [astro-ph.GA] (cit. on p. 22).

Coenders, S. "High-energy cosmic ray accelerators: searches with IceCube neutrinos. Probing seven years of IceCube muon data for time-integrated emission of point-like neutrino sources". PhD thesis. Technical University of Munich, 2016 (cit. on pp. 45, 101, 126).

Condon, J. J. "Radio emission from normal galaxies." *Ann. Rev. Astron. Astrophys.* 30 (Jan. 1992) 575–611 (cit. on pp. 18, 26).

Condon, J. J. et al. "The NRAO VLA Sky Survey". *Astronomical Journal* 115.5 (May 1998) 1693–1716 (cit. on p. 28).

de Angelis, A. et al. "Science with e-ASTROGAM. A space mission for MeV-GeV gamma-ray astrophysics". *Journal of High Energy Astrophysics* 19 (Aug. 2018) 1–106. arXiv:1711.01265 [astro-ph.HE] (cit. on pp. 34, 133).

Dempster, A. P. et al. "Maximum Likelihood from Incomplete Data via the EM Algorithm". *Journal of the Royal Statistical Society. Series B (Methodological)* 39.1 (1977) 1–38. ISSN: 00359246 (cit. on p. 85).

Dichiara, S. et al. "Swift J1913.1+1946 a new bright hard X-ray and optical transient". *GRB Coordinates Network* 32632 (Oct. 2022) 1 (cit. on p. 18).

Dolag, K. et al. "Mapping Deflections of Ultrahigh Energy Cosmic Rays in Constrained Simulations of Extragalactic Magnetic Fields". *Soviet Journal of Experimental and Theoretical Physics Letters* 79 (Jan. 2004) 583–587. arXiv:astro-ph/0310902 [astro-ph] (cit. on p. 8).

Duras, F. et al. "Universal bolometric corrections for active galactic nuclei over seven luminosity decades". *Astronomy & Astrophysics* 636, A73 (Apr. 2020) A73. arXiv:2001.09984 [astro-ph.GA] (cit. on p. 30).

Eichler, D. "High-energy neutrino astronomy: a probe of galactic nuclei?" *Astrophysical Journal* 232 (Aug. 1979) 106–112 (cit. on p. 32).

Eichmann, B. et al. "Solving the Multimessenger Puzzle of the AGN-starburst Composite Galaxy NGC 1068". *Astrophysical Journal* 939.1, 43 (Nov. 2022) 43. arXiv:2207.00102 [astro-ph.HE] (cit. on p. 27).

Esteban, I. et al. "Global analysis of three-flavour neutrino oscillations: synergies and tensions in the determination of $\theta_{23}$, $\delta_{CP}$, and the mass ordering". *Journal of High Energy Physics* 2019.1, 106 (Jan. 2019) 106. arXiv:1811.05487 [hep-ph] (cit. on p. 14).

Fabian, A. C., Lohfink, A., Belmont, R., et al. "Properties of AGN coronae in the NuSTAR era - II. Hybrid plasma". *Monthly Notices of the Royal Astronomical Society* 467.3 (May 2017) 2566–2570. arXiv:1701.06774 [astro-ph.HE] (cit. on p. 117).

Fabian, A. C., Lohfink, A., Kara, E., et al. "Properties of AGN coronae in the NuSTAR era". *Monthly Notices of the Royal Astronomical Society* 451.4 (Aug. 2015) 4375–4383. arXiv:1505.07603 [astro-ph.HE] (cit. on p. 20).

Fedynitch, A. et al. "Calculation of conventional and prompt lepton fluxes at very high energy". *European Physical Journal Web of Conferences*. Vol. 99. European Physical Journal Web of Conferences. Aug. 2015 08001 p. 08001. arXiv:1503.00544 [hep-ph] (cit. on pp. 44, 56).

Fermi, E. "Galactic Magnetic Fields and the Origin of Cosmic Radiation." *Astrophysical Journal* 119 (Jan. 1954) 1 (cit. on p. 16).

Fermi, E. "On the Origin of the Cosmic Radiation". *Physical Review* 75.8 (Apr. 1949) 1169–1174 (cit. on p. 16).

Fiore, F. et al. "AGN wind scaling relations and the co-evolution of black holes and galaxies". *Astronomy & Astrophysics* 601, A143 (May 2017) A143. arXiv:1702.04507 [astro-ph.GA] (cit. on p. 31).

Fiorillo, D. F. G. et al. "TeV Neutrinos and Hard X-Rays from Relativistic Reconnection in the Corona of NGC 1068". *Astrophysical Journal Letters* 961.1, L14 (Jan. 2024) L14. arXiv:2310.18254 [astro-ph.HE] (cit. on p. 124).

Formaggio, J. A. and Zeller, G. P. "From eV to EeV: Neutrino cross sections across energy scales". *Reviews of Modern Physics* 84.3 (July 2012) 1307–1341. arXiv:1305.7513 [hep-ex] (cit. on p. 40).

Frank, I. and Tamm, I. "Coherent Visible Radiation of Fast Electrons Passing Through Matter". *Selected Papers*. Ed. by Bolotovskii, B. M., Frenkel, V. Y., and Peierls, R. Berlin, Heidelberg: Springer Berlin Heidelberg, 1991 p. 29. ISBN: 978-3-642-74626-0 (cit. on p. 41).

Fuerst, P. M. et al. "Galactic and Extragalactic Analysis of the Astrophysical Muon Neutrino Flux with 12.3 years of IceCube Track Data". *Proceedings of 38th International Cosmic Ray Conference — PoS(ICRC2023)*. Vol. 444. 2023 p. 1046 (cit. on p. 155).

Gaisser, T. K. "Neutrino Astronomy: Physics Goals, Detector Parameters". *arXiv e-prints*, astro-ph/9707283 (July 1997) astro–ph/9707283. arXiv:astro-ph/9707283 [astro-ph] (cit. on p. 45).

Gaisser, T. K., Stanev, T., and Tilav, S. "Cosmic ray energy spectrum from measurements of air showers". *Frontiers of Physics* 8.6 (Dec. 2013) 748–758. arXiv:1303.3565 [astro-ph.HE] (cit. on p. 56).

Gaisser, T. K. "Spectrum of cosmic-ray nucleons, kaon production, and the atmospheric muon charge ratio". *Astroparticle Physics* 35.12 (July 2012) 801–806. arXiv:1111.6675 [astro-ph.HE] (cit. on pp. 6, 7, 44).

Gaisser, T. K., Engel, R., and Resconi, E. *Cosmic Rays and Particle Physics: 2nd Edition*. Cambridge University Press, June 2016. ISBN: 978-0-521-01646-9 (cit. on pp. 5, 6, 8, 10, 13, 17, 20, 40, 44).

Gallimore, J. F. et al. "The Subarcsecond Radio Structure in NGC 1068. I. Observations and Results". *Astrophysical Journal* 458 (Feb. 1996) 136 (cit. on p. 29).

Gandhi, R. et al. "Ultrahigh-energy neutrino interactions". *Astroparticle Physics* 5.2 (Aug. 1996) 81–110. arXiv:hep-ph/9512364 [hep-ph] (cit. on p. 41).

García-Burillo, S. et al. "Molecular line emission in NGC 1068 imaged with ALMA. I. An AGN-driven outflow in the dense molecular gas". *Astronomy & Astrophysics* 567, A125 (July 2014) A125. arXiv:1405.7706 [astro-ph.GA] (cit. on pp. 30, 31).

Gilli, R., Comastri, A., and Hasinger, G. "The synthesis of the cosmic X-ray background in the Chandra and XMM-Newton era". *Astronomy & Astrophysics* 463.1 (Feb. 2007) 79–96. arXiv:astro-ph/0610939 [astro-ph] (cit. on p. 35).

Giommi, P. and Padovani, P. "Astrophysical Neutrinos and Blazars". *Universe* 7.12 (Dec. 2021) 492. arXiv:2112.06232 [astro-ph.HE] (cit. on pp. 24, 125).

Glashow, S. L. "Resonant Scattering of Antineutrinos". *Physical Review* 118.1 (Apr. 1960) 316–317 (cit. on p. 40).

Glauch, T. "The Origin of High-Energy Cosmic Particles: IceCube Neutrinos and the Blazar Case". PhD thesis. Technische Universität München, 2021 (cit. on pp. 19, 49, 53, 54, 62, 67, 74).

Glauch, T. et al. "Searching for High-Energy Neutrino Emission from Seyfert Galaxies in the Northern Sky with IceCube". *arXiv e-prints*, arXiv:2308.00024 (July 2023) arXiv:2308.00024. arXiv:2308.00024 [astro-ph.HE] (cit. on pp. 35, 116, 118, 134).

Górski, K. M. et al. "HEALPix: A Framework for High-Resolution Discretization and Fast Analysis of Data Distributed on the Sphere". *Astrophysical Journal* 622.2 (Apr. 2005) 759–771. arXiv:astro-ph/0409513 [astro-ph] (cit. on pp. 75, 101).

Goswami, S. "Search for high-energy neutrino emission from hard X-ray AGN with IceCube". *arXiv e-prints*, arXiv:2307.15349 (July 2023) arXiv:2307.15349. arXiv:2307.15349 [astro-ph.HE] (cit. on pp. 35, 37, 116, 118, 133, 134).

Greisen, K. "End to the Cosmic-Ray Spectrum?" *Physical Review Letters* 16.17 (Apr. 1966) 748–750 (cit. on p. 8).

Haack, C. "Observation of high-energy neutrinos from the galaxy and beyond". Veröffentlicht auf dem Publikationsserver der RWTH Aachen University; Dissertation, RWTH Aachen University, 2020. Dissertation. Aachen: RWTH Aachen University, 2020 (cit. on p. 50).

Halzen, F. "High-Energy Neutrinos from the Cosmos". *Annalen der Physik* 533.11, 2100309 (Nov. 2021) 2100309 (cit. on p. 10).

Halzen, F. and Hooper, D. "High-energy neutrino astronomy: the cosmic ray connection". *Reports on Progress in Physics* 65.7 (July 2002) 1025–1078. arXiv:astro-ph/0204527 [astro-ph] (cit. on pp. 7, 8).

Han, J. L. et al. "Pulsar Rotation Measures and the Large-Scale Structure of the Galactic Magnetic Field". *Astrophysical Journal* 642.2 (May 2006) 868–881. arXiv:astro-ph/0601357 [astro-ph] (cit. on p. 7).

Harrison, C. M. "Impact of supermassive black hole growth on star formation". *Nature Astronomy* 1, 0165 (July 2017) 0165. arXiv:1703.06889 [astro-ph.GA] (cit. on p. 22).

Hess, V. F. "Über Beobachtungen der durchdringenden Strahlung bei sieben Freiballonfahrten". *Phys. Z.* 13 (1912) 1084–1091 (cit. on pp. 1, 5).

Hillas, A. M. "The Origin of Ultra-High-Energy Cosmic Rays". *Ann. Rev. Astron. Astrophys.* 22 (Jan. 1984) 425–444 (cit. on p. 17).

Hogg, D. W. "Distance measures in cosmology". *arXiv e-prints*, astro-ph/9905116 (May 1999) astro–ph/9905116. arXiv:astro-ph/9905116 [astro-ph] (cit. on p. 36).

Huang, Y. et al. "LHAASO observed GRB 221009A with more than 5000 VHE photons up to around 18 TeV". *GRB Coordinates Network* 32677 (Oct. 2022) 1 (cit. on p. 18).

Huber, M., Krings, K., et al. "Results of IceCube searches for neutrinos from blazars using seven years of through-going muon data". *35th International Cosmic Ray Conference (ICRC2017)*. Vol. 301. International Cosmic Ray Conference. July 2017 994 p. 994 (cit. on pp. 86, 125).

Huber, M. "Multi-Messenger correlation study of Fermi-LAT blazars and high-energy neutrinos observed in IceCube". PhD thesis. Technische Universität München, 2020 (cit. on pp. 17, 41, 44, 53).

IceCube Collaboration. "Detection of a particle shower at the Glashow resonance with IceCube". *Nature* 591.7849 (Mar. 2021) 220–224. arXiv:2110.15051 [hep-ex] (cit. on p. 40).

– "Evidence for High-Energy Extraterrestrial Neutrinos at the IceCube Detector". *Science* 342.6161, 1242856 (Nov. 2013) 1242856. arXiv:1311.5238 [astro-ph.HE] (cit. on pp. 1, 11, 61).

– "IceCube Data for Neutrino Point-Source Searches Years 2008-2018". *arXiv e-prints*, arXiv:2101.09836 (Jan. 2021) arXiv:2101.09836. arXiv:2101.09836 [astro-ph.HE] (cit. on pp. 2, 77, 78, 85, 128).

IceCube Collaboration et al. "Neutrino emission from the direction of the blazar TXS 0506+056 prior to the IceCube-170922A alert". *Science* 361.6398 (July 2018) 147–151. arXiv:1807.08794 [astro-ph.HE] (cit. on pp. 1, 13, 77, 85, 115).

Icecube Collaboration. "Observation of high-energy neutrinos from the Galactic plane". *Science* 380.6652 (June 2023) 1338–1343. arXiv:2307.04427 [astro-ph.HE] (cit. on pp. 12, 42, 75, 155).

IceCube Collaboration et al. "Multimessenger observations of a flaring blazar coincident with high-energy neutrino IceCube-170922A". *Science* 361.6398, eaat1378 (July 2018) eaat1378. arXiv:1807.08816 [astro-ph.HE] (cit. on pp. 1, 13, 115).

Impellizzeri, C. M. V. et al. "Counter-rotation and High-velocity Outflow in the Parsec-scale Molecular Torus of NGC 1068". *Astrophysical Journal Letters* 884.2, L28 (Oct. 2019) L28. arXiv:1908.07981 [astro-ph.GA] (cit. on p. 30).

Inoue, Y. et al. "On High-energy Particles in Accretion Disk Coronae of Supermassive Black Holes: Implications for MeV Gamma-rays and High-energy Neutrinos from AGN Cores". *Astrophysical Journal* 880.1, 40 (July 2019) 40. arXiv:1904.00554 [astro-ph.HE] (cit. on pp. 24, 124).

Karim, T. and Mamajek, E. E. "Revised geometric estimates of the North Galactic Pole and the Sun's height above the Galactic mid-plane". *Monthly Notices of the Royal Astronomical Society* 465.1 (Feb. 2017) 472–481. arXiv:1610.08125 [astro-ph.SR] (cit. on p. 14).

Karl, M., Padovani, P., and Giommi, P. "The spectra of IceCube Neutrino (SIN) candidate sources - IV. Spectral energy distributions and multiwavelength variability". *Monthly Notices of the Royal Astronomical Society* 526.1 (Nov. 2023) 661–681. arXiv:2309.03119 [astro-ph.GA] (cit. on p. 86).

Karl, M. S. "Unraveling the origin of high-energy neutrino sources: follow-up searches of IceCube alert events". PhD thesis. Technische Universität München, 2022 (cit. on p. 85).

Katrin Collaboration. "Direct neutrino-mass measurement with sub-electronvolt sensitivity". *Nature Physics* 18.2 (Feb. 2022) 160–166 (cit. on p. 11).

Kawai, H. et al. "Telescope Array Experiment". *Nuclear Physics B Proceedings Supplements* 175 (Jan. 2008) 221–226 (cit. on p. 6).

Kelner, S. R. and Aharonian, F. A. "Energy spectra of gamma rays, electrons, and neutrinos produced at interactions of relativistic protons with low energy radiation". *Physical Review D* 78.3, 034013 (Aug. 2008) 034013. arXiv:0803.0688 [astro-ph] (cit. on pp. 8, 9, 33).

Kennicutt Robert C., J. "Star Formation in Galaxies Along the Hubble Sequence". *Ann. Rev. Astron. Astrophys.* 36 (Jan. 1998) 189–232. arXiv:astro-ph/9807187 [astro-ph] (cit. on pp. 18, 28).

Kheirandish, A., Murase, K., and Kimura, S. S. "High-energy Neutrinos from Magnetized Coronae of Active Galactic Nuclei and Prospects for Identification of Seyfert Galaxies and Quasars in Neutrino Telescopes". *Astrophysical Journal* 922.1, 45 (Nov. 2021) 45. arXiv:2102.04475 [astro-ph.HE] (cit. on pp. 24, 110).

Kimura, S. S. "Neutrinos from Gamma-Ray Bursts". *The Encyclopedia of Cosmology*. Chap. Chapter 9 p. 433. eprint: https://www.worldscientific.com/doi/pdf/10.1142/9789811282645_0009 (cit. on p. 18).

Kontrimas, T. and Wolf, M. "The SkyLLH framework for IceCube point-source search". *Proceedings of 37th International Cosmic Ray Conference — PoS(ICRC2021)*. Vol. 395. 2021 p. 1073 (cit. on p. 77).

Koss, M. J. et al. "BASS. XXII. The BASS DR2 AGN Catalog and Data". *Astrophysical Journal Suppl. Ser.* 261.1, 2 (July 2022) 2. arXiv:2207.12432 [astro-ph.GA] (cit. on p. 38).

Lamastra, A. et al. "Galactic outflow driven by the active nucleus and the origin of the gamma-ray emission in NGC 1068". *Astronomy & Astrophysics* 596, A68 (Dec. 2016) A68. arXiv:1609.09664 [astro-ph.HE] (cit. on pp. 22, 31).

Learned, J. G. and Mannheim, K. "High-Energy Neutrino Astrophysics". *Annual Review of Nuclear and Particle Science* 50 (Jan. 2000) 679–749 (cit. on p. 49).

Liu, R.-Y. et al. "Can Winds Driven by Active Galactic Nuclei Account for the Extragalactic Gamma-Ray and Neutrino Backgrounds?" *Astrophysical Journal* 858.1, 9 (May 2018) 9. arXiv:1712.10168 [astro-ph.HE] (cit. on p. 22).

Lucarelli, F. et al. "AGILE Detection of a Candidate Gamma-Ray Precursor to the ICECUBE-160731 Neutrino Event". *Astrophysical Journal* 846.2, 121 (Sept. 2017) 121. arXiv:1707.08599 [astro-ph.HE] (cit. on p. 125).

Madau, P. and Dickinson, M. "Cosmic Star-Formation History". *Ann. Rev. Astron. Astrophys.* 52 (Aug. 2014) 415–486. arXiv:1403.0007 [astro-ph.CO] (cit. on p. 108).

Maki, Z., Nakagawa, M., and Sakata, S. "Remarks on the Unified Model of Elementary Particles". *Progress of Theoretical Physics* 28.5 (Nov. 1962) 870–880 (cit. on p. 13).

Margiotta, A. "The KM3NeT deep-sea neutrino telescope". *Nuclear Instruments and Methods in Physics Research A* 766 (Dec. 2014) 83–87. arXiv:1408.1392 [astro-ph.IM] (cit. on p. 135).

Marinucci, A. et al. "NuSTAR catches the unveiling nucleus of NGC 1068". *Monthly Notices of the Royal Astronomical Society* 456.1 (Feb. 2016) L94–L98. arXiv:1511.03503 [astro-ph.HE] (cit. on p. 30).

Markov, M. A. "On high energy neutrino physics". *10th International Conference on High Energy Physics*. 1960 p. 578 (cit. on pp. 39, 45).

Massaro, E. et al. "The 5th edition of the Roma-BZCAT. A short presentation". *Astrophysics and Space Science* 357.1, 75 (May 2015) 75. arXiv:1502.07755 [astro-ph.HE] (cit. on pp. 2, 99, 126).

Maurin, D. et al. "A cosmic-ray database update: CRDB v4.1". *European Physical Journal C* 83.10, 971 (Oct. 2023) 971. arXiv:2306.08901 [astro-ph.HE] (cit. on pp. 6, 15).

McDaniel, A., Ajello, M., and Karwin, C. "Gamma-Ray Emission from Galaxies Hosting Molecular Outflows". *Astrophysical Journal* 943.2, 168 (Feb. 2023) 168. arXiv:2301.02574 [astro-ph.HE] (cit. on p. 31).

Morrison, P. "On gamma-ray astronomy". *Il Nuovo Cimento* 7.6 (Mar. 1958) 858–865 (cit. on p. 10).

Mücke, A. et al. "Photohadronic Processes in Astrophysical Environments". *Publications of the Astronomical Society of Australia* 16.2 (Aug. 1999) 160–166. arXiv:astro-ph/9808279 [astro-ph] (cit. on p. 32).

Murase, K. "Hidden Hearts of Neutrino Active Galaxies". *Astrophysical Journal Letters* 941.1, L17 (Dec. 2022) L17. arXiv:2211.04460 [astro-ph.HE] (cit. on pp. 24, 33, 36, 124).

Murase, K., Ahlers, M., and Lacki, B. C. "Testing the hadronuclear origin of PeV neutrinos observed with IceCube". *Physical Review D* 88.12, 121301 (Dec. 2013) 121301. arXiv:1306.3417 [astro-ph.HE] (cit. on p. 111).

Murase, K., Guetta, D., and Ahlers, M. "Hidden Cosmic-Ray Accelerators as an Origin of TeV-PeV Cosmic Neutrinos". *Physical Review Letters* 116.7, 071101 (Feb. 2016) 071101. arXiv:1509.00805 [astro-ph.HE] (cit. on pp. 16, 32, 116).

Murase, K., Mukhopadhyay, M., et al. "Neutrinos from the Brightest Gamma-Ray Burst?" *Astrophysical Journal Letters* 941.1, L10 (Dec. 2022) L10. arXiv:2210.15625 [astro-ph.HE] (cit. on p. 18).

Naab, R. et al. "Measurement of the astrophysical diffuse neutrino flux in a combined fit of IceCube's high energy neutrino data". *Proceedings of 38th International Cosmic Ray Conference — PoS(ICRC2023)*. Vol. 444. 2023 p. 1064 (cit. on pp. 12, 15, 37, 45, 76, 133).

Nanni, R. et al. "The deep Chandra survey in the SDSS J1030+0524 field". *Astronomy & Astrophysics* 637, A52 (May 2020) A52. arXiv:2003.13710 [astro-ph.GA] (cit. on p. 35).

Neff, S. G. et al. "Ultraviolet Imaging of the AGN + Starburst Galaxy NGC 1068". *Astrophysical Journal* 430 (Aug. 1994) 545 (cit. on p. 23).

Neronov, A., Savchenko, D., and Semikoz, D. V. "Neutrino Signal from a Population of Seyfert Galaxies". *Physical Review Letters* 132.10, 101002 (Mar. 2024) 101002 (cit. on p. 35).

Neunhöffer, T. "Estimating the angular resolution of tracks in neutrino telescopes based on a likelihood analysis". *Astroparticle Physics* 25.3 (Apr. 2006) 220–225. arXiv:astro-ph/0403367 [astro-ph] (cit. on p. 51).

Oh, K. et al. "The 105-Month Swift-BAT All-sky Hard X-Ray Survey". *Astrophysical Journal Suppl. Ser.* 235.1, 4 (Mar. 2018) 4. arXiv:1801.01882 [astro-ph.HE] (cit. on p. 116).

Oikonomou, F. "High-energy neutrino emission from blazars". *Proceedings of 37th International Cosmic Ray Conference — PoS(ICRC2021)*. Vol. 395. 2022 p. 030 (cit. on p. 132).

Padovani, P. et al. "Active galactic nuclei: what's in a name?" *Astron. Astrophys. Rev.* 25.1, 2 (Aug. 2017) 2. arXiv:1707.07134 [astro-ph.GA] (cit. on pp. 19–22).

Padovani, P., Boccardi, B., et al. "PKS 1424+240: yet another masquerading BL Lac object as a possible IceCube neutrino source". *Monthly Notices of the Royal Astronomical Society* 511.4 (Apr. 2022) 4697–4701. arXiv:2202.04363 [astro-ph.HE] (cit. on p. 132).

Padovani, P., Gilli, R., et al. "The neutrino background from non-jetted active galactic nuclei". *Astronomy & Astrophysics* 684, L21 (Apr. 2024) L21. arXiv:2404.05690 [astro-ph.HE] (cit. on pp. 34, 124, 133).

Padovani, P., Giommi, P., et al. "The spectra of IceCube neutrino (SIN) candidate sources - II. Source characterization". *Monthly Notices of the Royal Astronomical Society* 510.2 (Feb. 2022) 2671–2688. arXiv:2112.05394 [astro-ph.HE] (cit. on p. 29).

Padovani, P., Petropoulou, M., et al. "A simplified view of blazars: the neutrino background". *Monthly Notices of the Royal Astronomical Society* 452.2 (Sept. 2015) 1877–1887. arXiv:1506.09135 [astro-ph.HE] (cit. on pp. 22, 38, 123, 124).

Padovani, P., Resconi, E., Ajello, M., et al. "Supermassive black holes and very high-energy neutrinos: the case of NGC 1068". *arXiv e-prints*, arXiv:2405.20146 (May 2024) arXiv:2405.20146. arXiv:2405.20146 [astro-ph.HE] (cit. on pp. 23, 133).

Padovani, P., Resconi, E., Giommi, P., et al. “Extreme blazars as counterparts of IceCube astrophysical neutrinos”. *Monthly Notices of the Royal Astronomical Society* 457.4 (Apr. 2016) 3582–3592. arXiv:1601.06550 [astro-ph.HE] (cit. on p. 125).

Padovani, P. “On the two main classes of active galactic nuclei”. *Nature Astronomy* 1, 0194 (Aug. 2017) 0194. arXiv:1707.08069 [astro-ph.GA] (cit. on pp. 21, 23, 28).

Palladino, A., Spurio, M., and Vissani, F. “Neutrino Telescopes and High-Energy Cosmic Neutrinos”. *Universe* 6.2, 30 (Feb. 2020) 30. arXiv:2009.01919 [astro-ph.HE] (cit. on p. 56).

Park, J. et al. “Kinematics of the M87 Jet in the Collimation Zone: Gradual Acceleration and Velocity Stratification”. *Astrophysical Journal* 887.2, 147 (Dec. 2019) 147. arXiv:1911.02279 [astro-ph.HE] (cit. on p. 28).

Particle Data Group. “Review of Particle Physics”. *Progress of Theoretical and Experimental Physics* 2020.8 (Aug. 2020) 083C01. ISSN: 2050-3911. eprint: https://academic.oup.com/ptep/article-pdf/2020/8/083C01/34673722/ptaa104.pdf (cit. on pp. 43, 45).

Peretti, E. et al. “Gamma-ray emission from the Seyfert galaxy NGC 4151 and multimessenger implications for ultra-fast outflows”. *arXiv e-prints*, arXiv:2303.03298 (Mar. 2023) arXiv:2303.03298. arXiv:2303.03298 [astro-ph.HE] (cit. on p. 122).

Peters, B. “Primary cosmic radiation and extensive air showers”. *Il Nuovo Cimento* 22.4 (Nov. 1961) 800–819 (cit. on p. 7).

Pillera, R. et al. “GRB 221009A: Fermi-LAT refined analysis”. *GRB Coordinates Network* 32658 (Oct. 2022) 1 (cit. on p. 18).

Pizzuto, A. et al. “Realtime follow-up of astrophysical transients with the IceCube Neutrino Observatory”. *37th International Cosmic Ray Conference*. Mar. 2022 952 p. 952. arXiv:2107.09551 [astro-ph.HE] (cit. on p. 108).

Plavin, A. V. et al. “Directional Association of TeV to PeV Astrophysical Neutrinos with Radio Blazars”. *Astrophysical Journal* 908.2, 157 (Feb. 2021) 157. arXiv:2009.08914 [astro-ph.HE] (cit. on p. 100).

Plavin, A. et al. “Observational Evidence for the Origin of High-energy Neutrinos in Parsec-scale Nuclei of Radio-bright Active Galaxies”. *Astrophysical Journal* 894.2, 101 (May 2020) 101. arXiv:2001.00930 [astro-ph.HE] (cit. on p. 100).

Poluektov, A. “Kernel density estimation of a multidimensional efficiency profile”. *Journal of Instrumentation* 10.2, P02011 (Feb. 2015) P02011. arXiv:1411.5528 [physics.data-an] (cit. on p. 67).

Pontecorvo, B. “Inverse beta processes and nonconservation of lepton charge”. *Zh. Eksp. Teor. Fiz.* 34 (1957) 247 (cit. on p. 13).

Rädel, L. “Measurement of High-Energy Muon Neutrinos withthe IceCube Neutrino Observatory”. Veröffentlicht auf dem Publikationsserver der RWTH Aachen University; Dissertation, RWTH Aachen University, 2017. Dissertation. Aachen: RWTH Aachen University, 2017 (cit. on p. 48).

Rädel, L. and Wiebusch, C. “Calculation of the Cherenkov light yield from electromagnetic cascades in ice with Geant4”. *Astroparticle Physics* 44 (Apr. 2013) 102–113. arXiv:1210.5140 [astro-ph.IM] (cit. on p. 41).

Reimann, R. “Search for the sources of the astrophysical high-energy muon-neutrino flux with the IceCube neutrino observatory”. PhD thesis. RWTH Aachen University, Germany, Jan. 2019 (cit. on pp. 48, 91, 94, 97).

Ricci, C. et al. "BAT AGN Spectroscopic Survey. V. X-Ray Properties of the Swift/BAT 70-month AGN Catalog". *Astrophysical Journal Suppl. Ser.* 233.2, 17 (Dec. 2017) 17. arXiv:1709.03989 [astro-ph.HE] (cit. on pp. 37, 116, 117, 134).

Riehn, F. et al. "The hadronic interaction model Sibyll 2.3c and Feynman scaling". *Proceedings of 35th International Cosmic Ray Conference — PoS(ICRC2017)*. Vol. 301. 2017 p. 301 (cit. on p. 56).

Rodrigues, X. et al. "The Spectra of IceCube Neutrino (SIN) candidate sources – V. Modeling and interpretation of multiwavelength and neutrino data". *arXiv e-prints*, arXiv:2406.06667 (June 2024) arXiv:2406.06667. arXiv:2406.06667 [astro-ph.HE] (cit. on p. 86).

Roy, A. L. et al. "Slow jets in Seyfert Galaxies: NGC 1068". *EVN Symposium 2000, Proceedings of the 5th european VLBI Network Symposium*. Ed. by Conway, J. E. et al. Jan. 2000 p. 7. arXiv:astro-ph/0009408 [astro-ph] (cit. on p. 28).

Rybicki, G. B. and Lightman, A. P. "Radiative Processes in Astrophysics". 1986 p. 42 (cit. on p. 25).

Sanders, D. B. et al. "The IRAS Revised Bright Galaxy Sample". *Astronomical Journal* 126.4 (Oct. 2003) 1607–1664. arXiv:astro-ph/0306263 [astro-ph] (cit. on p. 27).

Schneider, A. "Characterization of the Astrophysical Diffuse Neutrino Flux with IceCube High-Energy Starting Events". *36th International Cosmic Ray Conference (ICRC2019)*. Vol. 36. International Cosmic Ray Conference. July 2019 1004 p. 1004. arXiv:1907.11266 [astro-ph.HE] (cit. on p. 12).

Schwefer, G., Mertsch, P., and Wiebusch, C. "Diffuse Emission of Galactic High-energy Neutrinos from a Global Fit of Cosmic Rays". *Astrophysical Journal* 949.1, 16 (May 2023) 16. arXiv:2211.15607 [astro-ph.HE] (cit. on pp. 75, 155, 163).

Seyfert, C. K. "Nuclear Emission in Spiral Nebulae." *Astrophysical Journal* 97 (Jan. 1943) 28 (cit. on pp. 24, 118).

Silberberg, R. and Shapiro, M. M. "Neutrinos as a Probe for the Nature of and Processes in Active Galactic Nuclei". *International Cosmic Ray Conference*. Vol. 10. International Cosmic Ray Conference. Jan. 1979 p. 357 (cit. on p. 32).

Smith, M. W. E. et al. "The Astrophysical Multimessenger Observatory Network (AMON)". *Astroparticle Physics* 45 (May 2013) 56–70. arXiv:1211.5602 [astro-ph.HE] (cit. on p. 60).

Sommani, G., Franckowiak, A., et al. "Two 100 TeV neutrinos coincident with the Seyfert galaxy NGC 7469". *arXiv e-prints*, arXiv:2403.03752 (Mar. 2024) arXiv:2403.03752. arXiv:2403.03752 [astro-ph.HE] (cit. on p. 119).

Sommani, G., Lagunas Gualda, C., Niederhausen, H., et al. "Towards a more robust reconstruction method for IceCube's real-time program". *Proceedings of 38th International Cosmic Ray Conference — PoS(ICRC2023)*. Vol. 444. 2023 p. 1186 (cit. on p. 51).

Spinoglio, L., Fernández-Ontiveros, J. A., and Malkan, M. A. "The High-ionization IR Fine Structure Lines as Bolometric Indicators of the AGN Power: Study of the Complete 12 $\mu$m AGN Sample". *Astrophysical Journal* 941.1, 46 (Dec. 2022) 46. arXiv:2210.02488 [astro-ph.GA] (cit. on p. 30).

Spurio, M. *Particles and Astrophysics: A Multi-Messenger Approach*. Astronomy and Astrophysics Library. Springer International Publishing, 2014. ISBN: 9783319080512 (cit. on p. 7).

Spurio, M. *Probes of Multimessenger Astrophysics*. 2018 (cit. on pp. 9, 16, 18).

Stecker, F. W. "Diffuse fluxes of cosmic high-energy neutrinos." *Astrophysical Journal* 228 (Mar. 1979) 919–927 (cit. on p. 12).

Stettner, J. et al. "Measurement of the diffuse astrophysical muon-neutrino spectrum with ten years of IceCube data". *36th International Cosmic Ray Conference (ICRC2019)*. Vol. 36. International Cosmic Ray Conference. July 2019 1017 p. 1017. arXiv:1908.09551 [astro-ph.HE] (cit. on pp. 95, 107).

Tamborra, I., Ando, S., and Murase, K. "Star-forming galaxies as the origin of diffuse high-energy backgrounds: gamma-ray and neutrino connections, and implications for starburst history". *Journal of Cosmology and Astroparticle physics* 2014.9 (Sept. 2014) 043–043. arXiv:1404.1189 [astro-ph.HE] (cit. on p. 18).

Tanimoto, A. et al. "NuSTAR Observations of 52 Compton-thick Active Galactic Nuclei Selected by the Swift/Burst Alert Telescope All-sky Hard X-Ray Survey". *Astrophysical Journal Suppl. Ser.* 260.2, 30 (June 2022) 30. arXiv:2203.13266 [astro-ph.HE] (cit. on p. 124).

Tombesi, F. et al. "Evidence for ultra-fast outflows in radio-quiet AGNs. I. Detection and statistical incidence of Fe K-shell absorption lines". *Astronomy & Astrophysics* 521, A57 (Oct. 2010) A57. arXiv:1006.2858 [astro-ph.HE] (cit. on p. 122).

Tung, C. F. et al. "FIRESONG: A python package to simulate populations of extragalactic neutrino sources". *Journal of Open Source Software* 6.61 (2021) 3194 (cit. on p. 108).

Ueda, Y., Akiyama, M., Hasinger, G., et al. "Toward the Standard Population Synthesis Model of the X-Ray Background: Evolution of X-Ray Luminosity and Absorption Functions of Active Galactic Nuclei Including Compton-thick Populations". *Astrophysical Journal* 786.2, 104 (May 2014) 104. arXiv:1402.1836 [astro-ph.CO] (cit. on pp. 35, 37).

Ueda, Y., Akiyama, M., Ohta, K., et al. "Cosmological Evolution of the Hard X-Ray Active Galactic Nucleus Luminosity Function and the Origin of the Hard X-Ray Background". *Astrophysical Journal* 598.2 (Dec. 2003) 886–908. arXiv:astro-ph/0308140 [astro-ph] (cit. on p. 35).

Urry, C. M. and Padovani, P. "Unified Schemes for Radio-Loud Active Galactic Nuclei". *Publications of the Astronomical Society of the Pacific* 107 (Sept. 1995) 803. arXiv:astro-ph/9506063 [astro-ph] (cit. on pp. 19, 21, 125).

van Eijndhoven, N., Fadiran, O., and Japaridze, G. "Implementation of a Gauss convoluted Pandel PDF for track reconstruction in neutrino telescopes". *Astroparticle Physics* 28.4-5 (Dec. 2007) 456–462. arXiv:0704.1706 [astro-ph] (cit. on p. 49).

Veres, P. et al. "GRB 221009A: Fermi GBM detection of an extraordinarily bright GRB". *GRB Coordinates Network* 32636 (Oct. 2022) 1 (cit. on p. 18).

Völk, H. J., Aharonian, F. A., and Breitschwerdt, D. "The Nonthermal Energy Content and Gamma-Ray Emission of Starburst Galaxies and Clusters of Galaxies". *Space Science Reviews* 75.1-2 (Jan. 1996) 279–297 (cit. on pp. 10, 18).

Wang, J.-M. et al. "Dynamical evidence from the sub-parsec counter-rotating disc for a close binary of supermassive black holes in NGC 1068". *Monthly Notices of the Royal Astronomical Society* 497.1 (Sept. 2020) 1020–1028. arXiv:2005.01220 [astro-ph.GA] (cit. on p. 25).

Wang, J. et al. "Revisiting the Short-term X-ray Spectral Variability of NGC 4151 with Chandra". *Astrophysical Journal* 714.2 (May 2010) 1497–1510. arXiv:1003.6133 [astro-ph.CO] (cit. on p. 124).

Wang, X. and Loeb, A. "Cumulative neutrino background from quasar-driven outflows". *Journal of Cosmology and Astroparticle physics* 2016.12, 012 (Dec. 2016) 012. arXiv:1607.06476 [astro-ph.HE] (cit. on p. 22).

– "Probing the gaseous halo of galaxies through non-thermal emission from AGN-driven outflows". *Monthly Notices of the Royal Astronomical Society* 453.1 (Oct. 2015) 837–848. arXiv:1506.05470 [astro-ph.GA] (cit. on p. 22).

Waxman, E. "Cosmological Origin for Cosmic Rays above $10^{19}$ eV". *Astrophysical Journal Letters* 452 (Oct. 1995) L1. arXiv:astro-ph/9508037 [astro-ph] (cit. on p. 14).

Waxman, E. and Bahcall, J. "High energy neutrinos from astrophysical sources: An upper bound". *Physical Review D* 59.2, 023002 (Dec. 1998) 023002. arXiv:hep-ph/9807282 [hep-ph] (cit. on pp. 14, 15, 39).

Whitehorn, N., van Santen, J., and Lafebre, S. "Penalized splines for smooth representation of high-dimensional Monte Carlo datasets". *Computer Physics Communications* 184.9 (Sept. 2013) 2214–2220. arXiv:1301.2184 [physics.data-an] (cit. on pp. 50, 67).

Wilks, S. S. "The Large-Sample Distribution of the Likelihood Ratio for Testing Composite Hypotheses". *The Annals of Mathematical Statistics* 9.1 (1938) 60–62. ISSN: 00034851 (cit. on pp. 63, 84, 159).

Willox, E. and HAWC Collaboration. "HAWC Follow-up on IceCube evidence from NGC 1068". *The Astronomer's Telegram* 15765 (Nov. 2022) 1 (cit. on pp. 26, 116).

Wolf, M. "SkyLLH - A generalized Python-based tool for log-likelihood analyses in multi-messenger astronomy". *36th International Cosmic Ray Conference (ICRC2019)*. Vol. 36. International Cosmic Ray Conference. July 2019 1035 p. 1035. arXiv:1908.05181 [astro-ph.IM] (cit. on p. 77).

Zaino, A. et al. "Probing the circumnuclear absorbing medium of the buried AGN in NGC 1068 through NuSTAR observations". *Monthly Notices of the Royal Astronomical Society* 492.3 (Mar. 2020) 3872–3884. arXiv:2001.05499 [astro-ph.GA] (cit. on pp. 29, 30).

Zatsepin, G. T. and Kuz'min, V. A. "Upper Limit of the Spectrum of Cosmic Rays". *Soviet Journal of Experimental and Theoretical Physics Letters* 4 (Aug. 1966) 78 (cit. on p. 8).